

Sensitivity analysis and optimization in low order thermoacoustic models



José Guillermo Aguilar Pérez

Department of Engineering
University of Cambridge

This dissertation is submitted for the degree of
Doctor of Philosophy

Declaration

I hereby declare that except where specific reference is made to the work of others, the contents of this dissertation are original and have not been submitted in whole or in part for consideration for any other degree or qualification in this, or any other university. This dissertation is my own work and contains nothing which is the outcome of work done in collaboration with others, except as specified in the text and Acknowledgements. This dissertation contains fewer than 65,000 words including appendices, bibliography, footnotes, tables and equations and has fewer than 150 figures.

José Guillermo Aguilar Pérez
August 2018

Abstract

Sensitivity analysis and optimization in low order thermoacoustic models

José Guillermo Aguilar Pérez

Lean combustion technologies in gas turbines reduce the generation of NO_x but increase the susceptibility to thermoacoustic oscillations. These oscillations can produce structural damage and need to be eliminated. The stability of a given configuration can be examined with a thermoacoustic model. In this thesis a wave-based network model is used. Using adjoint methods the gradients of the eigenvalue with respect to system parameters can be obtained at a low computational cost. This information is used as an input to an optimization routine to find stable thermoacoustic configurations.

In this thesis thermocoustic oscillations are analysed using a linear low order network model. This modelling approach is used to predict the unstable modes of five different configurations: a Rijke tube, a choked combustor, a longitudinal combustor, a generic lean premix prevaporized annular combustor and the laboratory scale annular combustor built in Cambridge University Engineering Department. The continuous and discrete adjoint equations for the low order network model are derived. Using the adjoint equations the sensitivities of the eigenvalues to changes in base state parameters such as time delays, areas, lengths and mean radii are computed. Similarly, the sensitivity of the eigenvalues to the introduction of a feedback device such as a drag mesh or a secondary heat source is investigated. By fitting experimental data to a low Mach number model of the Rijke tube, the predictions of the growth rate and frequency shifts due to the presence of these mechanisms are improved. Finally, using the sensitivity information, two different optimization algorithms are developed to stabilize the thermoacoustic systems. Different stabilization scenarios are presented, showing the changes required in each section of the configurations to eliminate thermoacoustic oscillations.

The techniques presented as part of this thesis are readily scalable to more complex models and geometries and the inclusion of further constraints. This demonstrates that adjoint-based sensitivity analysis and optimization could become an indispensable tool for the design of thermoacoustically-stable combustors.

To my family.

Acknowledgements

First of all, I would like to thank my supervisor Professor Matthew Juniper who offered me the possibility of joining his group, challenged me to perform top quality research, and taught me to be very critical in writing and communicating scientific ideas. It was an extraordinary experience.

Special thanks to Dr. Luca Magri for his constant support throughout my entire PhD, especially during the first months of my studies, which were critical for my understating of the field. Thanks for all the guidance, discussions, and collaborations.

Moreover, I would like to extend my gratitude to Dr. Alessandro Orchini for solving all of my questions with regards to modelling, maths, coding, etc. Without his assistance I would have probably taken dozens of extra hours to figure things out.

My time in the office was amazing thanks to all of the people in it. In no particular order: Pau, Nick, Hans, Jack, Petr, Juan, Jenna, Tejal, Filip, Ubaid, Erwan, Maxim, Stefano, Caroline, Anh Khoa, Georgios, Bernhard, Jocelino, Francesca and Francesco. Tea time, conference trips, puzzles, barbecues and dinners would have not been the same without you.

A particular mention goes to Caroline, whom at the beginning of my PhD mentioned "life would be easier at constant specific heat capacities". After all the struggle I went using the variable specific heat formulation I can only say, "I totally agree with you".

Cambridge would not have been the same if I had not met all the incredible people from college, especially Henry, Johannes, Jos, Rachel, and Hayden. Thanks to you I did not have to talk about *rocket science* everywhere.

Thanks to the teams who kept me out of the office, in the river every morning, CCBC, and on the dance floor every Thursday night, BODT.

A special mention goes to Bianca, with whom I shared an amazing experience during the last year of my PhD and who probably pushed me more than anyone else to write this thesis.

Finally, I would like to thank my family, as their constant support was key for my success in this adventure.

This work was financially supported by CONACyT and Cambridge Trust.

Table of contents

List of figures	xv
List of tables	xix
1 Introduction	1
1.1 Thermoacoustic instabilities	1
1.1.1 The Rayleigh criterion	3
1.2 Thermoacoustic modelling	4
1.3 Linear stability analysis	7
1.4 Mitigating thermoacoustic instabilities	7
1.5 Adjoint methods in fluid problems	9
1.5.1 Adjoint methods in thermoacoustics	10
1.5.2 Optimization in Thermoacoustics	11
1.6 Thesis scope and structure	12
2 Low order network models	15
2.1 Low order modelling	15
2.2 The governing equations	16
2.3 Network modules	17
2.3.1 Straight ducts	17
2.3.2 Area increase	19
2.3.3 Area decrease	20
2.3.4 Ring of premix ducts	20
2.3.5 Heat Sources	21
2.3.6 Boundary conditions	23
2.4 Equations in the zero Mach number limit	25
2.4.1 Ducts	25
2.4.2 Area changes	26

2.4.3	Heat sources	26
2.5	Nonlinear eigenvalue problem	27
3	Stability analysis of thermoacoustic configurations	29
3.1	Stability analysis	29
3.2	Thermoacoustic models	31
3.3	The Rijke tube	31
3.4	Choked combustor	34
3.5	Longitudinal combustor	37
3.6	LPP annular combustor	40
3.7	CUED Annular combustor	42
4	Adjoint methods in wave based approaches	47
4.1	Introduction	47
4.2	The adjoint equations	48
4.2.1	Continuous adjoint	48
4.2.2	Discrete adjoint	49
4.2.3	Continuous vs discrete adjoint equations	50
4.3	Adjoint equations in the Rijke Tube: A worked example	50
4.3.1	Adjoint eigenvalue problem and sources of non-self-adjointness	52
4.4	Adjoint equations for network modules	53
4.4.1	Adjoint perturbation equations	54
4.4.2	Adjoint base flow equations	64
5	Sensitivity analysis of thermoacoustic configurations	75
5.1	Computing sensitivities of base state parameters	76
5.1.1	Continuous adjoint	76
5.1.2	Discrete adjoint	79
5.2	Computing sensitivities of feedback mechanisms	80
5.2.1	Feedback from unsteady mechanisms	80
5.2.2	Feedback from steady mechanisms	86
5.3	Continuous vs discrete approach	87
5.4	Finite difference method and the Taylor test	88
5.5	Sensitivity analysis of the Rijke tube	88
5.5.1	Experimental sensitivity analysis of the Rijke tube	90
5.6	Sensitivity analysis of the choked combustor	96

5.7	Sensitivity analysis of geometric parameters	100
5.7.1	Longitudinal combustor	100
5.7.2	LPP annular combustor	100
5.7.3	CUED annular combustor	101
5.7.4	Summary	102
6	Optimization in low order thermoacoustic networks	107
6.1	The optimization algorithms	108
6.1.1	Algorithm 1: Box search	108
6.1.2	Algorithm 2: Conjugate gradient	110
6.1.3	Parameter change in the implementation	112
6.2	Test Case	112
6.3	Stabilization of thermoacoustic configurations	114
6.3.1	Stabilizing the longitudinal combustor	115
6.3.2	Stabilizing the LPP annular combustor	119
6.3.3	Stabilizing the CUED annular combustor	125
6.3.4	Summary of optimization results	128
7	Conclusions and future work	131
7.1	Future work	135
	References	137
	Appendix A Flame transfer functions	149
A.1	V-shaped FTF	150
A.2	Annular cone FTF	154
	Appendix B Mean Flow matrix $L(\omega)$	157
	Appendix C Sensitivities to base flow modifications at the jump conditions	159
	Appendix D The triviality of choice of side on which a perturbation is applied	163
	Appendix E Computing matrix δL for the Rijke tube	165

List of figures

1.1	Ruben's tube.	1
1.2	Feedback loop in thermoacoustics.	2
1.3	Network modules.	6
1.4	Control strategies to eliminate thermoacoustic oscillations.	8
3.1	Dependence of acoustic driving $H(A)$ and damping $D(A)$ on amplitude A , from Lieuwen (2005)	29
3.2	Network model of the Rijke tube.	32
3.3	Logarithmic boundary error plot of the Rijke tube.	33
3.4	Pressure and velocity mode shapes of the Rijke tube.	34
3.5	Network model of a choked combustor.	35
3.6	Logarithmic boundary error plot for the choked combustor.	36
3.7	Pressure, velocity and density mode shapes for the choked combustor. . .	37
3.8	Schematic of the longitudinal combustor.	38
3.9	FTF for the annular-cone flame used in the longitudinal combustor. . . .	39
3.10	Logarithmic boundary error plot for the longitudinal combustor.	39
3.11	Network model of the LPP annular combustor.	40
3.12	Logarithmic boundary error plot for the LPP annular combustor with azimuthal wave numbers $n = 0$ and $n = \pm 1$	41
3.13	Network model of the CUED annular combustor.	43
3.14	Challenges in modelling the CUED annular combustor.	43
3.15	FTF for a V shaped flame with the geometric parameters of the CUED annular combustor.	44
3.16	Eigenvalues of the CUED annular combustor with azimuthal wave numbers $ n = 0, 1, \dots, 8$	45
3.17	Pressure mode shapes of the unstable modes around 1100 Hz in the CUED annular combustor.	46

5.1	Duct with area changes in both sides.	77
5.2	Splitting the network model due to feedback mechanisms.	83
5.3	Receptivity to the momentum and energy equations.	88
5.4	Eigenvalue shift caused by a change in the base state variables of the Rijke tube.	89
5.5	Eigenvalue shift for each feedback mechanism in the Rijke tube.	90
5.6	Growth rates and frequencies of the dominant mode in the Rijke tube.	91
5.7	Eigenvalue shift due to the unsteady and steady drag devices in the Rijke tube.	93
5.8	Total eigenvalue shift due to the presence of a drag device in the Rijke tube.	93
5.9	Eigenvalue shift due to the unsteady and steady heat source devices in the Rijke tube.	95
5.10	Total eigenvalue shift due to the presence of a secondary heat source in the Rijke tube.	96
5.11	Receptivities of the choked combustor.	97
5.12	Eigenvalue shift caused by a change in the base state variables of the choked combustor.	98
5.13	Eigenvalue shift for each feedback mechanism in the choked combustor.	99
5.14	Taylor tests for the longitudinal combustor.	101
5.15	Growth rate sensitivity maps for the unstable modes in the initial configuration of the longitudinal combustor.	102
5.16	Taylor tests for the LPP annular combustor.	103
5.17	Sensitivity to changes in the time delay of the LPP annular combustor.	103
5.18	Growth rate sensitivity maps for the unstable modes in the initial configuration of the LPP annular combustor.	104
5.19	Taylor tests for the CUED annular combustor.	104
5.20	Growth rate sensitivity maps for the unstable modes in the initial configuration of the CUED annular combustor.	105
6.1	Simplified network model for the test case.	112
6.2	Boundary error plot for the initial configuration of the test case network model.	113
6.3	Cost function for the test case.	113
6.4	Initial and final configurations for the test case.	114
6.5	Initial and final configuration of the longitudinal combustor after stabilizing all of the unstable modes by changing the areas and mean radii.	116

6.6	Initial and final configuration of the longitudinal combustor after stabilizing all of the unstable modes by changing the areas, mean radii and lengths.	117
6.7	Initial and final configuration of the longitudinal combustor after stabilizing all of the unstable modes by changing the areas, mean radii and lengths. Lowest frequency mode stabilized first.	118
6.8	Initial and final configuration of the LPP annular combustor after stabilizing all of the unstable modes by changing the areas.	120
6.9	Initial and final configuration of the LPP annular combustor after stabilizing all of the unstable modes by changing the areas and mean radii. . . .	121
6.10	Initial and final configuration of the LPP annular combustor after stabilizing all of the unstable modes by changing the areas and lengths.	122
6.11	Initial and final configuration of the LPP annular combustor after stabilizing all of the unstable modes by changing the areas, lengths and mean radii.	123
6.12	Initial and final configuration of the LPP annular combustor after stabilizing all of the unstable modes by changing the areas, lengths, mean radii and time delay.	124
6.13	Initial and final configuration of CUED annular combustor after stabilizing all of the unstable modes by changing the areas and mean radii.	126
6.14	Initial and final configuration of CUED annular combustor after stabilizing all of the unstable modes by changing the areas, mean radii and lengths.	127
A.1	Geometry of the flame holder and flame initiation surface from Dowling (1999)	150
A.2	Flame transfer function for a single burner used in the CUED annular combustor.	154
A.3	Geometry of the flame holder and flame initiation surface, adapted from Hubbard and Dowling (1998)	154
A.4	Components of the flame transfer function for the longitudinal combustor.	155

List of tables

2.1	Mean and fluctuating quantities for fluxes and entropy.	20
3.1	Frequencies of the unstable modes of the CUED annular combustor. . . .	45
5.1	Fitted values for the network model based on the experimental Rijke tube.	91
5.2	Mean wall temperatures at different positions in the experimental Rijke tube. Adapted from Fig. 4 in Jamieson et al. (2017)	94
6.1	Relative change of the final area/mean radius with respect to the initial area/mean radius of a section for case 1 in the stabilization of the longitudinal combustor.	116
6.2	Relative change of the final area/mean radius/length with respect to the initial area/mean radius/length of a section for case 2 in the stabilization of the longitudinal combustor.	117
6.3	Relative change of the final area/mean radius/length with respect to the initial area/mean radius/length of a section for case 2 (lowest frequency mode first) in the stabilization of the longitudinal combustor.	118
6.4	Relative change of the final area with respect to the initial area of a section for case 1 in the stabilization of the LPP annular combustor.	120
6.5	Relative change of the final area/mean radius with respect to the initial area/mean radius of a section for case 2 in the stabilization of the LPP annular combustor.	121
6.6	Relative change of the final area/length with respect to the initial area/length of a section for case 3 in the stabilization of the LPP annular combustor.	122
6.7	Relative change of the final area/length/mean radius with respect to the initial area/length/mean radius of a section for case 4 in the stabilization of the LPP annular combustor.	123

6.8	Relative change of the final area/length/mean radius/time delay with respect to the initial area/length/mean radius/time delay of a section for case 5 in the stabilization of the LPP annular combustor.	124
6.9	Relative change of the final area/mean radius with respect to the initial area/mean radius of a section for case 1 in the stabilization of the CUED annular combustor.	127
6.10	Relative change of the final area/length/mean radius with respect to the initial area/length/mean radius of a section for case 2 in the stabilization of the CUED annular combustor.	128

Chapter 1

Introduction

Standing waves of fire is how [Muller \(2014\)](#) describes the fascinating patterns generated by a two dimensional flame table, also known as a (2D) Ruben's tube. The device was originally designed by [Rubens and Krigar-Menzel \(1905\)](#) using a duct with regularly spaced holes through which flammable gas is burned (see Fig. 1.1). When the duct is forced with an organ pipe or a tuning fork at one of its natural frequencies, it enables the visualization of the standing wave patterns, which aided in the understanding of acoustics.

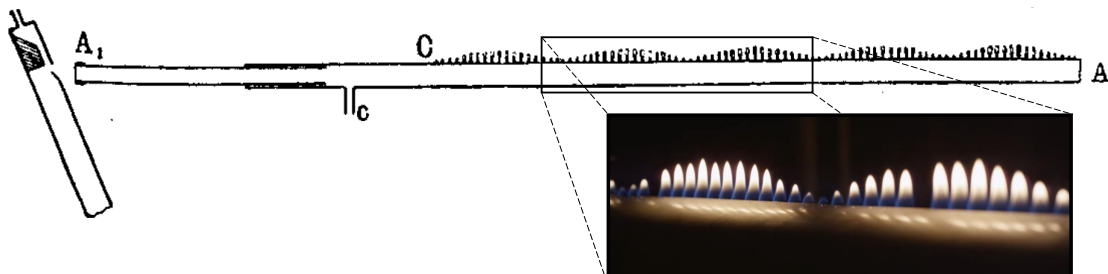


Fig. 1.1 Ruben's tube as detailed in [Rubens and Krigar-Menzel \(1905\)](#).

Perhaps more interesting than the visual aid, is the fact that the flames respond to the acoustic field. This phenomenon is critical in combustion dynamics because, when it is properly excited inside a cavity, a feedback loop can be created causing thermoacoustic instabilities.

1.1 Thermoacoustic instabilities

Thermoacoustic instabilities are a form of unstable combustion. They arise in devices that continuously burn fuel in order to generate thrust or some form of mechanical energy. In

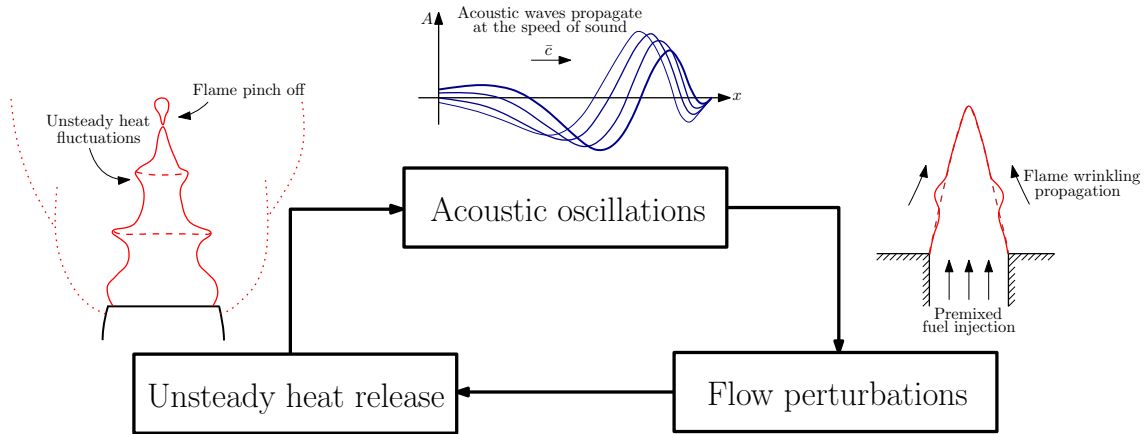


Fig. 1.2 Thermoacoustic oscillations are caused by unsteady heat release interacting with acoustics in a cavity, closing a feedback loop.

general, the steady state of combustion will be accompanied by small unsteady heat release fluctuations that, when coupled with pressure fluctuations, can cause thermoacoustic instabilities (Fig. 1.2). This is because the flame, being a source of volume, acts as a distribution of monopoles producing acoustic waves that propagate and then reflect at the boundaries to interact again with the flame. If the unsteadiness of the flame is sufficiently in phase with the acoustic field, small amplitude pressure oscillations will begin to grow in time and, after many cycles, gain a considerable amplification which could be enough to cause flame blow off or structural damage (Lieuwen and Yang, 2005).

The first account of thermoacoustic oscillations was in the 18th century due to Higgins who described the generation of *sweet sounds* coming out from a tube burning hydrogen (Higgins, 1802). At this point the phenomenon was not yet completely understood. It took nearly a century until Lord Rayleigh developed the theory behind the thermoacoustic effect (Rayleigh, 1878). Five decades after this publication, thermoacoustic instabilities became relevant for the aerospace industry. They were first observed in the late 1930s during the development of liquid and solid state rockets. Then, in the 1950s, they appeared in the afterburners and ramjets used in turbojet engines (Culick, 2006).

More recently, stringent emission regulations are motivating the development of aero-engine and gas turbine combustors that operate in lean regimes. These run at lower temperatures to prevent the dissociation of air molecules and therefore reduce the formation of NO_x gases. However, these operating conditions encourage the development of combustion instabilities (Lieuwen et al., 2001).

1.1.1 The Rayleigh criterion

The first qualitative explanation for the thermoacoustic mechanism was proposed by [Rayleigh \(1878\)](#):

If heat be given to the air at the moment of greatest condensation, or taken from it at the moment of greatest rarefaction, the vibration is encouraged. On the other hand, if heat be given at the moment of greatest rarefaction, or abstracted at the moment of greatest condensation, the vibration is discouraged.

The first mathematical formulation of the Rayleigh criterion was given in terms of acoustic energy (E_{ac}) by [Putnam and Dennis \(1954\)](#) and [Chu \(1956\)](#), which by assuming a zero mean flow and neglecting heat diffusivity and viscosity reads:

$$\underbrace{\frac{\partial}{\partial t} \left(\frac{1}{2} \bar{\rho} \mathbf{u}'^2 + \frac{1}{2} \frac{p'^2}{\gamma \bar{p}} \right)}_{E_{ac}} + \nabla \cdot (p' \mathbf{u}') = \frac{\gamma - 1}{\gamma \bar{p}} p' Q', \quad (1.1)$$

where p is the pressure, \mathbf{u} the velocity, ρ the density, γ the ratio of specific heat capacities, Q the heat release, the over bar ($\bar{}$) represents a mean quantity and the prime ($'$) denotes a fluctuating quantity. After integration in time and space, we observe that for the acoustic energy to grow, the heat release term must be larger than the energy dissipated at the boundaries. This is formally known as the extended the Rayleigh criterion:

$$\int_T \int_V \frac{\gamma - 1}{\gamma \bar{p}} p' Q' \, dV \, dt > \int_T \int_S p' \mathbf{u}' \cdot \mathbf{n} \, dS \, dt, \quad (1.2)$$

where T is a period of oscillation, V is the volume and \mathbf{n} is the unit vector normal to the boundaries which are represented by S . (The classic Rayleigh criterion does not take into account the energy dissipation at the boundaries.) When the magnitude of the phase difference between the pressure fluctuations p' and the heat release fluctuations Q' is less than ninety degrees, the constructive interference converts heat release (thermal energy) into acoustic energy (mechanical energy).

The previous formulation is for the case of zero mean flow. When there is a non-zero mean flow, acoustic and entropy fluctuations (which occur naturally when there is a source of heat input) become coupled. For this case [Chu \(1965\)](#) extended the energy norm to include entropy fluctuations. The reader is referred to [Myers \(1991\)](#) for a detailed derivation of the energy norm which includes a mean flow and to [Nicoud and Poinso \(2005\)](#) for its corresponding criteria for combustion instability.

1.2 Thermoacoustic modelling

Thermoacoustic oscillations are usually undesirable. They have been the focus of research in the last 70 years in order to develop strategies to prevent them. Most modelling approaches begin by applying conservation equations of mass, momentum and energy in a given domain. By assuming a steady and uniform mean flow the inhomogeneous (convected) wave equation together with the equations for entropy and vorticity perturbations are derived:

$$\frac{1}{\bar{c}^2} \frac{\bar{D}^2 p'}{Dt^2} - \nabla^2 p' = \frac{\gamma - 1}{\bar{c}^2} \frac{\bar{D} Q'}{Dt}, \quad (1.3)$$

$$\bar{\rho} \bar{T} \frac{\bar{D} s'}{Dt} = Q', \quad (1.4)$$

$$\frac{\bar{D} \boldsymbol{\xi}'}{Dt} = \mathbf{0}, \quad (1.5)$$

where c is the speed of sound, $\bar{D}/Dt \equiv \partial/\partial t + \bar{\mathbf{u}} \cdot \nabla$, T is the temperature, s is the entropy, $\boldsymbol{\xi}$ the vorticity and it is assumed that $\bar{\boldsymbol{\xi}} = \mathbf{0}$. Whenever the domain considered has no unsteady heat release [Chu and Kovásznyai \(1958\)](#) showed that to first order any wave can be considered as a linear superposition of acoustic, entropy or vorticity fluctuations. In this framework the acoustic fluctuations, which travel at the corrected speed of sound ($\bar{c} \pm \bar{u}$), are treated as isentropic and irrotational. Entropy fluctuations, which travel at the mean flow speed (\bar{u}), are treated as incompressible and irrotational. Vorticity waves, which propagate at the mean flow speed, are treated as incompressible and isentropic. At second order there are interactions between these fluctuations and they can no longer be considered independent. When compositional inhomogeneities are present in the flow, [Ihme \(2017\)](#) extended the previous analysis and introduced a compositional wave proportional to the mixture fraction of the flow, which is also convected at the mean flow speed.

The acceleration of waves that convect at the mean flow speed is of particular importance since they produce so-called indirect noise. If acceleration occurs in a combustion chamber due to a choked end at the outlet, these waves generate another mechanism of combustion instabilities. [Marble and Candel \(1977\)](#) showed that, for a compact nozzle, an accelerating entropy wave produces indirect noise. [Magri et al. \(2016c\)](#) extended that analysis to show a similar behaviour with compositional waves. [Dowling and Mahmoudi \(2015\)](#) demonstrated that the same occurs for vorticity waves but that their contribution to the total indirect noise is almost negligible.

To predict the onset of combustion instabilities, a variety of modelling techniques is available. [Nicoud and Wieczorek \(2009\)](#) classify them into 3 main groups:

- **Large Eddy Simulation (LES).** This describes the spatio-temporal evolution of all flow quantities. It can model turbulent, reacting and compressible flows in great detail (see for example [Selle et al. \(2004\)](#)). Its major drawback is the computational power required.
- **Helmholtz solvers.** They describe the spatio-temporal evolution of fluctuating quantities in a given domain by solving the Helmholtz equation, which is given by Eq. (1.3) in the low Mach number limit ($\bar{u} \rightarrow 0$) ([Nicoud et al., 2007](#)). It has the advantage of being able to describe multiple modes and boundary conditions, but it is constrained to the low Mach number approximation.
- **Low order network models.** These contain lumped elements that describe the wave amplitudes in each module at a given frequency (See for example [Lieuwen and Zinn \(2000\)](#)). They have the advantage of being able to handle complex boundary conditions and of being computationally cheap, but the drawback of only working with frequencies low enough such that the radial or transverse modes are cut off in the ducts and with area changes which span over a distance short enough such that they can be considered acoustically compact. Furthermore, the complex geometrical details of a real combustor cannot be accounted for.

Due to their speed and versatility, network models have found use in industry in academia, and therefore, are the core focus of this thesis. In these models, the inhomogeneous wave equation (1.3) is solved either in the time domain, or in the frequency domain. In the time domain, it is solved using state space models ([Bellucci et al., 2005](#)). In the frequency space, it is common to use Galerkin methods ([Culick, 1988](#)) or wave-based methods ([Dowling, 1995](#)). The second is more flexible when dealing with complicated geometries and is also less prone to numerical errors, such as those arising due to numerical discretization (Gibbs phenomenon), when attempting to capture velocity discontinuities across a heat source with continuous spatial modes.

Following this framework, in a low order network model the main elements are the ducts in which the waves propagate. To reproduce a full geometry, each of the ducts is connected with transfer matrices representing area changes, heat sources and boundary conditions (Fig. 1.3). These modules operate under the acoustically compact assumption. In order to guarantee that, for example, a flame can be treated as a compact element, the acoustic wave length (λ_a) must be much larger than the flame length (L_f): $L_f/\lambda_a \ll 1$

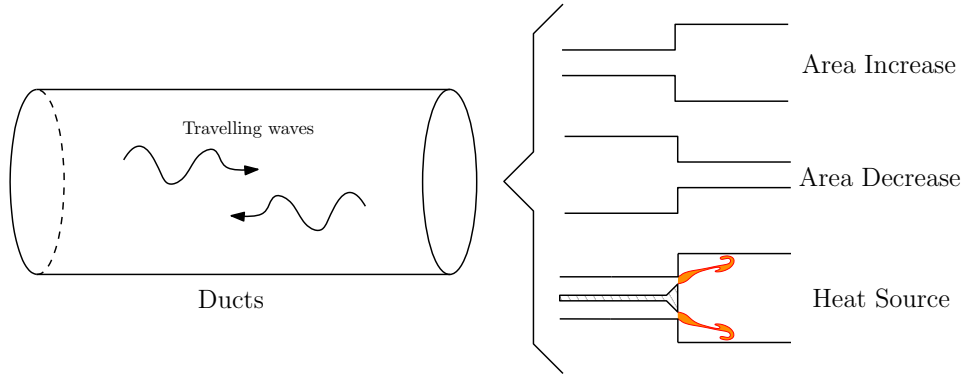


Fig. 1.3 The main elements of a network models are the ducts. These are connected with different modules that ensure conservation of different fluxes.

(Dowling, 1995; Poinso and Veynante, 2005). A similar conclusion can be drawn for other jump conditions such as area changes. The presence of disturbances that convect with the mean flow, such as equivalence ratio fluctuations or hot spots (entropy waves), impose a stricter condition. This requires the wave length of the convected disturbance λ_c to be much smaller than the length of the flame ($L_f/\lambda_c \ll 1$). These type of disturbances convect away with the mean flow. Therefore, for open ended boundary conditions at the exit, the latter condition can be relaxed. This is, as discussed above, not the case for compact nozzles or choked ends of a combustor and can introduce numerical errors in the computations (Nicoud and Wieczorek, 2009).

The key element of a network model in the analysis of thermoacoustic oscillations is the heat source, which is also the main nonlinear element in the system. The most general modelling approach is by means of a flame describing function (FDF) (Dowling, 1997, 1999), where the flame response is characterized at different levels of forcing. This can be done using a single forcing frequency (single input) as in Noiray et al. (2008) or with two forcing frequencies (double input) as in Orchini and Juniper (2016a). The FDF is proportional to one of the system's perturbation variables (Lieuwen, 2003). For longitudinal combustors, velocity or mass flow rate perturbations are commonly used, e.g., Keller (1995). For annular configurations, pressure perturbations have also been used, e.g., Ghirardo and Juniper (2013); Noiray and Schuermans (2013). In the limit in which the forcing amplitude of the FDF becomes infinitesimal, we obtain the linear model better known as the flame transfer function (FTF). From the linear models, Crocco's time lag model (Crocco and Cheng, 1956) is perhaps one of the most used in linear stability analysis of combustion systems.

1.3 Linear stability analysis

Low order network models often consider the base flow to be homogeneous and only varying in one spatial direction with superposed small amplitude perturbations. For these type of problems, the stability of the flow is assessed with linear stability tools (Juniper et al., 2014; Schmid and Brandt, 2014), such as Lyapunov stability. This concept assumes the existence of an equilibrium state (base flow), which is then subject to a perturbation. The system is deemed to be stable if, after applying a perturbation, the system returns back to the equilibrium state. It is deemed unstable if it diverges from the equilibrium state. Lyapunov stability allows an infinite time horizon for the system to return to equilibrium.

Throughout this thesis we are going to assume the existence of small amplitude perturbations. Once the linearly unstable resonant modes have been identified, the next stage is to eliminate them.

1.4 Mitigating thermoacoustic instabilities

Thermoacoustic oscillations are usually eliminated by a combination of modelling, trial and error experimental testing, and addition of passive control devices such as Helmholtz resonators (Fig. 1.4). Configurations that are thought to be stable after engine component tests often turn out to be unstable during full engine tests (Mongia et al., 2003). At this stage, it is possible to perform several full engine tests on slightly different configurations until one is found that is stable across the entire operating regime (Oefelein and Yang, 1993). Usually, however, this is prohibitively expensive. It is more common to add passive control methods, such as acoustic liners, Helmholtz resonators, quarter and half wave tubes, baffles etc. (Richards et al., 2003; Zhao and Li, 2015). These exploit vortex shedding and viscous losses to add acoustic damping at selected frequencies. For example Zahn et al. (2016) showed that a quarter wave tube positioned at the azimuthal mode antinode maximises the damping ratio of the system. Their major drawback is that the damped frequency range can be quite narrow and they are usually unable to adjust to different operating conditions.

Another option is feedback control. This has been shown to be effective in laboratory combustors, and several full-scale rigs (Dowling and Morgans, 2005; Huang and Yang, 2009; Zhao et al., 2018). It has the advantage that, in many scenarios, it can readily adapt to changes in the operation conditions but the disadvantage that it relies on the

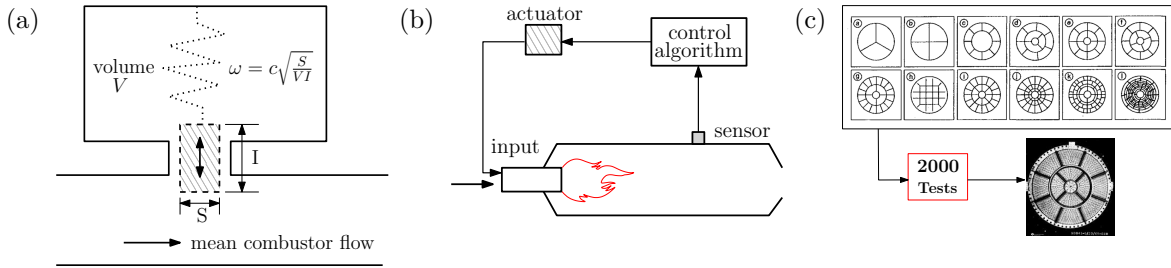


Fig. 1.4 Control strategies to eliminate thermoacoustic oscillations. Passive control includes Helmholtz resonators (a). Active control uses actuators or speakers to control the instabilities (b). Trial and error techniques (c), test different configurations until one of them is found to be stable. Oefelein and Yang (1993) show the different injector baffle patterns tested in the F-1 engine during the Apollo program.

effectiveness of the sensors and actuators, which must operate without fault for several million cycles. A few large scale implementation examples include:

- The first full scale implementation, which was performed in 1988 in an afterburner of a Rolls-Royce RB199 military turbofan engine, where a gain and time delay controller was used to reduce 12 dB of the preferred mode (Dowling and Morgans, 2005).
- Hermann and Hoffman (Lieuwen and Yang, 2005) managed to suppress combustion oscillations in a Siemens V94.3A heavy-duty gas turbine (267 MW) using active control by modulating the pilot gas mass flow out of phase of the heat release fluctuations.
- Johnson et al. (2001) used active control to modulate the fuel on a Siemens-Westinghouse Dry Low NO_x combustor. They managed to attenuate the dominant mode by 15 dB and reduce the broadband noise by 30-40%, as well as reducing NO_x emissions by 10%.
- Umeh et al. (2007) used pulsed modulations of the fuel to mitigate instabilities on a liquid-fuelled partially premixed high-pressure combustion test rig at GE.
- Richards et al. (2007) implemented active control via equivalence ratio modulation on a gas turbine engine. They managed to reduce the amplitudes of the oscillations by one third with the drawback of increasing CO emissions but the advantage of decreasing NO_x emissions.

Another approach is to tune passive control devices so that their effective frequency range can be adapted to the operating conditions. For example, Zhao and Morgans (2009)

and Zhao et al. (2011) tuned Helmholtz resonators and acoustic liners by varying their geometry, neck area or pipe length respectively. Bothien et al. (2013) increased the range of operability of a Helmholtz resonator by including multiple resonant cavities, where the neck geometries, bias flow and volume ratios were tuned in order to optimize damping performance. Both of these methods introduce new failure modes into the systems. This is undesirable and these methods are usually avoided if possible.

1.5 Adjoint methods in fluid problems

The elimination of thermoacoustic oscillations via any of the previous methods requires knowledge of the behaviour of the flow, particularly when positioning passive control devices or sensors and actuators. On complex fluid problems, where there is a wide variety of parameters that can affect the stability of the flow, obtaining this information via traditional methods (trial and error) is inefficient. In contrast, adjoint methods have proven to be very effective (Luchini and Bottaro, 2014), especially when the number of inputs (flow parameters) into the system is large when compared to the number of outputs (growth or decay rates of the flow). With a single computation of the adjoint equations we can quickly assess how the growth rate of a resonant mode is affected by every flow parameter. In a system with a handful of unstable eigenvalues but a multitude of parameters, this greatly reduces the number of calculations required to design a stable system. Given these features of adjoint methods they are perfectly suited for optimization and sensitivity problems in thermoacoustics.

Stability analysis using adjoint methods has, as primary objective, the study of the sensitivity of the eigenvalues. In flow instability, eigenvalue sensitivity is used to calculate the response of the flow to external forcing or the sensitivity of the eigenvalues to perturbations in the system. Pioneering this field was Hill (1992) who presented, for the first time, adjoint based sensitivity of a global mode in flow instability. It is well known that in open flow, the wake behind a cylinder becomes unstable when the Reynolds number exceeds around 47. This drives the flow to a two dimensional periodic oscillation better known as the von Kármán vortex street. The onset of instability was studied experimentally by Strykowski and Sreenivasan (1990) when a second smaller cylinder was inserted downstream. The novelty of Hill's work was using adjoint methods to map the sensitivity of the unstable mode to unsteady feedback caused by the second cylinder, and finding the point at which the system is most sensitive to this feedback. The same problem was studied later by Giannetti and Luchini (2007) while performing global analysis on the flow around the cylinder. They introduced concept of *structural*

*sensitivity*¹. These two approaches were different from the experimental results due to the fact that the sensitivity analysis did not account for the change in the mean flow induced by the cylinder in the experiments. The final resolution that combined the effect of the perturbation on the base flow and the time varying disturbance was done by [Marquet et al. \(2008\)](#) and [Luchini et al. \(2009\)](#), which produced sensitivity maps that match well with the experimental results of [Strykowski and Sreenivasan \(1990\)](#). One of the key findings was that the sensitivity of the eigenvalue to a steady force was around 5 times stronger than the sensitivity to unsteady feedback. Thorough reviews of this problem, along with other instabilities in fluids such as the Tollmien-Schlichting waves and the Görtler instability, are given by [Luchini and Bottaro \(2014\)](#); [Sipp et al. \(2010\)](#).

Some applications of adjoint methods in the field of hydrodynamics include the work of [Marino and Luchini \(2009\)](#) who explored the stability of a forward facing step using incompressible flow equations, or [Pralits et al. \(2010\)](#) studying the flow around a rotating cylinder. In low Mach number flows [Qadri et al. \(2013\)](#) studied the spiral vortex breakdown of swirling flows. Using compressible flows, [Spagnoli and Airiau \(2008\)](#) proposed noise mitigation strategies by using adjoint fields to identify the sources of noise in compressible mixing layers, and [Fosas de Pando et al. \(2017\)](#) investigated the tonal noise produced by an airfoil and identified the preferred zone to control it.

In the field of optimal design, specifically in aerodynamics we find the work of [Jameson \(1995\)](#). Using control theory aided by adjoint methods he computed the optimal design for a wing, reducing the drag by almost 50%. Similarly [Nielsen et al. \(2010\)](#) used adjoint methods for large scale optimization of a jet fighter and a tilted rotor to optimize the lift to drag ratio and the thrust coefficient respectively. [Freund \(2011\)](#) used adjoint-based optimization to produce an iterative algorithm that reduces jet noise.

1.5.1 Adjoint methods in thermoacoustics

In thermoacoustics, one of the first application of adjoint methods is presented in [Juniper \(2011\)](#), where the lowest initial energy required to trigger thermoacoustic oscillations in a Rijke tube is found by using nonlinear adjoint looping of the governing equations in an optimization routine. Using the same model, [Magri and Juniper \(2013b\)](#) perform linear eigenvalue sensitivity analysis using adjoint methods. They assess how the dominant eigenvalue changes when the base state parameters are modified and when a generic passive control element is added into the system (structural sensitivity). They find that a

¹The structural sensitivity is used to analyse the effect of forcing the mass, momentum or energy equations, with a feedback device proportional to a steady or unsteady variable of the flow. It is proportional to some product of the direct and adjoint eigenfunctions.

drag force applied to the momentum equation is the most stabilizing feedback mechanism and that a second hot wire positioned in the first half of the tube is also a stabilizing mechanism. From these key findings, the growth and decay rates are experimentally validated in [Jamieson and Juniper \(2017a,b\)](#); [Jamieson et al. \(2017\)](#); [Rigas et al. \(2016\)](#). The frequency shifts predicted by the experimental validation are different from the ones predicted with the adjoint theory, because the real model of the Rijke tube is inherently different to the simplified model used in the adjoint computations. [Magri and Juniper \(2014a\)](#) improves the model of the electrically heated Rijke tube, by considering a jump in temperature. [Magri and Juniper \(2013a\)](#) and [Magri and Juniper \(2014b\)](#) perform adjoint sensitivity analysis in a Rijke tube with a compact diffusion flame. They find that the tip of the flame is the most receptive region to external forcing and that perturbations in (i) the stoichiometric mixture fraction, (ii) the width of the fuel injection slots and (iii) the heat release parameters have the strongest influence on the eigenvalue.

[Orchini and Juniper \(2016b\)](#) analyse the linear response of a conical flame and use adjoint methods to measure the sensitivity to the convection speed. They observe that, as expected, the stability of the system is strongly influenced by the time scale given by the flow convection from the base until it reaches the flame front. [Magri et al. \(2016a\)](#) perform sensitivity analysis on degenerate modes which appear in annular configurations. [Magri et al. \(2016b\)](#); [Mensah et al. \(2017\)](#); [Silva et al. \(2016\)](#) perform adjoint-based uncertainty quantification to reduce the number of nonlinear eigenvalue problems solved in the Monte Carlo method or to avoid the Monte Carlo method at all. A recent review of sensitivity analysis in thermoacoustics can be read in [Juniper and Sujith \(2018\)](#).

Most of the previous analyses are performed with a first order, and in some cases a second order adjoint method. [Mensah and Moeck \(2016\)](#) propose a higher order adjoint perturbation analysis on a Rijke tube. [Mensah et al. \(2018\)](#) use a similar analysis to study the effect of symmetry breaking in annular combustors. They study how the eigenvalue drifts when a degenerate mode becomes non degenerate due to the perturbation in the system.

1.5.2 Optimization in Thermoacoustics

An application of adjoint based shape optimization in aero-acoustics can be seen in [Caeiro et al. \(2017\)](#). In such study the geometry of the neck of a Helmholtz resonator is optimized to obtain a desired impedance. On a similar line, [Mensah and Moeck \(2017\)](#) use adjoint methods to tune and position multiple acoustic dampers to stabilize a 2D periodic configuration that resembles an annular configuration. [Giauque et al. \(2013\)](#) perform shape optimization on a subsonic nozzle to find the most silent (and most noisy)

configuration. However, this study is performed without the use of adjoint methods, so the sensitivities are computed by comparing different individual configurations, similar to a finite difference scheme.

1.6 Thesis scope and structure

Low order network models are the preferred method to analyse thermoacoustic instabilities in early design stages. They provide an excellent platform with which to analyse the influence of base state parameters and feedback devices on the eigenvalue. This sensitivity information can be used as an input to iterative algorithms for optimization purposes. Given that adjoint-based methods have proven to be very effective at extracting gradient information from a system, the aim of this thesis is to develop an analytical framework of a thermoacoustic network model and to incorporate adjoint-based sensitivity analysis. This includes the derivation of the adjoint equations and subsequent use in the computation of gradient information of base state parameters and feedback mechanisms. The first goal is to use this information to perform sensitivity analysis on several configurations and devise passive control strategies to mitigate thermoacoustic instabilities. The second goal is to use the gradient information as an input to an optimization routine, which, by making small changes in the geometry, stabilizes all of the unstable modes of a configuration on a given frequency range. The development of these strategies are available in PILOT, a Matlab code for the computation of thermoacoustic instabilities for which adjoint based sensitivity analysis and optimization is available.

Structure of the thesis

The thesis is divided into 7 chapters, including this introduction. It begins in chapter 2 where the low order network model of [Stow and Dowling \(2001, 2003, 2004\)](#) is presented. This model, which has been used in numerous studies, sets the baseline from which the thermoacoustic instabilities are calculated. In this chapter the governing equations to model a straight duct are presented first. Then all of the modules that join ducts are developed as a set of jump conditions. These include area changes, heat sources and different boundary conditions.

Chapter 3 contains all the configurations which will be examined. The first configurations are the Rijke tube and a simple choked combustor. Given the low dimensionality of these models, their nonlinear eigenvalue problems are fully detailed. Then, a longitudinal combustor (Rama Balachandran's burner ([Balachandran, 2005](#))), is examined. This

is followed by two annular configurations: first a generic lean premixed prevaporized combustor ([Morgans and Stow, 2007](#)) and then the annular test rig built in Cambridge University Engineering Department ([Worth and Dawson, 2013b](#)).

Chapter 4 contains the adjoint derivation of the network model presented in chapter 2. The continuous and discrete adjoint formulations are presented. Then the continuous adjoint equations for the unsteady and steady equations of all the modules in chapter 2 are derived.

Chapter 5 makes use of the adjoint equations in chapter 4 to perform sensitivity analysis of the thermoacoustic configurations. First, adjoint based sensitivity analysis is presented using the continuous and the discrete adjoint. Then, for each configuration, the base state sensitivities are computed and, where relevant, the feedback sensitivities are also presented.

Chapter 6 uses the sensitivity information of chapter 5 to perform optimization routines to stabilize three of the presented systems. Two different algorithms for the stabilization of thermoacoustic instabilities via small geometry changes are presented. They are then applied to a test case to examine the differences between the algorithms. Finally, optimization is performed on three of the configurations in which we found geometries that are stable within the examined frequency range.

The thesis finishes in chapter 7 with some concluding remarks and suggestions of future work.

Chapter 2

Low order network models

2.1 Low order modelling

The prediction and control of thermoacoustic oscillations is still one of the biggest challenges faced by the gas turbine industry. In the last few decades a variety of methods have been developed to predict the onset of combustion instabilities which can be categorized into two main groups: numerical simulations (CFD), and low order models.

In the first group are highly resolved numerical simulations such as LES. These are able to predict flame acoustic interaction ([Schmitt et al., 2007](#)) and hence thermoacoustic oscillations. In such simulations, the complex combustor geometries are modelled and they may include the inlet and outlet nozzles or the first or last blade rows of the compressor or the turbine in order to accurately capture the boundary conditions. This enables modelling of the full flow field and the corresponding unstable modes with great accuracy. For example, [Staffelbach et al. \(2009\)](#) model the full annular combustor of a helicopter engine and capture a self excited spinning mode in the chamber. However, these methods have the major drawback of being computationally expensive, and hence not very attractive for industrial purposes.

In the other group we have the low order models, also known as network models. In thermoacoustics, network models exploit the fact that inside a duct, acoustic wave behaviour is linear. This allows us to represent an entire combustion system as a series of lumped elements which are geometrically simple and are interconnected by transfer matrices. As stated in [Krüger et al. \(1999\)](#) the advantage of the network concept is that it has the possibility of incorporating experimental and numerical results into the network, such as those that define the boundary conditions or the complex behaviour of the flame. The drawbacks of these models is that they are only able to capture the first longitudinal or circumferential modes of the system (low frequency behaviour), because

the ducts are modelled considering frequencies low enough such that the radial modes are cut off and most of the modules for area changes and heat sources span over a distance short enough to be considered to be acoustically compact.

Low order models have been used to predict the onset of thermoacoustic oscillations (Dowling and Stow, 2003; Schuermans et al., 2003), as well as limit cycles (Han et al., 2015; Stow and Dowling, 2004). In similar fields they have been used to study the generation and propagation of combustion noise (Dowling and Mahmoudi, 2015), and in more specific cases they have been used to study the effects of accelerating entropy waves in nozzles (Rolland et al., 2017) and even in the development of passive control approaches to prevent the onset of combustion instabilities with tuned damping devices (Bothien et al., 2013).

Due to their versatility and speed, they are widely used both in industry and academia. Bothien (2008) provides a good reference of several thermoacoustic network models currently in use. A few of them include LOTAN (Stow and Dowling, 2009), OSCILOS (Li et al., 2017), TA3 (Bellucci et al., 2005), among others.

Our thermoacoustic network model is based upon LOTAN's approach, originally developed in Stow and Dowling (2001, 2003, 2004). Therefore, in this chapter we are going to limit the description of the model to the governing equations and the assumptions underlying the model. This will enable us to have an insight into the physics of each of the modules and will serve as the baseline for the development of the adjoint equations in chapter 4, the sensitivity analysis of chapter 5 and optimization routines of chapter 6.

2.2 The governing equations

The network model is developed considering cylindrical polar coordinates, and is governed by the mass, momentum and energy equations, assuming no viscosity or heat conduction and the equation of state:

$$\frac{\partial \rho}{\partial t} + \nabla \cdot (\rho \mathbf{u}) = 0, \quad (2.1a)$$

$$\rho \frac{\partial \mathbf{u}}{\partial t} + \rho(\mathbf{u} \cdot \nabla) \mathbf{u} + \nabla p = 0, \quad (2.1b)$$

$$\frac{\partial p}{\partial t} + \mathbf{u} \cdot \nabla p + \gamma p \nabla \cdot \mathbf{u} = (\gamma - 1)Q, \quad (2.1c)$$

$$p = \rho R_g T, \quad (2.1d)$$

where $\mathbf{u} = [u, v, w]^T$ represents the velocities in the x , r and θ directions, ρ is the density, p is the pressure, Q is the heat addition, γ is the ratio of specific heat capacities, R_g is the ideal gas constant and T is the temperature.

Many industrial applications include annular combustors where the radial spacing is shorter than the axial length and much shorter than the circumference. Under these conditions it is common to assume a narrow gap approximation (Dowling and Stow, 2003). In such situations, we can neglect all dependencies in the radial (r) direction and consider $v = 0$, yielding a 2D configuration (x, θ) .

Following the formalism developed in Stow and Dowling (2001) we linearise the governing equations around a steady and uniform base flow, which varies only in the axial direction, and we assume that there is no mean swirl (hence, $\bar{w} = 0$). The flow variables take the form $p = \bar{p}(x) + p'(x, \theta, t)$. We then consider flow perturbations with complex frequency ω and circumferential wave number n . The disturbances become $p'(x, \theta, t) = \hat{p}(x)e^{i\omega t + in\theta}$.

2.3 Network modules

A combustor can be separated into a network of modules. The key modules are the straight ducts (§ 2.3.1) which propagate travelling waves. The ducts are connected through compact area changes (§ 2.3.2 and § 2.3.3), a compact heat source (§ 2.3.5), or a ring of premix ducts (§ 2.3.4). The full configuration is initiated with an inlet boundary condition (§ 2.3.6) and terminated with an outlet boundary condition (§ 2.3.6).

2.3.1 Straight ducts

Every duct has an associated cross sectional area A , length L and mean radius $R = (r_2 + r_1)/2$, where r_2 and r_1 are the outer and inner radii, respectively, that characterize the annular gap. Given the assumptions in § 2.2, the base flow equations for the ducts are simplified to:

$$\bar{\rho} \frac{d\bar{u}}{dx} + \bar{u} \frac{d\bar{\rho}}{dx} = 0, \quad (2.2a)$$

$$\bar{\rho} \bar{u} \frac{d\bar{u}}{dx} + \frac{d\bar{p}}{dx} = 0, \quad (2.2b)$$

$$\frac{d\bar{w}}{dx} = 0, \quad (2.2c)$$

$$\bar{u} \frac{d\bar{p}}{dx} + \gamma \bar{p} \frac{d\bar{u}}{dx} = 0. \quad (2.2d)$$

From these, it can be deduced that every duct has a constant and homogeneous base flow. The unsteady perturbation equations become:

$$i\omega\hat{\rho} + \frac{in}{R}\bar{\rho}\hat{w} + \bar{\rho}\frac{d\hat{u}}{dx} + \bar{u}\frac{d\hat{\rho}}{dx} = 0, \quad (2.3a)$$

$$i\omega\bar{\rho}\hat{u} + \bar{\rho}\bar{u}\frac{d\hat{u}}{dx} + \frac{d\hat{p}}{dx} = 0, \quad (2.3b)$$

$$i\omega\bar{\rho}\hat{w} + \frac{in}{R}\hat{p} + \bar{\rho}\bar{u}\frac{d\hat{w}}{dx} = 0, \quad (2.3c)$$

$$i\omega\hat{p} + \frac{in}{R}\gamma\bar{p}\hat{w} + \bar{u}\frac{d\hat{p}}{dx} + \gamma\bar{p}\frac{d\hat{u}}{dx} = 0. \quad (2.3d)$$

Wave decomposition

Considering $\hat{\mathbf{y}} = [\hat{\rho}, \hat{u}, \hat{w}, \hat{p}]^T$, we can rewrite the system of equations (2.3) as:

$$\frac{d\hat{\mathbf{y}}}{dx} = iK\hat{\mathbf{y}}. \quad (2.4)$$

Where the matrix K depends on the frequency ω and the base flow properties, which are constant in a given duct. Hence, the solution to Eq. (2.4) is given by the linear combination of pure solutions:

$$\hat{\mathbf{y}}(x) = \sum_{n=1}^4 A_n e^{ik_n x} \mathbf{z}_n,$$

where A_n represents the wave amplitude, k_n the eigenvalue, and \mathbf{z}_n the corresponding eigenvector. The eigenvalues of matrix K are the streamwise wavenumbers

$$k_1 \text{ and } k_2 \text{ are given by: } k_0 = -\frac{\omega}{\bar{u}}, \quad (2.5a)$$

$$k_3 \text{ and } k_4 \text{ are given by: } k_{\pm} = \frac{\bar{M}\omega \mp \sqrt{\omega^2 - \frac{n^2\bar{c}^2}{R^2}(1 - \bar{M}^2)}}{\bar{c}(1 - \bar{M}^2)}, \quad (2.5b)$$

where $\bar{M} = \bar{u}/\bar{c}$ is the Mach number and $\bar{c} = \sqrt{\gamma R_g \bar{T}}$ is the mean speed of sound. The first eigenvalue (k_0) has multiplicity of 2, and is associated with waves convecting at the base flow speed: one corresponding to an entropy wave with amplitude A_E and the other corresponding to a vorticity wave with amplitude A_V . The second eigenvalue (k_+) is associated with acoustic waves travelling downstream in the duct with amplitude A_+ . The last eigenvalue (k_-) corresponds to acoustic waves travelling upstream in the duct

with amplitude A_- . The mode shapes are given by:

$$\hat{p}(x) = A_+ e^{ik_+ x} + A_- e^{ik_- x}, \quad (2.6a)$$

$$\hat{\rho}(x) = \frac{1}{\bar{c}^2} \left(A_+ e^{ik_+ x} + A_- e^{ik_- x} - A_E e^{ik_0 x} \right), \quad (2.6b)$$

$$\hat{u}(x) = \frac{1}{\bar{\rho}} \left(-\frac{k_+}{\alpha_+} A_+ e^{ik_+ x} - \frac{k_-}{\alpha_-} A_- e^{ik_- x} + \frac{n}{\bar{c}} A_V e^{ik_0 x} \right), \quad (2.6c)$$

$$\hat{w}(x) = \frac{1}{\bar{\rho}} \left(-\frac{n}{R\alpha_+} A_+ e^{ik_+ x} - \frac{n}{R\alpha_-} A_- e^{ik_- x} - \frac{k_0 R}{\bar{c}} A_V e^{ik_0 x} \right), \quad (2.6d)$$

where $\alpha_{\pm} = \omega + \bar{u}k_{\pm}$.

An interesting case is when only plane waves propagate, i.e., $n = 0$. This allows us to use the same equations to model one dimensional longitudinal combustors, where the length of the device is much larger than its diameter.

Fluxes for conservation equations

Joining ducts requires the conservation of quantities, such as mass flux $m = A\rho u$, axial momentum flux $f_x = Ap + mu$, angular momentum flux $f_{\theta} = Rmw$, energy flux $e = m(h + \frac{1}{2}(u^2 + w^2))$, and in some cases entropy $s = s^o - R_g \ln(p)$. Here $h = \int c_p(T) dT$ is the enthalpy and $s^o = \int c_p(T)/T dT$ is the entropy function that varies only with temperature, $c_p(T)$ is the specific heat capacity at constant pressure, and we introduce $c_v(T) = c_p(T) - R_g$ as the specific heat capacity at constant volume. The previous flux formulation is valid for perfect gases, in which the specific heat capacities are constant, and semi-perfect gases, in which the specific heat capacities are functions of temperature (see [Li and Morgans \(2016\)](#) for details). The mean and fluctuating quantities of the fluxes are given in table 2.1.

Further details on conversion between wave amplitudes, flow perturbations and flux perturbations as well as wave propagation inside the ducts can be found in [Stow and Dowling \(2001\)](#). For simplicity we will consider the fluxes in vector form such that $\mathbf{f}_i = [m_i, f_{x_i}, f_{\theta_i}, e_i]^T$ and $\mathbf{s}_i = [m_i, s_i, f_{\theta_i}, e_i]^T$ where the subindex i represents a side of the control volume.

2.3.2 Area increase

A region of area increase is often regarded as a sudden expansion which is non-isentropic. We assume that the region of area increase is compact; i.e., the length of the section is much shorter than the axial wavelength of the fluctuations. A control volume analysis

Quantity	Steady base flow	Fluctuating flow
Mass (m)	$\bar{m} = A\bar{\rho}\bar{u}$	$\hat{m} = A(\bar{\rho}\hat{u} + \hat{\rho}\bar{u})$
Axial m. (f_x)	$\bar{f}_x = A(\bar{p} + \bar{\rho}\bar{u}^2)$	$\hat{f}_x = A(\hat{p} + \hat{\rho}\bar{u}^2 + 2\bar{\rho}\bar{u}\hat{u})$
Angular m. (f_θ)	$\bar{f}_\theta = 0$	$\hat{f}_\theta = AR\bar{\rho}\bar{u}\hat{w}$
Energy (e)	$\bar{e} = \bar{m} \left(\bar{h} + \frac{1}{2}\bar{u}^2 \right)$	$\hat{e} = A \left(\frac{\gamma\bar{u}}{\gamma-1}\hat{p} + \bar{\rho} \left(\bar{h} + \frac{3}{2}\bar{u}^2 \right) \hat{u} + \dots \right.$ $\left. \bar{u} \left(\bar{h} - \frac{\gamma\bar{p}}{(\gamma-1)\bar{\rho}} + \frac{1}{2}\bar{u}^2 \right) \hat{\rho} \right)$
Entropy (s)	$\bar{s} = \bar{s}^o - R_g \ln(\bar{p})$	$\hat{s} = c_v \left(\frac{\hat{p}}{\bar{p}} - \gamma \frac{\hat{\rho}}{\bar{\rho}} \right)$

Table 2.1 Mean and fluctuating quantities for fluxes and entropy.

indicates conservation of mass, angular momentum and energy fluxes. The momentum flux is increased by the force on the sides of the control surface:

$$f_{x_2} = f_{x_1} + \int_{A_1}^{A_2} p \, dA,$$

where the subscripts 1 and 2 have been used to indicate the positions upstream and downstream of the area increase. The integral term is often approximated using the product between the pressure upstream p_1 , a loss coefficient that allows some pressure recovery and the difference in areas. Here, we assume that the loss coefficient is 1. The jump conditions for an area increase are given by:

$$\mathbf{f}_2 = \mathbf{f}_1 + [0, p_1(A_2 - A_1), 0, 0]^T \quad (2.7)$$

2.3.3 Area decrease

A region of area decrease is assumed to be compact and isentropic. Control volume analysis indicates that mass, angular momentum and energy fluxes are conserved:

$$\mathbf{s}_2 = \mathbf{s}_1. \quad (2.8)$$

2.3.4 Ring of premix ducts

A ring of premix ducts is a common feature of annular combustors. To model them, [Stow and Dowling \(2004\)](#) considered a ring with D premix ducts. At the start of the premix ducts an area decrease is observed. The premix ducts are modelled as one dimensional

elements. Therefore angular velocity fluctuations are zero. Thus, angular momentum is not conserved. Control volume analysis in a sector of the annulus that discharges into a single premix duct ensures conservation of mass and energy fluxes. The entropy in the premix duct is considered to be the average of the value in the annular sector. The jump conditions for the steady base flow are the same as in § 2.3.3. For the fluctuating flow, they are given by:

$$\hat{\mathbf{s}}_2 = \kappa_n [\hat{m}_1, \hat{s}_1, 0, \hat{e}_1]^T. \quad (2.9)$$

where $\kappa_n = D \sin(\pi n/D)/(\pi n)$, is a factor that appears due to the integration of quantities in the annular sector.

At the end of the premix ducts, the combustion chamber is again modelled as a thin annulus. An area increase section is observed. Control volume analysis indicates that mass, angular momentum and energy fluxes are conserved. The axial momentum is increased by the pressure from the walls. The jump conditions for the steady flow are the same as in § 2.3.2. The jump conditions for the fluctuating flow are given by:

$$\hat{\mathbf{f}}_2 = \frac{1}{\kappa_n} [\hat{m}_1, \hat{f}_{x_1} + \hat{p}_1(A_2\kappa_n - A_1), 0, \hat{e}_1]^T. \quad (2.10)$$

This modelling approach sets a restriction on the maximum azimuthal wave number used, which has to be less than half of the number of premix ducts in the configuration (Evesque and Polifke, 2002; Stow and Dowling, 2004).

2.3.5 Heat Sources

Heat sources model the effect of heat addition into the system. Two kinds of compact heat sources are examined. The first is a heat source at rest, such as heating grids where heat addition occurs at a constant location. In this model we will assume that the rate of steady heat addition \bar{Q} is given. The second is a kinematic heat source, such as a flame where the flame front is constantly moving. In this model we will assume that the rate of heat addition is given by:

$$Q = \eta \rho S_u(\phi) h_r(\phi) A_f. \quad (2.11)$$

Where η is the combustion efficiency, ρ is the density of the unburned mixture, $S_u(\phi)$ represents the flame propagation speed, $h_r(\phi)$ is the enthalpy of reaction and A_f is the flame area. The flame propagation speed and the enthalpy of reaction depend on ϕ , which is the equivalence ratio of the mixture.

Heat sources at rest

For a heat source at rest, control volume analysis indicates that mass and momentum fluxes are conserved. The energy flux is increased by heat addition:

$$\mathbf{f}_2 = \mathbf{f}_1 + [0, 0, 0, Q]^T. \quad (2.12)$$

Kinematic heat sources

As pointed out by [Strobio-Chen et al. \(2016\)](#) (originally from [Chu \(1956\)](#)), heat sources such as flames have, acoustically speaking, a dynamical behaviour, and are able to move from their mean position. Hence, they are regarded as kinematic heat sources. As stated in [Strobio-Chen et al. \(2016\)](#), control volume analysis across a thin discontinuity, such as a shock or a planar flame¹, that is moving with speed u_s , requires the use of the Rankine-Hugoniot conditions, which yield:

$$\mathbf{f}_2 = \mathbf{f}_1 + u_s \begin{bmatrix} A_2 \rho_2 - A_1 \rho_1 \\ m_2 - m_1 \\ R_2 A_2 \rho_2 w_2 - R_1 A_1 \rho_1 w_1 \\ A_2 \rho_2 \left(h_2 - \frac{p_2}{\rho_2} + \frac{1}{2} (u_2^2 + w_2^2) \right) - A_1 \rho_1 \left(h_1 - \frac{p_1}{\rho_1} + \frac{1}{2} (u_1^2 + w_1^2) \right) \end{bmatrix} + \begin{bmatrix} 0 \\ 0 \\ 0 \\ Q \end{bmatrix}. \quad (2.13)$$

In our model the heat source is taken to be anchored. Therefore, $\bar{u}_s = 0$. Following [Bloxsidge et al. \(1988\)](#), mass conservation across the flame front relates the unsteady flame speed to the incoming mass perturbations and the unsteady heat release:

$$\hat{u}_s = \bar{u}_1 \left(\frac{\hat{m}_1}{\bar{m}_1} - \frac{\hat{Q}}{\bar{Q}} \right). \quad (2.14)$$

Unsteady heat release models

To fully define the system of equations (2.12) and (2.13), we need to relate the unsteady heat release to the perturbation variables. For linear regimes, the most common approach is the use of a flame transfer function (FTF), \mathcal{F}_t , proportional to a linear combination of

¹This control volume approach is only valid for planar flames. If the flame has a different shape such as conical, wedge, V shaped, etc. this formalism is no longer appropriate. In such cases it is more convenient to use a transfer matrix approach derived from experimental or high fidelity simulations.

the velocity, density and/or pressure perturbations:

$$\frac{\hat{Q}}{\bar{Q}} = \mathcal{F}_t \left(\mu_r \frac{\hat{\rho}_i}{\bar{\rho}_i} + \mu_u \frac{\hat{u}_i}{\bar{u}_i} + \mu_p \frac{\hat{p}_i}{\bar{p}_i} \right), \quad (2.15)$$

where the subindex i denotes the measurement or reading point position in the network which is modelled as in § 2.3.2 using $A_2 = A_1$ and the variables $\mu_u, \mu_r, \mu_p \in \{0, 1\}$ are used to denote the active perturbation variables. For example, a velocity driven unsteady heat release model has $\mu_u = 1$ and $\mu_r = \mu_p = 0$, a mass driven unsteady heat release model has $\mu_u = \mu_r = 1$ and $\mu_p = 0$. The FTF can be estimated via analytical models, numerical tools (such as LES), or via experimental data. For the present study we will use analytical models which are appropriate for compact heat sources. The most simple one is the time lag model from Crocco (1969), which consists of a constant gain k and a constant time delay τ :

$$\mathcal{F}_t = k e^{-i\omega\tau}. \quad (2.16)$$

Two analytical FTFs derived using a level set method which are incorporated into our model can be found in appendix A. In this thesis we assume that if the FTF depends on the mean flow variables, these correspond to those at the measurment point, that is:

$$\mathcal{F}_t \rightarrow \mathcal{F}_t(\bar{\rho}_i, \bar{u}_i, \bar{p}_i). \quad (2.17)$$

2.3.6 Boundary conditions

The final part of the model is the specification of the boundary conditions.

Inlet boundary conditions

For this model we assume that the inlet is located at $x = 0$ and consider the following boundary conditions at the inlet:

- *Open inlet*: An open inlet is modelled such that there are no pressure perturbations at the inlet, $\hat{p} = 0$. Hence we set $A_+ = 1$ and $A_- = -1$. We further assume that there are no entropy or vorticity fluctuations, $A_E = A_V = 0$.
- *Closed inlet*: For a closed inlet we assume no axial velocity at the wall, $\hat{u} = 0$. Therefore, we use $A_+ = 1$ and $A_- = -k_+ \alpha_- / (k_- \alpha_+)$, and again consider $A_E = A_V = 0$.
- *Choked inlet*: A choked inlet Stow et al. (2002) assumes that the mass, angular momentum and energy fluxes are zero at the inlet, $\hat{m} = 0, \hat{f}_\theta = 0$ and $\hat{e} = 0$. To

fully characterize the system we set the pressure perturbations to 1 and solve for the rest of the variables: $\hat{p} = 1$, $\hat{\rho} = \gamma/(\bar{c}^2 + (\gamma - 1)\bar{u}^2)$, $\hat{u} = -\gamma\bar{u}/(\bar{\rho}(\bar{c}^2 + (\gamma - 1)\bar{u}^2))$ and $\hat{w} = 0$.

- *Acoustic reflection coefficient:* An acoustic reflection coefficient R_c assumes no entropy or vorticity generation at the inlet and is given as the ratio between reflected and incident acoustic waves:

$$A_+ - R_c A_- = 0. \quad (2.18a)$$

In perturbation variables it can be expressed as:

$$\hat{p} \left(\frac{k_-}{\alpha_-} + R_c \frac{k_+}{\alpha_+} \right) + \bar{\rho} \hat{u} (1 + R_c) = 0. \quad (2.18b)$$

The reflection coefficient is, in general, a function of the frequency. However over a limited band of frequencies it can be approximated by a constant. For this reason the model can receive as an input a reflection coefficient which is a constant complex number ($R_c = R_r + iR_i$) or a function of the frequency $R_c = R_c(\omega)$. In this thesis we treat the inlet R_c as a constant and give it a small imaginary part to represent the energy lost on reflection.

Outlet boundary conditions

The outlet boundary conditions considered for this model are:

- *Open outlet:* For an open outlet we consider that there are no pressure perturbations, $\hat{p} = 0$.
- *Closed outlet:* A closed end considers that there is no axial velocity due to the presence of a wall, $\hat{u} = 0$.
- *Choked outlet:* The choked outlet gives the following condition ([Marble and Candel, 1977](#)):

$$\frac{2\hat{u}}{\bar{u}} + \left(1 - \frac{dc_p(\bar{T})}{d\bar{T}} \frac{(\gamma - 1)^2}{\gamma} \frac{\bar{T}}{R_g} \right) \left(\frac{\hat{\rho}}{\bar{\rho}} - \frac{\hat{p}}{\bar{p}} \right) = 0. \quad (2.19)$$

- *Acoustic reflection coefficient:* The outlet reflection coefficient is defined in a similar way to the inlet reflection coefficient:

$$A_- e^{ik_- L_t} - R_c A_+ e^{ik_+ L_t} = 0. \quad (2.20a)$$

where L_t represents the position of the outlet boundary. In fluctuating variables this is equivalent to:

$$\begin{aligned} \hat{p} \left(\frac{1}{\bar{\rho}\alpha_+} \left(k_+ + \frac{n^2}{R^2 k_0} \right) + \frac{R_c}{\bar{\rho}\alpha_-} \left(k_- + \frac{n^2}{R^2 k_0} \right) \right) + \dots \\ \hat{u} (1 + R_c) + \hat{w} \left(\frac{n}{R k_0} (1 + R_c) \right) = 0. \end{aligned} \quad (2.20b)$$

As mentioned above for the inlet reflection coefficient, R_c is, in general, a function of the frequency, but on certain frequency ranges it is well approximated by a constant. In this thesis, we set as an input to the outlet reflection coefficient one of the two options: a constant complex value or a function that depends on the frequency. For the latter we will consider the reflection coefficient of a circular duct radiating sound, originally proposed by [Levine and Schwinger \(1948\)](#). This model was extended to consider a mean flow in [Cargill \(1982\)](#). We will use the simplified version proposed by [Peters et al. \(1993\)](#). Taking r as the duct radius the reflection coefficient gives:

$$R_c = - \left(1 + \bar{M} A(S_t) \right) \left(1 - \frac{1}{2} \left(\frac{\omega r}{\bar{c}} \right)^2 \right) e^{i(k_+ - k_-)\delta(S_t)}, \quad (2.21)$$

where $S_t = \text{Re}\{\omega\}r/(2\pi\bar{u})$ is the Strouhal number, $A(S_t)$ is a mean flow correction and $\delta(S_t)$ is the end correction. The last two are functions that depend on the Strouhal number only. In the cases that we will be exploring, the Mach number is small and the frequencies big enough to consider the limiting behaviour of these quantities which are $A(S_t) = 0.90$ for $S_t \rightarrow \infty$ and $\delta(S_t) = 0.6133r$ for $\bar{M} \rightarrow 0$ and $S_t \rightarrow \infty$.

2.4 Equations in the zero Mach number limit

Many industrial applications, such as land based gas turbine combustors operate at a low Mach number. Under these conditions the governing equations and jump conditions can be further simplified.

2.4.1 Ducts

Assuming a zero Mach number limit, i.e., $\bar{u} = 0$, for a straight duct, the steady base flow equations are reduced to $d\bar{p}/dx = 0$. The unsteady momentum and energy perturbation

equations become:

$$i\omega\bar{\rho}\hat{u} + \frac{d\hat{p}}{dx} = 0, \quad (2.22a)$$

$$i\omega\hat{p} + \gamma\bar{p}\frac{d\hat{u}}{dx} = 0, \quad (2.22b)$$

Note that, in the zero Mach number limit, the continuity equation and the energy equation (in terms of pressure) represent the same dynamics (Dowling and Stow, 2003). This follows by recasting the energy equation using the isentropic relations ($A_E = 0$): $\hat{p} = \hat{\rho}\bar{c}^2$ and $\gamma\bar{p} = \bar{\rho}\bar{c}^2$. Using Eqs (2.22) we can build the simple wave equation, which has the following shapes:

$$\hat{p}(x) = A_+e^{-i\omega x/\bar{c}} + A_-e^{i\omega x/\bar{c}}, \quad (2.23a)$$

$$\hat{u}(x) = \frac{1}{\bar{\rho}\bar{c}} \left(A_+e^{-i\omega x/\bar{c}} - A_-e^{i\omega x/\bar{c}} \right). \quad (2.23b)$$

2.4.2 Area changes

For an area change the steady base flow equations reduce to $[\bar{p}]_1^2 = 0$. The momentum and energy jump conditions for the fluctuating flow are given by:

$$\hat{p}_2 = \hat{p}_1, \quad (2.24a)$$

$$A_2\hat{u}_2 = A_1\hat{u}_1. \quad (2.24b)$$

2.4.3 Heat sources

For a heat source, the steady base flow equations are again $[\bar{p}]_1^2 = 0$. This implies that mean pressure is continuous everywhere in the network. Under the zero Mach number assumption, the steady energy equation can only be satisfied if $\bar{Q} = 0$, because any heat added is not convected away. Therefore to model a jump in temperature we need to specify $\Delta\bar{T}$ instead of \bar{Q} . The fluctuation equations reduce to:

$$\hat{p}_2 = \hat{p}_1, \quad (2.25a)$$

$$A_2\frac{\gamma_2\bar{p}_2}{\gamma_2 - 1}\hat{u}_2 = A_1\frac{\gamma_1\bar{p}_1}{\gamma_1 - 1}\hat{u}_1 + \hat{Q}. \quad (2.25b)$$

The reader is warned that taking the limit of Eqs (2.12) when $\bar{u} \rightarrow 0$ to recover the jump conditions for a heat source in the zero Mach number limit, is not straightforward. As indicated by Bauerheim et al. (2015a); Dowling (1995), the strength of the entropy wave

A_E tends to infinity whenever \bar{u} tends to zero. Hence, a careful manipulation of the equations is required.

2.5 Nonlinear eigenvalue problem

Using the different modules described above we can build a network model that resembles a combustor. To obtain the eigenvalues of the system we build a nonlinear eigenvalue problem of the form:

$$L(\omega, \mathbf{p})\mathbf{q} = \mathbf{0} \quad (2.26)$$

where \mathbf{p} are the parameters of the system such as base flow quantities, reflection coefficients, time delays, etc. and \mathbf{q} is a vector that contains the wave amplitudes of the ducts. To obtain the eigenvalues ($\omega_j = \sigma_j - i\lambda_j$, where σ_j is the angular frequency and λ_j is the growth rate) we solve the dispersion relation obtained by setting the determinant of L to 0.

Alternatively, we can obtain the eigenvalues by using a shooting method. This is essentially another method to construct the same dispersion relation. First, we give an initial guess for ω and starting from the inlet boundary condition we propagate the solution through each module until we reach the outlet boundary condition. In general, this condition will not be satisfied. Hence, we create an iterative method to update the value of ω until the outlet boundary condition is satisfied. The value of ω is then an eigenvalue of the system.

Chapter 3

Stability analysis of thermoacoustic configurations

3.1 Stability analysis

Unstable combustion is driven by a complex interaction of linear and nonlinear processes. As shown in Fig. 3.1 the amplitude of acoustic oscillations, A , increases when the magnitude of the driving forces $H(A)$ (such as background noise) is bigger than the magnitude of the damping mechanisms $D(A)$. Small perturbations in this region are asymptotically unstable and will grow with exponential envelope until the magnitude of the damping mechanisms surpasses that of the driving forces, at point A_c , which sets a limit cycle (Lieuwen, 2005).

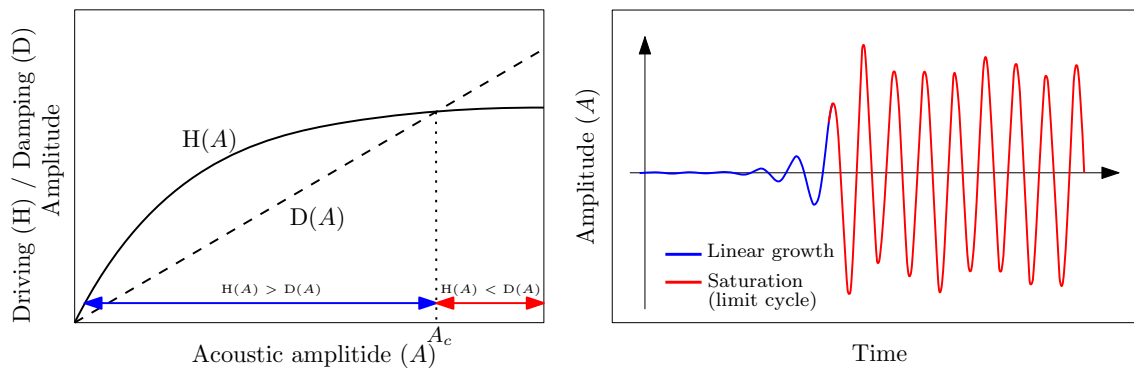


Fig. 3.1 Dependence of acoustic driving $H(A)$ and damping $D(A)$ on amplitude A , from Lieuwen (2005).

As stated in § 1.3, for this thesis, stability analysis is focused in the linear region¹ before saturation occurs. In this neighbourhood eigenvalue analysis allows us to assess the linear behaviour of the perturbations.

To compute the spectrum of the system we follow the approaches presented in § 2.5. One challenge of using these methods is that an initial guess is required for every computed eigenvalue. Hence, to compute all of the eigenvalues in a certain region we need to provide an initial grid fine enough so that each of them is captured.

The logarithmic boundary condition error map and the pseudo-spectrum of the operator are methods to verify that all of the eigenvalues in the region of interest are being captured. For the first one, given a grid of different values of ω we can propagate the wave amplitudes from the inlet boundary condition through the entire system until we reach the outlet boundary condition. This process is equivalent to evaluating the determinant of matrix $L(\omega)$. In general the outlet boundary condition will not be satisfied, and the amplitude that corresponds to this deviation is called the boundary condition error (BC_E):

$$BC_E = \log_{10} ||BC_{actual} - BC_{required}||. \quad (3.1)$$

The points where the error is minimal (strictly speaking zero) are eigenvalues of the system.

The logarithmic boundary condition error map is closely linked to the pseudo-spectrum of the system. The resolvent of the nonlinear eigenvalue problem is given by: $R(\omega) = L(\omega)^{-1}$. An extension of the definition of ϵ -pseudo-spectrum (Λ_ϵ) (Trefethen and Embree, 2005) to nonlinear eigenvalue problems is given by:

$$\Lambda_\epsilon = \left\{ \omega \in \mathbb{C} : ||R(\omega)|| \geq \epsilon^{-1} \right\} \quad (3.2)$$

where, we considered $|| \cdot ||$ to be the 2-norm of the resolvent matrix. Given these definitions we observe that near an eigenvalue the logarithmic boundary error gives small values, whereas the pseudo-spectrum will produce large values. The visualization obtained by superimposing the spectrum over the logarithmic boundary condition map or the ϵ -pseudo-spectrum allows us to validate that the initial grid used to compute the eigenvalues is indeed capturing all of the resonant modes of the system on the specified regime. Due to the ease in the implementation the boundary condition error plot is preferred.

¹In the linear region we consider the two possible scenarios: when the flow is unstable ($H(A) > D(A)$), and when the flow is stable ($H(A) < D(A)$).

3.2 Thermoacoustic models

The thermoacoustic configurations detailed in this chapter have been chosen to contain most of the thermoacoustic features of combustion chambers. We begin with the Rijke tube, the simplest thermoacoustic system. It consists of a duct with a heating gauze and can be prone to self excited oscillations. The next is a choked combustor, which contains a kinematic flame and a choked end capable of producing indirect noise. The third model is a longitudinal combustor, known in the literature as Rama Balachandran's burner ([Balachandran, 2005](#); [Balachandran et al., 2005, 2008](#)). This is a 10kW rig used to study the nonlinear response of turbulent premixed flames. The fourth model is a lean premix pre-vaporized (LPP) annular combustor consisting of a plenum, a ring of premix ducts and a combustion chamber, which has been used in [Morgans and Stow \(2007\)](#) to develop active control strategies to stabilize circumferential modes. The final is an annular model gas turbine combustor built in Cambridge University Engineering Department (CUED) to examine heat release dynamics in self-excited oscillations ([Worth and Dawson, 2013b](#)).

The first two models have been considered in [Aguilar et al. \(2017\)](#) in collaboration with Dr. Luca Magri. The longitudinal combustor has been considered in [Aguilar and Juniper \(2018b\)](#) and the annular combustor has been considered in [Aguilar and Juniper \(2018a\)](#).

3.3 The Rijke tube

Due to its simplicity, the Rijke tube is one of the preferred configurations to study thermoacoustic instabilities. First devised by [Rijke \(1859\)](#), and extensively studied ever since (see for example, [Matveev \(2003\)](#)), the configuration in its simplest form consists of an open ended tube with a heating gauze located somewhere in the tube. In a vertical pipe, the heat release causes a natural convection driven flow. Depending on the position and the power input of the heating gauze, thermoacoustic oscillations can be unstable. For a heat release model with small time delays, the most unstable position is when the gauze lies at $1/4$ of the total length of the tube.

Network model

To model the Rijke tube, we consider a perfect gas in a one dimensional network model composed of a duct of length b , a compact heat source at rest located at $x = b$ followed by another duct of length $L_n - b$ as shown in Fig. [3.2](#).

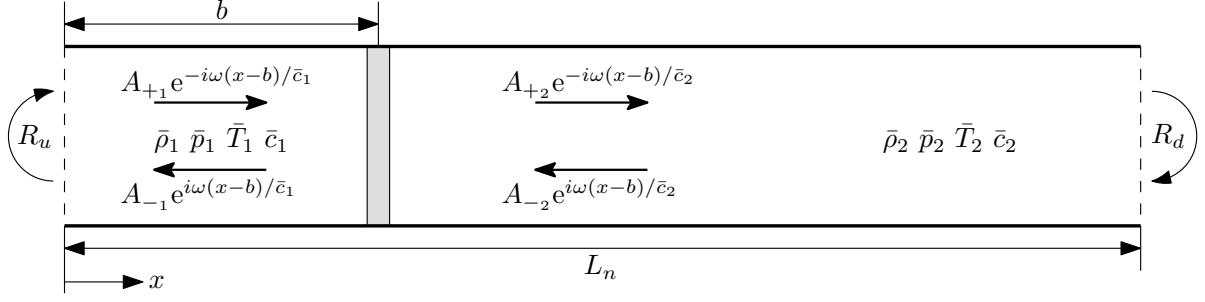


Fig. 3.2 Network model of the Rijke tube. The heat source located at $x = b$ divides the duct into two segments. The arrows represent the travelling waves moving at the local speed of sound, which are labelled A_{+1} and A_{-1} upstream of the heat source and A_{+2} and A_{-2} downstream. The waves' reflection coefficients at each end are R_u and R_d .

Due to the low speed in the mean flow, we choose the formulation in the zero Mach number limit (§ 2.4). The unsteady heat release model is given by a velocity driven $n - \tau$ model, which in the zero Mach number limit is given by:

$$\hat{Q} = \hat{u}_1 \beta e^{-i\omega\tau}, \quad (3.3)$$

where β is the interaction index, which in the zero mean flow case represents the energy added per unit volume and has dimensions $[\text{kgm}^{-1}\text{s}^{-2}]$, τ is the time delay and the subindex 1 represents the value of the velocity fluctuations just before the heating gauze.

Due to the low dimensionality of the system, we can write down the nonlinear eigenvalue problem as in Eq. (2.26). After centering the network at $x = b$, the boundary conditions are set by means of the upstream, $R_u(\omega)$, and downstream, $R_d(\omega)$, reflection coefficients. Matching the values of A_{+1} with A_{-1} , and A_{+2} with A_{-2} at $x = b$, after reflection off the boundaries gives:

$$A_{+1}(\omega) = R_u(\omega)A_{-1}(\omega)e^{-i\omega\tau_u} \quad \tau_u = 2b/\bar{c}_1, \quad (3.4)$$

$$A_{-2}(\omega) = R_d(\omega)A_{+2}(\omega)e^{-i\omega\tau_d} \quad \tau_d = 2(L_n - b)/\bar{c}_2. \quad (3.5)$$

We can therefore express the linearised jump conditions Eqs. (2.25) in matrix form:

$$\begin{bmatrix} -1 - R_u e^{-i\omega\tau_u} & 1 + R_d e^{-i\omega\tau_d} \\ (1 - R_u e^{-i\omega\tau_u}) \left(1 + \frac{\gamma-1}{\gamma\bar{p}_1} \beta e^{-i\omega\tau}\right) & \frac{\bar{c}_2}{\bar{c}_1} (1 - R_d e^{-i\omega\tau_d}) \end{bmatrix} \begin{bmatrix} A_{-1} \\ A_{+2} \end{bmatrix} = \begin{bmatrix} 0 \\ 0 \end{bmatrix}. \quad (3.6)$$

Model inputs

For the Rijke tube, the variables are non-dimensionalized using the following reference scales for length, time, speed and pressure, respectively: L_n , L_n/\bar{c}_1 , \bar{c}_1 and $\gamma\bar{p}_1$. The non-dimensional variables are written with a tilde, i.e., $\tilde{\omega} = \omega \times L_n/\bar{c}_1$. Pressure eigenfunctions for the direct variables are normalized as $\int_0^{L_n} \hat{p}(x)\hat{p}(x)^* dx = 1$. We consider a Rijke tube of length $L_n = 1$ m; the working fluid is assumed to behave as a perfect gas with dry air properties, $\gamma = 1.40$ and $R = 287.1$ Jkg⁻¹K⁻¹; inlet pressure of $\bar{p}_1 = 101.3$ kPa and inlet temperature of $\bar{T}_1 = 300.0$ K; open ends at the inlet and outlet, $R_u = -1$, $R_d = -1$; jump in temperature of $\Delta\bar{T} = 300.0$ K caused by the heating gauze located at $b = 0.250$ m with interaction index $\beta = 360.0 \times 10^3$ kgm⁻¹s⁻² and time delay $\tau = 1.00 \times 10^{-3}$ s.

Stability analysis

Following the procedure in § 2.5 Fig. 3.3 shows the logarithmic boundary error plot and the spectrum for the Rijke tube. We observe that in the studied regime there are 2 unstable eigenvalues at 222 and 670 Hz. The dominant eigenvalue is $\omega_1 = (2\pi \times 222.2 - 134.1i)$ rad s⁻¹, or in non-dimensional units: $\tilde{\omega}_1 = 4.021 - 0.3862i$.

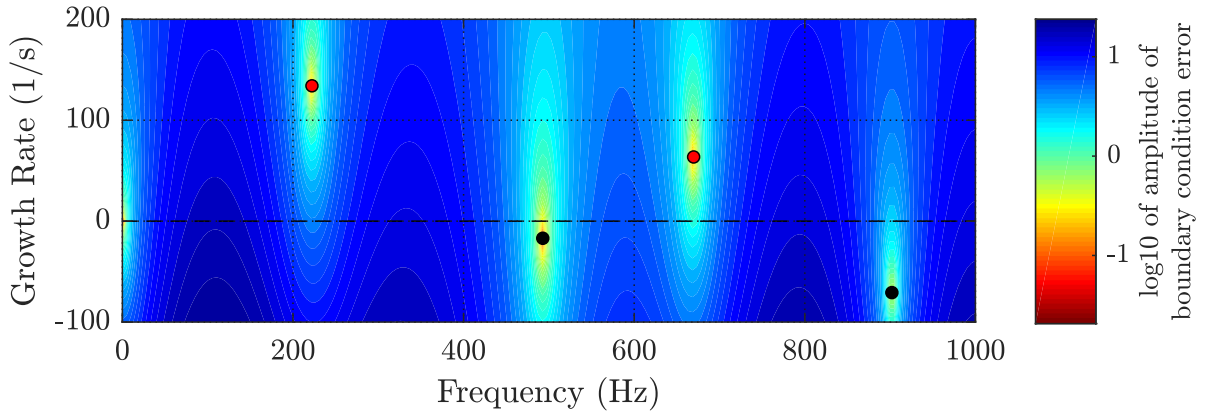


Fig. 3.3 Logarithmic boundary error plot for the Rijke tube. The red markers denote unstable eigenvalues and the black markers denote stable eigenvalues.

For the Rijke tube, the pressure and velocity mode shapes of the dominant eigenvalue in Fig. 3.4 display several important characteristics of thermoacoustic systems. The pressure is continuous at the heating gauze, with a slight change of gradient, while the velocity has a jump at the heat source, as expected from the jump conditions (2.24). For the duct equations in the zero mean flow case, Eq. (2.22), it is easy to show that when a Dirichlet boundary condition is imposed on \hat{p} , a Neumann boundary condition is instantly

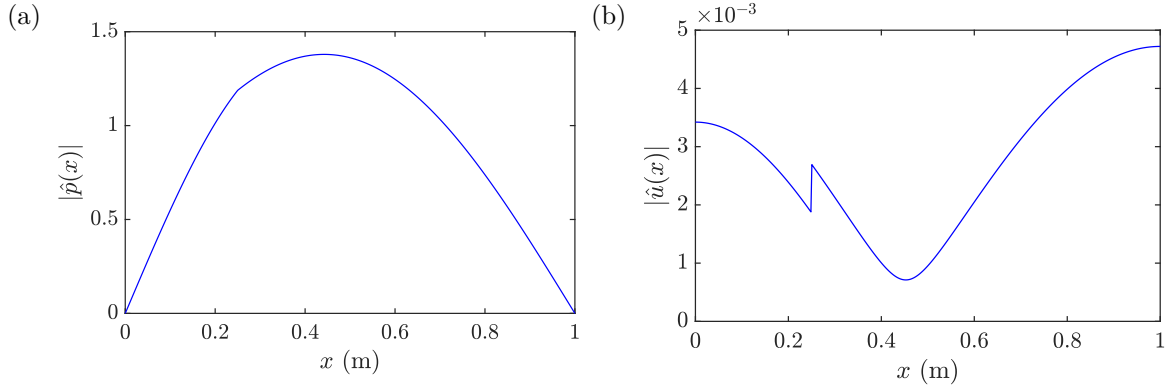


Fig. 3.4 Normalised relative amplitudes between pressure (a) and velocity (b) fluctuations, i.e., $\hat{p}(x) = |\hat{p}(x)|e^{i\theta}$.

imposed on \hat{u} , and vice versa. The former statement is depicted in the amplitudes of the direct mode shapes.

3.4 Choked combustor

Combustors often operate with mean flows at low Mach numbers. This allows the generation of entropy waves at the heat source, which when accelerated, for example at a nozzle, reflect back as acoustic waves (Marble and Candel, 1977). This is a mechanism for the generation of indirect noise (Goh and Morgans, 2013; Morgans and Duran, 2016). For a combustor the heat source is a flame, which has a dynamical behaviour. That is, it responds to the flow perturbations and is allowed to move from its mean position.

Network model

To model the choked combustor of Fig. 3.5, we assume a similar network structure as with the Rijke tube. However, the flame is considered to be anchored at $x = b$ and is modelled with the kinematic heat source in Eqs. (2.13). The heat release model is taken to be proportional to velocity fluctuations and the FTF is another $n - \tau$ model.

The boundary condition for the upstream acoustic waves defined through the reflection coefficient from Eq. (3.4) remains almost unaltered. Only the time delay associated with the length of the upstream duct changes to $\tau_u = 2b\bar{c}_1/(\bar{c}_1^2 - \bar{u}_1^2)$. The downstream boundary condition is a compact nozzle which is modelled as the choked outlet in Eq. 2.19. This condition allows acoustic fluctuations to be generated from the acceleration of

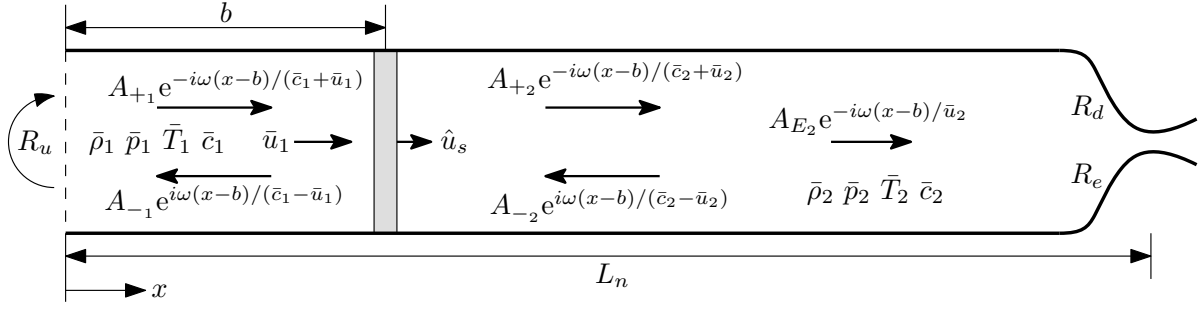


Fig. 3.5 Network model of a choked combustor. The setup considers a mean flow \bar{u} and a choked end. Compared to Fig. 3.2, this model includes corrections for the propagation speeds of the waves, and an entropy wave generated after the flame. The downstream end is now choked by a compact nozzle. The reflection coefficient R_e represents the strength of the acoustic wave generated by the entropy wave A_{E2} .

the entropy waves. Thus:

$$A_{-2}(\omega) = R_d A_{+2}(\omega) e^{-i\omega\tau_d} + R_e \mathcal{A}_{E2}(\omega) e^{-i\omega\tau_e} \quad (3.7a)$$

with reflection coefficients depending on the local Mach number:

$$R_d = \frac{1 - \frac{1}{2}(\gamma - 1)\bar{M}_2}{1 + \frac{1}{2}(\gamma - 1)\bar{M}_2} \quad \tau_d = 2(L_n - b)\bar{c}_2/(\bar{c}_2^2 - \bar{u}_2^2), \quad (3.7b)$$

$$R_e = -\frac{\frac{1}{2}\bar{M}_2}{1 + \frac{1}{2}(\gamma - 1)\bar{M}_2} \quad \tau_e = \frac{(L_n - b)\bar{c}_2}{\bar{u}_2(\bar{c}_2 - \bar{u}_2)}. \quad (3.7c)$$

Entropy fluctuations are often considered as convected hot spots generated by the flame. Therefore they are set to zero at the inlet, $A_{E1} = 0$. Following a similar approach as in § 2.5 we create an eigenvalue problem: $L(\omega)\hat{\mathbf{q}} = \mathbf{0}$. $L(\omega)$ is a matrix that includes the effects of the mean flow, \bar{u} , through the Mach number (the components are shown in appendix: B). The vector $\hat{\mathbf{q}} = [A_{-1} \ A_{+2} \ \mathcal{A}_{E2}]^T$ now contains the relative amplitudes between the acoustic and entropy waves. The problem is again nonlinear in the eigenvalue ω .

Model inputs

For this configuration, we use similar nondimensional variables and same properties for the air and inlet conditions as for the Rijke tube. However, we now assume a mean flow Mach number of $\bar{M}_1 = 5.00 \times 10^{-2}$, which requires an inlet steady flow of $\bar{u}_1 = 17.4 \text{ ms}^{-1}$. The flame causes a jump in temperature reaching $\bar{T}_2 = 1500 \text{ K}$ in the downstream side, which corresponds to a mean steady heat release of $\bar{Q}/A = 24.7 \text{ MWm}^{-2}$, which is similar

to the heat release of an intermediate scale rig (Lieuwen and Yang, 2005). The flame interaction index is chosen to be $k = 1.00$ and the time delay $\tau = 1.00 \times 10^{-3}$ s.

Stability analysis

The logarithmic boundary error plot for the choked combustor is shown in Fig. 3.6. There are 2 unstable modes at 184 and 551 Hz, with the latter being the most unstable. Further analyses in this configuration will focus on the first unstable mode: $\omega_1 = (2\pi \times 184.4 - 145.2i)$ rad s⁻¹ or $\tilde{\omega}_1 = 3.336 - 0.4180i$.

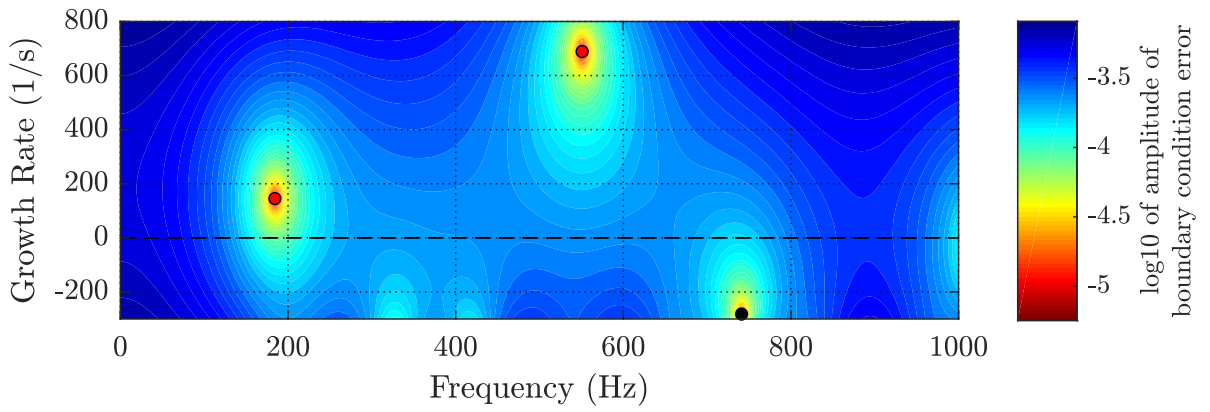


Fig. 3.6 Logarithmic boundary error plot for the choked combustor. The red markers denote unstable eigenvalues and the black markers denote stable eigenvalues.

The mode shapes for this configuration are shown in Fig. 3.7. Pressure (Fig. 3.7a) displays the open ended inlet condition and a jump caused by the combined effect of the mean flow and unsteady heat release Eq. (2.13). Velocity (Fig. 3.7b) has a jump at the flame location and shows the behaviour of a nearly closed end due to the choked boundary condition. In the region upstream of the flame, density (Fig. 3.7c) shows a similar behaviour as the pressure (scaled by a $1/\bar{c}_1^2$ factor). After the flame, density is the only mode shape that contains the influence of both acoustic and entropy waves. Small amplitude entropy waves appear in the downstream region because the acoustic fluctuations change the temperature upstream (and the model assumes that the mean heat release is kept constant, the flame front is planar rather than conical or V-shaped and the Mach number is very small.²) (Strobro-Chen et al., 2016). The generated hot spots are accelerated at the nozzle and converted into indirect acoustic waves. The ratio between the amplitudes of the indirect acoustic wave and the direct acoustic wave is 0.53%, which directly correlates to the small contribution of indirect noise in perfectly

²For this prediction to hold, strictly speaking, it is required that the mean flow is neglected.

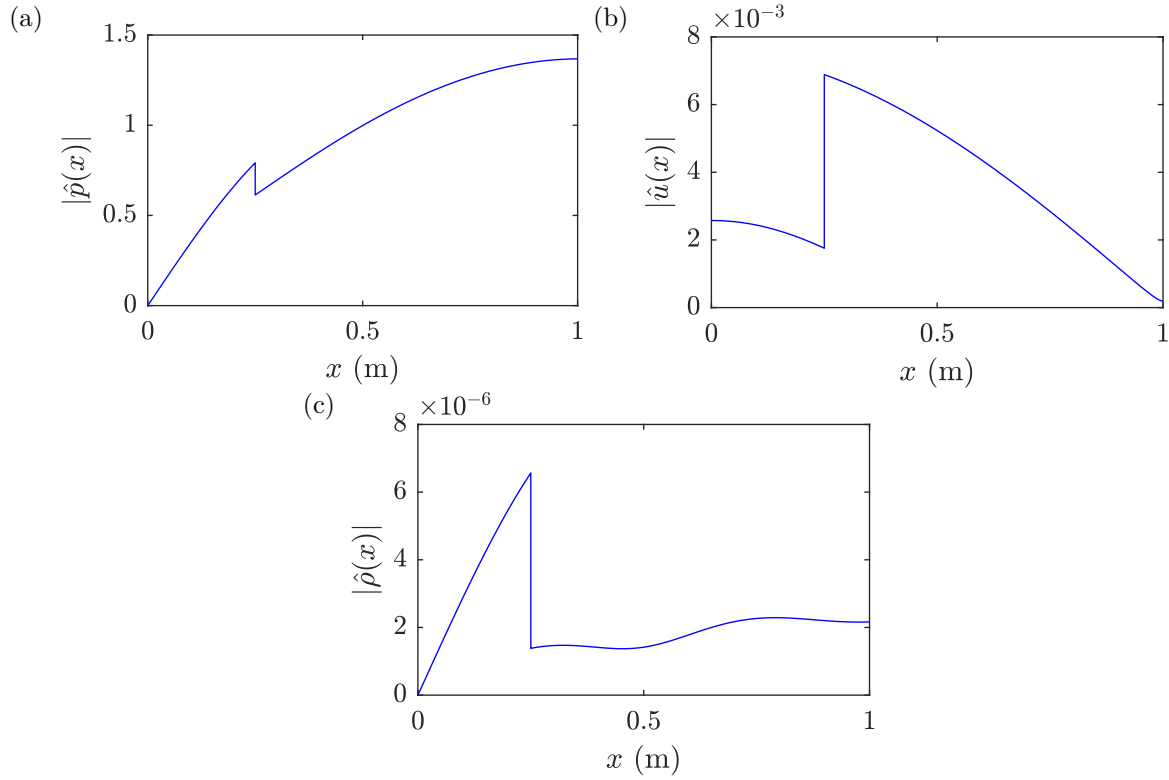


Fig. 3.7 Mode shapes for the first unstable mode in the choked combustor. The plots show the normalised relative amplitudes between pressure (a), velocity (b) and density (c) fluctuations, i.e., $\hat{p}(x) = |\hat{p}(x)|e^{i\theta}$.

premixed flames. For comparison, in the same configuration a heat source at rest ($\hat{u}_s = 0$) with the same heating capacity, such as a gauze heater, gives a ratio of 20.70%.

3.5 Longitudinal combustor

Rama Balachandran's burner is a 10 kW longitudinal combustor built in Cambridge University Engineering Department, originally intended for the experimental investigation of the response of turbulent premixed flames to acoustic oscillations (Balachandran, 2005). One of the experimental cases focuses on a configuration with no swirl and imperfectly premixed combustion prone to self-excited oscillations. The geometry consists of an inlet duct connected to a plenum with a varying cross section at both ends. This is followed by the neck which contains the fuel injection plane and a centred bluff body used to stabilize the flame. The outlet is a cylindrical pipe enclosure which contains the flame. The configuration is shown in Fig. 3.8.

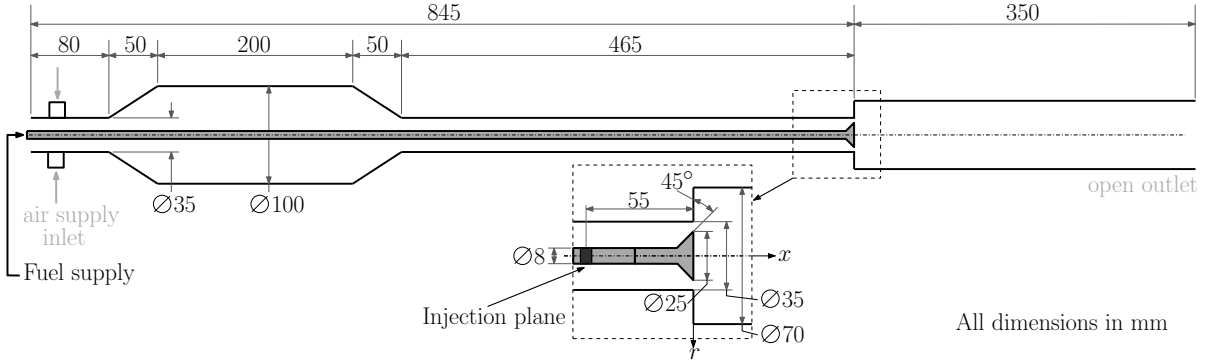


Fig. 3.8 Schematic of the longitudinal combustor.

Network model

To model the rig we consider a total of 124 straight ducts. The varying cross sections of the plenum are modelled as a sequence of 50 area increase steps and 50 area decrease steps in order to model the conical sections very accurately. To model the bluff body we further consider 20 area decrease steps.

Model inputs

We consider the working fluid to be a semi-perfect gas with air properties as given in [McBride et al. \(2002\)](#). At the inlet we use a temperature of 300 K. We assume that air is supplied with a constant mass flow rate of $\dot{m} = 5.518 \times 10^{-3} \text{ kgs}^{-1}$ to match the experimental measurement at the bluff body of $\bar{u} = 9.90 \text{ m/s}$ ([Balachandran, 2005](#)). We consider an open outlet at atmospheric pressure and a flame anchored to the bluff body. To match the experimental results and LES simulations ([Han et al., 2015](#)) we model the steady heat input with a combustion efficiency of $\eta = 95\%$, fuel properties of ethylene (See appendix A) and an equivalence ratio of $\phi = 0.61$.

For the boundary conditions we consider an inlet modelled by an acoustic reflection coefficient with $R_c = 0.85 + 0.10i$, which resembles the impedance of an end which is almost closed. The outlet is modelled with the frequency-dependent reflection coefficient of a circular duct radiating sound of Eq. (2.21).

For the heat source, we will use a velocity driven kinematic flame³ Eq. (2.13), with the annular cone flame transfer function as given in Eq. (A.13) and shown in Fig. 3.9, which approximately matches the flame structure and the results reported in [Balachandran \(2005\)](#).

³For this configuration we will assume the validity of the kinematic heat source for the given FTF. See footnote in §2.3.5 for details.

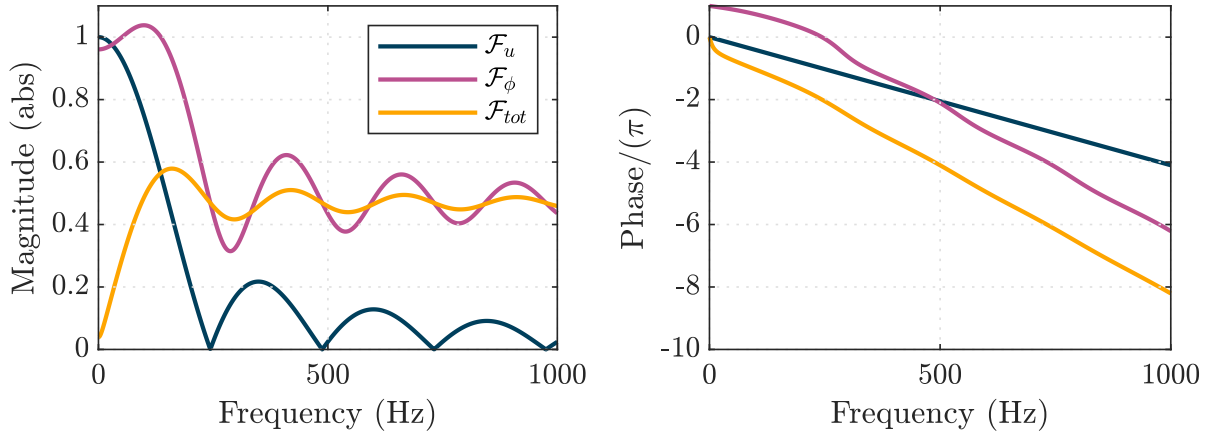


Fig. 3.9 Gain and phase of the flame transfer function used in the longitudinal combustor. F_u is the component of the flame transfer function due to velocity perturbations, F_ϕ is the component due to equivalence ratio fluctuations and F_{tot} is the addition of the other two.

Stability Analysis

The boundary error plot in Fig. 3.10 shows 4 unstable eigenvalues at 58, 364, 606 and 781 Hz. The second and most unstable resonant mode has a frequency which is close to the reported one (348 Hz in Balachandran (2005)) at which the self-excited oscillations saturate.

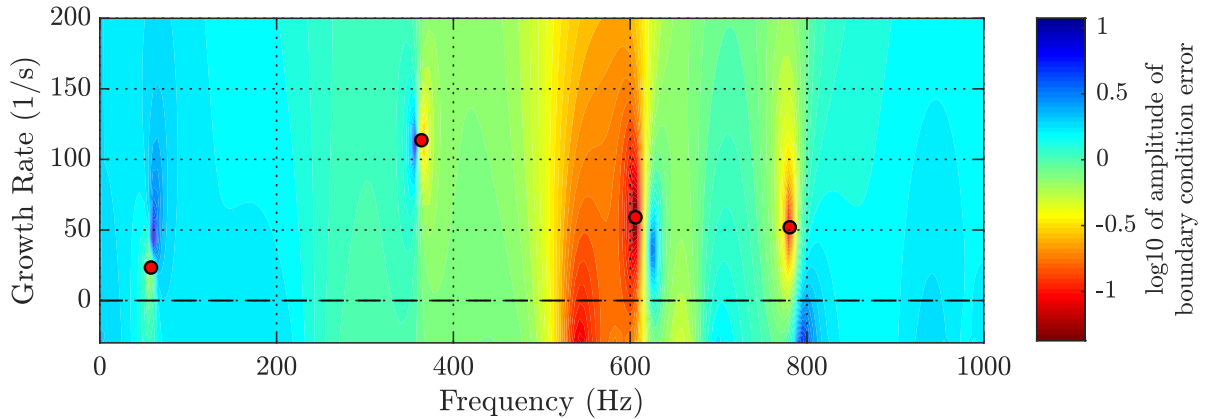


Fig. 3.10 Logarithmic boundary error plot for the longitudinal combustor. The red markers denote unstable eigenvalues and the black markers denote stable eigenvalues.

3.6 LPP annular combustor

Annular combustor geometries are typical of aero-engines. They are characterized by a ring of premix ducts where fuel is injected. Then the mixture is convected into the combustion chamber where reaction occurs. The annular combustor geometry considered is the same as in [Morgans and Stow \(2007\)](#), used to develop active control strategies to stabilize the circumferential modes in lean premixed prevaporized combustors. The geometry is shown in Fig. 3.11. It consists of a thin annular plenum, followed by a ring of 20 premix ducts, and an annular combustion chamber.

Model inputs

At the inlet the flow is choked and has a pressure of 5 bar, a temperature of 1000 K and a mass flow rate of 100 kg/s. In order to match closely the results reported in [Morgans and Stow \(2007\)](#), we consider that (i) the gas is a perfect gas, (ii) the flame is at rest, i.e., there is no moving flame front, and (iii) the combustion zone has a steady heat input of $\bar{Q} = 151.1$ MW, with interaction index of $k = -4$, and time delay of $\tau = 1.5 \times 10^{-3}$ s. At the outlet of the combustion chamber there is another choked end. Given that the system is linear and that we are not introducing elements that break the symmetry of the configuration, such as Helmholtz resonators ([Stow and Dowling, 2003](#)), the system will not present circumferential modal coupling.

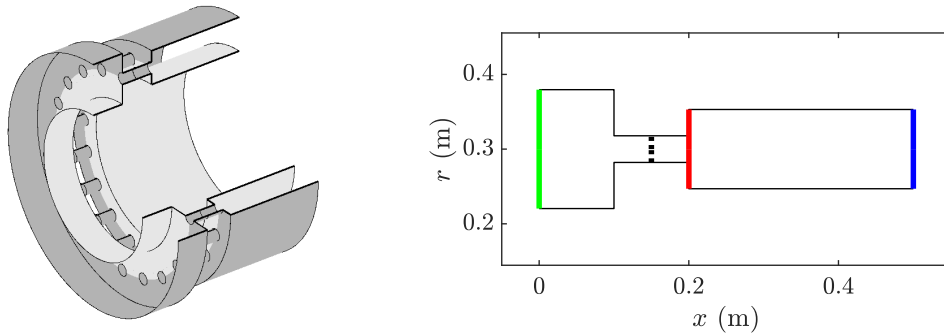


Fig. 3.11 Network model of the LPP annular combustor and cross sectional cut. The green and blue lines at the inlet and outlet represent choked ends respectively, the dotted line in the premix ducts represent the injection point and the red line represents single flame zone in the combustion chamber.

Stability analysis

To perform the stability analysis, we need to consider all possible azimuthal wave numbers n , where n is an integer. However, for high values of $|n|$ the modes rapidly decay and do not need to be considered any further. Therefore, the highest azimuthal wave number we consider for this configuration is $|n| = 3$. This is less than the maximum $|n|$ imposed by the model, which has the constraint that $|n| < D/2$ where $D = 20$ is the number of premix ducts (Stow and Dowling, 2004).

For frequencies up to 1000 Hz, Fig. 3.12 shows the error of the boundary condition at the outlet of the annular combustor for azimuthal wave numbers $n = 0$, and $n = \pm 1$. All of the eigenvalues at higher azimuthal wave numbers are stable (not shown here). For $n = 0$ (plane waves) there is an unstable mode at 57 Hz. For $n = \pm 1$ (first helical mode) there is an unstable mode at 547 Hz, which is very close to the one reported in Morgans and Stow (2007). The difference between the unstable modes reported in Morgans and Stow (2007) and the present analysis are due to the convective waves. In their model

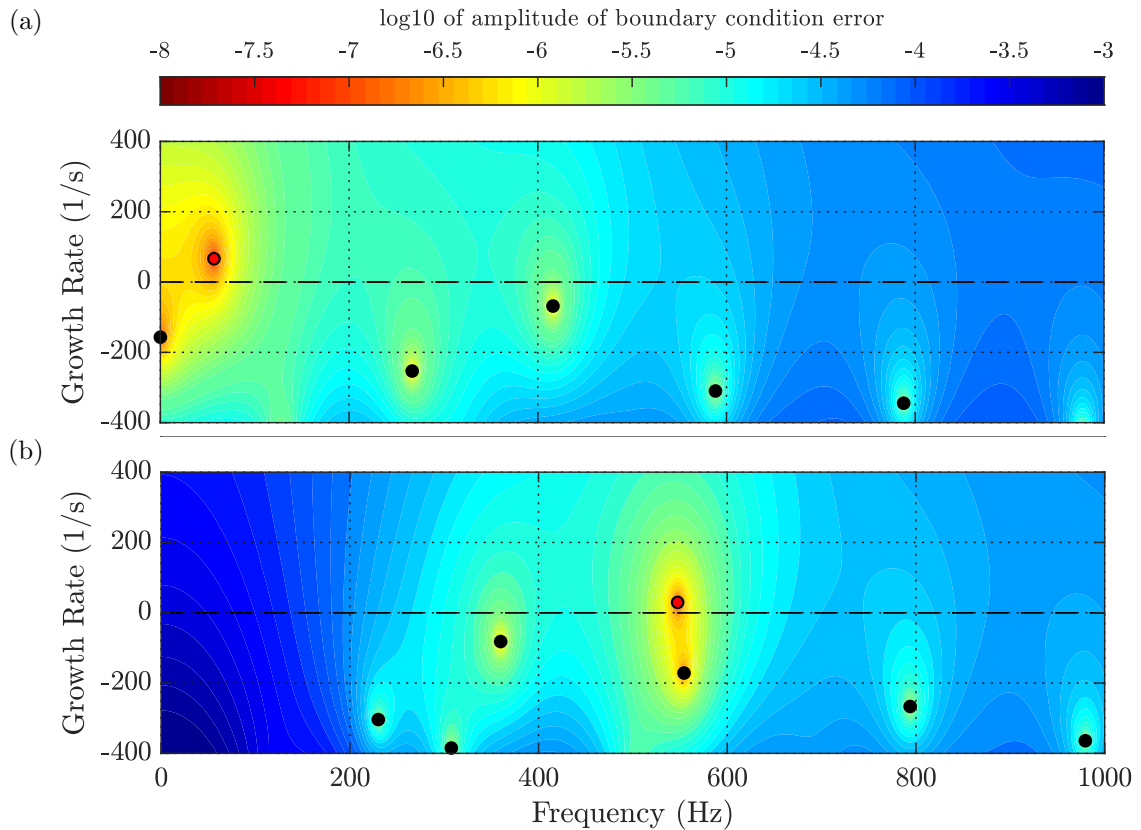


Fig. 3.12 Logarithmic boundary error plot for the LPP annular combustor. Plot (a) corresponds to azimuthal wave number $n = 0$ and plot (b) to $n = \pm 1$. The red markers denote unstable eigenvalues and the black markers denote stable eigenvalues.

they are assumed to dissipate before they reach the outlet boundary condition, which is not true for ours. For the mode at 547 Hz, the combustion chamber has mean velocity of $\bar{u} = 84.63 \text{ ms}^{-1}$. This translates to a convected wavelength of $\lambda_c = 0.1546 \text{ m}$, which is about twice the length of the combustion chamber. Therefore, we assume that the convective waves do not diffuse by the time they reach the outlet boundary condition.

3.7 CUED Annular combustor

The laboratory scale annular combustor built in CUED has been the subject of numerous experimental studies i.e., [Connor et al. \(2013\)](#); [Dawson and Worth \(2013\)](#); [Worth and Dawson \(2013a,b\)](#). Most of them are concerned with the flame dynamics in the annular combustor undergoing self-excited azimuthal instabilities. One of the experimental cases consisted of 18 evenly separated premixed bluff-body flames. The experiment ran on an ethylene-air mixture and used the equivalence ratio ϕ as bifurcation parameter to trigger self-excited azimuthal instabilities. The instabilities appeared at a frequency of around 1700 to 1800 Hz ([Worth and Dawson, 2013b](#)). Using LES and a Helmholtz solver [Bauerheim et al. \(2015b\)](#) was able to predict the stability of the combustor under the specified conditions. The geometry (see Fig. 3.13) consists of a plenum followed by a spherical flow divider, which is connected to the ring of premix ducts with the bluff bodies. This is followed by an annular enclosure with outer walls larger than the inner walls.

Network Model

The network model consists of 55 straight ducts. The varying cross section of the plenum is modelled with 20 area increase steps and the spherical flow divider is modelled with 20 area decrease steps. To model the bluff body we use a sequence of 10 area decrease steps in order to get the same flame holder area as in the experimental case.

There are a few challenges in trying to model this combustor using the network model approach, as shown in Fig. 3.14. The first is with regards to the validity of the narrow annular gap approximation. From the inlet of the combustor until around 30% of the length of the spherical flow divider the geometry is such that it permits radial wave propagation. To overcome this problem we assume that only plane waves propagate, i.e., $n = 0$. This is a reasonable approach given that the combustor has a honeycomb flow divider which does not allow the propagation of radial waves. The next challenge is to model the outlet boundary condition. On the one hand the outlet duct cannot be

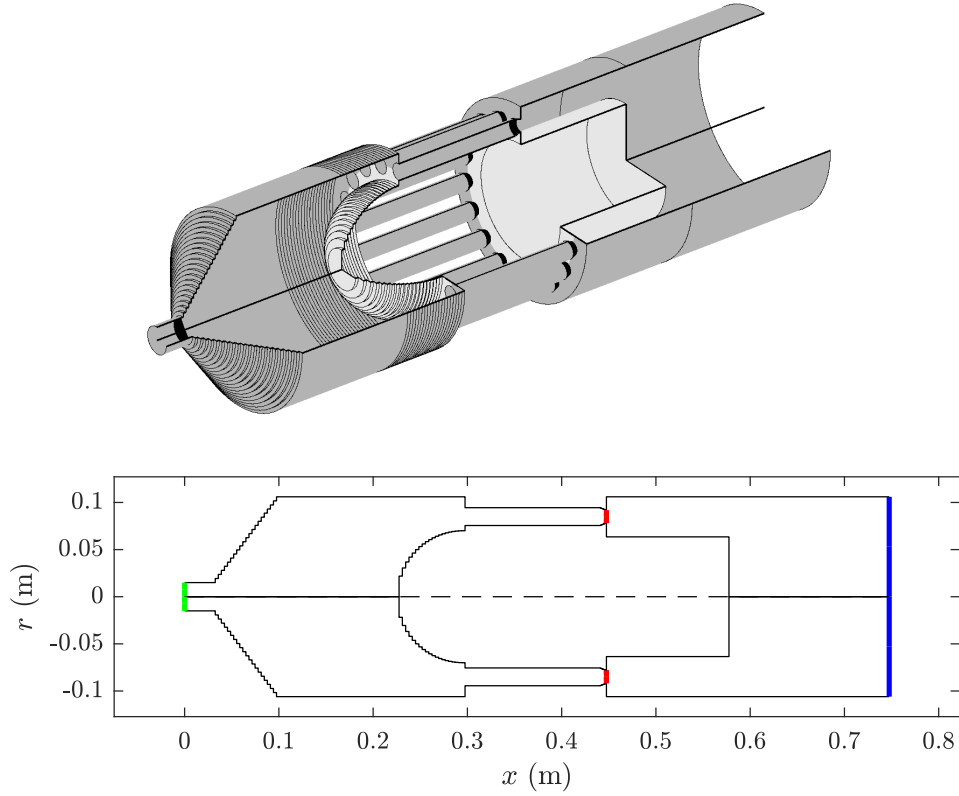


Fig. 3.13 Network model of the CUED annular combustor and cross sectional cut. The green line at the inlet represents a choked end and the blue line at the outlet represents the open outlet used in the model.

modelled using the narrow annular gap approximation, therefore, we assume that only plane waves propagate in this region. On the other hand, this duct has two open ended boundary conditions. In the model we only consider the right end as an open end and the left end is modelled as a wall. As mentioned in [Worth and Dawson \(2013b\)](#) this boundary condition may be critical in rendering the system unstable.

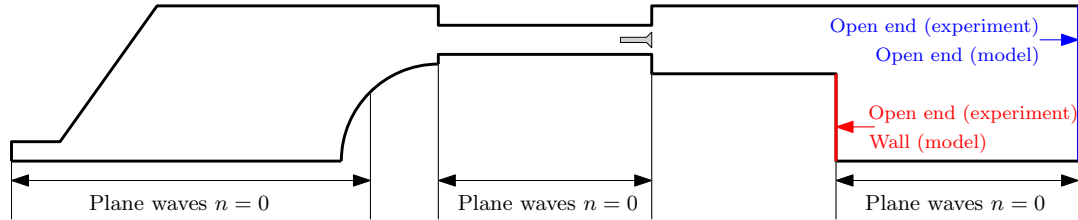


Fig. 3.14 Challenges in modelling the CUED annular combustor using the network model approach. 1) The narrow annular gap approximation is only valid in some regions of the rig. 2) The outlet boundary condition is not modelled exactly as in the experiments.

Model Inputs

The flow is modelled with the properties of air using a semi-perfect gas approximation as in § 3.5. The inlet of the configuration is considered as choked with a temperature of 300 K and a mass flow rate of $57.20 \times 10^{-3} \text{ kgs}^{-1}$ to match the speed at the bluff body of $\bar{u} = 18.0 \text{ ms}^{-1}$ (Worth and Dawson, 2013b). We consider the open outlet at atmospheric pressure. The steady heat input considers a combustion efficiency of $\eta = 100\%$, the fluctuating heat release is modelled with the velocity driven kinematic flame⁴ in Eqs. (2.13). The FTF for this model corresponds to a V shaped flame given in Eq. (A.12) and plotted in Fig. 3.15. This flame model resembles the structure of the flames in the experiments and LES simulations, but lacks important properties such as swirl, or flame-flame and flame-boundary interactions which can be fundamental to trigger the azimuthal instabilities (Bauerheim et al., 2015b; Worth and Dawson, 2013b).

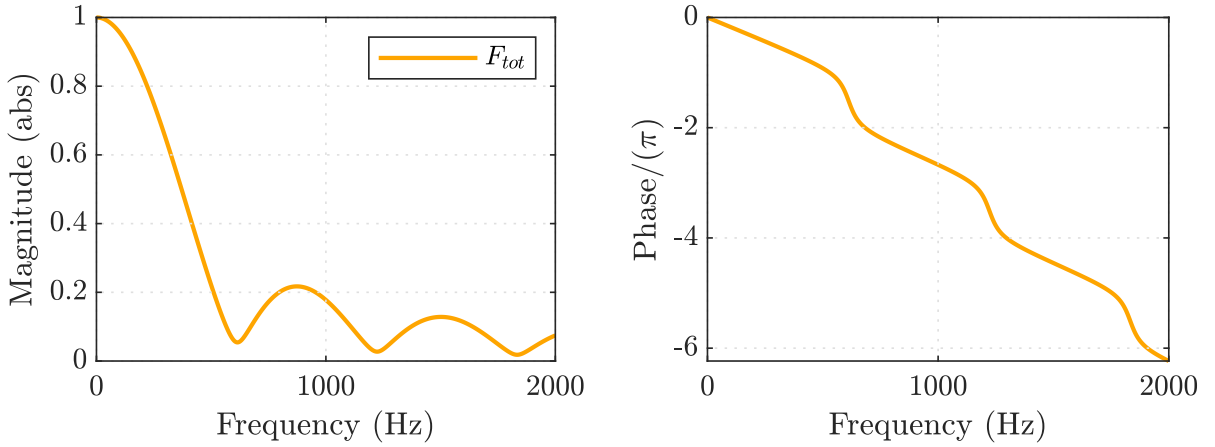


Fig. 3.15 Gain and phase of the flame transfer function used in the CUED annular combustor. F_{tot} is the component of the flame transfer function due to velocity perturbations.

Stability Analysis

For this configuration we consider azimuthal wave numbers from $n = 0$ up to the highest possible azimuthal wave number, i.e., $|n| = 8$. For frequencies up to 2000 Hz, Fig. 3.16 shows the eigenvalues of the system. The low order model predicts a total of 10 unstable modes, which are detailed in table 3.1. The unstable eigenvalues can be grouped in 3 categories:

- 1 unstable longitudinal mode.

⁴For this configuration we will assume the validity of the kinematic heat source for the given FTF. See footnote in §2.3.5 for details.

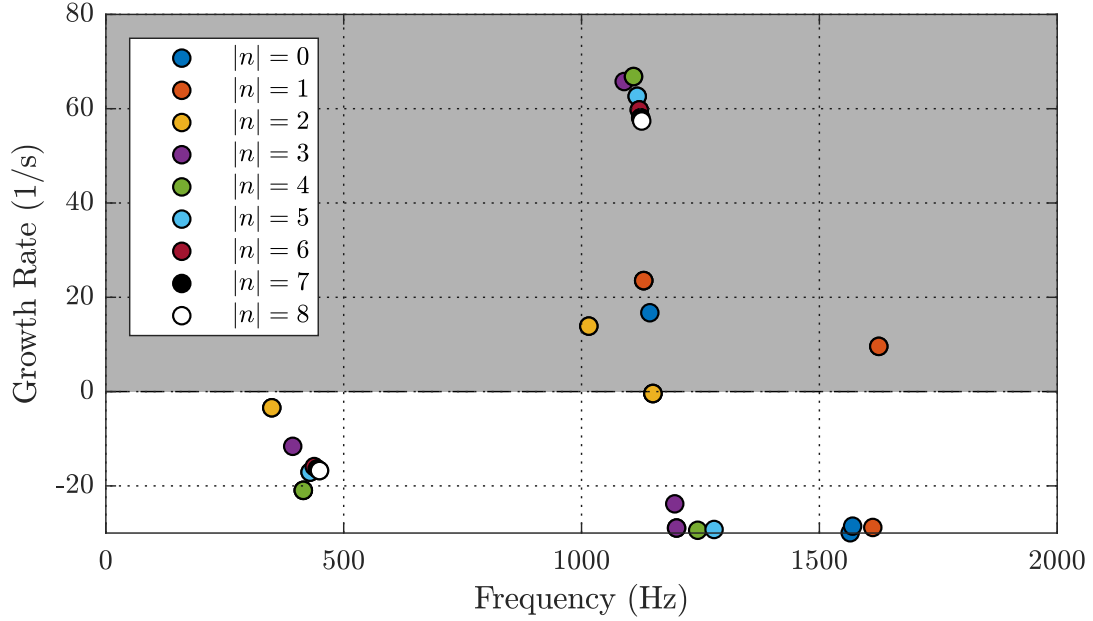


Fig. 3.16 Eigenvalues of the CUED annular combustor with azimuthal wave numbers $|n| = 0, 1, \dots, 8$. The gray region denotes the unstable half plane.

Azimuthal wave number ($ n $)	Frequencies of unstable modes (Hz)	Azimuthal wave number ($ n $)	Frequencies of unstable modes (Hz)
0	1144	5	1117
1	1131, 1625	6	1121
2	1015	7	1124
3	1090	8	1127
4	1109		

Table 3.1 Frequencies of the unstable modes of the CUED annular combustor.

- 2 unstable azimuthal modes with $|n| = 1$ at a frequency of 1131 and 1625 Hz, the latter is close to the reported frequency at which the system undergoes a limit cycle oscillation ([Bauerheim et al., 2015b](#); [Worth and Dawson, 2013b](#)).
- 7 unstable high order azimuthal modes which share the following characteristics:
 - they cluster in groups that share similar frequencies (observe that there is a similar group in the stable plane at around 400 Hz),
 - changing the outlet boundary condition (by gradually reducing the magnitude of the reflection coefficient from 1 to 0) does not change (within numerical error) the value of this modes. This is due to their axial cut off behaviour, see [Fig. 3.17](#).

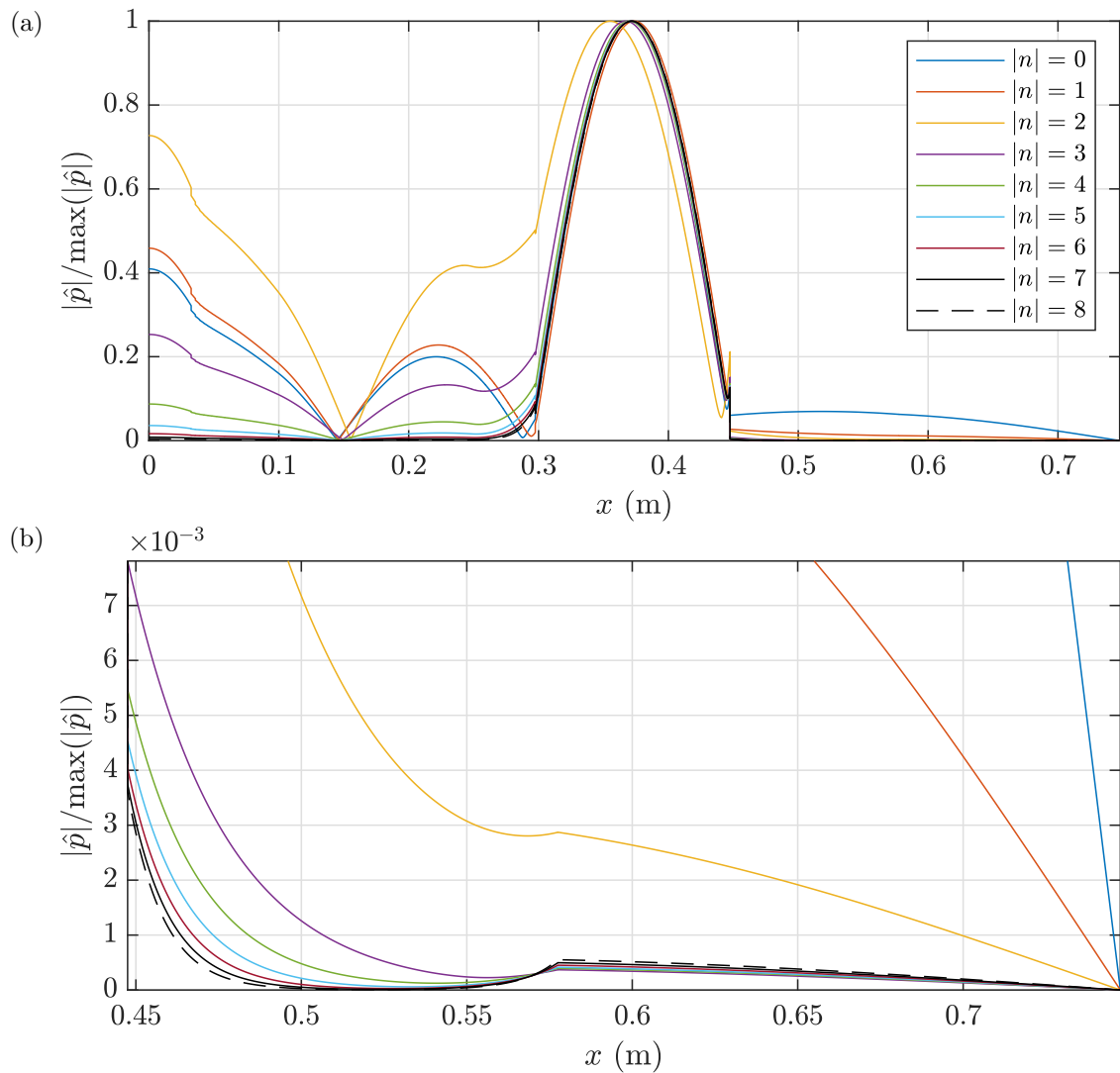


Fig. 3.17 Pressure mode shapes of the unstable modes around 1100 Hz in the CUED annular combustor. Plot (a) shows the normalized pressure mode shapes and (b) is a zoom in to the outlet region. Notice the scale difference in the plots, this indicates the cut off behaviour of the modes with large n .

Chapter 4

Adjoint methods in wave based approaches

4.1 Introduction

As reviewed by [Luchini and Bottaro \(2014\)](#) one of the major advantages of adjoint methods is the ability to obtain the sensitivity of a global quantity to all of the inputs in a complex problem at the computational cost of a single run of the corresponding adjoint algorithm. In flow control, adjoints often appear as a mechanism to enforce constraints of a cost functional, for example, when drag is minimized by enforcing the Navier-Stokes equations ([Jameson, 1995](#)). Hence, as explained by [Schmid and Brandt \(2014\)](#) the adjoint variables can be interpreted as cost functional gradients. These gradients can be used to design control techniques or to perform optimization.

The major drawbacks of adjoint methods are i) the need to derive the adjoint problem and ii) if the direct problem has singularities, such as shockwaves in compressible flows, a careful perturbation analysis is required such that the adjoint problem is well posed.

In thermoacoustics we are often interested in the response of the eigenvalue to changes in the system. Consequently, it is appropriate to treat the eigenvalue as the cost function with respect to which all of the sensitivities need to be computed. In this chapter, we first show the procedure to obtain the adjoint equations for wave-based approaches § 4.2. Then, in § 4.3 we derive the full set of adjoint equations in the Rijke tube and discuss the symmetries between the direct and the adjoint problems, as well as the sources of non-self adjointness that appear in thermoacoustics. Finally in § 4.4 we present the continuous adjoint equations for the network modules in chapter 2.

Part of the content in this chapter has appeared in the following publications: [Aguilar et al. \(2017\)](#) in collaboration with Dr. Luca Magri and [Aguilar and Juniper \(2018a,b\)](#).

4.2 The adjoint equations

Wave-based methods produce a nonlinear eigenvalue problem (see § 2.5) of the form:

$$L(\omega, \mathbf{p})\mathbf{q} = \mathbf{0}, \quad (4.1)$$

where ω is the eigenvalue and \mathbf{p} are the parameters of the system such as reflection coefficients, time delays and heat source parameters. The calculation of the adjoint equations depends on the approach taken. In a simple form, the adjoint of a linear operator L can be defined through a bilinear form $[\cdot, \cdot]$ such that for arbitrary \mathbf{a} and \mathbf{b} :

$$[\mathbf{a}, L\mathbf{b}] - [L^+\mathbf{a}, \mathbf{b}] = \text{constant}. \quad (4.2)$$

where L^+ is the adjoint operator. An operator L is said to be normal if its eigenfunctions \mathbf{q} are orthogonal, or equivalently, if $LL^+ = L^+L$. An operator is normal if it is self-adjoint, i.e., $L^+ = L$.

In this section we firstly examine the continuous adjoint derivation and secondly the discrete adjoint derivation.

4.2.1 Continuous adjoint

To obtain the continuous adjoint equations we create a Lagrangian functional. Considering $[\cdot, \cdot]$ as an appropriate inner product, the functional in its most general form is given by:

$$\mathcal{L} \equiv \omega - [\hat{\mathbf{q}}^+, \mathbf{P}(\omega, \hat{\mathbf{q}}, G)] - [\mathbf{G}^+, \mathbf{B}(G)], \quad (4.3)$$

where ω is the eigenvalue of interest. $\hat{\mathbf{q}}^+$ is the vector of Lagrange multipliers associated with $\mathbf{P}(\omega, \hat{\mathbf{q}}, G)$. $\mathbf{P}(\omega, \hat{\mathbf{q}}, G) = \mathbf{0}$, is the vector of fluctuating flow equations, jump conditions, and boundary conditions that equate to zero. These equations depend on the eigenvalue ω , the fluctuating variables $\hat{\mathbf{q}}$ and the base flow variables G . \mathbf{G}^+ is another vector of Lagrange multipliers associated with $\mathbf{B}(G)$. $\mathbf{B}(G) = \mathbf{0}$, is the vector of steady base flow equations, jump conditions and boundary conditions that equate to zero. These equations depend on the base flow variables G .

Ducts are governed by spatially varying functions, for example $a(x)$ and $b(x)$. Thus, the corresponding inner product is given by:

$$\langle a(x), b(x) \rangle \equiv \int_{x_0}^{x_1} a(x)^* b(x) \, dx, \quad (4.4)$$

where $*$ represents complex conjugation, and x_0 and x_1 represent the duct inlet and outlet positions. Jump conditions and boundary conditions are defined locally at positions x_0 or x_1 by single valued functions, for example c and d . Hence, the corresponding inner product is given by

$$\{c, d\} \equiv c^* d. \quad (4.5)$$

To determine the sensitivity functions of the eigenvalue following a Lagrangian approach (Gunzburger, 1997), any first variation of the Lagrangian with respect to a variable ξ must be equal to 0, for any arbitrary value of $\delta\xi$:

$$\frac{\partial \mathcal{L}}{\partial \xi} \delta\xi \equiv \lim_{\epsilon \rightarrow 0} \left(\frac{\mathcal{L}(\xi + \epsilon \delta\xi) - \mathcal{L}(\xi)}{\epsilon} \right) = 0. \quad (4.6)$$

For this problem, there are four sets of variables of interest. Vanishing the derivatives of \mathcal{L} in Eq. (4.3) with respect to the:

1. **adjoint variables** (components of vectors $\hat{\mathbf{q}}^+$ and \mathbf{G}^+), corresponds to the trivial case since they return the already known perturbation $\mathbf{P}(\omega, \hat{\mathbf{q}}, G) = 0$ and base flow equations $\mathbf{B}(G) = 0$;
2. **fluctuating variables** $\hat{\mathbf{q}}$, returns the adjoint fluctuating equations, used to compute the sensitivities of the eigenvalue to changes in the unsteady flow;
3. **base flow variables** G , returns the adjoint base flow equations, used to compute the sensitivities of the eigenvalue to changes in the steady base flow;
4. **eigenvalue** ω , returns the normalization condition.

4.2.2 Discrete adjoint

For the nonlinear eigenvalue problem (2.26) there exists an adjoint eigenvector $\hat{\mathbf{q}}^\dagger$ that satisfies:

$$(\hat{\mathbf{q}}^\dagger)^H \mathbf{L}(\omega, \mathbf{p}) = \mathbf{0}, \quad (4.7)$$

which is the corresponding discrete adjoint eigenvalue problem.

4.2.3 Continuous vs discrete adjoint equations

At this stage it is easy to see that the discrete adjoint is easier to implement, since we only need to compute the left eigenvectors of the system's matrix L . On the contrary, for the continuous approach we need to derive analytically all of the continuous adjoint equations and then solve for the corresponding adjoint variables. The main advantage of the continuous approach is that the adjoint variables are directly expressed in physical space, i.e., the adjoint eigenfunctions are known. For the reasons stated in § 5.3, given the modelling approach used, we favour the continuous adjoint.

4.3 Adjoint equations in the Rijke Tube: A worked example

Due to the simplicity of the Rijke tube, it is practical to derive the corresponding continuous adjoint equations alongside some observations concerning the self-adjointness of thermoacoustic systems. Since the Rijke tube is modelled with a zero Mach number formulation in this section, we will not cover the adjoint base flow formulation.

For the Rijke tube (§ 3.3) the fluctuating governing equations and jump conditions are given by Eqs. (2.22) and (2.25) respectively. Recalling that the fluid is a perfect gas ($\gamma_2 = \gamma_1 = \gamma$), that the heat source is located at $x = b$ and that the duct's area is constant ($A_1 = A_2$), gives:

$$E_1 \equiv i\omega\bar{\rho}\hat{u} + \frac{d\hat{p}}{dx} = 0, \quad (4.8a)$$

$$E_2 \equiv i\omega\hat{p} + \gamma\bar{p}\frac{d\hat{u}}{dx} = 0, \quad (4.8b)$$

$$J_1 \equiv \hat{p}_2 - \hat{p}_1 = 0, \quad (4.8c)$$

$$J_2 \equiv \frac{\gamma\bar{p}_2}{\gamma-1}\hat{u}_2 - \frac{\gamma\bar{p}_1}{\gamma-1}\hat{u}_1 - \beta\hat{u}_1e^{-i\omega\tau} = 0, \quad (4.8d)$$

where the subscript 1 represents the condition before the heating grid ($x = b^-$) and the subscript 2 represents the conditions just after it ($x = b^+$).

For the set of governing equations defined in $x \in [0, b^-) \cup (b^+, L_n]$ there exists a corresponding set of adjoint variables ($\hat{u}^+(x)$, $\hat{p}^+(x)$). Similarly, for the set of jump conditions defined only at $x = b$, there exists a corresponding set of adjoint variables (\hat{g}^+ , \hat{h}^+).

Using the direct equations (4.8) and the adjoint variables, we create a Lagrangian functional¹ (Magri and Juniper, 2014a):

$$\mathcal{L} \equiv \omega - \langle \hat{u}^+, E_1 \rangle - \langle \hat{p}^+, E_2 \rangle - \{\hat{g}^+, J_1\} - \{\hat{h}^+, J_2\}. \quad (4.9)$$

To determine the sensitivity functions of the eigenvalue following a Lagrangian approach, any first variation of the Lagrangian with respect to a variable ξ must be equal to 0. For this problem, there are only three sets of variables of interest: the direct variables (\hat{u}, \hat{p}) , the adjoint variables $(\hat{u}^+, \hat{p}^+, \hat{g}^+, \hat{h}^+)$ and the eigenvalue s . The trivial cases are the derivatives of the Lagrangian with respect to the adjoint variables, for example:

$$\frac{\partial \mathcal{L}}{\partial \hat{u}^+} \delta \hat{u}^+ = \langle \delta \hat{u}^+, E_1 \rangle = 0 \implies E_1 = 0 \quad (4.10)$$

which give the direct Eqs. (4.8). The derivatives with respect to the direct variables require integration by parts and give the adjoint equations:

$$i\omega^* \bar{\rho} \hat{u}^+ + \gamma \bar{p} \frac{d\hat{p}^+}{dx} = 0, \quad (4.11a)$$

$$i\omega^* \hat{p}^+ + \frac{d\hat{u}^+}{dx} = 0, \quad (4.11b)$$

along with boundary terms. Given the unsteady heat release model, the boundary terms defined just after the heating gauze ($x = b^+$) relate the adjoint variables defined at the jump to those defined in the rest of the domain. After some manipulation (Aguilar, 2015) they give:

$$\hat{g}^+ = \hat{u}_2^+, \quad (4.12a)$$

$$\hat{h}^+ = (\gamma - 1) \hat{p}_2^+. \quad (4.12b)$$

Similarly, the terms defined just before the heating gauze ($x = b^-$) provide the adjoint jump conditions:

$$\frac{\gamma \bar{p}_2}{\gamma - 1} \hat{p}_2^+ - \frac{\gamma \bar{p}_1}{\gamma - 1} \hat{p}_1^+ + \beta \hat{p}_2^+ e^{i\omega^* \tau} = 0, \quad (4.13a)$$

$$\hat{u}_2^+ - \hat{u}_1^+ = 0. \quad (4.13b)$$

¹The pairing between adjoint variables and direct equations is arbitrary. However, by using an adjoint variable with the same character as the perturbation variable that is multiplying the eigenvalue in a given equation, for instance, using \hat{u}^+ as adjoint variable to the equation that contains $i\omega \bar{\rho} \hat{u}$, the resultant adjoint equations display a similar structure as the direct problem.

Finally, boundary terms defined either at the inlet or outlet relate the direct boundary conditions to the adjoint boundary conditions:

$$\hat{u}^{+*} \hat{p} + \hat{p}^{+*} \gamma \bar{p} \hat{u} = 0. \quad (4.14)$$

The last quantity of interest in the Lagrangian is the eigenvalue. The Lagrangian's derivative with respect to the eigenvalue yields the normalization condition:

$$\langle \hat{u}^+, \bar{\rho} \hat{u} \rangle + \langle \hat{p}^+, \hat{p} \rangle + \{ \hat{h}^+, \tau \beta \hat{u}_1 e^{-i\omega\tau} \} = 1. \quad (4.15)$$

We recall that the first two inner products span the full domain of the ducts $x \in [0, b^-) \cup (b^+, L_n]$, and thus one integration is required for each duct.

4.3.1 Adjoint eigenvalue problem and sources of non-self-adjointness

In the zero Mach number limit we can make the variable change $\hat{\psi}^+ = \gamma \bar{p} \hat{p}^+$. Recalling that the product $\gamma \bar{p}$ is constant through the heat source, after some manipulation the adjoint system becomes:

$$i\omega^* \bar{\rho} \hat{u}^+ + \frac{\partial \hat{\psi}^+}{\partial x} = 0, \quad (4.16a)$$

$$i\omega^* \hat{\psi}^+ + \gamma \bar{p} \frac{\partial \hat{u}^+}{\partial x} = 0, \quad (4.16b)$$

$$\frac{\gamma \bar{p}_2}{\gamma - 1} \hat{\psi}_2^+ - \frac{\gamma \bar{p}_1}{\gamma - 1} \hat{\psi}_1^+ = -\beta \hat{\psi}_2^+ e^{i\omega^* \tau}, \quad (4.16c)$$

$$\hat{u}_2^+ - \hat{u}_1^+ = 0. \quad (4.16d)$$

After considering that the adjoint eigenvalue is the complex conjugate of the direct one, the adjoint equations governing the ducts Eqs. (4.16a) and (4.16b) are the same as in the direct case Eqs. (4.8a) and (4.8b). These equations, without considering boundary conditions, are those for pure acoustics. Unsurprisingly, this analysis shows that they are self-adjoint.

On the other hand, it is evident that the heat source makes the system non-self-adjoint through the jump conditions. The unsteady heat release term has switched from the \hat{u}^+ jump condition to the $\hat{\psi}^+$ jump condition. It has changed sign and now relies on a time in the future, $+\tau$. (The latter point shows that the adjoint equations naturally evolve backwards in time.)

After decoupling the system (as in § 2.3.1), we define the adjoint reflection coefficients, R_u^+ and R_d^+ , as for the direct case Eqs. (3.4) and (3.5). By applying Eq. (4.14), which links boundary terms at the inlet and outlet, we obtain:

$$R_u^+ = \frac{1}{R_u^*}, \quad (4.17a)$$

$$R_d^+ = \frac{1}{R_d^*}. \quad (4.17b)$$

The adjoint reflection coefficients are the inverse conjugates of the direct reflection coefficients. At first sight, this suggests that the system will be non-self-adjoint whenever $|R_u| \neq 1$ or $|R_d| \neq 1$ (and hence, non-normal as pointed out, for example, by [Mangesius and Polifke \(2011\)](#)). However, the direction of the travelling waves in the adjoint case is opposite to that in the direct case (i.e., A_{+1}^+ corresponds to A_{-1} and A_{-2}^+ corresponds to A_{+2}). This results in the following adjoint eigenvalue problem:

$$\begin{bmatrix} -1 - R_u^* e^{i\omega^* \tau_u} & (1 + R_d^* e^{i\omega^* \tau_d}) \left(1 + \frac{\gamma-1}{\gamma \bar{p}_1} \beta e^{i\omega^* \tau}\right) \\ 1 - R_u^* e^{i\omega^* \tau_u} & \frac{\bar{c}_2}{\bar{c}_1} (1 - R_d^* e^{i\omega^* \tau_d}) \end{bmatrix} \begin{bmatrix} A_{+1}^+ \\ A_{-2}^+ \end{bmatrix} = \mathbf{0}, \quad (4.18)$$

which can be written as $L^+(\omega) \hat{\mathbf{q}}^+ = \mathbf{0}$. Comparing it with the direct matrix L from Eq. (3.6), the unsteady heat release term has switched from the bottom-left element to the top-right element. The determinant, however, remains the same apart from the complex conjugation of the frequency-dependent terms, which arises due to the definition of the inner product in (4.4). Hence, we confirm that the adjoint eigenvalues are the complex conjugates of the direct eigenvalues ([Magri and Juniper, 2013b](#)), but the adjoint eigenvectors are *not* the complex conjugate of the direct eigenvectors, due to the re-positioning of the heat release term. Note that, in the absence of the unsteady heat release, matrices L and L^{+*} are identical, and the system is self-adjoint even when the magnitudes of the reflection coefficients are not 1.

4.4 Adjoint equations for network modules

In the following section an extensive derivation of the continuous adjoint equations for the different modules of chapter 2 is presented. Alongside the equations, relevant observations on how the assumptions made for the direct equations impact the development of the adjoint equations are discussed. Firstly, the adjoint perturbation equations are presented followed by the adjoint base flow equations.

4.4.1 Adjoint perturbation equations

To compute the adjoint perturbation equations we are interested in the first inner product of the Lagrangian functional as presented in Eq. (4.3).

Straight ducts

For a straight duct, the relevant components of vector \mathbf{P} in Eq. (4.3) are given by Eqs. (2.3). Their corresponding adjoint variables or Lagrange multipliers (components of vector $\hat{\mathbf{q}}^+$) are given by the spatial functions $[\hat{\rho}^+(x), \hat{u}^+(x), \hat{w}^+(x), \hat{p}^+(x)]^T$ respectively. The resulting adjoint perturbation equations are:

$$i\omega^* \hat{\rho}^+ + \bar{u} \frac{d\hat{\rho}^+}{dx} = 0, \quad (4.19a)$$

$$i\omega^* \bar{\rho} \hat{u}^+ + \bar{\rho} \bar{u} \frac{d\hat{u}^+}{dx} + \bar{\rho} \frac{d\hat{\rho}^+}{dx} + \gamma \bar{p} \frac{d\hat{p}^+}{dx} = 0, \quad (4.19b)$$

$$i\omega^* \bar{\rho} \hat{w}^+ + \frac{in}{R} \bar{\rho} \hat{\rho}^+ + \frac{in}{R} \gamma \bar{p} \hat{p}^+ + \bar{\rho} \bar{u} \frac{d\hat{w}^+}{dx} = 0, \quad (4.19c)$$

$$i\omega^* \hat{p}^+ + \bar{u} \frac{d\hat{p}^+}{dx} + \frac{in}{R} \hat{w}^+ + \frac{d\hat{u}^+}{dx} = 0. \quad (4.19d)$$

The associated boundary terms are:

$$\left[\left(\hat{\rho}^{+*} \bar{u} \right) \delta \hat{\rho} + \left(\hat{\rho}^{+*} \bar{\rho} + \hat{u}^{+*} \bar{\rho} \bar{u} + \hat{p}^{+*} \gamma \bar{p} \right) \delta \hat{u} + \left(\hat{u}^{+*} + \hat{p}^{+*} \bar{u} \right) \delta \hat{p} + \left(\hat{w}^{+*} \bar{\rho} \bar{u} \right) \delta \hat{w} \right]_{x_0}^{x_1} = 0, \quad (4.20)$$

where the δ symbol preceding the perturbation variables indicate that the boundary terms should vanish for any value of the perturbation variable. These terms are used to compute the jump conditions and to set the adjoint boundary conditions of the entire system.

Decoupling the system

We can decouple the system of adjoint equations (4.19) as in § 2.3.1. The resulting adjoint eigenvalues are the same as in the direct case, except for the complex conjugation in the frequency terms (ω). The adjoint system is again composed of four travelling waves: two adjoint acoustic waves with amplitudes A_+^+ and A_-^+ , which propagate downstream and upstream respectively, and two convective waves with amplitudes A_E^+ for an adjoint entropy wave and A_V^+ for an adjoint vorticity wave. The adjoint perturbation variables

can now be decomposed into waves:

$$\hat{\rho}^+(x) = -\bar{c}^2 A_E^+ e^{ik_0 x} \quad (4.21a)$$

$$\hat{p}^+(x) = A_+^+ e^{ik_+ x} + A_-^+ e^{ik_- x} + A_E^+ e^{ik_0 x} \quad (4.21b)$$

$$\hat{u}^+(x) = -\frac{k_+ \bar{c}^2}{\alpha_+} A_+^+ e^{ik_+ x} - \frac{k_- \bar{c}^2}{\alpha_-} A_-^+ e^{ik_- x} - \frac{n}{Rk_0} A_V^+ e^{ik_0 x} \quad (4.21c)$$

$$\hat{w}^+(x) = -\frac{n\bar{c}^2}{R\alpha_+} A_+^+ e^{ik_+ x} - \frac{n\bar{c}^2}{R\alpha_-} A_-^+ e^{ik_- x} + A_V^+ e^{ik_0 x} \quad (4.21d)$$

For modules that are governed by the mass, axial momentum, angular momentum and energy fluxes it is convenient to define the following adjoint perturbation fluxes that depend on the side i of the jump condition:

$$\hat{f}_{m_i}^+ = \frac{1}{A_i} \left(\hat{\rho}_i^+ - \bar{u}_i \hat{u}_i^+ + \left(\frac{1}{2}(\gamma_i - 1) \bar{u}_i^2 + \bar{c}_i^2 - (\gamma_i - 1) \bar{h}_i \right) \hat{p}_i^+ \right), \quad (4.22a)$$

$$\hat{f}_{x_i}^+ = \frac{1}{A_i} \left(\hat{u}_i^+ - (\gamma_i - 1) \bar{u}_i \hat{p}_i^+ \right), \quad (4.22b)$$

$$\hat{f}_{\theta_i}^+ = \frac{1}{A_i} \left(\frac{\hat{w}_i^+}{R_i} \right), \quad (4.22c)$$

$$\hat{f}_{e_i}^+ = \frac{1}{A_i} (\gamma_i - 1) \hat{p}_i^+, \quad (4.22d)$$

which in vector form is: $\hat{\mathbf{f}}_i^+ = [\hat{f}_{m_i}^+, \hat{f}_{x_i}^+, \hat{f}_{\theta_i}^+, \hat{f}_{e_i}^+]^T$. Similarly, for modules governed by mass, angular momentum and energy fluxes together with entropy conservation the following adjoint perturbation fluxes are defined:

$$\hat{s}_{m_i}^+ = \frac{1}{A_i} \left(\hat{\rho}_i^+ - \left(\frac{1}{2} \bar{u}_i + \frac{\bar{h}_i}{\bar{u}_i} \right) \hat{u}_i^+ + \bar{c}_i^2 \hat{p}_i^+ \right), \quad (4.23a)$$

$$\hat{s}_{s_i}^+ = \frac{1}{R_g} \left(\bar{p}_i \bar{u}_i (\gamma_i - 1) \hat{p}_i^+ - \bar{p}_i \hat{u}_i^+ \right), \quad (4.23b)$$

$$\hat{s}_{\theta_i}^+ = \frac{1}{A_i} \left(\frac{\hat{w}_i^+}{R_i} \right), \quad (4.23c)$$

$$\hat{s}_{e_i}^+ = \frac{1}{A_i} \left(\frac{\hat{u}_i^+}{\bar{u}_i} \right), \quad (4.23d)$$

which in vector form is: $\hat{\mathbf{s}}_i^+ = [\hat{s}_{m_i}^+, \hat{s}_{s_i}^+, \hat{s}_{\theta_i}^+, \hat{s}_{e_i}^+]^T$.

Area increase

For an area increase the components of vector \mathbf{P} are given by fluctuating quantities of Eq. (2.7). Their corresponding Lagrange multipliers are given by the numbers $\hat{\mathbf{a}}^+ = [a_m^+, a_x^+, a_\theta^+, a_e^+]^T$ respectively. The relationship between adjoint variables at the area change and those defined in the ducts is given by: $\hat{\mathbf{a}}^+ = \hat{\mathbf{f}}_2^+$. The corresponding adjoint jump conditions for an area increase are given by:

$$\hat{\mathbf{f}}_1^+ = \hat{\mathbf{f}}_2^+ + \hat{\phi}^+ \left[\left(\bar{h}_1 - \frac{\bar{u}_1^2}{2} \right) (\gamma_1 - 1) - 2\bar{c}_1^2, \frac{\bar{c}_1^2}{\bar{u}_1} + (\gamma_1 - 1)\bar{u}_1, 0, -(\gamma_1 - 1) \right]^T, \quad (4.24)$$

where

$$\hat{\phi}^+ = \frac{A_2 - A_1}{A_1} \left(\frac{\bar{u}_1}{\bar{c}_1^2 - \bar{u}_1^2} \right) \hat{f}_{x_2}^+.$$

Area decrease

For an area decrease the components of vector \mathbf{P} are given by the fluctuating quantities of Eq. (2.8). Their corresponding Lagrange multipliers are given by the numbers $\hat{\mathbf{b}}^+ = [b_m^+, b_s^+, b_\theta^+, b_e^+]^T$ respectively. The relationship between adjoint variables at the area change and those defined in the ducts is given by: $\hat{\mathbf{b}}^+ = \hat{\mathbf{s}}_2^+$. The corresponding adjoint jump conditions for an area decrease are given by:

$$\hat{\mathbf{s}}_1^+ = \hat{\mathbf{s}}_2^+. \quad (4.25)$$

Ring of premix ducts

At the start of a ring of premix ducts an area decrease is observed, so the components of vector \mathbf{P} are given by Eq. (2.9). The corresponding Lagrange multipliers are given by the numbers $\hat{\mathbf{b}}^+ = [b_m^+, b_s^+, b_\theta^+, b_e^+]^T$ respectively. The relationship between adjoint variables at the start of the premix ducts and those defined in the ducts is given by: $\hat{\mathbf{b}}^+ = \hat{\mathbf{s}}_2^+$. The corresponding adjoint jump conditions are:

$$\hat{\mathbf{s}}_1^+ = \kappa_n \left[\hat{s}_{m_2}^+, \hat{s}_{s_2}^+, 0, \hat{s}_{e_2}^+ \right]^T, \quad (4.26)$$

where κ_n is the integration factor defined in § 2.3.4. At the end of the premix ducts an area increase is observed. The components of vector \mathbf{P} are given by Eq. (2.10). The corresponding Lagrange multipliers are given by the numbers $\hat{\mathbf{a}}^+ = [a_m^+, a_x^+, a_\theta^+, a_e^+]^T$ respectively. The relationship between adjoint variables at the start of the premix ducts and those defined in the ducts is given by: $\hat{\mathbf{a}}^+ = \hat{\mathbf{f}}_2^+$. The corresponding adjoint jump

conditions are:

$$\hat{\mathbf{f}}_1^+ = \frac{1}{\kappa_n} \begin{bmatrix} \hat{f}_{m_2}^+ \\ \hat{f}_{x_2}^+ \\ 0 \\ \hat{f}_{e_2}^+ \end{bmatrix} + \hat{\phi}_\kappa^+ \begin{bmatrix} \left(\bar{h}_1 - \frac{\bar{u}_1^2}{2} \right) (\gamma_1 - 1) - 2\bar{c}_1^2 \\ \frac{\bar{c}_1^2}{\bar{u}_1} + (\gamma_1 - 1)\bar{u}_1 \\ 0 \\ -(\gamma_1 - 1) \end{bmatrix}, \quad (4.27)$$

where

$$\hat{\phi}_\kappa^+ = \frac{A_2 - A_1/\kappa_n}{A_1} \left(\frac{\bar{u}_1}{\bar{c}_1^2 - \bar{u}_1^2} \right) \hat{f}_{x_2}^+.$$

Heat source at rest

The adjoint perturbation equations for a heat source at rest depend on the form of the unsteady heat release and need to be analysed together with the measurement point. The components of vector \mathbf{P} are given by the fluctuating quantities of Eqs. (2.7) for the measurement point (assuming constant area) and Eqs. (2.12) for the heat source at rest. We will denote with subindices 1 and 2 the points before and after the measurement point and with 3 and 4 the points before and after the heat source. The corresponding Lagrange multipliers are $\hat{\mathbf{a}}^+ = [a_m^+, a_x^+, a_\theta^+, a_e^+]^T$ for the measurement point and $\hat{\mathbf{c}}^+ = [c_m^+, c_x^+, c_\theta^+, c_e^+]^T$ for the heat source at rest. The relationship between adjoint variables at the measurement point and those defined in the ducts are given by: $\hat{\mathbf{a}}^+ = \hat{\mathbf{f}}_2^+$. For the heat source, they are given by $\hat{\mathbf{c}}^+ = \hat{\mathbf{f}}_4^+$. The corresponding adjoint jump conditions for the measurement point for the generic unsteady heat release in Eq. (2.15) are given by:

$$\hat{\mathbf{f}}_1^+ = \hat{\mathbf{f}}_2^+ + \hat{Q}^+ \left(\mu_r \left(\mathbf{f}_{c_1} + \begin{bmatrix} \bar{c}_1^2 - \bar{u}_1^2 \\ 0 \\ 0 \\ 0 \end{bmatrix} \right) - \mu_u (\mathbf{f}_{c_1}) + \mu_p \gamma_1 \bar{M}_1^2 \left(\mathbf{f}_{c_1} - \begin{bmatrix} \bar{c}_1^2 - \bar{u}_1^2 \\ \frac{\bar{c}_1^2 - \bar{u}_1^2}{\bar{u}_1} \\ 0 \\ 0 \end{bmatrix} \right) \right) \quad (4.28)$$

where

$$\hat{Q}^+ = \frac{\bar{Q}}{\bar{m}_1 (\bar{c}_1^2 - \bar{u}_1^2)} \mathcal{F}_t^* \hat{f}_{e_4}^+, \quad (4.29)$$

$$\mathbf{f}_{c_i} = \left[\bar{h}_i(\gamma_i - 1) - \bar{c}_i^2 - \frac{1}{2} \bar{u}_i^2(\gamma_i + 1), \gamma_i \bar{u}_i, 0, -(\gamma_i - 1) \right]^T. \quad (4.30)$$

The unsteady adjoint equations for the measurement point are forced by the unsteady heat release at the heat source position. The adjoint jump conditions for the heat source are:

$$\hat{\mathbf{f}}_3^+ = \hat{\mathbf{f}}_4^+ \quad (4.31)$$

Kinematic heat source

For a kinematic heat source, the only change from the previous formulation is that the fluctuating equations for a heat source considered are now given by Eqs. (2.13) and (2.14). The adjoint jump conditions at the measurement point are given by:

$$\begin{aligned} \hat{\mathbf{f}}_1^+ &= \hat{\mathbf{f}}_2^+ \cdots \\ &+ \left(\hat{Q}^+ - \hat{u}_{sq}^+ \right) \left(\mu_r \left(\mathbf{f}_{c_1} + \begin{bmatrix} \bar{c}_1^2 - \bar{u}_1^2 \\ 0 \\ 0 \\ 0 \end{bmatrix} \right) - \mu_u (\mathbf{f}_{c_1}) + \mu_p \frac{\gamma_1 \bar{u}_1^2}{\bar{c}_1^2} \left(\mathbf{f}_{c_1} - \begin{bmatrix} \bar{c}_1^2 - \bar{u}_1^2 \\ \bar{c}_1^2 - \bar{u}_1^2 \\ \bar{u}_1 \\ 0 \\ 0 \end{bmatrix} \right) \right) \end{aligned} \quad (4.32)$$

where

$$\hat{u}_{sq}^+ = \frac{\bar{u}_3}{\bar{m}_1 (\bar{c}_1^2 - \bar{u}_1^2)} \mathcal{F}_t^* \left(\hat{f}_{m_4}^+ \bar{m}_{u_s} + \hat{f}_{e_4}^+ \bar{e}_{u_s} \right), \quad (4.33a)$$

$$\bar{m}_{u_s} = A_4 \bar{\rho}_4 - A_3 \bar{\rho}_3, \quad (4.33b)$$

$$\bar{e}_{u_s} = A_4 \bar{\rho}_4 \left(\bar{h}_4 - \frac{\bar{p}_4}{\bar{\rho}_4} + \frac{1}{2} \bar{u}_4^2 \right) - A_3 \bar{\rho}_3 \left(\bar{h}_3 - \frac{\bar{p}_3}{\bar{\rho}_3} + \frac{1}{2} \bar{u}_3^2 \right), \quad (4.33c)$$

the adjoint unsteady heat release term \hat{Q}^+ stays as in Eq. (4.29) and \mathbf{f}_{c_1} as in Eq. (4.30). The jump conditions for the heat source are given by:

$$\hat{\mathbf{f}}_3^+ = \hat{\mathbf{f}}_4^+ + \left[\hat{u}_{sm}^+, 0, 0, 0 \right]^T, \quad (4.34)$$

with

$$\hat{u}_{sm}^+ = \frac{\bar{u}_3}{\bar{m}_3} \left(\hat{f}_{m_4}^+ \bar{m}_{u_s} + \hat{f}_{e_4}^+ \bar{e}_{u_s} \right). \quad (4.35)$$

For kinematic heat sources, we observe that the adjoint equivalent of the heat source speed splits in two. The part corresponding to the unsteady heat release (\hat{u}_{sq}^+) forces the measurement point, while the part corresponding to the local mass flow rate fluctuations (\hat{u}_{sm}^+) forces the heat source.

Inlet boundary conditions

For an inlet boundary condition, the component of vector \mathbf{P} is given by the relevant boundary condition from those discussed in § 2.3.6. The corresponding Lagrange multiplier is b_i^+ . The relationship between the adjoint variables defined in the ducts and those defined at the boundary is given by:

- *Open end*: $b_i^+ = \hat{u}^+ + \bar{u}\hat{p}^+$;
- *Closed end*: $b_i^+ = \bar{\rho}\hat{p}^+ + \bar{\rho}\bar{u}\hat{u}^+ + \gamma\bar{p}\hat{p}^+$;
- *Choked end*: for this condition we defined four equations. Therefore, there must be the same number of adjoint variables, which we define as $b_{i_p}^+, b_{i_\rho}^+, b_{i_u}^+, b_{i_w}^+$. The corresponding relationships are given by:

$$b_{i_p}^+ = \hat{u}^+ + \bar{u}\hat{p}^+, \quad b_{i_\rho}^+ = \bar{u}\hat{\rho}^+, \quad b_{i_u}^+ = \bar{\rho}\hat{\rho}^+ + \bar{\rho}\bar{u}\hat{u}^+ + \gamma\bar{p}\hat{p}^+, \quad b_{i_w}^+ = \bar{\rho}\bar{u}\hat{w}^+;$$

- *Acoustic reflection coefficient*: $b_i^+ = 1/(1 + R_c^*) (\hat{\rho}^+ + \bar{u}\hat{u}^+ + \bar{c}^2\hat{p}^+)$.

As discussed before, the adjoint method evolves backwards in time. Therefore, the shooting method on the adjoint equations is performed from the outlet to the inlet. In this case, the most general adjoint inlet boundary condition for any direct inlet boundary condition is given by Eq. (4.20), rewritten here without the deltas, because at the boundaries the choice of the values of the adjoint variables must be such that the entire equation is equal to zero:

$$\hat{\rho}^{+*}\bar{u}\hat{\rho} + \hat{\rho}^{+*}\bar{\rho}\hat{u} + \hat{u}^{+*}\bar{\rho}\bar{u}\hat{u} + \hat{p}^{+*}\gamma\bar{p}\hat{u} + \hat{u}^{+*}\hat{p} + \hat{p}^{+*}\bar{u}\hat{p} + \hat{w}^{+*}\bar{\rho}\bar{u}\hat{w} = 0. \quad (4.36)$$

By substituting the direct inlet boundary conditions into the above equation we obtain simplified expressions for the adjoint inlet boundary conditions. For simplicity, they will be expressed in terms of adjoint wave amplitudes:

- *Open inlet:*

$$A_+^+ + \frac{\alpha_+}{\alpha_-} A_-^+ = 0. \quad (4.37)$$

- *Closed inlet:*

$$A_+^+ + \frac{\alpha_+}{\alpha_-} \left(\frac{\bar{c}^2 k_- - \bar{u} \alpha_- + \bar{c}^2 n^2 / (R^2 k_0)}{\bar{c}^2 k_+ - \bar{u} \alpha_+ + \bar{c}^2 n^2 / (R^2 k_0)} \right) A_-^+ = 0. \quad (4.38)$$

- *Choked inlet:*

$$\begin{aligned} A_+^+ + \frac{\alpha_+}{\alpha_-} \left(\frac{\bar{c}^2 k_- + (\gamma - 1) \bar{u} \alpha_-}{\bar{c}^2 k_+ + (\gamma - 1) \bar{u} \alpha_+} \right) A_-^+ + \left(\frac{\bar{u} (\gamma - 1) \alpha_+}{\bar{c}^2 k_+ + (\gamma - 1) \bar{u} \alpha_+} \right) A_E^+ \dots \\ - \left(\frac{n \bar{u} \alpha_+}{R \omega (\bar{c}^2 k_+ + (\gamma - 1) \bar{u} \alpha_+)} \right) A_V^+ = 0. \end{aligned} \quad (4.39)$$

- *Acoustic reflection coefficient:*

$$A_+^+ + \frac{\alpha_+^2}{\alpha_-^2} \left(\frac{B_1}{B_2} \right) A_-^+ = 0, \quad (4.40)$$

where

$$\begin{aligned} B_1 &= \alpha_-^2 \bar{u} (1 + R_c^*) + \left(R_c^* \frac{\alpha_-}{\alpha_+} + 1 \right) \frac{\bar{c}^2 n^2 \bar{u}}{R^2} - \bar{c}^2 k_- \left(\alpha_- (1 + R_c^*) + \omega \left(1 + R_c^* \frac{\alpha_- k_+}{\alpha_+ k_-} \right) \right), \\ B_2 &= \alpha_+^2 \bar{u} (1 + R_c^*) + \left(R_c^* + \frac{\alpha_+}{\alpha_-} \right) \frac{\bar{c}^2 n^2 \bar{u}}{R^2} - \bar{c}^2 k_+ \left(\alpha_+ (1 + R_c^*) + \omega \left(\frac{\alpha_+ k_-}{\alpha_- k_+} + R_c^* \right) \right). \end{aligned}$$

Outlet boundary conditions

In this case, the component of vector \mathbf{P} is given by the relevant boundary condition from those discussed in § 2.3.6. The corresponding Lagrange multiplier is b_o^+ . The relationship between the adjoint variables defined in the ducts and that defined at the boundary is given by:

- *Open end:* $b_o^+ = -(\hat{u}^+ + \bar{u} \hat{p}^+)$.
- *Closed end:* $b_o^+ = -(\bar{\rho} \hat{p}^+ + \bar{\rho} \bar{u} \hat{u}^+ + \gamma \bar{p} \hat{p}^+)$.
- *Choked end:* $b_o^+ = -(\bar{\rho} \bar{u} \hat{p}^+) / \left(1 - \frac{dc_p(\bar{T})}{dT} \frac{(\gamma-1)^2}{\gamma} \frac{\bar{T}}{R_g} \right)$.
- *Acoustic reflection coefficient:* $b_o^+ = -1 / (1 + R_c^*) (\bar{\rho} \hat{p}^+ + \bar{\rho} \bar{u} \hat{u}^+ + \gamma \bar{p} \hat{p}^+)$.

As explained in the previous section, the outlet becomes the starting point when using the adjoint equations in a shooting method. For this reason it is necessary to explore each of the boundary conditions independently. In general, to compute the corresponding adjoint boundary condition, we first substitute the wave forms of the direct and adjoint perturbation variables Eqs. (2.6) and (4.21) into the boundary terms Eq. (4.36). Then, we apply the direct boundary condition, and finally we seek the values of the adjoint wave amplitudes that will set the boundary terms to zero. In some cases convective waves reflect back as acoustic waves. Therefore, to get the values of the adjoint wave amplitudes we need to solve for the acoustic, entropy and vorticity contributions separately. The same process applied to the direct equations is performed in Stow et al. (2002).

- *Open outlet:* For an open end outlet, we assume that $\hat{p} = 0$ and that entropy and vorticity waves convect away from the system. Hence there is no interaction between acoustic and convective waves at the boundary. Therefore, we set $A_E^+ = 0$ and $A_V^+ = 0$. We assume $A_-^+ = 1$ and solve for A_+^+ which gives:

$$A_+^+ = -\frac{\alpha_+}{\alpha_-} e^{i(k_- - k_+)L_t}. \quad (4.41)$$

- *Closed outlet:* For a closed end we assume $\hat{u} = 0$. Entropy waves are assumed to convect away, so they have no interaction with the boundary. Hence, $A_E^+ = 0$. We set $A_-^+ = 1$, and solve for the acoustic contributions to get A_+^+ . We note that vorticity waves reflect back as acoustic waves, so we again set $A_-^+ = 1$ and use the vorticity contributions to solve for A_V^+ :

$$A_+^+ = -\frac{\alpha_+}{\alpha_-} \left(\frac{\bar{u}\alpha_- - \bar{c}^2(k_- + n^2/(R^2k_0))}{\bar{u}\alpha_+ - \bar{c}^2(k_+ + n^2/(R^2k_0))} \right) e^{i(k_- - k_+)L_t}, \quad (4.42a)$$

$$A_V^+ = \frac{n}{R\alpha_-} \left(\frac{(k_- - k_+)(\bar{u}\alpha_- - \bar{c}^2(k_- + n^2/(R^2k_0)))}{(k_-k_+)(1 + n^2/(R^2k_0^2))} \right) e^{i(k_- - k_0)L_t}. \quad (4.42b)$$

- *Choked outlet:* Assumes that the fluctuations in the Mach number are zero $\hat{M} = 0$. Entropy and vorticity modes generate acoustic fluctuations. We set $A_-^+ = 1$ and solve for the acoustic, entropy, and vorticity contributions for A_+^+ , A_E^+ and A_V^+ :

$$A_+^+ = -\frac{\alpha_+}{\alpha_-} \left(\frac{X_-}{X_+} \right) e^{i(k_- - k_+)L_t}, \quad (4.43a)$$

$$A_E^+ = \frac{\bar{c}^2\omega}{\alpha_-} \left(\frac{(k_- - k_+)(\zeta - 1)X_-}{Y_+Y_-} \right) e^{i(k_- - k_0)L_t}, \quad (4.43b)$$

$$A_V^+ = \frac{n}{R\alpha_-} \left(\frac{2\bar{c}^4 X_-}{(1 + n^2/(R^2 k_0^2)) Y_+ Y_-} \right) e^{i(k_- - k_0)L_t}, \quad (4.43c)$$

where

$$\begin{aligned} X_{\pm} &= \omega \bar{u}(\gamma + 1 - (\gamma - 1)\zeta) - 2k_{\pm}(\bar{c}^2 - \bar{u}^2) - \frac{n^2}{R^2 k_0}(2\bar{c}^2 + \bar{u}^2(\gamma - 1)(1 - \zeta)), \\ Y_{\pm} &= 2\bar{c}^2 k_{\pm} + \bar{u}\alpha_{\pm}(\gamma - 1)(1 - \zeta), \\ \zeta &= \frac{dc_p(\bar{T})}{d\bar{T}} \frac{(\gamma - 1)^2}{\gamma} \frac{\bar{T}}{R_g}. \end{aligned}$$

These are the adjoint equivalent of those derived for a choked outlet in [Stow et al. \(2002\)](#).

- *Reflection coefficient:* Assumes $A_- e^{ik_- L_t} - R_c A_+ e^{ik_+ L_t} = 0$. Therefore, there are no entropy or vorticity wave interactions at the boundary. Hence, we set $A_E^+ = 0$ and $A_V^+ = 0$. Then, we set $A_-^+ = 1$ and solve the acoustic contributions for A_-^+ .

$$A_+^+ = \frac{\alpha_+}{\alpha_-} R_c^* e^{i(k_- - k_+)L_t}. \quad (4.44)$$

The adjoint eigenvalues

As stated above, the adjoint problem is solved by shooting backwards in the network model. Given the definition of the inner products used to compute the adjoint equations, the adjoint eigenvalues are the complex conjugate of the direct eigenvalues. In general, once we know a direct eigenvalue, we will use its complex conjugate to shoot through the network to compute all of the adjoint variables which will be used for the sensitivity analysis in § 5.

The normalization condition

Eigenvalue sensitivity analysis in chapter 5 requires the direct and adjoint variables to be normalized. The normalization condition is constructed with the derivatives with respect to the eigenvalue of all of the frequency-dependent terms in the Lagrangian functional Eq. (4.3). In its most general form it is given by:

$$i \left(\langle \hat{p}^+, \hat{p} \rangle + \langle \hat{u}^+, \bar{\rho} \hat{u} \rangle + \langle \hat{w}^+, \bar{\rho} \hat{w} \rangle + \langle \hat{p}^+, \hat{p} \rangle \right) + F_{\omega} = 1, \quad (4.45)$$

where $F_{\omega} = \sum_{i=1}^N F_{\omega_i}$ is the sum of the N inner products between the corresponding adjoint variables and the derivatives of the frequency dependent terms with respect to ω

that appear in the jump conditions or the boundary conditions of the functional. The model described so far has frequency-dependent terms in the heat sources and in the boundary conditions that have an acoustic reflection coefficient. Let $\partial_\omega(f) \equiv \partial f / \partial \omega$, then the inner products for the model are:

- *Heat Source at rest:*

$$F_{\omega_1} = \left\{ \hat{c}_e^+, -\partial_\omega(\hat{Q}) \right\}.$$

- *Heat source in motion:*

$$\begin{aligned} F_{\omega_1} &= \left\{ \hat{c}_m^+, -\partial_\omega(\hat{u}_s) \bar{m}_{u_s} \right\}, \\ F_{\omega_2} &= \left\{ \hat{c}_e^+, -\partial_\omega(\hat{Q}) - \partial_\omega(\hat{u}_s) \bar{e}_{u_s} \right\}. \end{aligned}$$

- *Inlet acoustic reflection coefficient:*

$$F_{\omega_1} = \left\{ \hat{b}_i^+, \hat{p} \left(\frac{1}{\alpha_-} \left(\partial_\omega(k_-) - \partial_\omega(\alpha_-) \frac{k_-}{\alpha_-} \right) + \frac{R_c}{\alpha_+} \left(\partial_\omega(k_+) - \partial_\omega(\alpha_+) \frac{k_+}{\alpha_+} \right) \right) \right\}.$$

As stated in § 2.3.6, we have assumed that R_c is not frequency-dependent at the inlet.

- *Outlet acoustic reflection coefficient:*

$$F_{\omega_1} = \left\{ \hat{b}_o^+, \hat{p} (B_{\omega_1} + B_{\omega_2} + B_{\omega_3}) + \hat{u} (B_{\omega_4}) + \hat{w} (B_{\omega_5}) \right\},$$

with

$$\begin{aligned} B_{\omega_1} &= \frac{1}{\bar{\rho} \alpha_+} \left(\partial_\omega(k_+) - \partial_\omega(k_0) \frac{n^2}{R^2 k_0^2} - \frac{\partial_\omega(a_+)}{\alpha_+} \left(k_+ + \frac{n^2}{R^2 k_0} \right) \right), \\ B_{\omega_2} &= \frac{R_c}{\bar{\rho} \alpha_-} \left(\partial_\omega(k_-) - \partial_\omega(k_0) \frac{n^2}{R^2 k_0^2} - \frac{\partial_\omega(a_-)}{\alpha_-} \left(k_- + \frac{n^2}{R^2 k_0} \right) \right), \\ B_{\omega_3} &= \frac{\partial_\omega(R_c)}{\bar{\rho} \alpha_-} \left(k_- + \frac{n^2}{R^2 k_0} \right), \\ B_{\omega_4} &= \partial_\omega(R_c), \\ B_{\omega_5} &= \frac{n}{\bar{u} R k_0^2} (1 + R_c) + \partial_\omega(R_c) \frac{n}{R k_0}. \end{aligned}$$

Here we assumed that R_c can be frequency-dependent as in Eq. (2.21). Otherwise, we set $\partial_\omega(R_c) = 0$.

4.4.2 Adjoint base flow equations

The adjoint base flow equations serve as an aid to quickly assess the effect that the variations of the steady base flow have on the system. For example, geometric changes such as changes in the area of a duct induce base flow variations. Hence, when computing sensitivities to such changes, we need to account for the change generated in the fluctuating equations and the change made to the base flow. To compute the latter we require the adjoint base flow equations. These are obtained following a similar procedure to that in [Marquet et al. \(2008\)](#) and resemble the unsteady adjoint equations to a certain extent. To derive the adjoint base flow equations we are interested in both inner products of Eq. (4.3).

Straight ducts

For a straight duct, the relevant components of vector \mathbf{B} are given by Eqs. (2.2). The corresponding Lagrange multipliers (components of vector \mathbf{G}^+) are given by the spatial functions $[R^+(x), U^+(x), W^+(x), P^+(x)]^T$ respectively. The resulting adjoint base flow equations are given by:

$$\bar{u} \frac{dR^+}{dx} = -i\omega^*(\hat{w}^* \hat{w}^+ + \hat{u}^* \hat{u}^+) - \frac{in}{R} \hat{w}^* \hat{\rho}^+ + \bar{u} \hat{w}^+ \frac{d\hat{w}^*}{dx} + (\hat{\rho}^+ + \bar{u} \hat{u}^+) \frac{d\hat{u}^*}{dx} \dots \quad (4.46a)$$

$$-\hat{p}^+ \bar{p} \frac{d\gamma}{d\bar{p}} \left(-\frac{in}{R} \hat{w}^* + \frac{d\hat{u}^*}{dx} \right),$$

$$\bar{\rho} \frac{dR^+}{dx} + \bar{\rho} \bar{u} \frac{dU^+}{dx} + \gamma \bar{p} \frac{dP^+}{dx} = \hat{\rho}^+ \frac{d\hat{\rho}^*}{dx} + \bar{\rho} \hat{w}^+ \frac{d\hat{w}^*}{dx} + \bar{\rho} \hat{u}^+ \frac{d\hat{u}^*}{dx} + \hat{p}^+ \frac{d\hat{p}^*}{dx}, \quad (4.46b)$$

$$\frac{dU^+}{dx} + \bar{u} \frac{dP^+}{dx} = \left(\gamma + \bar{p} \frac{d\gamma}{d\bar{p}} \right) \hat{p}^+ \left(-\frac{in}{R} \hat{w}^* + \frac{d\hat{u}^*}{dx} \right), \quad (4.46c)$$

$$\frac{dW^+}{dx} = 0, \quad (4.46d)$$

where

$$\frac{d\gamma}{d\bar{p}} = -\frac{d\gamma}{dT} \frac{\bar{p}}{\bar{\rho}^2 R_g}, \quad \frac{d\gamma}{d\bar{p}} = \frac{d\gamma}{dT} \frac{1}{\bar{\rho} R_g}.$$

The corresponding boundary terms are:

$$\left[(R^+ \bar{u}) \delta \bar{\rho} + (R^+ \bar{\rho} + U^+ \bar{\rho} \bar{u} + P^+ \gamma \bar{p}) \delta \bar{u} + W^+ \delta \bar{w} + (U^+ + \bar{u} P^+) \delta \bar{p} \right]_{x_0}^{x_1} = 0. \quad (4.47)$$

where the δ preceding the base flow terms works in a similar manner to that in the perturbation equations. As seen in Eqs. (4.46), the adjoint base flow equations require

knowledge of the adjoint perturbation variables. Hence, once the unsteady adjoint problem is solved, we can proceed to solve for the adjoint base flow variables. The solutions are:

$$R^+(x) = R^+(x_1) - \int_x^{x_1} \frac{\nabla_M}{\bar{u}} dx, \quad (4.48a)$$

$$P^+(x) = P^+(x_1) - \int_x^{x_1} \frac{-\bar{\rho}\nabla_M + \bar{u}\nabla_F - \bar{\rho}\bar{u}^2\nabla_E}{\gamma\bar{p}\bar{u} - \bar{\rho}\bar{u}^3} dx, \quad (4.48b)$$

$$U^+(x) = U^+(x_1) - \int_x^{x_1} \frac{\bar{\rho}\nabla_M - \bar{u}\nabla_F + \gamma\bar{p}\nabla_E}{\gamma\bar{p} - \bar{\rho}\bar{u}^2} dx, \quad (4.48c)$$

$$W^+(x) = C, \quad (4.48d)$$

where, in the definition of [Marquet et al. \(2008\)](#), the equivalent of the sensitivity to base flow modifications inside a duct are:

$$\begin{aligned} \nabla_M &= -i\omega^*(\hat{w}^*\hat{w}^+ + \hat{u}^*\hat{u}^+) - \frac{in}{R}\hat{w}^*\hat{\rho}^+ + \bar{u}\hat{w}^+\frac{d\hat{w}^*}{dx} + (\hat{\rho}^+ + \bar{u}\hat{u}^+)\frac{d\hat{u}^*}{dx} \dots \\ &\quad - \hat{p}^+\bar{p}\frac{d\gamma}{d\bar{\rho}}\left(-\frac{in}{R}\hat{w}^* + \frac{d\hat{u}^*}{dx}\right), \\ \nabla_F &= \hat{\rho}^+\frac{d\hat{\rho}^*}{dx} + \bar{\rho}\hat{w}^+\frac{d\hat{w}^*}{dx} + \bar{\rho}\hat{u}^+\frac{d\hat{u}^*}{dx} + \hat{p}^+\frac{d\hat{p}^*}{dx}, \\ \nabla_E &= \left(\gamma + \bar{p}\frac{d\gamma}{d\bar{p}}\right)\hat{p}^+\left(-\frac{in}{R}\hat{w}^* + \frac{d\hat{u}^*}{dx}\right). \end{aligned}$$

For modules governed by mass, axial momentum and energy fluxes, it is convenient to define the following adjoint base flow fluxes, which depend on the side i of the jump condition:

$$F_{m_i}^+ = \frac{1}{A_i} \left(R_i^+ - \bar{u}_i U_i^+ + \left(\bar{c}_i^2 - \bar{h}_i(\gamma_i - 1) + \frac{1}{2}(\gamma_i - 1)\bar{u}_i^2 \right) P_i^+ \right) + J_{M_i}, \quad (4.49a)$$

$$F_{x_i}^+ = \frac{1}{A_i} \left(U_i^+ - (\gamma_i - 1)\bar{u}_i P_i^+ \right) + J_{X_i}, \quad (4.49b)$$

$$F_{\theta_i}^+ = 0, \quad (4.49c)$$

$$F_{e_i}^+ = \frac{1}{A_i}(\gamma_i - 1)P_i^+ + J_{E_i}, \quad (4.49d)$$

where the sensitivity to base flow modifications in the jump conditions are given by J_{M_i} , J_{X_i} , and J_{E_i} . These are functions of the unsteady variables (direct and adjoint) and are detailed in appendix C. In vector form we will express the base flow fluxes as $\mathbf{F}_i^+ = [F_{m_i}^+, F_{x_i}^+, F_{\theta_i}^+, F_{e_i}^+]^T$. For modules governed by mass and energy fluxes together

with entropy conservation we define the following adjoint base flow fluxes:

$$S_{m_i}^+ = \frac{1}{A_i} \left(R_i^+ - \left(\frac{1}{2} \bar{u}_i + \frac{\bar{h}_i}{\bar{u}_i} \right) U_i^+ + \bar{c}_i^2 P_i^+ \right) + G_{M_i}, \quad (4.50a)$$

$$S_{s_i}^+ = \frac{1}{R_g} \left(\bar{p}_i \bar{u}_i (\gamma_i - 1) P_i^+ - \bar{p}_i U_i^+ \right) + G_{S_i}, \quad (4.50b)$$

$$S_{\theta_i}^+ = 0, \quad (4.50c)$$

$$S_{e_i}^+ = \frac{1}{A_i} \left(\frac{U_i^+}{\bar{u}_i} \right) + G_{E_i}. \quad (4.50d)$$

As before, the base flow modifications for this jump G_{M_i} , G_{S_i} , and G_{E_i} are detailed in appendix C. The fluxes in vector form are expressed as: $\mathbf{S}_i^+ = [S_{m_i}^+, S_{s_i}^+, S_{\theta_i}^+, S_{e_i}^+]^T$.

Area increase

For an area increase the relevant components of vector \mathbf{B} are given by the steady quantities of Eq. (2.7), and the corresponding Lagrange multipliers are given by the numbers $\mathbf{A}^+ = [A_m^+, A_x^+, A_\theta^+, A_e^+]^T$ respectively. The relationship between adjoint variables at the area increase and those defined at the duct is given by: $\mathbf{A}^+ = \mathbf{F}_2^+$. The adjoint base flow jump conditions for an area increase are given by:

$$\mathbf{F}_1^+ = \mathbf{F}_2^+ + \Phi^+ \left[\left(\bar{h}_1 - \frac{\bar{u}_1^2}{2} \right) (\gamma_1 - 1) - 2\bar{c}_1^2, \frac{\bar{c}_1^2}{\bar{u}_1} + (\gamma_1 - 1)\bar{u}_1, 0, -(\gamma_1 - 1) \right]^T, \quad (4.51)$$

where

$$\Phi^+ = \frac{A_2 - A_1}{A_1} \left(\frac{\bar{u}_1}{\bar{c}_1^2 - \bar{u}_1^2} \right) F_{x_2}^+.$$

Area decrease

For an area decrease the relevant components of vector \mathbf{B} are given by the steady quantities of Eq. (2.8), and the corresponding Lagrange multipliers are given by the numbers $\mathbf{B}^+ = [B_m^+, B_s^+, B_\theta^+, B_e^+]^T$ respectively. The relationship between adjoint variables at the area decrease and those defined at the duct is given by: $\mathbf{B}^+ = \mathbf{S}_2^+$. The adjoint base flow jump conditions for an area decrease are given by:

$$\mathbf{S}_1^+ = \mathbf{S}_2^+. \quad (4.52)$$

Ring of premix ducts

At the start of the ring of premix ducts there is an area decrease. The adjoint base flow jump conditions are the same as those for an area decrease Eq. (4.52) and only the sensitivities to base flow modifications before the area decrease need to be updated with the integration factor κ_n according to:

$$[G_{M_1}, G_{S_1}, G_{E_1}] \rightarrow \kappa_n [G_{M_1}, G_{S_1}, G_{E_1}]. \quad (4.53)$$

At the end of the ring an area increase is observed. Again, the only difference in the adjoint base flow jump conditions with respect to those derived for an area increase in Eq. (4.51) is due to the update required for the sensitivities to base flow modifications in the adjoint fluxes, which are given by:

$$[J_{M_1}, J_{X_1}, J_{E_1}] \rightarrow \frac{1}{\kappa_n} [J_{M_1}, J_{X_1}, J_{E_1}]. \quad (4.54)$$

Heat source at rest

Heat sources need to be analysed together with the measurement points. The components of vector \mathbf{B} are given by the steady quantities of Eqs. (2.7) for the measurement point (assuming constant area) and Eqs. (2.12) for the heat source. We will denote with subindices 1 and 2 the positions before and after the measurement point and with 3 and 4 the positions before and after the heat source. The Lagrange multipliers that correspond to the measurement point are given by the numbers $\mathbf{A}^+ = [A_m^+, A_x^+, A_\theta^+, A_e^+]^T$, and for the heat source by: $\mathbf{C}^+ = [C_m^+, C_x^+, C_\theta^+, C_e^+]^T$. Their relationship to the variables defined in the ducts is given by: $\mathbf{A}^+ = \mathbf{F}_2^+$ and $\mathbf{C}^+ = \mathbf{F}_4^+$, respectively. The adjoint base flow jump conditions for the measurement point are given by:

$$\begin{aligned} \mathbf{F}_1^+ = \mathbf{F}_2^+ \dots \\ + \hat{Q}^+ \left(\mu_u \frac{\hat{u}_1^*}{\bar{u}_1} \mathbf{f}_{c_1} - \mu_r \frac{\hat{p}_1^*}{\bar{\rho}_1} \left(\mathbf{f}_{c_1} + \begin{bmatrix} \bar{c}_1^2 - \bar{u}_1^2 \\ 0 \\ 0 \\ 0 \end{bmatrix} \right) - \left(\gamma_1 \bar{M}_1^2 \right) \mu_p \frac{\hat{p}_1^*}{\bar{p}_1} \left(\mathbf{f}_{c_1} + \begin{bmatrix} \frac{\bar{u}_1^2 - \bar{c}_1^2}{\bar{u}_1} \\ \bar{c}_1^2 - \bar{u}_1^2 \\ 0 \\ 0 \end{bmatrix} \right) \right) \dots \end{aligned} \quad (4.55)$$

$$\begin{aligned}
& + \frac{\hat{Q}^+}{\mathcal{F}_t^*} \left(\mu_u \frac{\hat{u}_1^*}{\bar{u}_1} + \mu_r \frac{\hat{\rho}_1^*}{\bar{\rho}_1} + \mu_p \frac{\hat{p}_1^*}{\bar{p}_1} \right) \left(\frac{\partial \mathcal{F}_t^*}{\partial \bar{u}_1} (-\bar{u}_1) \mathbf{f}_{c_1} + \frac{\partial \mathcal{F}_t^*}{\partial \bar{\rho}_1} \bar{\rho}_1 \left(\mathbf{f}_{c_1} + \begin{bmatrix} \bar{c}_1^2 - \bar{u}_1^2 \\ 0 \\ 0 \\ 0 \end{bmatrix} \right) \right) \cdots \\
& + \frac{\partial \mathcal{F}_t^*}{\partial \bar{p}_1} \bar{p}_1 \bar{u}_1^2 \left(\mathbf{f}_{c_1} + \begin{bmatrix} \bar{u}_1^2 - \bar{c}_1^2 \\ \bar{c}_1^2 - \bar{u}_1^2 \\ \bar{u}_1 \\ 0 \\ 0 \end{bmatrix} \right) \Bigg) .
\end{aligned}$$

where the adjoint unsteady heat release \hat{Q}^+ is given by Eq. (4.29) and the vector \mathbf{f}_{c_1} is defined in Eq. (4.30). For the heat source, the corresponding jump conditions depend on the way the steady heat enters into the model. If \bar{Q} is given as a quantity, independent of the base flow variables, such as in the models where the $n - \tau$ FTF is used, the corresponding jump conditions are:

$$\mathbf{F}_3^+ = \mathbf{F}_4^+. \quad (4.56)$$

If the steady heat input is given as in Eq. (2.11) (detailed in appendix A), the heat release, being proportional to the mass flow rate, requires the following jump conditions:

$$\mathbf{F}_3^+ = \mathbf{F}_4^+ + \left[\eta h_r \left(\mathcal{F}_t^* \left(\mu_u \frac{\hat{u}_1^*}{\bar{u}_1} + \mu_r \frac{\hat{\rho}_1^*}{\bar{\rho}_1} + \mu_p \frac{\hat{p}_1^*}{\bar{p}_1} \right) \hat{f}_{e_4}^+ + F_{e_4}^+ \right), 0, 0, 0 \right]^T. \quad (4.57)$$

Kinematic Heat Source

The steady and unsteady equations for a measurement point remain the same as for the heat source at rest. Therefore, the only updates required in the jump conditions for the measurement point are due to the unsteady heat source speed \hat{u}_s . The corresponding jump conditions are given by:

$$\mathbf{F}_1^+ = \mathbf{F}_2^+ \cdots \quad (4.58)$$

$$\begin{aligned}
& + \left(\hat{Q}^+ - \hat{u}_{sq}^+ \right) \left(\mu_u \frac{\hat{u}_1^*}{\bar{u}_1} \mathbf{f}_{c_1} - \mu_r \frac{\hat{\rho}_1^*}{\bar{\rho}_1} \left(\mathbf{f}_{c_1} + \begin{bmatrix} \bar{c}_1^2 - \bar{u}_1^2 \\ 0 \\ 0 \\ 0 \end{bmatrix} \right) - \gamma_1 \bar{M}_1^2 \mu_p \frac{\hat{p}_1^*}{\bar{p}_1} \left(\mathbf{f}_{c_1} + \begin{bmatrix} \bar{u}_1^2 - \bar{c}_1^2 \\ \frac{\bar{c}_1^2 - \bar{u}_1^2}{\bar{u}_1} \\ 0 \\ 0 \end{bmatrix} \right) \right) \dots \\
& + \frac{(\hat{Q}^+ - \hat{u}_{sq}^+)}{\mathcal{F}_t^*} \left(\mu_u \frac{\hat{u}_1^*}{\bar{u}_1} + \mu_r \frac{\hat{\rho}_1^*}{\bar{\rho}_1} + \mu_p \frac{\hat{p}_1^*}{\bar{p}_1} \right) \left(\frac{\partial \mathcal{F}_t^*}{\partial \bar{u}_1} (-\bar{u}_1) \mathbf{f}_{c_1} + \frac{\partial \mathcal{F}_t^*}{\partial \bar{\rho}_1} \bar{\rho}_1 \left(\mathbf{f}_{c_1} + \begin{bmatrix} \bar{c}_1^2 - \bar{u}_1^2 \\ 0 \\ 0 \\ 0 \end{bmatrix} \right) \right) \dots \\
& + \frac{\partial \mathcal{F}_t^*}{\partial \bar{p}_1} \bar{\rho}_1 \bar{u}_1^2 \left(\mathbf{f}_{c_1} + \begin{bmatrix} \bar{u}_1^2 - \bar{c}_1^2 \\ \frac{\bar{c}_1^2 - \bar{u}_1^2}{\bar{u}_1} \\ 0 \\ 0 \end{bmatrix} \right).
\end{aligned}$$

where the adjoint unsteady heat release \hat{Q}^+ is given by Eq. (4.29) and the adjoint heat source speed \hat{u}_{sq}^+ is given by Eqs. (4.33).

Given that the heat source is considered to be anchored $\bar{u}_s = 0$, the steady base flow equations remain the same as with the heat source at rest. The unsteady equations, however, contain heat source speed terms which depend on the base flow quantities at both sides of the jump condition. This introduces an update into the steady adjoint base flow fluxes, which is given by:

$$\begin{aligned}
\mathbf{H}_4^+ &= \mathbf{F}_4^+ \dots \\
& + \frac{\hat{u}_s^*}{\bar{u}_4(\bar{c}_4^2 - \bar{u}_4^2)} \left(\hat{f}_{m_4}^+ \left(\mathbf{f}_{c_4} + \begin{bmatrix} \bar{c}_4^2 - \bar{u}_4^2 \\ 0 \\ 0 \\ 0 \end{bmatrix} \right) + \hat{f}_{e_4}^+ \left(\left(\bar{h}_4 - \frac{\bar{u}_4^2}{2} \right) \mathbf{f}_{c_4} + (\bar{c}_4^2 - \bar{u}_4^2) \begin{bmatrix} \bar{u}_4^2 \\ -\bar{u}_4 \\ 0 \\ 1 \end{bmatrix} \right) \right).
\end{aligned} \tag{4.59}$$

This update needs to be considered in the definition of the Lagrange multipliers at the kinematic heat source, that is, $\mathbf{C}^+ = \mathbf{H}_4^+$. Again, The jump conditions become:

$$\mathbf{F}_3^+ = \mathbf{H}_4^+ + \left[\eta h_r \left(\mathcal{F}_t^* \left(\mu_u \frac{\hat{u}_1^*}{\bar{u}_1} + \mu_r \frac{\hat{\rho}_1^*}{\bar{\rho}_1} + \mu_p \frac{\hat{p}_1^*}{\bar{p}_1} \right) \hat{f}_{e_4}^+ + F_{e_4}^+ \right), 0, 0, 0 \right]^T. \tag{4.60}$$

Notice that the forcing term, needs to be set to zero if the steady heat release \bar{Q} is given as a quantity as in the $n - \tau$ model. Finally, we need to update the adjoint fluxes on the opposite side according to:

$$\begin{aligned} \mathbf{H}_3^+ = \mathbf{F}_3^+ \dots & \quad (4.61) \\ & - \frac{\hat{u}_s^*}{\bar{u}_3(\bar{c}_3^2 - \bar{u}_3^2)} \left(\hat{f}_{m_4}^+ \left(\mathbf{f}_{c_3} + \begin{bmatrix} \bar{c}_3^2 - \bar{u}_3^2 \\ 0 \\ 0 \\ 0 \end{bmatrix} \right) + \hat{f}_{e_4}^+ \left(\left(\bar{h}_3 - \frac{\bar{u}_3^2}{2} \right) \mathbf{f}_{c_3} + (\bar{c}_3^2 - \bar{u}_3^2) \begin{bmatrix} \bar{u}_3^2 \\ -\bar{u}_3 \\ 0 \\ 1 \end{bmatrix} \right) \right) \dots \\ & + \frac{\hat{u}_{sm}^+}{\bar{c}_3^2 - \bar{u}_3^2} \left(\left(\frac{\hat{Q}^*}{\bar{Q}} - 2 \frac{\hat{\rho}_3^*}{\bar{\rho}_3} \right) \mathbf{f}_{c_3} - \frac{\hat{\rho}_3^*}{\bar{\rho}_3} \begin{bmatrix} \bar{c}_3^2 - \bar{u}_3^2 \\ 0 \\ 0 \\ 0 \end{bmatrix} \right), \end{aligned}$$

with \hat{u}_{sm}^+ defined in Eq. (4.35).

Inlet boundary conditions

At the inlet of the studied configurations, due to the assumptions from the model $\bar{w} = 0$, we also specify the mean pressure \bar{p} , the mean temperature \bar{T} and either the mean velocity \bar{u} or the mean mass flow rate \bar{m} . These are the components of vector \mathbf{B} in Eq. (4.3). Their corresponding Lagrange multipliers are given by $B_{i_w}^+$, $B_{i_p}^+$, $B_{i_\rho}^+$, $B_{i_u}^+$. The relationship between the adjoint variables defined in the ducts and those defined at the boundary depends on whether we have specified the velocity or the mass flow rate. For the first case (\bar{u} is given) they are:

$$B_{i_p}^+ = U^+ + \bar{u}P^+, \quad (4.62a)$$

$$B_{i_\rho}^+ = \bar{u}R^+, \quad (4.62b)$$

$$B_{i_u}^+ = \bar{\rho}R^+ + \bar{\rho}\bar{u}U^+ + \gamma\bar{p}P^+, \quad (4.62c)$$

$$B_{i_w}^+ = 0. \quad (4.62d)$$

For the second case (\bar{m} is given) they are:

$$B_{i_p}^+ = U^+ + \bar{u}P^+, \quad (4.63a)$$

$$B_{i_\rho}^+ = -\bar{u}^2 U^+ - \bar{u}\bar{c}^2 P^+, \quad (4.63b)$$

$$B_{i_u}^+ = \frac{1}{A} \left(R^+ + \bar{u}U^+ + \bar{c}^2 P^+ \right), \quad (4.63c)$$

$$B_{i_w}^+ = 0. \quad (4.63d)$$

In this situation, x_0 from Eq. (4.47) represents the inlet of the configuration. At this position there are fixed properties (\bar{w} , \bar{p} , \bar{T} and \bar{u} or \bar{m}). This implies that their corresponding perturbations (δ terms) are zero, given that their values lie outside of the computational domain (Marquet et al., 2008). Hence, $\delta\bar{w} = 0$ and $\delta\bar{p} = 0$. Fixing the mean temperature (and the mean pressure) implies fixing the mean density (through the ideal gas law), so, $\delta\bar{\rho} = 0$. Providing \bar{u} or \bar{m} together with the fixed mean density implies that $\delta\bar{u} = 0$. The previous considerations make the boundary terms at the inlet vanish. Therefore the adjoint base flow variables can take any value.

Outlet boundary conditions

The outlet sets the initial point for the adjoint base flow calculations. No mean properties are fixed at the outlet, and there are therefore no steady components in vector \mathbf{B} and related Lagrange multipliers. Hence, the same analysis as with the inlet boundary conditions cannot be carried out and the delta terms are not zero at this position. To ensure that the boundary terms vanish, we need to analyse each of the boundary conditions independently.

- *Open outlet:* The assumption is that $\hat{p} = 0$, so there are no base flow variations. To make the adjoint base flow boundary terms Eq. (4.47) vanish, the corresponding values for the adjoint base flow variables are given by:

$$R^+(L_t) = 0, \quad (4.64a)$$

$$P^+(L_t) = 0, \quad (4.64b)$$

$$U^+(L_t) = 0, \quad (4.64c)$$

$$W^+(L_t) = 0. \quad (4.64d)$$

- *Closed outlet:* Same as the open outlet.

- *Choked end:* This condition has a dependency on base flow terms, so, the full set of boundary terms becomes:

$$\begin{aligned}
& \left(R^+ \bar{u} + b_o^+ \left(-\frac{\partial \zeta}{\partial \bar{\rho}} \left(\frac{\hat{\rho}^*}{\bar{\rho}} - \frac{\hat{p}^*}{\bar{p}} \right) + (1 - \zeta) \left(-\frac{\hat{\rho}^*}{\bar{\rho}^2} \right) \right) \right) \delta \bar{\rho} \dots \\
& + \left(R^+ \bar{p} + U^+ \bar{\rho} \bar{u} + P^+ \gamma \bar{p} + b_o^+ \left(-\frac{2\hat{u}^*}{\bar{u}^2} \right) \right) \delta \bar{u} + W^+ \delta \bar{w} \dots \\
& + \left(U^+ + \bar{u} P^+ + b_o^+ \left(-\frac{\partial \zeta}{\partial \bar{p}} \left(\frac{\hat{\rho}^*}{\bar{\rho}} - \frac{\hat{p}^*}{\bar{p}} \right) + (1 - \zeta) \left(\frac{\hat{p}^*}{\bar{p}^2} \right) \right) \right) \delta \bar{p} = 0,
\end{aligned} \tag{4.65}$$

where

$$\zeta(\bar{T}) = \frac{dc_p(\bar{T})}{d\bar{T}} \frac{(\gamma - 1)^2}{\gamma} \frac{\bar{T}}{R_g}, \quad \frac{\partial \zeta}{\partial \bar{\rho}} = \frac{\partial \zeta}{\partial \bar{T}} \left(-\frac{\bar{p}}{\bar{\rho}^2 R_g} \right), \quad \frac{\partial \zeta}{\partial \bar{p}} = \frac{\partial \zeta}{\partial \bar{T}} \left(\frac{1}{\bar{\rho} R_g} \right),$$

and \hat{b}_o^+ is given in § 4.4.1. To set the previous equation to zero, the values for the adjoint variables need to be given by:

$$R^+(L_t) = \frac{b_o^+}{\bar{u}} \left(\frac{\partial \zeta}{\partial \bar{\rho}} \left(\frac{\hat{\rho}^*}{\bar{\rho}} - \frac{\hat{p}^*}{\bar{p}} \right) + (1 - \zeta) \frac{\hat{\rho}^*}{\bar{\rho}^2} \right), \tag{4.66a}$$

$$\begin{aligned}
P^+(L_t) = & \frac{1}{\gamma \bar{p} - \bar{\rho} \bar{u}^2} \left(-\bar{\rho} R^+(L_t) \dots \right. \\
& \left. + b_o^+ \left(\bar{\rho} \bar{u} \left(-\frac{\partial \zeta}{\partial \bar{p}} \left(\frac{\hat{\rho}^*}{\bar{\rho}} - \frac{\hat{p}^*}{\bar{p}} \right) + (1 - \zeta) \left(\frac{\hat{p}^*}{\bar{p}^2} \right) \right) + \frac{2\hat{u}^*}{\bar{u}} \right) \right),
\end{aligned} \tag{4.66b}$$

$$U^+(L_t) = -\bar{u} P^+(L_t) - b_o^+ \left(-\frac{\partial \zeta}{\partial \bar{p}} \left(\frac{\hat{\rho}^*}{\bar{\rho}} - \frac{\hat{p}^*}{\bar{p}} \right) + (1 - \zeta) \frac{\hat{p}^*}{\bar{p}^2} \right), \tag{4.66c}$$

$$W^+(L_t) = 0. \tag{4.66d}$$

- *Acoustic reflection coefficient:* As in the previous case, this condition depends on the base flow terms. To set the full set of boundary terms to zero, the values of the adjoint variables at the outlet are:

$$R^+(L_t) = -b_o^+ \frac{B_R}{\bar{u}}, \tag{4.67a}$$

$$P^+(L_t) = b_o^+ \frac{\bar{\rho} B_R - \bar{u} B_U + \bar{\rho} \bar{u}^2 B_P}{\bar{u} (\gamma \bar{p} - \bar{\rho} \bar{u}^2)}, \tag{4.67b}$$

$$U^+(L_t) = -b_o^+ \frac{\bar{\rho} B_R - \bar{u} B_U + \gamma \bar{p} B_P}{\gamma \bar{p} - \bar{\rho} \bar{u}^2}, \tag{4.67c}$$

$$W^+(L_t) = 0. \tag{4.67d}$$

where

$$\begin{aligned}
B_R &= \hat{p}^* \left(\frac{1}{\bar{\rho}\alpha_+} \left(\partial_{\bar{\rho}}(k_+) - \left(\frac{1}{\bar{\rho}} + \frac{\partial_{\bar{\rho}}(\alpha_+)}{\alpha_+} \right) \left(k_+ + \frac{n^2}{R^2 k_0} \right) \right) + \dots \right. \\
&\quad \left. \frac{R_c^*}{\bar{\rho}\alpha_-} \left(\partial_{\bar{\rho}}(k_-) + \left(\frac{\partial_{\bar{\rho}}(R_c^*)}{R_c^*} - \frac{1}{\bar{\rho}} - \frac{\partial_{\bar{\rho}}(\alpha_-)}{\alpha_-} \right) \left(k_- + \frac{n^2}{R^2 k_0} \right) \right) \right) + \dots \\
&\quad \hat{u}^* (\partial_{\bar{\rho}}(R_c^*)) + \hat{w}^* \left(\frac{\partial_{\bar{\rho}}(R_c^*)n}{Rk_0} \right), \\
B_U &= \hat{p}^* \left(\frac{1}{\bar{\rho}\alpha_+} \left(\partial_{\bar{u}}(k_+) - \partial_{\bar{u}}(k_0) \frac{n^2}{R^2 k_0^2} - \frac{\partial_{\bar{u}}(\alpha_+)}{\alpha_+} \left(k_+ + \frac{n^2}{R^2 k_0} \right) \right) + \dots \right. \\
&\quad \left. \frac{R_c^*}{\bar{\rho}\alpha_-} \left(\partial_{\bar{u}}(k_-) - \partial_{\bar{u}}(k_0) \frac{n^2}{R^2 k_0^2} + \left(\frac{\partial_{\bar{u}}(R_c^*)}{R_c^*} - \frac{\partial_{\bar{u}}(\alpha_-)}{\alpha_-} \right) \left(k_- + \frac{n^2}{R^2 k_0} \right) \right) \right) + \dots \\
&\quad \hat{u}^* (\partial_{\bar{u}}(R_c^*)) + \hat{w}^* \left(\partial_{\bar{u}}(R_c^*) \frac{n}{Rk_0} - \partial_{\bar{u}}(k_0) (1 + R_c^*) \frac{n}{Rk_0^2} \right), \\
B_P &= \hat{p}^* \left(\frac{1}{\bar{\rho}\alpha_+} \left(\partial_{\bar{p}}(k_+) - \frac{\partial_{\bar{p}}(\alpha_+)}{\alpha_+} \left(k_+ + \frac{n^2}{R^2 k_0} \right) \right) + \dots \right. \\
&\quad \left. \frac{R_c^*}{\bar{\rho}\alpha_-} \left(\partial_{\bar{p}}(k_-) + \left(\frac{\partial_{\bar{p}}(R_c^*)}{R_c^*} - \frac{\partial_{\bar{p}}(\alpha_-)}{\alpha_-} \right) \left(k_- + \frac{n^2}{R^2 k_0} \right) \right) \right) + \dots \\
&\quad \hat{u}^* (\partial_{\bar{p}}(R_c^*)) + \hat{w}^* \left(\frac{\partial_{\bar{p}}(R_c^*)n}{Rk_0} \right),
\end{aligned}$$

and $\partial_{\bar{\rho}}(f) \equiv \partial f / \partial \bar{\rho}$, $\partial_{\bar{u}}(f) \equiv \partial f / \partial \bar{u}$, $\partial_{\bar{p}}(f) \equiv \partial f / \partial \bar{p}$.

Chapter 5

Sensitivity analysis of thermoacoustic configurations

Depending on the sensitivity information desired, the governing equations need to be perturbed. Two different types of perturbation are defined:

- when the parameters, such as areas, lengths, etc., are perturbed, the resulting sensitivity is named *base state sensitivity*;
- when the system is perturbed by adding a small feedback mechanism, which is linearly proportional to one of the perturbation or steady variables, such as \hat{p} or \bar{m} , the resulting sensitivity is called *feedback sensitivity* (also known as *structural sensitivity* in [Giannetti and Luchini \(2007\)](#) and [Magri and Juniper \(2013b\)](#)). Feedback mechanisms that cause mass addition, momentum addition, and/or energy addition are considered.

The sensitivity of an eigenvalue to changes in the system can have contributions from:

- the unsteady flow only, if the perturbation acts only in the unsteady flow equations. For this case only the knowledge of the adjoint unsteady variables is required.
- the steady and unsteady flow, if the perturbation acts on the steady flow, which influences the unsteady flow or if the perturbation acts on both the steady and unsteady flow. In this scenario we require the knowledge of both adjoint unsteady variables and adjoint steady variables.

In this chapter we first show the procedure to compute the sensitivities, as presented in [Aguilar et al. \(2017\)](#) in collaboration with Dr. Luca Magri. Finally, we perform sensitivity analysis on the configurations of chapter [3](#).

5.1 Computing sensitivities of base state parameters

The process to compute the base state sensitivities depends on the choice of the formulation of the adjoint problem. In this section, the procedure with the continuous adjoint is presented first, followed by the discrete adjoint. Finally the convenience of using one or the other is discussed.

5.1.1 Continuous adjoint

The eigenvalue drift associated with base state sensitivities using a continuous approach is derived through the following steps ([Aguilar, 2015](#)):

1. From the eigenvalue problem Eq. (2.26) we compute the eigenvalue of interest, ω_j .
2. We obtain the values of the direct perturbation variables \hat{p} , $\hat{\rho}$, \hat{u} and \hat{w} from the direct eigenvalue problem. Similarly, from the adjoint eigenvalue problem, we obtain the adjoint perturbation variables: \hat{p}^+ , $\hat{\rho}^+$, \hat{u}^+ and \hat{w}^+ . If the base state variable also modifies the base flow, we further compute the values of the adjoint base flow variables P^+ , R^+ , U^+ , W^+ .
3. We normalize using Eq. (4.45).
4. We obtain the first variation of the Lagrangian with respect to the base state variable of interest, which provides the eigenvalue drift. For the base state variable τ in the Lagrangian functional of Eq. (4.9) this is:

$$\frac{\partial \mathcal{L}}{\partial \tau} \delta \tau = 0 \implies \delta \omega = - \left\{ \hat{h}^+, \beta \hat{u}_1 e^{-i\omega \tau} i\omega \delta \tau \right\}. \quad (5.1)$$

The relevant base state parameters of the network model can be separated into: heat source parameters and geometric parameters. Heat source parameters are concerned with the parameters of the FTF, such as time delays and interaction indices in the $n - \tau$ model. Since these elements only appear in the heat source the computation of their sensitivities is straightforward as given in the above procedure, so they are not discussed any further. On the other hand, the geometric parameters such as areas, lengths and mean radii enter in the Lagrangian of a complex network less trivially, so their implementation is further discussed.

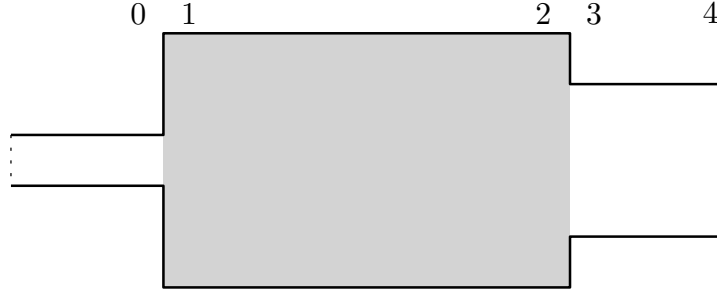


Fig. 5.1 A duct (highlighted in gray) with an area increase at the inlet and an area decrease at the outlet. The dotted lines represent other jumps or a boundary conditions.

Area

A change in area induces variations in the perturbation equations (\mathbf{P}) and in the base flow equations (\mathbf{B}). Therefore, we consider the contributions of each of them separately and then add them together. An area variation affects the jump conditions at the duct inlet and at the outlet (See Fig. 5.1). Thus setting the derivative of the Lagrangian with respect to the area to zero gives:

$$\frac{\partial \mathcal{L}}{\partial A} \delta A = 0 \implies \frac{\delta \omega}{\delta A} = \left(\frac{\delta \omega}{\delta A} \Big|_{\mathbf{P}} + \frac{\delta \omega}{\delta A} \Big|_{\mathbf{B}} \right)_{inlet} + \left(\frac{\delta \omega}{\delta A} \Big|_{\mathbf{P}} + \frac{\delta \omega}{\delta A} \Big|_{\mathbf{B}} \right)_{outlet}. \quad (5.2)$$

For the duct highlighted in Fig. 5.1, we consider that the flow variables at the duct inlet are given by subscript 1 and the variables just before the duct inlet are given by subscript 0. The area sensitivities at the duct inlet are given by:

$$\begin{aligned} \left(\frac{\delta \omega}{\delta A} \Big|_{\mathbf{P}} \right)_{inlet} &= - \left\{ \hat{a}_m^+, \bar{\rho}_1 \hat{u}_1 + \hat{\rho}_1 \bar{u}_1 \right\} - \left\{ \hat{a}_x^+, \hat{p}_1 + \hat{\rho}_1 \bar{u}_1^2 + 2\bar{\rho}_1 \bar{u}_1 \hat{u}_1 - \hat{p}_0 \right\} \dots \\ &\quad - \left\{ \hat{a}_\theta^+, R_1 \bar{\rho}_1 \bar{u}_1 \hat{w}_1 \right\} \dots \\ &\quad - \left\{ \hat{a}_e^+, \frac{\gamma_1 \bar{u}_1}{\gamma_1 - 1} \hat{p}_1 + \bar{\rho}_1 \left(\bar{h}_1 + \frac{3}{2} \bar{u}_1^2 \right) \hat{u}_1 + \bar{u}_1 \left(\bar{h}_1 - \frac{\bar{c}_1^2}{(\gamma_1 - 1)} + \frac{\bar{u}_1^2}{2} \right) \hat{p}_1 \right\}, \\ \left(\frac{\delta \omega}{\delta A} \Big|_{\mathbf{B}} \right)_{inlet} &= - \left\{ A_m^+, \bar{\rho}_1 \bar{u}_1 \right\} - \left\{ A_x^+, \bar{p}_1 + \bar{\rho}_1 \bar{u}_1^2 - \bar{p}_0 \right\} - \left\{ A_e^+, \bar{\rho}_1 \bar{u}_1 \left(\bar{h}_1 + \frac{1}{2} \bar{u}_1^2 \right) \right\}. \end{aligned}$$

We consider that the flow variables at the duct outlet are given by subscript 2 and the variables just after the duct outlet are given by subscript 3. The area sensitivities at the

duct outlet are given by:

$$\begin{aligned} \left(\frac{\delta\omega}{\delta A} \right)_{\mathbf{P}}^{\text{outlet}} &= - \left\{ \hat{b}_m^+, -(\bar{\rho}_2 \hat{u}_2 + \hat{\rho}_2 \bar{u}_2) \right\} - \left\{ \hat{b}_\theta^+, -(R_2 \bar{\rho}_2 \bar{u}_2 \hat{w}_2) \right\} \cdots \\ &\quad - \left\{ \hat{b}_e^+, - \left(\frac{\gamma_2 \bar{u}_2}{\gamma_2 - 1} \hat{p}_2 + \bar{\rho}_2 \left(\bar{h}_2 + \frac{3}{2} \bar{u}_2^2 \right) \hat{u}_2 + \bar{u}_2 \left(\bar{h}_2 - \frac{\bar{c}_2^2}{(\gamma_2 - 1)} + \frac{\bar{u}_2^2}{2} \right) \hat{\rho}_2 \right) \right\}, \\ \left(\frac{\delta\omega}{\delta A} \right)_{\mathbf{B}}^{\text{outlet}} &= - \left\{ B_m^+, -(\bar{\rho}_2 \bar{u}_2) \right\} - \left\{ B_e^+, - \left(\bar{\rho}_2 \bar{u}_2 \left(\bar{h}_2 + \frac{1}{2} \bar{u}_2^2 \right) \right) \right\}. \end{aligned}$$

Length

In a given network model, the axial position of a jump condition or boundary condition is determined by the sum of the ducts' length that appear before that jump or boundary i.e., $x = L_1 + L_2 + \cdots + L_n$. To compute the local value of the perturbation variables at those locations, the axial position is required. Hence, to compute the sensitivity to a variation in a duct's length, we need to include all of the perturbation variables that used that length to compute its local value. Thus, setting the derivative of the Lagrangian with respect to the length to zero gives:

$$\frac{\partial \mathcal{L}}{\partial L} \delta L = 0 \implies \frac{\delta\omega}{\delta L} = \sum_{i=1}^N \frac{\delta\omega}{\delta L_i} \quad (5.3)$$

where N is the number of jump conditions that appear after the desired duct length plus one that represents the outlet boundary condition, and $\delta\omega/\delta L_i$ represents the sensitivity of the length at a single location.

For example, we consider that position 4 in Fig. 5.1 represents an open end boundary condition. We let the subscript L represent a derivative of a perturbation variable or a perturbation flux with respect to L , i.e.,

$$\hat{p}_L = \frac{\partial \hat{p}}{\partial L} = A_+ i k_+ e^{ik_+ x} + A_- i k_- e^{ik_- x}.$$

Then the sensitivity of the eigenvalue to variations of the highlighted duct's length is given by:

$$\frac{\partial \mathcal{L}}{\partial L} = \frac{\delta\omega}{\delta L_j} + \frac{\delta\omega}{\delta L_b}$$

where

$$\begin{aligned}\frac{\delta\omega}{\delta L_j} &= -\left\{\hat{b}_m^+, \hat{m}_{L_3} - \hat{m}_{L_2}\right\} - \left\{\hat{b}_s^+, \hat{s}_{L_3} - \hat{s}_{L_2}\right\} - \left\{\hat{b}_\theta^+, \hat{f}_{\theta L_3} - \hat{f}_{\theta L_2}\right\} - \left\{\hat{b}_e^+, \hat{e}_{L_3} - \hat{e}_{L_2}\right\}, \\ \frac{\delta\omega}{\delta L_b} &= -\left\{\hat{b}_o^+, \hat{p}_{L_4}\right\},\end{aligned}$$

and to avoid confusion we have used the subscript j to denote the jump condition and b to denote the boundary condition.

Mean radius

To compute the sensitivities to changes in the mean radius a similar approach to that of the areas is taken because the variable appears at the inlet and outlet of the duct. We also use the subscript R to denote the derivative of a perturbation variable or flux with respect to the mean radius and note that the mean radius enters the perturbation variables through the wave numbers k_\pm and α_\pm and the angular momentum flux. Setting the derivative of the Lagrangian with respect to the mean radius to zero gives:

$$\frac{\partial \mathcal{L}}{\partial R} \delta R = 0 \implies \frac{\delta\omega}{\delta R} = \left(\frac{\delta\omega}{\delta R}\right)_{inlet} + \left(\frac{\delta\omega}{\delta R}\right)_{outlet}. \quad (5.4)$$

For the example in Fig 5.1, these are given by:

$$\begin{aligned}\left(\frac{\delta\omega}{\delta R}\right)_{inlet} &= -\left\{\hat{a}_m^+, \hat{m}_{R_1}\right\} - \left\{\hat{a}_x^+, \hat{f}_{x R_1}\right\} - \left\{\hat{a}_\theta^+, \hat{f}_{\theta R_1}\right\} - \left\{\hat{a}_e^+, \hat{e}_{R_1}\right\}, \\ \left(\frac{\delta\omega}{\delta R}\right)_{outlet} &= -\left\{\hat{b}_m^+, -\hat{m}_{R_2}\right\} - \left\{\hat{b}_s^+, -\hat{s}_{R_2}\right\} - \left\{\hat{b}_\theta^+, -\hat{f}_{\theta R_2}\right\} - \left\{\hat{b}_e^+, -\hat{e}_{R_2}\right\}.\end{aligned}$$

5.1.2 Discrete adjoint

To compute the eigenvalue drift associated with the discrete adjoint problem, first we need to compute the eigenvalue ω_j , then the associated adjoint eigenvector $\hat{\mathbf{q}}^\dagger$ as given in Eq. (4.7). For these problems, Jankovic (1988); Magri (2015); Magri et al. (2016a) derived the following eigenvalue drift formula:

$$\delta\omega_j = -\frac{(\hat{\mathbf{q}}^\dagger)^H \delta\mathbf{L}(\omega_j, \mathbf{p}) \hat{\mathbf{q}}}{(\hat{\mathbf{q}}^\dagger)^H \frac{\partial \mathbf{L}(\omega_j, \mathbf{p})}{\partial \omega_j} \hat{\mathbf{q}}}, \quad (5.5)$$

where the matrix $\delta\mathbf{L}$ represents the first variation of a variable in matrix \mathbf{L} . For example, for the base state variable τ in the eigenvalue problem of Eq. (3.6), the matrix $\delta\mathbf{L}$ and

the corresponding sensitivity are given by:

$$\delta L = \frac{\partial L}{\partial \tau} \delta \tau, \quad \frac{\delta \omega}{\delta \tau} = - \frac{(\hat{\mathbf{q}}^\dagger)^H \frac{\partial L(\omega_j)}{\partial \tau} \hat{\mathbf{q}}}{(\hat{\mathbf{q}}^\dagger)^H \frac{\partial L(\omega_j)}{\partial \omega_j} \hat{\mathbf{q}}}.$$

In theory, the computation of the first variation of a variable in the nonlinear eigenvalue operator, L , should be a straightforward analytical task. However, when the variable also affects the base flow such as the area, computing the first variation could be a cumbersome task. The base flow varies nonlinearly throughout the network so analytical solutions might not be available as an input into the nonlinear eigenvalue problem. Furthermore, a variation of the base flow in a given element changes the base flow in all elements downstream. The problem reduces to the building of the appropriate chain of base flow derivatives that depend on the base state variable. This approach is not developed as part of this thesis.

5.2 Computing sensitivities of feedback mechanisms

Sensitivities of the eigenvalue to feedback mechanisms provide important information about the response of the resonant modes to changes in the flow. In this section we study first the unsteady mechanisms that are proportional to a perturbation variable, and then the steady mechanisms that are proportional to a steady quantity. Both are studied using the continuous adjoint, and, where relevant, also the discrete adjoint.

5.2.1 Feedback from unsteady mechanisms

The model has four different perturbation variables and four governing equations providing a total of 16 different unsteady mechanisms. The devices that act on the mass equation, axial momentum equation, azimuthal momentum equation and energy equation are labelled \mathcal{M} , \mathcal{F} , \mathcal{F}_θ and \mathcal{Q} respectively.

Continuous adjoint

Using a continuous adjoint formulation, we follow the same steps as in § 5.1.1, except that after normalization (step 3), we introduce the feedback device into the system. The feedback perturbation is inserted at position x_0 and has the form $\mathcal{X}_y \hat{y} \delta(x - x_0)$, where \mathcal{X}_y represents the feedback mechanism, and \hat{y} is a perturbation variable (i.e., \hat{p} , $\hat{\rho}$, \hat{u} , \hat{w}). The main assumption is that this perturbation does not produce any change to the base

flow parameters. The general formulation to obtain the eigenvalue drift is given by:

$$\frac{\partial \mathcal{L}}{\partial \mathcal{X}_y} \delta \mathcal{X}_y \implies \frac{\delta \omega}{\delta \mathcal{X}_y} = \langle \hat{x}^+, \hat{y} \delta(x - x_0) \rangle = \hat{x}^+(x_0)^* \hat{y}(x_0), \quad (5.6)$$

where \hat{x}^+ is the adjoint variable that depends on which equation is being forced. For feedback mechanisms that force:

- the mass equation ($\mathcal{X} = \mathcal{M}$): $\hat{x}^+ = \hat{p}^+ + \bar{c}^2 \hat{\rho}^+$,
- the axial momentum equation ($\mathcal{X} = \mathcal{F}$): $\hat{x}^+ = \hat{u}^+$,
- the azimuthal momentum equation ($\mathcal{X} = \mathcal{W}$): $\hat{x}^+ = \hat{w}^+$,
- the energy equation ($\mathcal{X} = \mathcal{Q}$): $\hat{x}^+ = \hat{p}^+$.

It is important to note that since the continuity equation (2.3a), multiplied by a factor of \bar{c}^2 , is used to derive the energy equation in terms of pressure (2.3d), it will appear twice in the Lagrangian functional Eq. (4.3). Therefore, the receptivity to the mass equation, used to compute the corresponding feedback mechanisms, is given by $\hat{\rho}^+(x) + \bar{c}^2 \hat{p}^+(x)$.

For example, if we want to consider the effect of a drag device located at position x_0 inside a duct, the axial momentum equation needs to be forced with a mechanism proportional to the unsteady velocity:

$$i\omega \bar{\rho} \hat{u} + \bar{\rho} \bar{u} \frac{d\hat{u}}{dx} + \frac{d\hat{p}}{dx} - \mathcal{F}_u \hat{u} \delta(x - x_0) = 0. \quad (5.7)$$

Then, after normalization, the sensitivity of the eigenvalue to the drag device at the given position is:

$$\frac{\partial \mathcal{L}}{\partial \mathcal{F}_u} \delta \mathcal{F}_u = 0 \implies \frac{\delta \omega}{\delta \mathcal{F}_u} = \langle \hat{u}^+, \hat{u} \delta(x - x_0) \rangle = \hat{u}^+(x_0)^* \hat{u}(x_0). \quad (5.8)$$

As can be observed in the continuous adjoint formulation, the feedback sensitivity is given as product of the direct and adjoint eigenfunctions.

Discrete adjoint

Using a discrete adjoint formulation to compute the matrix δL in Eq. (5.5), we need to introduce the feedback mechanism as a jump condition. This splits the domain spanned by a duct in two. The associated jump conditions are given by integration of the spatial terms in the axial direction of Eq. (2.3). For the drag device in Eq. (5.7) the

corresponding jump conditions are given by:

$$[\bar{\rho}\hat{u} + \bar{u}\hat{\rho}]_{x_0^-}^{x_0^+} = 0, \quad (5.9a)$$

$$[\bar{\rho}\bar{u}\hat{u} + \hat{p}]_{x_0^-}^{x_0^+} = \mathcal{F}_u \hat{u}(x_0^-), \quad (5.9b)$$

$$[\bar{\rho}\bar{u}\hat{w}]_{x_0^-}^{x_0^+} = 0, \quad (5.9c)$$

$$[\bar{u}\hat{p} + \gamma\bar{p}\hat{u}]_{x_0^-}^{x_0^+} = 0. \quad (5.9d)$$

In appendix D we prove that, to first order, the side (x_0^- or x_0^+) in which the perturbation is applied has no influence in the computation. However, in a shooting method, the values just before the jump are preferred. Once the jump condition has been identified, the next step is to compute matrix δL .

Since the elements of matrix L are the coefficients of the amplitudes of wave forms (A_+, A_-, A_E, A_V), the elements of matrix δL should be their first variations ($\delta A_+, \delta A_-, \delta A_E, \delta A_V$) induced by the application of the perturbations ($\mathcal{M}, \mathcal{F}, \mathcal{W}, \mathcal{Q}$), which is: $\delta L \rightarrow \delta L(\mathcal{M}, \mathcal{F}, \mathcal{W}, \mathcal{Q})$. To get the wave forms together with their first variations (i.e., $A_+ + \delta A_+$), we solve the 4×4 system generated by the new set of jump conditions. Then, after application of the boundary conditions and substitution into the jump conditions of the unperturbed system, we obtain the desired system:

$$(L + \delta L)(\hat{\mathbf{q}} + \delta \hat{\mathbf{q}}) = \mathbf{0}, \quad (5.10)$$

from which the matrix δL is readily available.

To illustrate the former procedure, consider the Rijke tube from § 3.3. The unperturbed nonlinear eigenvalue problem is given by Eq. (3.6). Since it is only governed by the momentum and energy equations, we can only consider feedback mechanisms that correspond to adding a force (\mathcal{F}) or energy (\mathcal{Q})¹. The original domain, which consists of two ducts, is now divided into four segments as shown in Fig. 5.2. Following the notation in the figure, the set of jump conditions upstream of the heat source ($x = a$) is:

$$p'_{ii} - p'_i = \mathcal{F}_{p_1} p'_i + \mathcal{F}_{u_1} u'_i, \quad (5.11a)$$

$$\gamma \bar{p}_1 (u'_{ii} - u'_i) = \mathcal{Q}_{p_1} p'_i + \mathcal{Q}_{u_1} u'_i. \quad (5.11b)$$

¹To give an example, a feedback mechanism proportional to the pressure fluctuations after the flame (\hat{p}_2) that acts on the energy equation (\mathcal{Q}) is denoted by \mathcal{Q}_{p_2} .

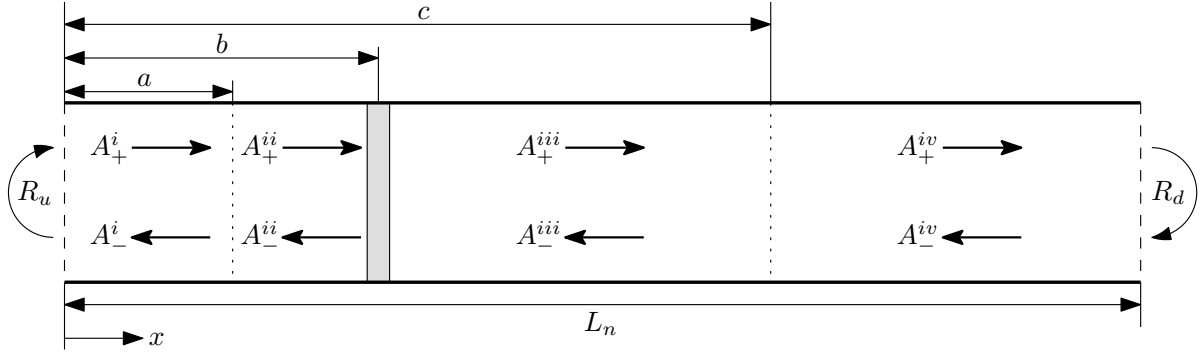


Fig. 5.2 A network model split into 4 regions due to the presence of feedback devices at $x = a$ and $x = c$. The original system can be thought of as being the heat source and the ducts from regions ii and iii . Since the perturbations must be introduced from the surroundings into the system (see Eqs.(5.11) and (5.12)), the depicted wave-forms from regions i and iv represent the unperturbed waves ($A_+^i = A_{+1}$ and $A_+^{iv} = A_{+2}$), while the wave-forms of regions ii and iii represent the perturbed waves ($A_+^{ii} = A_{+1} + \delta A_{+1}$ and $A_+^{iii} = A_{+2} + \delta A_{+2}$)

The set of jump conditions downstream of the heat source ($x = c$) is:

$$p'_{iv} - p'_{iii} = \mathcal{F}_{p_2} p'_{iv} + \mathcal{F}_{u_2} u'_{iv}, \quad (5.12a)$$

$$\gamma \bar{p}_2 (u'_{iv} - u'_{iii}) = \mathcal{Q}_{p_2} p'_{iv} + \mathcal{Q}_{u_2} u'_{iv}. \quad (5.12b)$$

The wave forms and their first variations are given by solving both 2×2 systems generated by the new sets of jump conditions (Eqs. 5.11 and 5.12) for the waves in regions ii and iii . For example, consider the feedback mechanism located in the duct before the heat source ($x = a$). For simplicity, we will only consider the device acting on the momentum equation proportional to the velocity fluctuations (\mathcal{F}_{u_1}). If the strength of the feedback mechanism is exactly 0, the waves before and after the jump are exactly the same, i.e.,

$$A_+^i = A_+^{ii}, \quad (5.13a)$$

$$A_-^i = A_-^{ii}, \quad (5.13b)$$

where we have dropped the frequency and spatial dependency of the waves to ease in the development of the upcoming equations. Note that by setting $A_+^i = A_{+1}$ and $A_-^i = A_{-1}$, we recover the original formulation for the Rijke tube.

Now let the strength of the feedback mechanism have a small but finite value. The presence of this device induces perturbations on the waves before and after the feedback

device:

$$A_+^i \rightarrow A_+^i + \delta A_+^i, \quad A_+^{ii} \rightarrow A_+^{ii} + \delta A_+^{ii}, \quad (5.14)$$

$$A_-^i \rightarrow A_-^i + \delta A_-^i, \quad A_-^{ii} \rightarrow A_-^{ii} + \delta A_-^{ii}. \quad (5.15)$$

After substituting the perturbed waves into the jump conditions (5.11), and by using Eq. (5.13) we obtain the following system of equations:

$$\delta A_+^{ii} + \delta A_-^{ii} - (\delta A_+^i + \delta A_-^i) = \frac{\mathcal{F}_{u_1}}{\bar{\rho}_1 \bar{c}_1} (A_+^i - A_-^i) + \frac{\mathcal{F}_{u_1}}{\bar{\rho}_1 \bar{c}_1} (\delta A_+^i - \delta A_-^i), \quad (5.16a)$$

$$\frac{1}{\bar{\rho}_1 \bar{c}_1} (\delta A_+^{ii} - \delta A_-^{ii}) - \frac{1}{\bar{\rho}_1 \bar{c}_1} (\delta A_+^i - \delta A_-^i) = 0. \quad (5.16b)$$

After dropping out second order terms (last term in Eq. (5.16a)) and solving for the first variation of the waves in region ii we obtain:

$$\delta A_+^{ii} = \delta A_+^i + \frac{1}{2} \frac{\mathcal{F}_{u_1}}{\bar{\rho}_1 \bar{c}_1} (A_+^i - A_-^i), \quad (5.17a)$$

$$\delta A_-^{ii} = \delta A_-^i + \frac{1}{2} \frac{\mathcal{F}_{u_1}}{\bar{\rho}_1 \bar{c}_1} (A_+^i - A_-^i), \quad (5.17b)$$

Since the variation of both waves is similar, we will focus only on the downstream propagating wave. The full perturbed wave solution considering the frequency and spatial dependency, all of the feedback mechanisms and using $A_+^i = A_{+1}$ and $A_-^i = A_{-1}$, is given by:

$$\begin{aligned} A_+^{ii} + \delta A_+^{ii} = & \underbrace{A_{+1}}_{(a)} + \underbrace{\frac{1}{2} \left(\mathcal{F}_{p_1} (A_{+1} + A_{-1} e^{-i\omega\tau_a}) + \frac{\mathcal{F}_{u_1}}{\bar{\rho}_1 \bar{c}_1} (A_{+1} - A_{-1} e^{-i\omega\tau_a}) \right)}_{(b)} \dots \\ & + \underbrace{\frac{\mathcal{Q}_{p_1}}{\bar{c}_1} (A_{+1} + A_{-1} e^{-i\omega\tau_a}) + \frac{\mathcal{Q}_{u_1}}{\bar{\rho}_1 \bar{c}_1^2} (A_{+1} - A_{-1} e^{-i\omega\tau_a})}_{(b)} + \underbrace{\delta A_+^i}_{(c)}, \end{aligned} \quad (5.18)$$

where $\tau_a = 2(b - a)/\bar{c}_1$. This equation can be separated in 3 parts:

- (a) corresponds to the unperturbed wave, which is used to form matrix L .
- (b) corresponds to the terms proportional to the unperturbed waves and the feedback mechanisms. These are used to form matrix δL .
- (c) corresponds to the first variation of wave which goes into the vector $\delta \hat{q}$.

The other three perturbed wave solutions have a similar structure in terms of coefficients. After applying the same boundary conditions and substituting into the original jump conditions Eq. (2.25), we obtain the perturbed system $(L + \delta L)(\hat{\mathbf{q}} + \delta \hat{\mathbf{q}}) = \mathbf{0}$. The full matrix δL is computed in appendix E following the above procedure.

We recall that in order to compute the eigenvalue drift the full perturbation expansion due to the presence of the feedback device leads to:

$$\left(L + \delta L(\mathcal{F}_{u_1}) + \delta \omega_j \frac{\partial L}{\partial \omega_j} \right) (\hat{\mathbf{q}} + \delta \hat{\mathbf{q}}) = \mathbf{0}. \quad (5.19)$$

After expanding and retaining only first order terms gives:

$$L \delta \hat{\mathbf{q}} + \delta \omega_j \frac{\partial L}{\partial \omega_j} \hat{\mathbf{q}} + \delta L(\mathcal{F}_{u_1}) \hat{\mathbf{q}} = \mathbf{0}. \quad (5.20)$$

Premultiplying the equation by the adjoint vector $\hat{\mathbf{q}}^\dagger$ eliminates the first term, and thus the requirement to compute the first variations of the waves. After some manipulations the previous equation leads to the eigenvalue drift formula Eq. (5.5).

To show some of the differences when a mean flow is included, we consider the choked combustor in § 3.4. For this case, the feedback sensitivity can now consider the effects of mass injection, \mathcal{M} , and feedback devices can be extended to include density fluctuations. Hence, instead of four possible feedback mechanisms (as in the Rijke tube) there are now nine. The inclusion of entropy waves makes the sets of jump relations change slightly. The jump conditions upstream of the flame ($x = a$) become:

$$\bar{u}_1(\rho'_{ii} - \rho'_i) + \bar{\rho}_1(u'_{ii} - u'_i) = \mathcal{M}_{p_1} p'_i + \mathcal{M}_{u_1} u'_i + \mathcal{M}_{r_1} \rho'_i, \quad (5.21a)$$

$$\bar{\rho}_1 \bar{u}_1(u'_{ii} - u'_i) + (p'_{ii} - p'_i) = \mathcal{F}_{p_1} p'_i + \mathcal{F}_{u_1} u'_i + \mathcal{F}_{r_1} \rho'_i, \quad (5.21b)$$

$$\bar{u}_1(p'_{ii} - p'_i) + \gamma \bar{p}_1(u'_{ii} - u'_i) = \mathcal{E}_{p_1} p'_i + \mathcal{E}_{u_1} u'_i + \mathcal{E}_{r_1} \rho'_i, \quad (5.21c)$$

while the jump conditions downstream of the flame ($x = c$) become

$$\bar{u}_2(\rho'_{iv} - \rho'_{iii}) + \bar{\rho}_2(u'_{iv} - u'_{iii}) = \mathcal{M}_{p_2} p'_{iv} + \mathcal{M}_{u_2} u'_{iv} + \mathcal{M}_{r_2} \rho'_{iv}, \quad (5.22a)$$

$$\bar{\rho}_2 \bar{u}_2(u'_{iv} - u'_{iii}) + (p'_{iv} - p'_{iii}) = \mathcal{F}_{p_2} p'_{iv} + \mathcal{F}_{u_2} u'_{iv} + \mathcal{F}_{r_2} \rho'_{iv}, \quad (5.22b)$$

$$\bar{u}_2(p'_{iv} - p'_{iii}) + \gamma \bar{p}_2(u'_{iv} - u'_{iii}) = \mathcal{E}_{p_2} p'_{iv} + \mathcal{E}_{u_2} u'_{iv} + \mathcal{E}_{r_2} \rho'_{iv}, \quad (5.22c)$$

where the term $\mathcal{E} \equiv \mathcal{Q} + \bar{c}^2 \mathcal{M}$ arises due to the use of the continuity equation to express the energy equation in terms of pressure. Some features of the wave-forms together with their first variations (δA_+ , δA_- , δA_E) are that the acoustic waves (A_+ and A_-) are affected by

mass, momentum and energy addition and are accompanied by a $1/(2(\bar{M} \pm 1))$ factor, while the entropy waves (A_E) are only affected by energy addition and accompanied by a $1/\bar{M}$ factor.

5.2.2 Feedback from steady mechanisms

Consider the steady feedback mechanisms $\delta\bar{m}$, $\delta\bar{f}$, $\delta\bar{f}_\theta$, and $\delta\bar{e}$, corresponding to steady mass, axial momentum, angular momentum and energy addition, which are introduced at position x_0 in the base flow equations (2.2):

$$\bar{\rho} \frac{d\bar{u}}{dx} + \bar{u} \frac{d\bar{\rho}}{dx} = \frac{\delta\bar{m}}{A} \delta(x - x_0), \quad (5.23a)$$

$$\bar{\rho}\bar{u} \frac{d\bar{u}}{dx} + \frac{d\bar{p}}{dx} = \frac{\delta\bar{f}_x}{A} \delta(x - x_0), \quad (5.23b)$$

$$\frac{d\bar{w}}{dx} = \frac{\delta\bar{f}_\theta}{A} \delta(x - x_0), \quad (5.23c)$$

$$\bar{u} \frac{d\bar{p}}{dx} + \gamma\bar{p} \frac{d\bar{u}}{dx} = (\gamma - 1) \frac{\delta\bar{e}}{A} \delta(x - x_0). \quad (5.23d)$$

The network model requires each of the ducts to have homogeneous properties, so that wave separation is allowed. Hence, the feedback mechanisms have to split the domain of a duct and they have to enter into the system as a set of jump conditions. These are given by:

$$[\bar{m}]_{x_0^-}^{x_0^+} = \delta\bar{m}. \quad (5.24a)$$

$$[\bar{f}_x]_{x_0^-}^{x_0^+} = \delta\bar{f}_x + \bar{u}(x_0^-) \delta\bar{m}, \quad (5.24b)$$

$$[\bar{e}]_{x_0^-}^{x_0^+} = \delta\bar{e} + \bar{u}(x_0^-) \delta\bar{f}_x + \left(\bar{h}(x_0^-) - \frac{\bar{c}(x_0^-)^2}{\gamma(x_0^-) - 1} + \frac{1}{2} \bar{u}(x_0^-)^2 \right) \delta\bar{m}. \quad (5.24c)$$

The angular momentum flux has been dropped because, by construction of the network model, it is zero everywhere. For steady feedback sensitivities only the continuous adjoint is developed.

Continuous adjoint

By using jump conditions to introduce the feedback devices, the sensitivities cannot be obtained as in § 5.2.1 using a continuous adjoint formulation. In other words, they are no longer calculated as an inner product between the adjoint base flow variable of a duct equation and the feedback mechanism. Instead, since the device is introduced at a jump

condition, which has a similar structure to an area increase or a heat source (without their respective forcing terms), the corresponding adjoint variables are given by the adjoint base flow fluxes (4.49), i.e., $\mathbf{A}^+ = \mathbf{F}_{x_0}^+$, where the subindex denotes the position of the device in the network. For the generic devices, the corresponding eigenvalue shifts are then given by:

$$\delta\omega = \left\{ F_{m_{x_0}}^+ + \bar{u}F_{x_{x_0}}^+ + \left(\bar{h} - \frac{\bar{c}^2}{\gamma - 1} + \frac{1}{2}\bar{u}^2 \right) F_{e_{x_0}}^+, \delta\bar{m} \right\}, \quad (5.25a)$$

$$\delta\omega = \left\{ F_{x_{x_0}}^+ + \bar{u}F_{e_{x_0}}^+, \delta\bar{f}_x \right\}, \quad (5.25b)$$

$$\delta\omega = \left\{ F_{e_{x_0}}^+, \delta\bar{e} \right\}. \quad (5.25c)$$

These expressions can be simplified further to show that, as expected, mass, momentum and energy addition are proportional to R^+ , U^+ and P^+ respectively, plus some contributions from the base flow modifications in the jump conditions.

5.3 Continuous vs discrete approach

The main advantage of the continuous adjoint approach is that the adjoint variables are directly expressed in physical space, i.e., the adjoint spatial functions are known. This means that (i) base state and feedback sensitivities for steady and unsteady flows are computed as inner products between direct and adjoint variables and (ii) one can obtain good physical understanding of the spatial system's receptivity to harmonic forcing². The main disadvantage is that the adjoint equations, boundary conditions and normalization condition, need to be derived analytically.

The main advantage of the discrete adjoint is that, as long as the operator L is known, computing the base state sensitivities for unsteady flows does not require any further implementation other than a complex transpose (see § 5.1.2). The main disadvantage is that, to compute the feedback sensitivity for unsteady flows, we need to introduce the feedback perturbations by splitting the domain as in Fig. 5.2. This implementation is more complicated than that of the continuous approach. Furthermore when the perturbation also modifies the base flow, the discrete approach needs to consider the chain of base flow derivatives from the perturbation until the end of the network. If it is a long network this could be a cumbersome task.

²The reason why the adjoint variables represent the receptivity of the system originates from bi-orthogonal decomposition [Luchini and Bottaro \(2014\)](#); [Magri and Juniper \(2014a\)](#).

5.4 Finite difference method and the Taylor test

Another way to compute the sensitivity of a system is by means of finite differences. After perturbing any of the equations or variables in the system, we re-compute the perturbed eigenvalue, $\omega + \delta\omega$, and then subtract from it the unperturbed eigenvalue, ω . The major drawback is that, unlike adjoint methods, this requires another full computation for every perturbation. This finite-difference method is used throughout this thesis to check the feedback sensitivities provided by the adjoint equations. For base state sensitivities we perform finite differencing in the form of the Taylor test. This test compares the eigenvalue drift calculated with the adjoint method ($\delta\omega_A$) against the one computed via a finite difference ($\delta\omega_F$). Given a small change in a parameter (δx), the difference between eigenvalue drifts ($|\delta\omega_F - \delta\omega_A|$) should grow linearly with the square of the small change (δx^2). If it grows linearly with δx , then there is a bug in the code.

5.5 Sensitivity analysis of the Rijke tube

We begin by analysing the adjoint eigenfunctions of the most unstable mode in the Rijke tube of § 3.3. Pressure eigenfunctions for the adjoint variables are normalized as $\int_0^{L_n} \hat{p}^+(x) \hat{p}^+(x)^* dx = 1$. In Fig. 5.3 we observe that the receptivity to the energy equation (\hat{p}^+) inherits the jump at the heat source location from \hat{u} and the boundary conditions from \hat{p} . Additionally, note that the receptivity to the momentum equation, \hat{u}^+ , is now continuous with a slight change of gradient at the heating gauze location. Although not shown here, with zero unsteady heat release the direct pressure mode shape is identical to the adjoint pressure mode shape, and the direct velocity mode shape is identical to the adjoint velocity mode shape (see § 4.3.1).

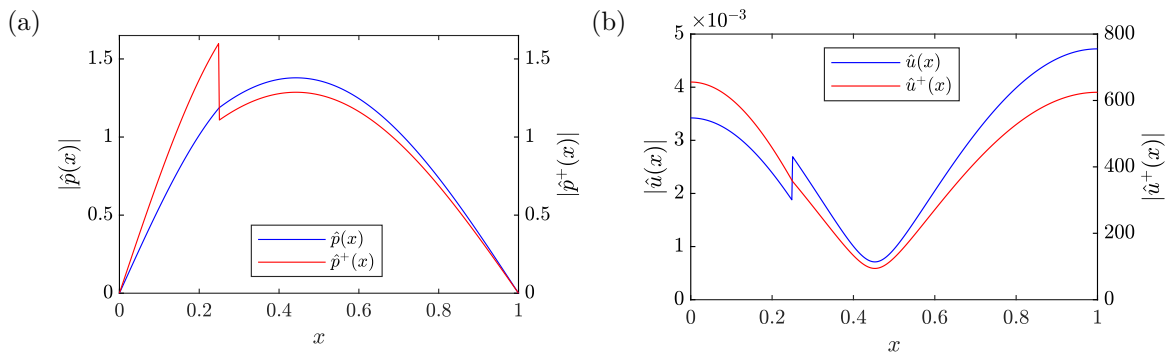


Fig. 5.3 Normalised relative amplitudes (i.e., $\hat{p}^+(x) = |\hat{p}(x)|e^{i\theta}$) of the receptivity of the energy equation $\hat{p}^+(x)$ (a) and the receptivity of the momentum equation $\hat{u}^+(x)$ (b) on top of the pressure and velocity eigenfunctions.

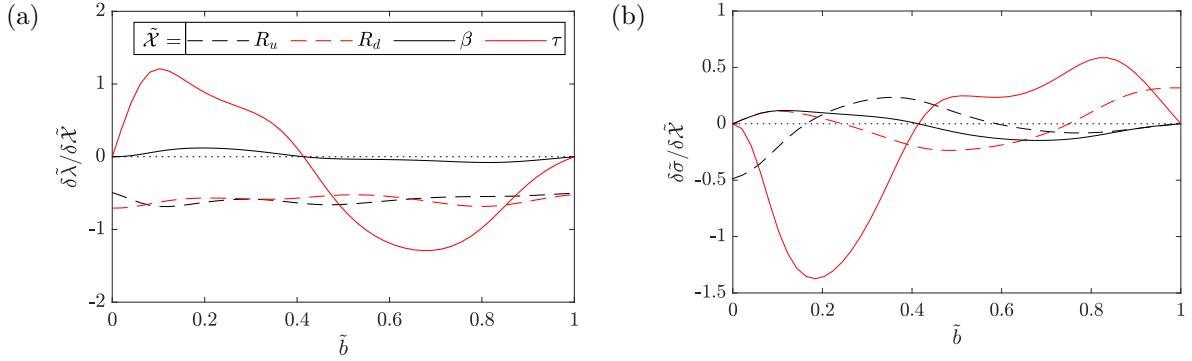


Fig. 5.4 Growth rate shift $\delta\tilde{\lambda}$ (a) and angular frequency shift $\delta\tilde{\sigma}$ (b) caused by a change in the base state variables, denoted by $\tilde{\mathcal{X}}$, for different positions of the heating gauze, \tilde{b} , along the duct length.

In a self-adjoint system, the best position for a Helmholtz resonator is where $\hat{p}\hat{p}^*$ is maximal, which is at the centre of the tube. In a system that it is not self-adjoint, this is no longer true. Even though the pressure is still maximum around the centre of the tube, the system is more receptive before the heating gauze location. The best location to place the Helmholtz resonator in such a system is where the amplitude of $\hat{p}\hat{p}^{+*}$ is maximum, which, in this case, is slightly upstream of the centre of the tube (Fig. 5.3a). The sensitivities of the eigenvalue computed using continuous and discrete approaches are the same to machine precision, and they match the results by finite difference.

The base state sensitivities for different positions of the heating gauze are presented in Fig. 5.4. It can be seen that any small increase (from -1) in the reflection coefficients, R_u and R_d , makes the system more stable. This is because less acoustic energy is reflected back into the tube. The interaction index, β , has the smallest amplitude and it predicts, as expected, that a heating gauze in the second half of the duct will stabilize the system. The time delay, τ , of the unsteady heat release has a great impact on the eigenvalue drift. Any increase will destabilize the system if the heating gauze is located in the first half of the duct before $\tilde{b} = 0.4$. Many of these remarks can be made from physical arguments. The novelty is that, with these adjoint methods, they can be calculated cheaply by an automated process and therefore could be used in a gradient-based optimization routine (see chapter 6).

The unsteady feedback sensitivity encompasses four feedback mechanisms, shown in Fig 5.5. The figure recovers similar results as those obtained using Galerkin methods, by Magri and Juniper (2013b) for uniform temperature and in Magri and Juniper (2014a) considering a jump in temperature. This achieves this thesis's aim of validating the wave-based adjoint method.

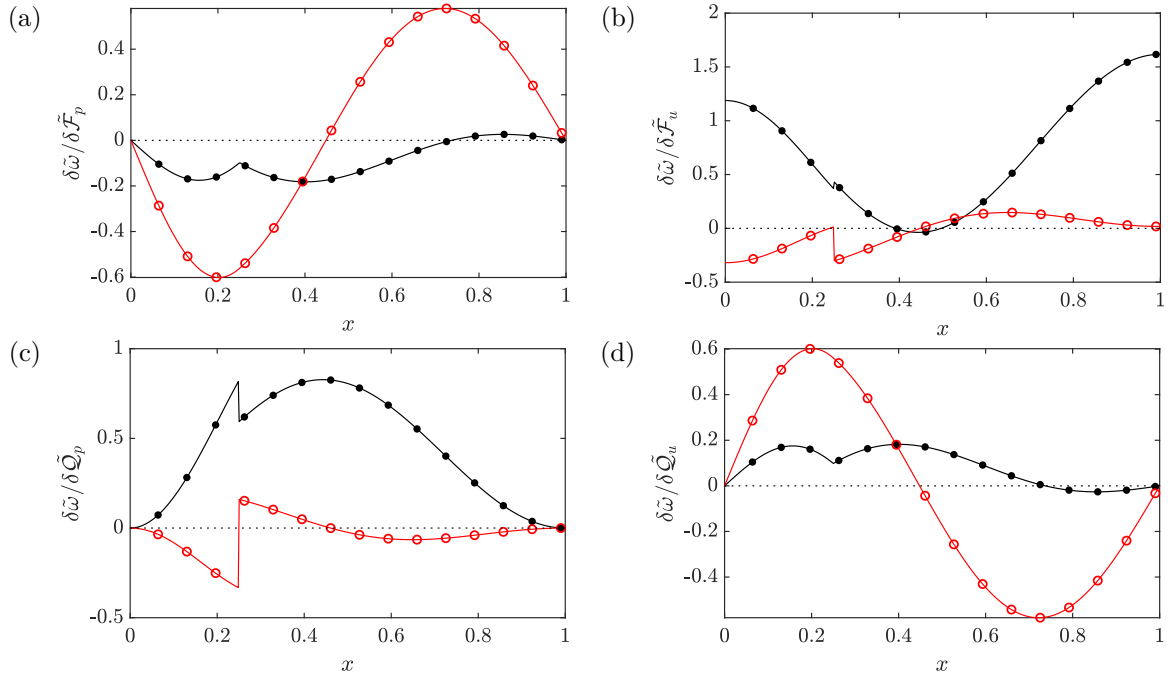


Fig. 5.5 Growth rate shift $\delta\tilde{\omega}$ denoted by —, ●, and angular frequency shift $\delta\tilde{\sigma}$ denoted by —, ○, for each feedback mechanism. (a) and (b) display the drifts due to forcing the momentum equation with a force proportional to pressure and velocity fluctuations respectively. Similarly (c) and (d) show the drifts due to heat addition into the system. The continuous lines (—, —) represent one calculation (via the adjoint method) while the circles (●, ○) represent 15 computations (via the finite difference method).

5.5.1 Experimental sensitivity analysis of the Rijke tube

Jamieson and Juniper (2017b) present experimental sensitivity analysis in the Rijke tube using a pulsed forced technique to obtain the growth/decay rates of two passive control devices: a drag mesh and a hot wire. They show that the growth rate shifts in both cases are accurately captured, but the frequency shifts are substantially different from those predicted by the original model. In this section, we present a new model of the Rijke tube which, aided by the sensitivity analysis presented above, is able to capture qualitatively well the growth rate shift shown by both experiments. The predictions for the frequency shift due to the drag mesh are improved and although numerical comparison is still poor the results show the right correct trends with varying grid position. For the secondary heater the frequency shift is captured qualitatively and quantitatively well.

Model

The physical model of the Rijke tube has the same elements as the one presented in § 3.3. The tube is 1 m in length and 47.4 mm in diameter. To match the experimental results, we consider a temperature of 296 K at the inlet and a pressure of 1 atm. The device has the main heater located at 0.25 m from the inlet, which is operated with a power of 170 W. In order to better represent the physics in the device, we introduce a small mean flow \bar{u}_R . Therefore, all of the analysis is now carried with the equations given in § 2.3. We further consider constant specific heat capacities, boundary conditions modelled with reflection coefficients $R_c = R_r + iR_i$ and a velocity driven heat source model (Eq. (2.15) with $\mu_u = 1$, $\mu_r = 0$ and $\mu_p = 0$) with an $n - \tau$ model as FTF with interaction index k_R , and time delay τ_R . To get a good approximation of the real model, we use the experimental data in Yu (2017), to fit the last five parameters ($\bar{u}_R, R_r, R_i, k_R, \tau_R$). The results are shown in table 5.1 and Fig. 5.6. Using this values the temperature downstream of the heater gives 439 K. Once the model has been developed, we proceed to identify the control methods using eigenvalue sensitivity analysis.

Quantity	Variable	Value
Inlet velocity	\bar{u}_R	0.5626 m/s
Reflection coefficients	$R_c = R_r + iR_i$	$-0.9584 + 0.1375i$
Interaction index	k_R	0.3080
Time delay	τ_R	2.398×10^{-3} s

Table 5.1 Fitted values for the network model based on the experimental Rijke tube.

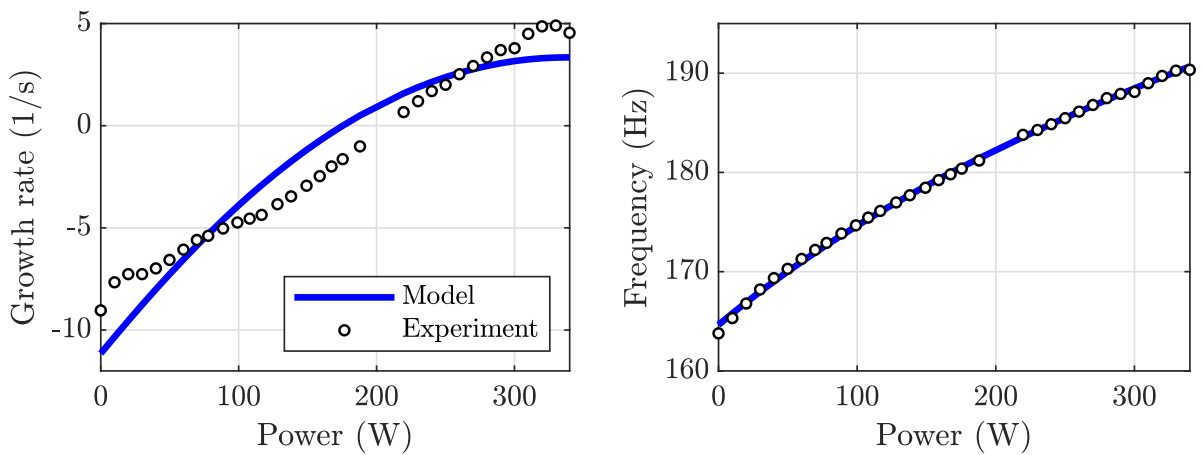


Fig. 5.6 Growth rates and frequencies of the dominant mode in the Rijke tube. The blue line represents the model fitted with the experimental data given by the circle markers.

Control via a passive drag device

The drag device as a control mechanism for the Rijke tube has already been identified in the zero mean flow configuration as the unsteady feedback device proportional to velocity acting in the momentum equation (Fig. 5.5b). To obtain the eigenvalue shift due to a drag device in the new model, we introduce the following drag force into the momentum equations:

$$F_D = -\frac{1}{2}\rho u^2 C_D A_m, \quad (5.26)$$

where C_D is the drag coefficient and A_m is the area of the object, in this case the control mesh. Given the low Mach number of the flow, we neglect the influence of the density perturbations and split the drag force into its mean and fluctuating parts:

$$F_D = \underbrace{-\frac{1}{2}C_D A_m \bar{\rho} \bar{u}^2}_{\delta \bar{f}_x} - \underbrace{C_D A_m \bar{\rho} \bar{u} \hat{u}}_{\delta \mathcal{F}_u \hat{u}}. \quad (5.27)$$

To obtain the eigenvalue shift we consider the contribution from the steady mechanism $\delta\omega(\delta \bar{f}_x)$ and the unsteady mechanism $\delta\omega(\delta \mathcal{F}_u \hat{u})$. Therefore, the full eigenvalue shift at position x_0 is given by:

$$\delta\omega = \left\{ F_x^+, -\frac{1}{2}C_D A_m \bar{\rho} \bar{u}^2 \right\} + \left\langle \hat{u}^+, -C_D \frac{A_m}{A_{duct}} \bar{\rho} \bar{u} \hat{u} \delta(x - x_0) \right\rangle, \quad (5.28)$$

where the duct area A_{duct} appears because the feedback mechanism is acting in the unsteady momentum equation (2.3b) which is given per unit area of the duct. According to Dowling (1995) the drag coefficient of a drag mesh can be computed as a function of the blockage ratio $B_r = A_m/A_{duct}$

$$C_D = \left(1 - (1 - B_r)^{-1}\right)^2. \quad (5.29)$$

Using $A_m = 0.00108 \text{ m}^2$ (as measured from the mesh) provides a blockage ratio of circa 61% and a drag coefficient of 2.47. The eigenvalue shifts for the two mechanisms are given in Fig. 5.7. From these figures we observe that, in the unsteady mechanism, the growth rate shift is larger than the angular frequency shift. In the steady mechanism the opposite is true. The magnitude of the eigenvalue shift given by the unsteady mechanism is much larger than that of the steady mechanism, which implies that the drift is mostly driven by the unsteady flow. Fig. 5.8 merges these two mechanisms and compares them to the experimental results of Jamieson and Juniper (2017b). The growth rate shifts compare qualitatively well. The experiment and the model share similar structures and

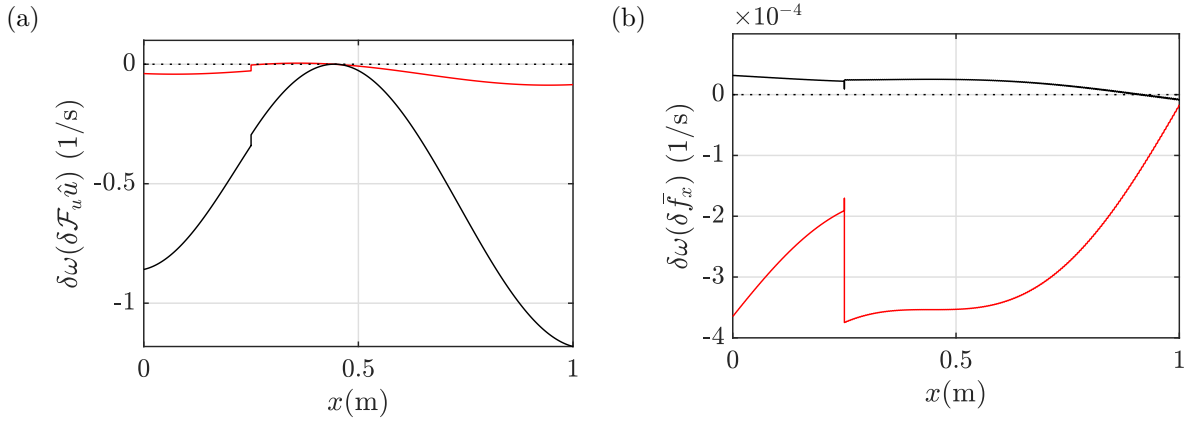


Fig. 5.7 Growth rate shift $\delta\lambda$ denoted by —, and angular frequency shift $\delta\sigma$ denoted by —, for the new model of the Rijke tube. Figure (a) shows the eigenvalue shift due to the unsteady drag device and figure (b) shows the eigenvalue shift due to the steady drag device.

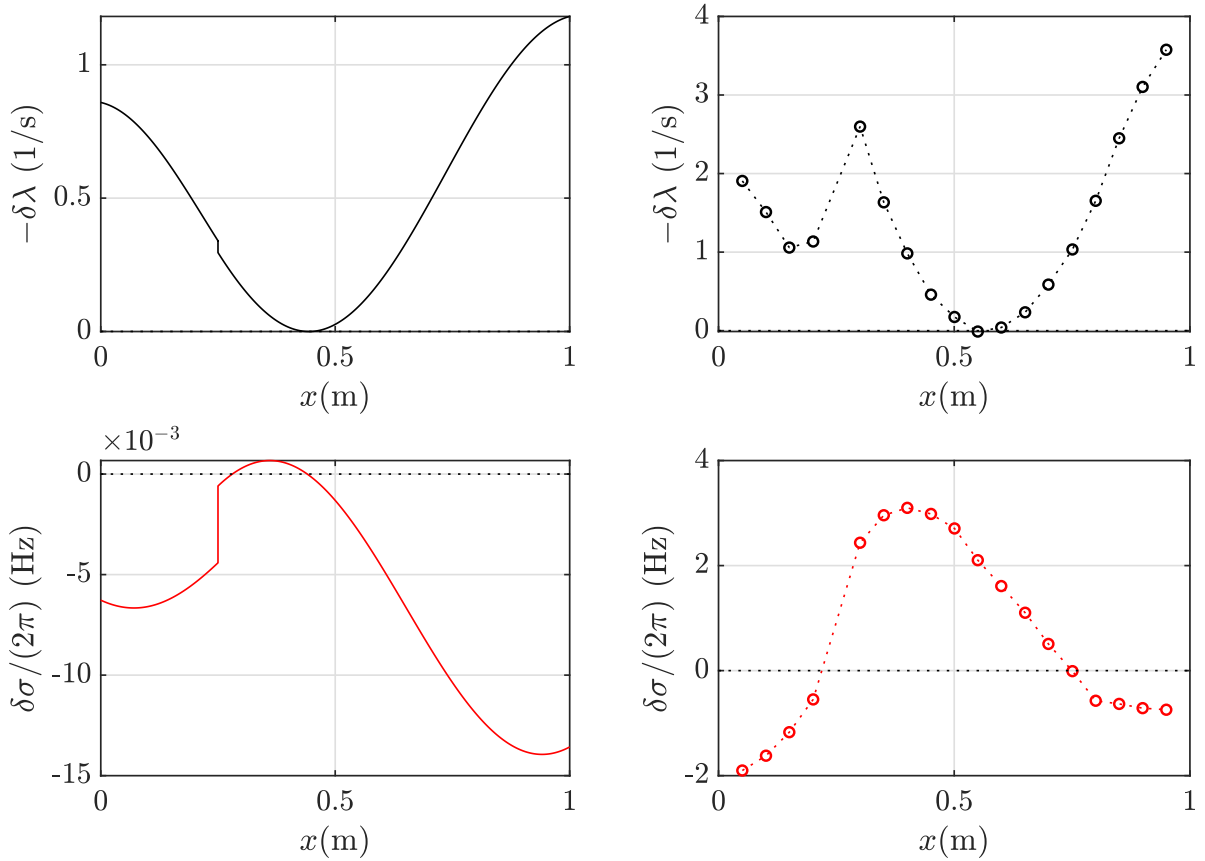


Fig. 5.8 Total eigenvalue shift due to the presence of a drag device in the Rijke tube. The left column shows the shift predicted by the model and the right column shows the shift measured in the experiments (Jamieson and Juniper, 2017b).

similar magnitudes. However, the jump at the heat source is not well captured by the new model. The frequency shift predicted by the new model improves substantially from the one to which the experimental results were originally compared. Now, the structure of the shift is predicted qualitatively well, with an increase from the inlet, a jump at the heater to values above zero, and then decay towards the outlet. The magnitude, however, is still different by 3 orders of magnitude. This discrepancy is due to defects in the model, not defects in the adjoint method. The discrepancies on the computation of the frequency shift can be explained due to the lack of temperature gradients in the model. On the one hand, the model considers an inlet temperature of 296 K which is kept constant until the flow reaches the heating gauze. The heat added increases the temperature to 439 K and this value is kept constant through the rest of the tube. On the other hand, as suggested by the mean wall temperatures of the Rijke tube (see table 5.2), the experiment is exposed to strong temperature gradients. These generate a mean flow temperature variation that affect the natural frequency of the duct, but not the growth rate (Nicoud and Wieczorek, 2009). Hence the frequency shift obtained from the experiment must contain to leading order the contribution of this mechanism, which is not included in the model.

Wall position (x/L_n)	0.05	0.25	0.50	0.75	0.95
Temperature (K)	301.84	425.97	365.62	352.50	348.43

Table 5.2 Mean wall temperatures at different positions in the experimental Rijke tube. Adapted from Fig. 4 in Jamieson et al. (2017).

Control via a secondary heat source

Given the original model of the Rijke tube, the unsteady secondary heater of Fig. 5.5d, predicts stabilization if it is located towards the end of the duct. To obtain the eigenvalue shift due to a secondary heat source in the new model of the Rijke tube, we introduce another heat source driven by the unsteady velocity with an $n - \tau$ FTF into the energy equations:

$$\delta Q_s = \underbrace{\delta \bar{Q}_s}_{\delta \bar{e}} + \underbrace{\delta \bar{Q}_s \frac{\hat{u}}{u}}_{\delta Q_u \hat{u}} k_s e^{-i\omega \tau_s}, \quad (5.30)$$

where the delta preceding the mean heat release terms indicates that the power used is less than the mean heat release of the primary heater (45 W in the experiments). The interaction index (k_s) and time delay (τ_s) of the secondary heater are chosen to be

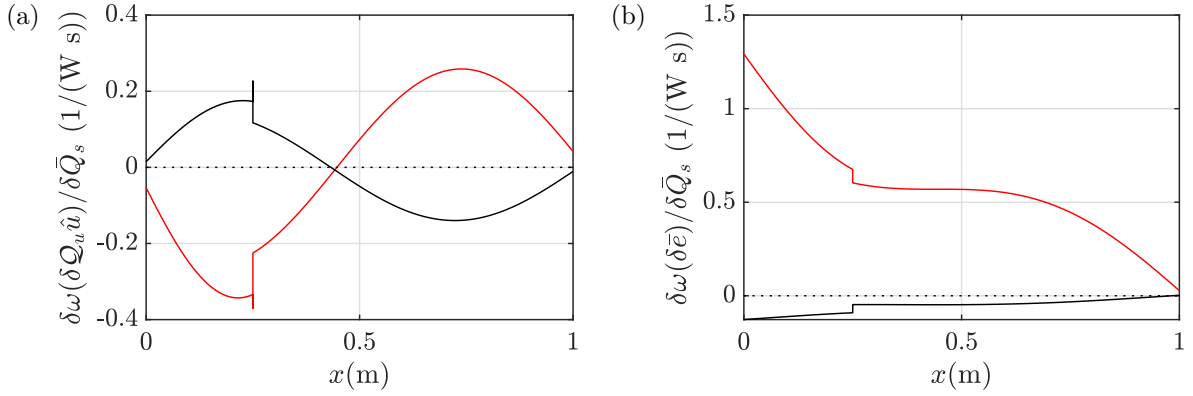


Fig. 5.9 Growth rate shift $\delta\lambda$ denoted by —, and angular frequency shift $\delta\sigma$ denoted by —, for the new model of the Rijke tube. Figure (a) shows the eigenvalue shift due to the unsteady heat source and figure (b) shows the eigenvalue shift due to the steady heat source.

the same as the primary heater. Again, considering the contributions from the steady mechanism $\delta\omega(\delta\bar{e})$ and the unsteady mechanism $\delta\omega(\delta Q_u \hat{u})$, the full eigenvalue drift per unit of energy at position x_0 is given by:

$$\frac{\delta\omega}{\delta Q_s} = \{F_e^+, 1\} + \left\langle \hat{p}^+, \frac{1}{A_{duct}} \frac{\hat{u}}{\bar{u}} k_s e^{-i\omega\tau_s} \delta(x - x_0) \right\rangle, \quad (5.31)$$

Fig. 5.9 shows the two mechanisms. From these plots we observe that in terms of growth rate shift, both mechanisms share similar magnitudes, but in terms of angular frequency shift the steady mechanism is dominant. The comparison between the experimental and the predicted eigenvalue shift can be seen in Fig. 5.10. From this figure we observe that the structure and the magnitude of both frequency and growth rate shifts are very well captured by the network model and the sensitivity analysis. In this occasion the influence of the base flow sensitivity is clear, explaining the shift observed in the frequency of the experimental results.

In summary, the adjoint based sensitivity analysis developed as part of this thesis, aided with a better network model of the Rijke tube, is able to predict qualitatively the structure of the eigenvalue drift due to the effects of a drag device or a secondary heat source. It is important to mention that the difference between the model and the experimental data is due to the limitations of the modelling approach not the adjoint method. The experimental Rijke tube is driven by convection due to the thermal difference of the air in the tube, while the model has a forced inlet velocity. Thus, a modelling approach that considers natural convection might improve the predictions.

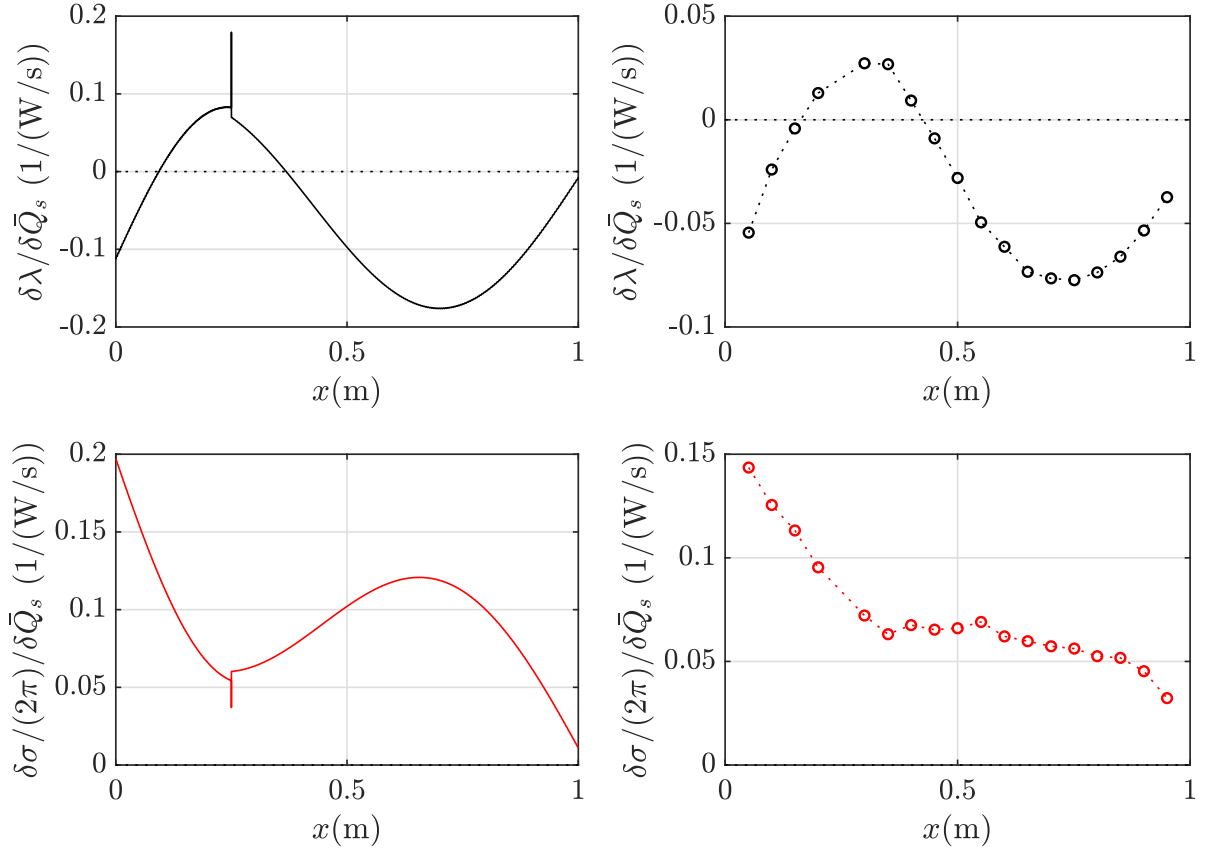


Fig. 5.10 Total eigenvalue shift due to the presence of a secondary heat source in the Rijke tube. The left column shows the shift predicted by the model and the right column shows the shift measured in the experiments ([Jamieson and Juniper, 2017b](#)).

5.6 Sensitivity analysis of the choked combustor

Following a similar approach as for the Rijke tube, we begin by analysing the adjoint mode shapes for the choked combustor of § 3.4. Adjoint entropy waves appear upstream and downstream of the flame in the component of the receptivity of the continuity equation (\hat{p}^+ in Fig. 5.11c) and as oscillations in the receptivity of the energy equation (\hat{p}^+ in Fig. 5.11a). In the latter, they appear in the upstream region mainly due to the effect of the flame. They appear in the downstream region due to the choked end³. This physically means that to produce a change in the generation of entropy waves through the unsteady flame speed, we need to force the energy equation before the flame, as

³Due to the choked end, the downstream acoustic and entropy waves are reflected as an acoustic wave. In the adjoint problem, however, the outgoing adjoint acoustic wave at the choked end creates both a backward adjoint acoustic wave and a backward adjoint entropy wave. This is because the direct equations propagate quantities forwards in time, while the adjoint equations propagate receptivities backwards in time.

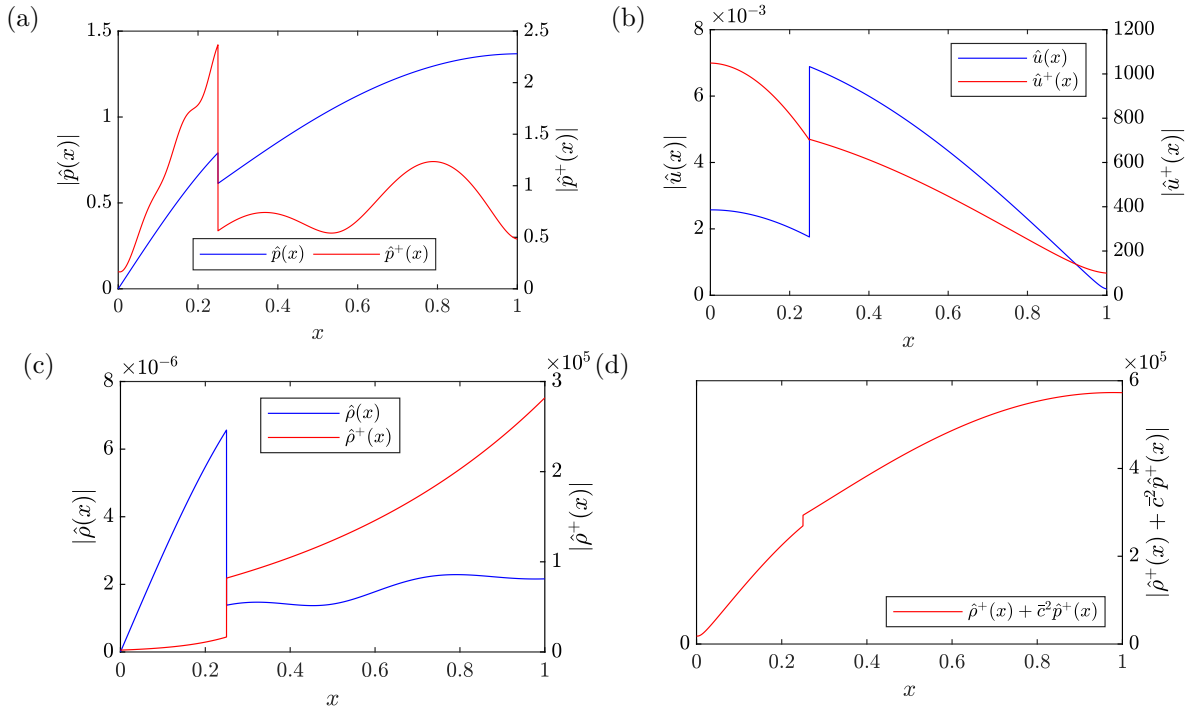


Fig. 5.11 Mode shapes for the direct and adjoint variables. (a), (b) and (c) show the receptivity to the energy equation, momentum equation and a component of the continuity equation respectively (computed using the continuous adjoint approach) on top of the pressure, velocity and density mode shapes. (d) represents the full receptivity of the continuity equation (See § 5.2.1).

intuitively expected. Forcing the energy equation after the flame changes the intensity with which the entropy waves interact with the choked end.

As with the Rijke tube, for this configuration the sensitivities computed using a discrete and continuous adjoint are the same to machine precision. The base state sensitivities for different flame positions are plotted in Fig. 5.12. (The choked end does not allow a variation of the reflection coefficients in the downstream end, and its sensitivity is thus omitted.) The upstream reflection coefficient shows a similar behaviour to that in the Rijke tube. The sensitivity of the flame interaction index shows that any increase in its value when the flame is in the first fifth of the duct will stabilize the system but will destabilize the system everywhere else. On the other hand the frequency is affected greatly when the flame is located in the first half of the duct, when compared to the second half. This is because the unsteady heat release is proportional to velocity, whose magnitude is reduced towards the choked end. The time delay is the most influential parameter.

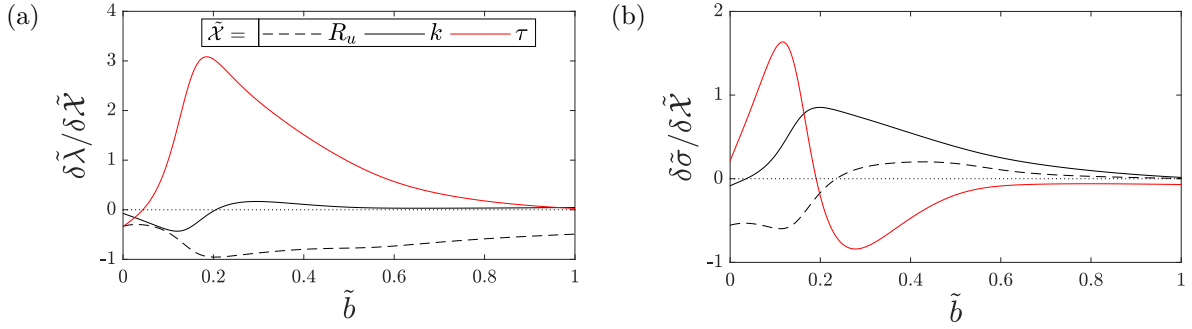


Fig. 5.12 Growth rate (a) and angular frequency (b) shifts caused by a change in the base state variables, denoted by $\tilde{\mathcal{X}}$, for different positions of the flame, \tilde{b} , along the duct length considering a mean flow, \bar{u} , and a moving flame front.

For the unsteady feedback sensitivity, we first analyse the mechanisms that cause mass injection (row 1 of Fig. 5.13). For this system any feedback mechanism that causes mass addition in phase with \hat{p} , \hat{u} , or $\hat{\rho}$, will destabilize the system, as seen by the growth rate shifts. The most physical mechanism is represented by feedback from pressure Fig. 5.13a, which models the effect of positioning a Helmholtz resonator in the duct. (The phase of the resultant mass addition depends on the oscillation frequency relative to the Helmholtz resonator frequency.) In a system with a choked end, the most influential position to locate such a device is towards the exit $x = 0.96$, which is not quite the antinode of the resonant mode.

The mechanisms that cause momentum addition in phase with \hat{p} , \hat{u} , or $\hat{\rho}$, are shown in row 2 of Fig. 5.13. The most physical mechanism would be the drag device from Fig. 5.13e, which forces the flow π out of phase with (i.e., in the opposite direction to) the local velocity, and is strongly stabilizing. This can be seen by taking the negative of the growth rate (continuous black line or filled dots) in Fig. 5.13e.

The mechanisms that cause heat addition in phase with \hat{p} , \hat{u} , or $\hat{\rho}$, are shown in row 3 of Fig. 5.13. In all of these mechanisms there are oscillations upstream and downstream of the flame. These are caused by the entropy waves and their contribution, after being accelerated at the choked end, as acoustic waves. If entropy waves were allowed to convect away from the system, the mechanisms would be similar to those for mass injection, with oscillations only upstream of the flame. For example, any mechanism that causes increased heat input in phase with the pressure will destabilize the system, as is the case for solid rocket propellants.

In a choked nozzle two upstream-propagating acoustic waves are generated at the throat: one by the entropy wave and one by the downstream-propagating acoustic wave. If the superposition of the two upstream propagating waves is constructive, the feedback

mechanisms will have similar shapes but with larger amplitudes. If the superposition of waves is destructive, the feedback mechanisms will have similar shapes but smaller amplitudes. For this particular configuration the superposition is destructive, so the feedback devices are weakened by the indirect noise. In general when the length of the duct between the combustion chamber and the exit nozzle changes by $\pi\bar{u}/\omega$ the interaction between the two upstream propagating waves can be expected to change between destructive and constructive interaction.

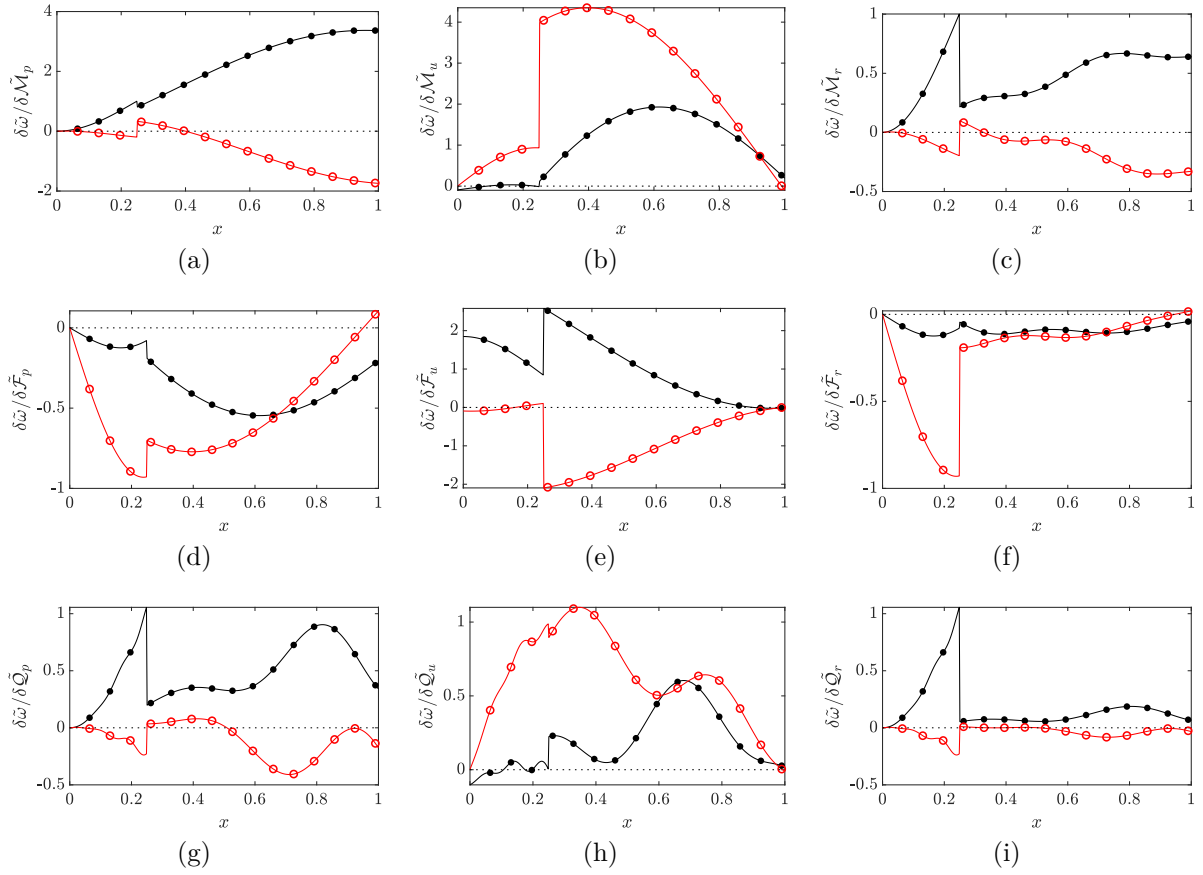


Fig. 5.13 Growth rate shift, $\delta\tilde{\omega}$ denoted by —, ●, and angular frequency shift, $\delta\tilde{\omega}$ denoted by —, ○, for each feedback mechanism. The rows display the continuity, momentum and energy equations, while the columns represent feedback from pressure, velocity and density respectively. The continuous lines (—, —) represent one calculation via the adjoint method while the circles (●, ○) represent 15 computations via the finite difference method.

5.7 Sensitivity analysis of geometric parameters

So far the effects of feedback devices and base state parameters such as interaction indices, time delays and reflection coefficients have been investigated in simple network models. For the more complicated network models the focus will be on the geometric parameters such as areas, lengths and mean radii. The knowledge of these sensitivities is useful during pre-design stages, given that small variations, for example, due to manufacturing processes, can change the stability of a combustor. Furthermore, since this information will be used to perform optimization in chapter 6, sensitivity analysis of the initial configurations provides a good estimate of the changes that the configuration will go through during the optimization process.

In this section, sensitivity analysis of geometric parameters is performed first on the longitudinal combustor, then on the LPP annular combustor and finally on the CUED annular combustor. Given that the focus of this thesis is to devise strategies to stabilize all of the unstable modes in a configuration, the following sensitivity analysis will only focus in the growth rate shifts.

5.7.1 Longitudinal combustor

The relevant geometric parameters of the longitudinal combustor, presented in § 3.5 are the areas, lengths and mean radii. To ensure that the sensitivities with respect to these parameters are correctly computed, we perform Taylor tests around the most unstable eigenvalue. The results are shown in Fig. 5.14.

For the longitudinal combustor the growth rate sensitivity maps are shown in Fig. 5.15. The first observation is that length and mean radius sensitivities are on average 2 orders of magnitude smaller than area sensitivities. The former can be explained given that a change in area causes base flow variations, while a change in length or mean radius does not. Hence, for area changes, the base flow sensitivity adds to the unsteady sensitivity. The most influential region is at the flame holder, where the area and mean radius sensitivities have their largest magnitudes. The second most influential zone is the neck area, with a large positive sensitivity. In order to stabilize this burner, we expect a reduction in the flame holder and neck areas as well as shortening of the plenum's length.

5.7.2 LPP annular combustor

For the LPP annular combustor the relevant geometrical parameters are the areas, lengths, mean radii and time delay, since this element can be interpreted as the distance from

injection until the flame front is reached. The Taylor tests for this configuration are shown in Fig. 5.16. From Fig. 5.17 we observe that the sensitivity of the time delay is at least one order of magnitude larger than any of the geometric parameters (see Fig. 5.18). In this case, increasing the time delay decreases the growth rate of the two unstable modes but decreases the decay rate of most of the stable modes. This shows, as expected, that the time delay is one of the most influential elements of a thermoacoustic system, and that it influences all modes differently. When the sensitivity to the time delay is summed over all eigenvalues in the cost function, we expect the algorithm to impose, for this case, small changes. The growth rate sensitivity maps for the geometric parameters are shown in Fig. 5.18. The magnitudes of the sensitivities to changes in area are one order of magnitude larger than length and mean radius sensitivities. The most influential regions are given by the premix ducts' area, the plenum's length and the combustion chamber's mean radius.

5.7.3 CUED annular combustor

The last configuration is the CUED annular combustor. For this configuration the relevant geometric parameters are the areas, lengths and mean radii. The corresponding Taylor tests are shown in Fig. 5.19. The growth rate sensitivity maps are shown in Fig. 5.20. The patterns are very similar to the previous two configurations. The most influential zone is the area at the flame holder, followed by the area of the ring of premix ducts. In order to stabilize this configuration we expect the premix ducts' area to reduce,

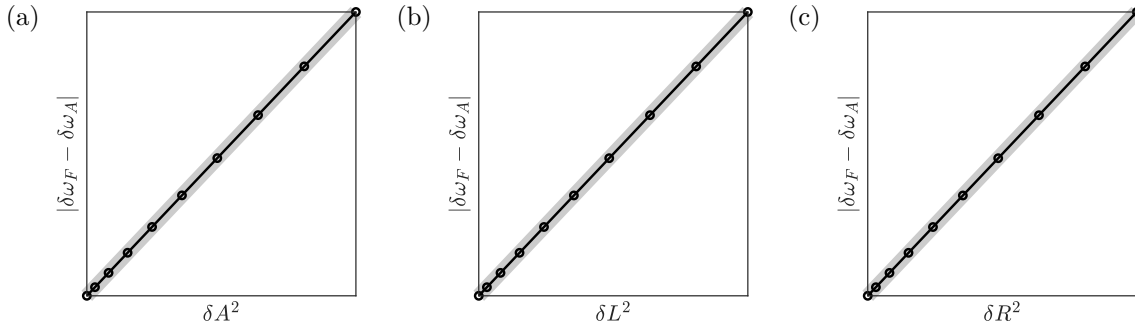


Fig. 5.14 Taylor tests for different parameters of the longitudinal combustor. The eigenvalue drift is computed for the mode near 364 Hz. A similar behaviour is expected for any other mode. (a), (b), (c) show the Taylor tests generated by introducing small changes in all of the areas (δA), lengths (δL), and mean radii (δR) of the configuration respectively. The gray line in the background is a straight line between the initial and final point, plotted for comparison. The figures confirm that the eigenvalue shift predicted with the adjoint method is indeed correct to first order in δA , δL and δR .

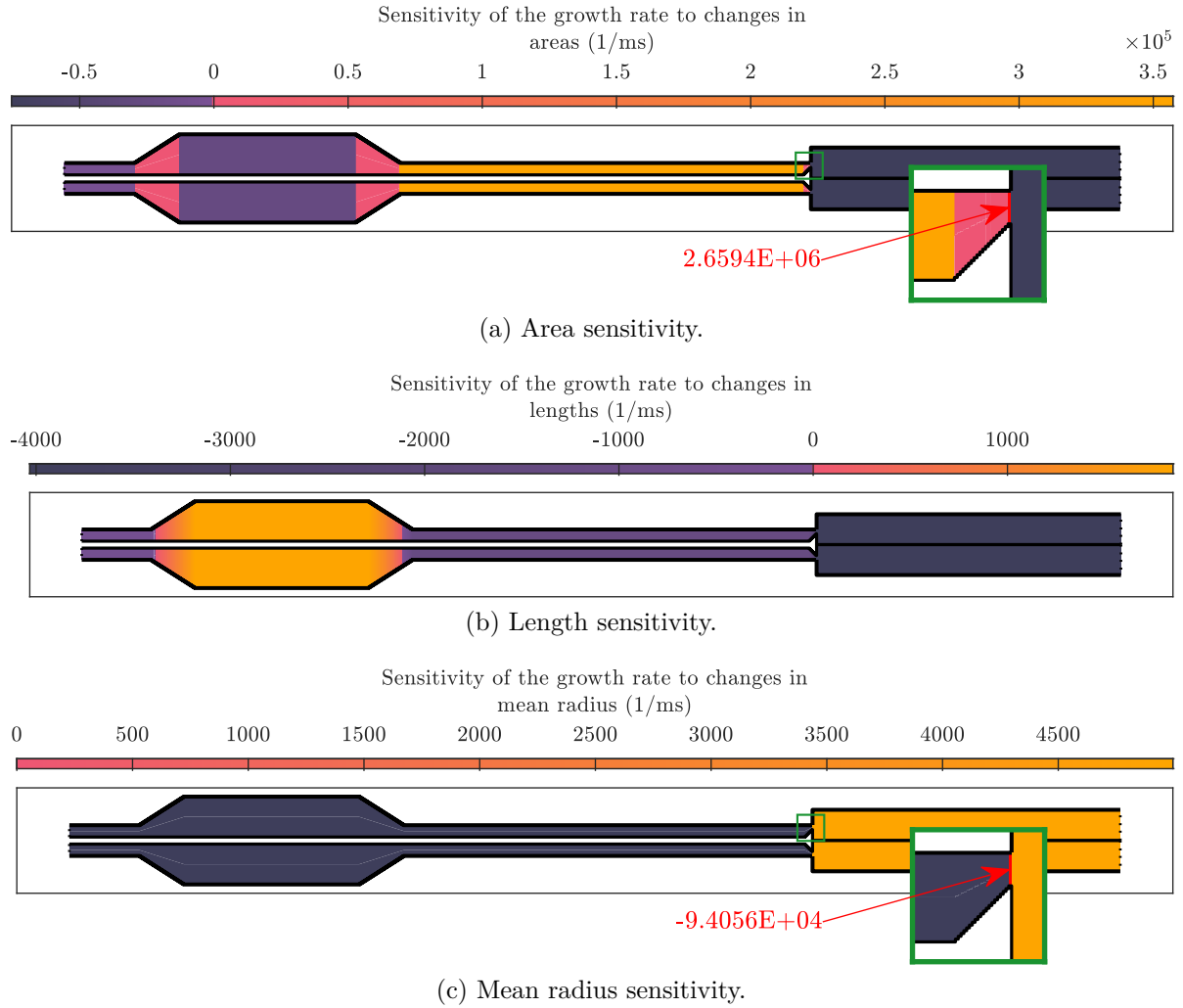


Fig. 5.15 Growth rate sensitivity maps for the unstable modes in the initial configuration of the longitudinal combustor. The maps show the sum of the growth rate sensitivities of the unstable modes due to changes in areas (a), lengths (b) and mean radii (c). In (a) and (c) the sensitivity at the flame holder location is indicated in red.

the flame holder area to increase, the premix ducts' to elongate and the combustion chamber to increase its mean radius. It is worth noting that all the higher order ($|n| \geq 2$) unstable azimuthal modes have sensitivities that point in the same direction.

5.7.4 Summary

From the previous sensitivity analysis a few conclusions are derived. First, the heat source regions or heat source parameters have the largest sensitivities, which shows that thermoacoustic systems are very sensitive to small changes. Second, from all the

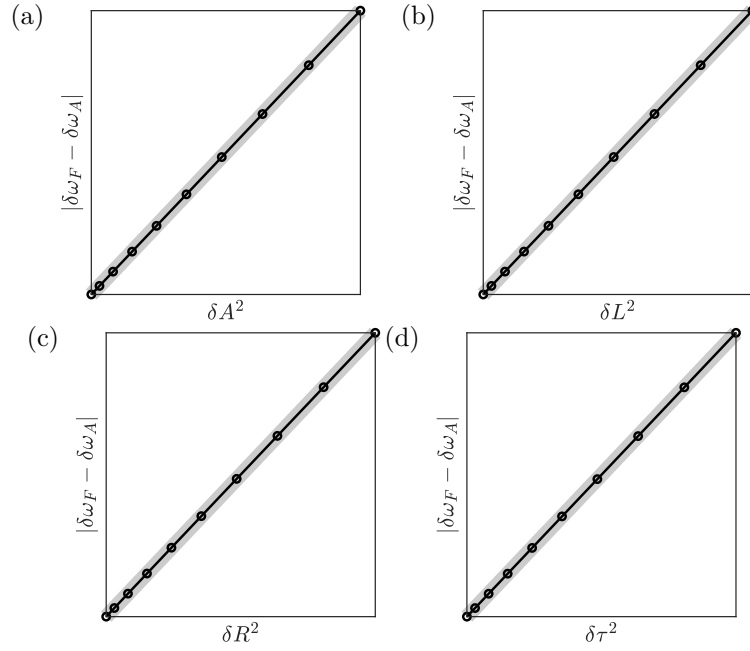


Fig. 5.16 Taylor tests for different parameters of the LPP annular combustor. The eigenvalue drift is computed for the mode near 547 Hz, $|n| = 1$. See Fig. 5.14 for further interpretation.

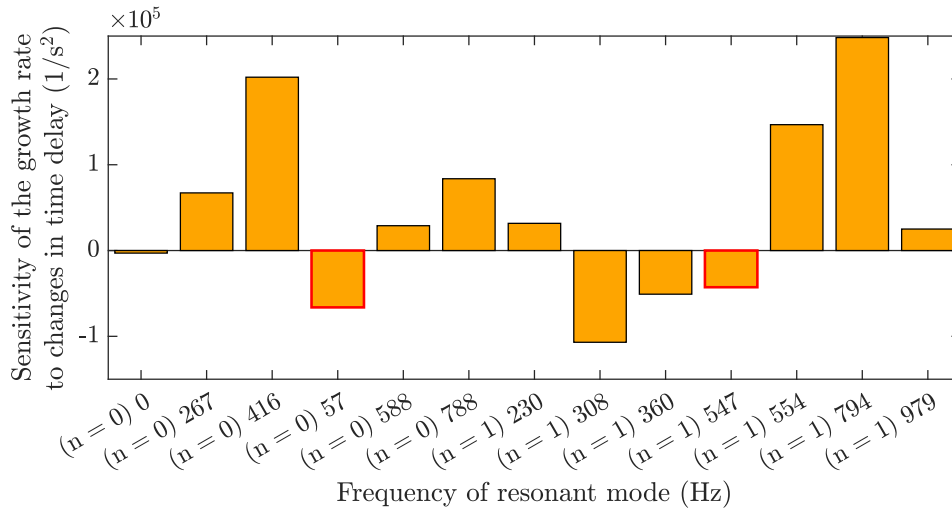


Fig. 5.17 Sensitivity of the growth rates to changes in the time delay for all the resonant modes in the LPP annular combustor with azimuthal number $n = 0$ and $|n| = 1$. The red box denotes an unstable mode.

geometric parameters analysed, the areas have, on average, the largest sensitivities due to their influence in the mean flow. Third, the unstable modes of the longitudinal and annular configurations show similar sensitivity patterns.

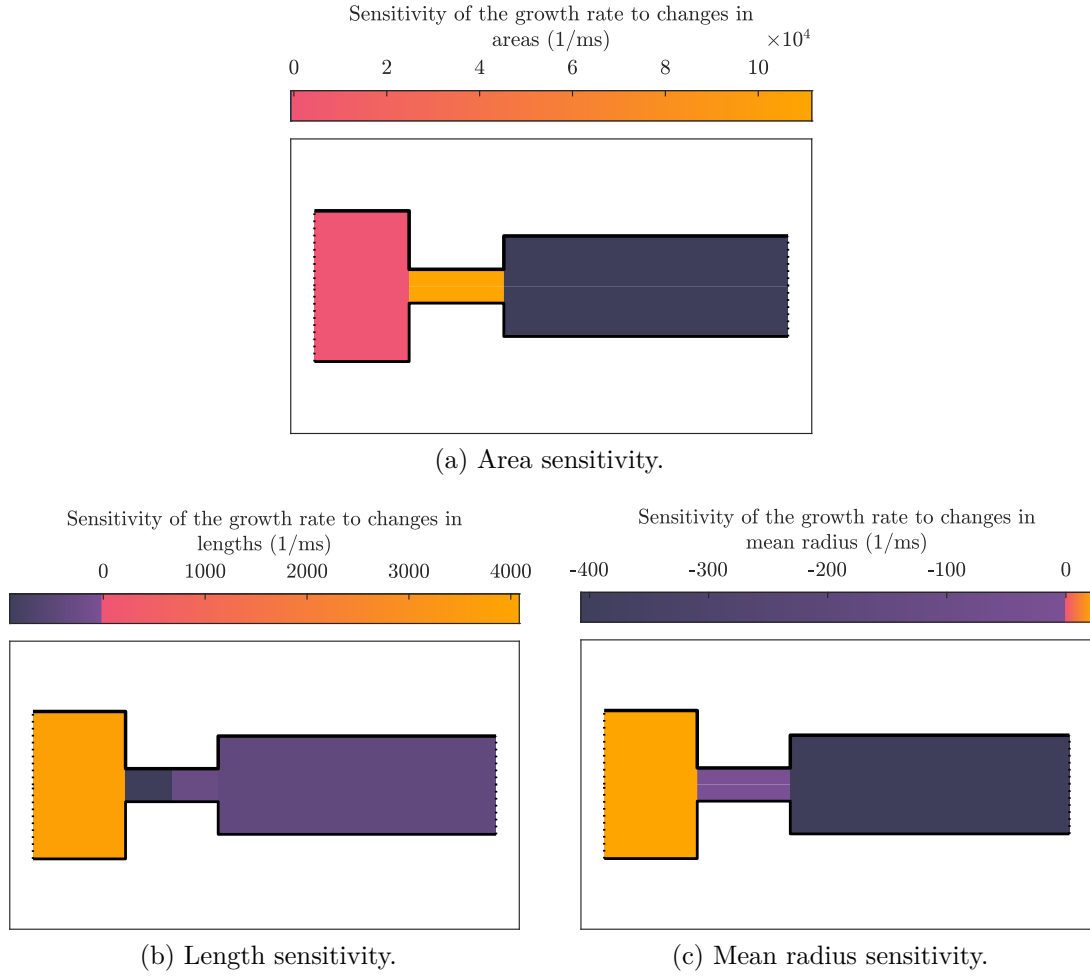


Fig. 5.18 Growth rate sensitivity maps for the unstable modes in the initial configuration of the LPP annular combustor. The maps show the sum of the growth rate sensitivities of the unstable modes due to changes in areas (a), lengths (b) and mean radii (c).

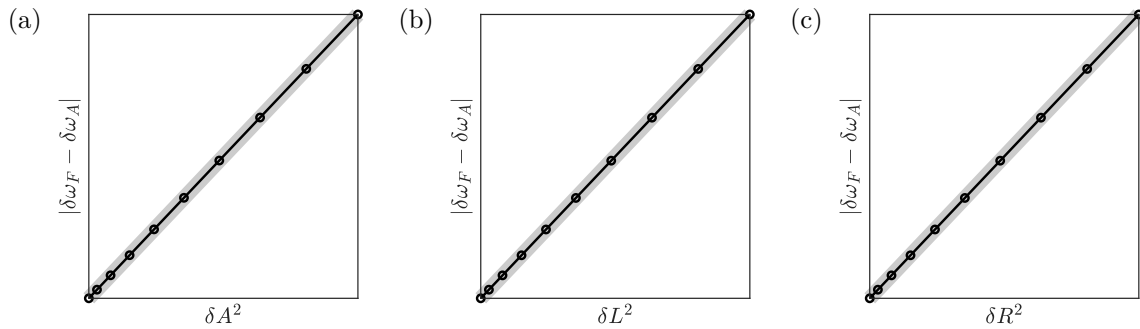
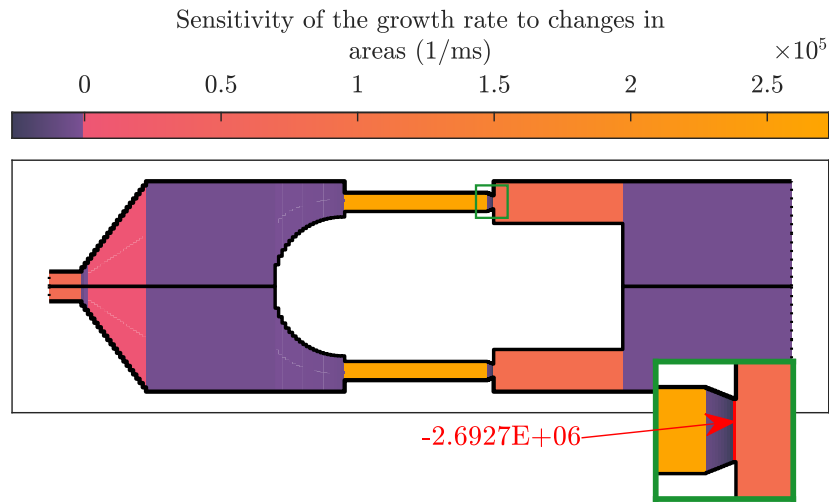
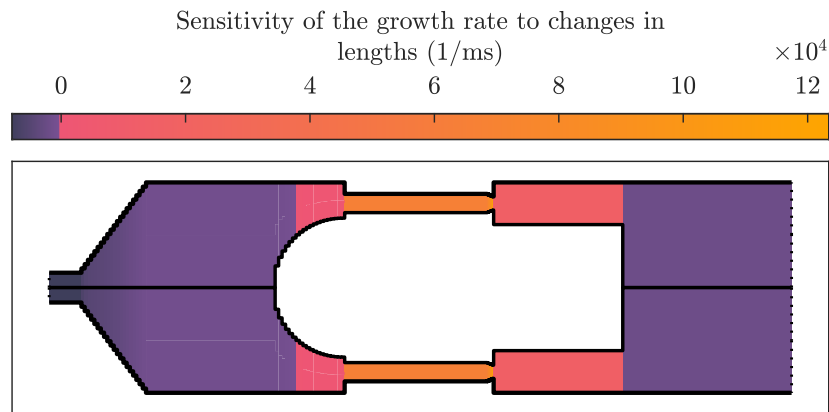


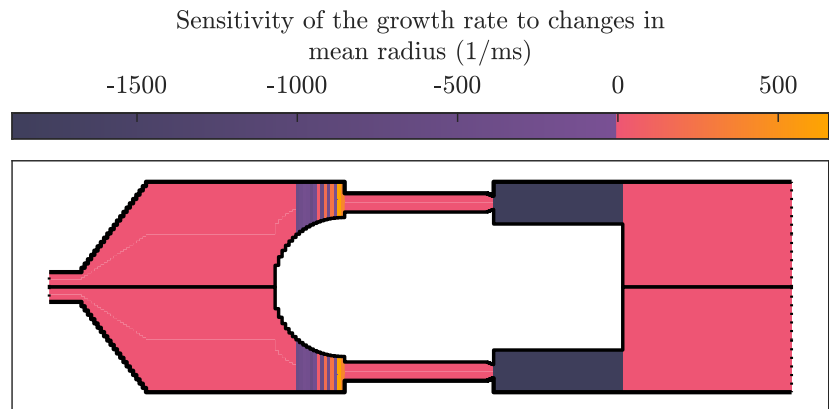
Fig. 5.19 Taylor tests for different parameters of the CUED annular combustor. The eigenvalue drift is computed for the mode near 1131 Hz, $|n| = 1$. See Fig. 5.14 for further interpretation.



(a) Area sensitivity.



(b) Length sensitivity.



(c) Mean radius sensitivity.

Fig. 5.20 Growth rate sensitivity maps for the unstable modes in the initial configuration of the CUED annular combustor. The maps show the sum of the growth rate sensitivities of the unstable modes due to changes in areas (a), lengths (b) and mean radii (c). In (a) the sensitivity at the flame holder location is indicated in red.

Chapter 6

Optimization in low order thermoacoustic networks

The aim of this project is to stabilize all of the thermoacoustically unstable modes of a system. This is one of multiple requirements for gas turbines. Others include reduction of emissions, optimization of fuel consumption and ease of serviceability ([Lieuwen and Yang, 2013](#)).

Thermoacoustic systems are exceedingly sensitive to small changes ([Juniper and Sujith, 2018](#)) and can usually be stabilized by making only small changes. The ideal approach is to tweak the shape of the system until a stable configuration is achieved. The challenge is to identify these small changes before the full engine test stage. By combining the sensitivity information of chapter 5 with an optimization routine, we can stabilize all of these thermoacoustic modes by slightly modifying the geometry. Any stable modes that become unstable can also be targeted and stabilized. The advantage of this approach is that, unlike a Helmholtz resonator, it stabilizes all unstable frequencies. The disadvantage is that it relies on an accurate model of the real system (a disadvantage shared by any method that relies on such model).

The optimization process requires a cost function. To stabilize a combustor within a given frequency range, the cost function can be proportional to the sum of the growth rates of the unstable modes. In order to perform this minimization process, a handful of parameters can be varied such as FTF parameters or geometric parameters (See chapter 5). We use the first order sensitivities of this cost function within a convex optimization algorithm in order to find a stable configuration for the given operation conditions.

6.1 The optimization algorithms

The adjoint-based sensitivity analysis described in chapter 5 gives the gradient of each eigenvalue with respect to the geometric parameters. These gradients can be used in a gradient descent algorithm. Our aim is to stabilize all of the thermoacoustic modes of a given configuration simultaneously and we must allow for unstable modes to disappear or re-appear during the optimization process. In general, to perform an optimization routine, we follow the next steps:

1. Compute the resonant thermoacoustic modes of the system (the eigenvalues).
2. Compute the sensitivity of the eigenvalues with respect to the geometric parameters (areas A , lengths L , mean radii R , and time delay τ).
3. Given a set of constraints and maximum allowed displacements, use an optimization algorithm to compute the changes in the parameters such that the cost function is optimally reduced.
4. Update the configuration and iterate until all the modes are stable.

As part of this thesis we explore two different algorithms: the box search and the conjugate gradient.

6.1.1 Algorithm 1: Box search

The first algorithm is a routine that resembles a descent method to find local minima. To develop the cost function we begin by introducing a small change to some of the system's parameters denoted by δp_k for $k = 1, 2, 3, \dots, N_x$, where N_x is the number of parameters in the system. These cause the eigenvalues to shift. The predicted eigenvalue Ω_j is given by: $\Omega_j = \omega_j + \delta\omega_j$, where ω_j is an eigenvalue of the system, and $\delta\omega_j$ is the corresponding eigenvalue drift. The eigenvalue drift is given by the sum of the sensitivities times the perturbation size:

$$\delta\omega_j = \sum_{k=1}^{N_x} \frac{\partial\omega_j}{\partial p_k} \delta p_k, \quad (6.1)$$

In the studied frequency range the system will have N_ω resonant modes, each of them represented by: $\omega_j = \sigma_j - i\lambda_j$. Our objective is to stabilize all of the resonant modes (i.e., $\lambda_j < 0$ for $j = 1, \dots, N_\omega$) by introducing small changes into the system. To ensure that all the modes end up with a negative (rather than zero) growth rate we set an objective growth rate λ_o such that $\lambda_o \leq 0$. Once λ_j reaches λ_o we do not seek to stabilize mode ω_j further.

Let $\Gamma(\delta p)$ be the function that denotes the difference between the perturbed and the objective growth rates, which is given by:

$$\Gamma(\delta p) = \lambda_j + \underbrace{\sum_{k=1}^{N_x} \frac{\partial \lambda_j}{\partial p_k} \delta p_k}_{-\text{Im}\{\Omega_j(\delta p)\}} - \lambda_o. \quad (6.2)$$

With this we build a predictor function $\Psi_j(\delta p)$, that gives 0 if a mode has growth rate less than λ_o or the difference Γ if the growth rate is larger than λ_o . Mathematically:

$$\Psi_j(\delta p) = H_s(\Gamma) \Gamma(\delta p), \quad (6.3)$$

where $H_s(\Gamma)$ is the Heaviside step function, which in our model will be approximated by the smooth function:

$$H_s(\Gamma) = \frac{1}{2} \left(1 + \tanh \left(\frac{\Gamma}{\mu} \right) \right), \quad (6.4)$$

where $\mu = 1 \times 10^{-3}$ is a small number that controls the sharpness of the step. The reduced version of the cost function $\mathcal{J}(\delta p)$, which we minimize, is then given by one half of the sum of the square of the predictor functions over all of the eigenvalues of the system.

We can further add a small constraint to the cost function in order to select the parameters that produce the smallest variations in the configuration. By considering δp_{m_k} , the maximum allowed change of the k th parameter, the cost function becomes:

$$\underbrace{\mathcal{J}(\delta p) = \sum_j^{N_\omega} \frac{1}{2} (\Psi_j(\delta p))^2}_{\text{Reduced version}} + \frac{1}{N_x} \sum_{k=1}^{N_x} \left(\frac{\delta p_k}{\delta p_{m_k}} \right)^2. \quad (6.5)$$

In order to compute the changes in the parameters that best reduce the cost function, we use the logarithmic barrier method in [Boyd and Vandenberghe \(2010\)](#). The constrained minimization problem becomes:

$$\begin{array}{ll} \text{minimize} & \mathcal{J}(\delta p) \\ \text{subject to} & -\delta p_{m_k} \leq \delta p_k \leq \delta p_{m_k}, \quad k = 1, \dots, N_x \end{array}$$

where δp_{m_k} is given as a small percentage of the parameter's value.

The name of the algorithm "*Box search*", comes from the fact that the routine searches in the domain (box) set by the maximum allowed changes for the point that minimizes

the cost function. This point may not be in the same direction as the equivalent point obtained using a steepest descent or conjugate gradient method. That is, the box search does not prioritize the changes of the parameters with the largest sensitivities. However, this algorithm has the advantage that it is less prone to becoming trapped in a local minimum that does not stabilize all of the modes. It is also able to determine whether a given change in the system will destabilize a given mode.

6.1.2 Algorithm 2: Conjugate gradient

Due to its ease of implementation, the conjugate gradient method is one of the most used convex optimization algorithms. Following a similar procedure as in § 6.1.1, the cost function for the conjugate gradient algorithm is given by:

$$\mathcal{J}(\delta p) = \frac{1}{2} \sum_{j=1}^{N_\omega} (\lambda_j(\delta p) - \lambda_o)^2 \quad (6.6)$$

The major changes between the cost functions in both algorithms are:

1. For the conjugate gradient algorithm, the sensitivity information does not enter the cost function any more. Instead the sensitivity information goes directly into the computation of the gradient.
2. If a change in parameters causes a mode to become unstable, the box search algorithm accounts for this in the same iteration, but the conjugate gradient algorithm takes no account of this until the following iteration.

The conjugate gradient (CG) method is a simple extension of the steepest descent. The full algorithm is presented here in order to point out the subtleties that the cost function in Eq. (6.6) produces during its implementation. Given a function $f(x)$, where f represents the cost function (\mathcal{J}) and x the changes in the parameters (δp) the conjugate gradient algorithm (Press et al., 1992) is:

Algorithm Conjugate gradient method.

Require: a starting point $x_0 \in \text{dom } f$.

$\Delta x_0 := -\nabla f(x_0)$.

Line search. Choose step size t_0 via backtracking line search.

Update. $x_1 := x_0 + t_0 \Delta x_0$

$s_0 := \Delta x_0$.

...

repeat

$\Delta x_n := -\nabla f(x_n)$.

CG update parameter. Choose step size β_n (see below)

Update conjugate direction. $s_n = \Delta x_n + \beta_n s_{n-1}$.

Line search. Choose step size t_n via backtracking line search.

Update. $x_{n+1} := x_n + t_n s_n$.

until stopping criterion is satisfied.

The CG update parameter is given by:

$\beta_n = 0$ for steepest descent.

$\beta_n = \frac{\Delta x_n^T \Delta x_n}{\Delta x_{n-1}^T \Delta x_{n-1}}$ for Fletcher–Reeves CG.

$\beta_n = \frac{\Delta x_n^T (\Delta x_n - \Delta x_{n-1})}{\Delta x_{n-1}^T \Delta x_{n-1}}$, and restart if $\beta_n = \max \{0, \beta_n\}$ for Polak–Ribiere CG.

When this algorithm is implemented, there is a problem in the line search procedure. The eigenvalues of thermoacoustic systems can be very sensitive (Juniper and Sujith, 2018). Therefore the computed gradients can be exceedingly large. Updating the changes in the parameters with these values may result in a non-physical geometry. To take this into account, we begin the line search by ensuring that the parameters do not change by more than a given percentage, which is enforced with a backtracking procedure. The backtracking line search algorithm can be either linear (Boyd and Vandenberghe, 2010) or parabolic:

Algorithm Backtracking line search.

Require: a descent direction Δx for f at $x \in \text{dom } f$, $\alpha \in (0, 0.5)$, $\beta \in (0, 1)$.

Ensure: $t := 1$

while $f(x + t\Delta x) > f(x) + \alpha t \nabla f(x)^T \Delta x$ **do**

Linear: $t := \beta t$.

Parabolic: Compute $f(x + t\Delta x)$ at $t_0 = 0$, $t_1 = t/2$, $t_2 = t$ and find vertex t_v .

if $t_v < 0$ **then**

Perform linear backtracking: $t := \beta t$.

else

$t := t_v$

end if

end while

In general the parabolic method performs fewer computations. For this reason it is the method used in this chapter. The next subtlety appears in the computation of the CG update parameter, which due to the interference from the previous search direction (via β_n), this parameter can change the search direction to an ascent direction, making the algorithm useless. Therefore, at every iteration we test to see whether the conjugate direction s_n is a descent direction. If it fails, we restart the method by setting $\beta_n = 0$.

6.1.3 Parameter change in the implementation

In chapter 5 the sensitivities to geometric parameters such as areas, lengths and mean radii were found. To ensure an optimal performance of the algorithms, all the parameters are required to have similar magnitudes throughout the optimization. For this reason, the optimization procedure uses inner radius, outer radius, and length rather than area, mean radius and length.

6.2 Test Case

To show the differences between the algorithms we consider the following test case. The geometry of the test configuration is given by a simplified model of the longitudinal combustor, as shown in Fig. 6.1. The major differences are that we consider a perfect gas, the area variations of the plenum and bluff body are computed as sets of only 2 steps, and the flame model is an $n - \tau$ model with parameters $k = 0.5$ and $\tau = 0.001$ s. For this configuration the boundary error plot is given in Fig. 6.2. From this we can observe that the initial configuration has one unstable mode at 568 Hz with a growth rate of 127 s^{-1} . The objective growth rate is set to $\lambda_o = -5 \text{ s}^{-1}$. In order to stabilize the system we are going to allow changes in only two parameters of the network. The first is the area of the enclosure (last duct in the network model), which is going to be changed through the variation of the outer radius r_E . The second is the length of the enclosure L_E .

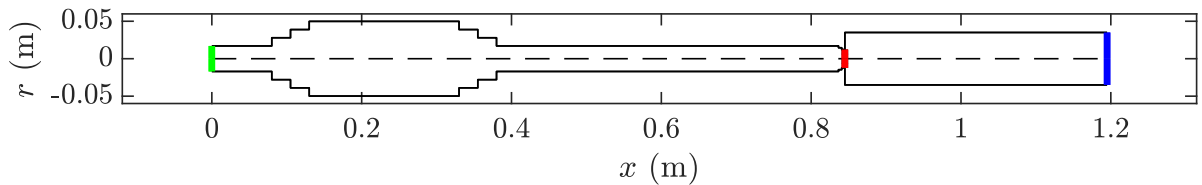


Fig. 6.1 Simplified network model for the test case.

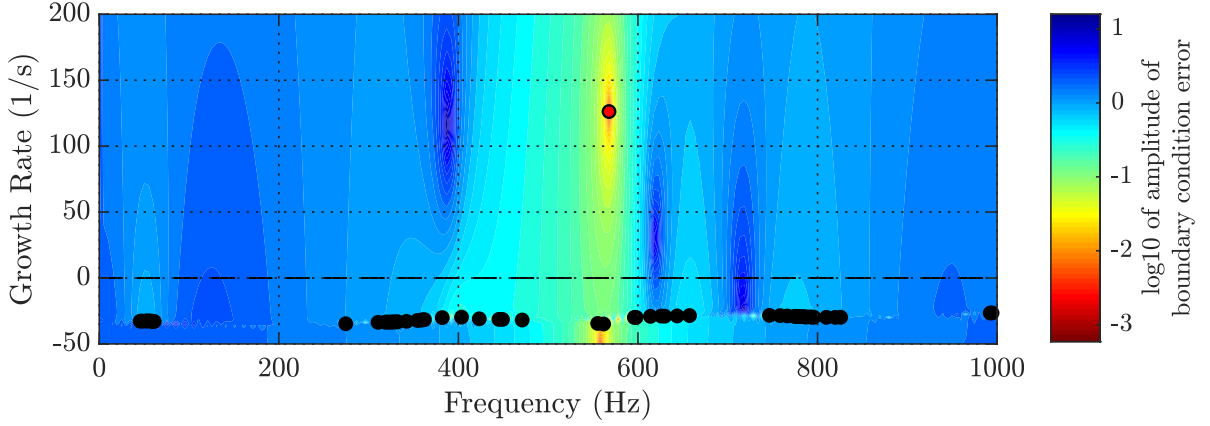


Fig. 6.2 Boundary error plot for the initial configuration of the test case network model.

Four optimization routines are performed in order to stabilize the system: box search, steepest descent and the two variants of the CG. The paths taken by each of the algorithms on top of the cost function (6.6) are shown in Fig. 6.3.

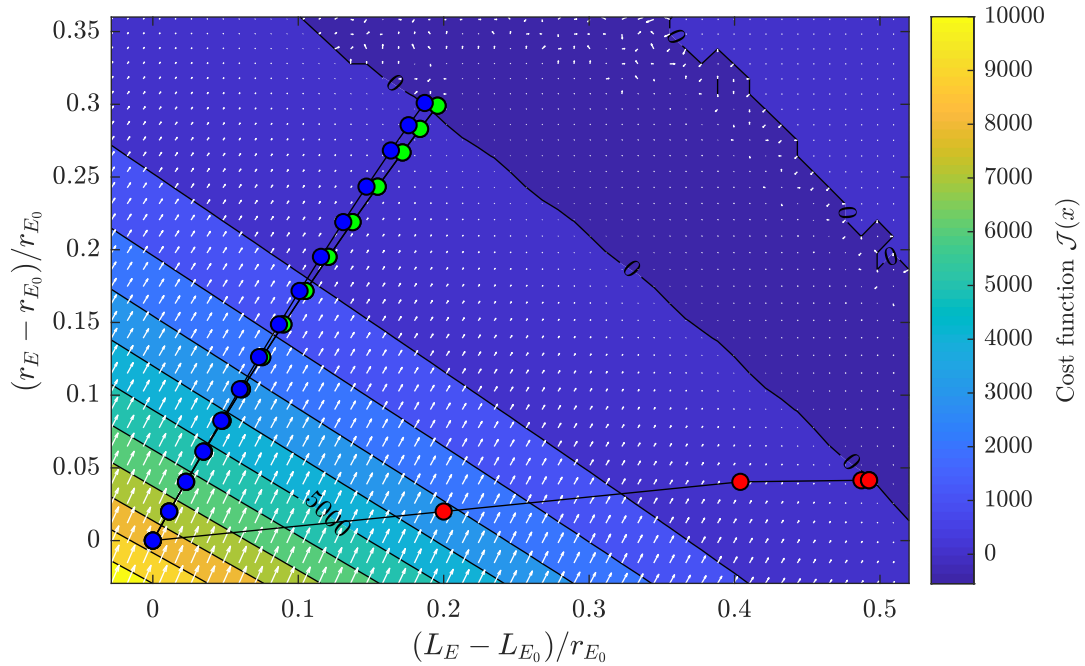


Fig. 6.3 Cost function for the test case. The blue, green and red markers denote the paths taken by the CG Fletcher Reeves, CG Polak Ribiere and Box search respectively until full stability is achieved. The steepest descent algorithm follows the same path as the CG Polak Ribiere. The white arrows show the direction of the local gradient. r_{E_0} and L_{E_0} denote the outer radius and the enclosure length of the initial configuration.

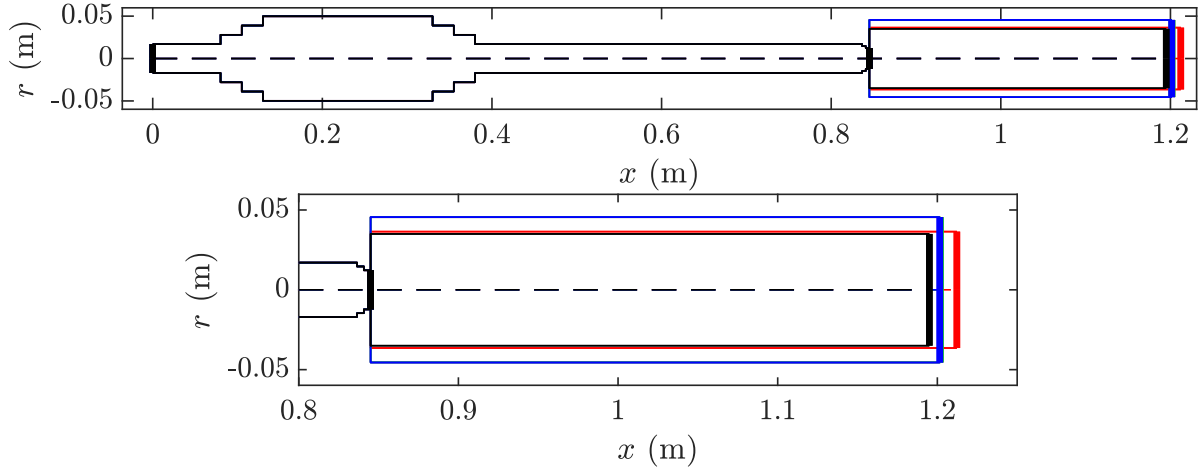


Fig. 6.4 Initial and final configurations of the test cases. The black line represents the initial configuration, and the blue, green and red colours represent the final configurations reached by the CG Fletcher Reeves, CG Polak Ribiere and the Box search respectively. The blue line lies almost on top of the green.

From this figure it is clear that the box search does not follow the steepest descent direction. Given that this algorithm is aided with a penalty function to ensure small changes, it reaches the objective (zero in the cost function) without overshooting. For this specific minimization process, the steepest decent and CG (Polak Ribiere) paths are almost the same. As can be seen in Fig. 6.3, the CG algorithms follow a direction close to the steepest descent direction and reach a different configuration from that of the box search algorithm, by slightly overshooting the objective.

The different final configurations are shown in Fig. 6.4. This figure shows two of the configurations that stabilize the system and that the final configuration is determined as much by the optimization algorithm as by the system being stabilized.

From Fig. 6.3 it should be clear that any configuration that lies within the boundary set by the zero in the cost function is a configuration that meets the requirements of being stable in the analysed frequency range. These algorithms, however, have the limitation that although providing a stable configuration, they do not assess which one is the best. Defining what is best could be done by means of a robustness analysis which is left for future investigation.

6.3 Stabilization of thermoacoustic configurations

In the following sections we stabilize the longitudinal combustor, the LPP annular combustor and then the CUED annular combustor. For each of the configurations we

first define the parameters to be optimized and then we perform a Box search and a CG routine in order to find a stable configuration. All of the optimization routines have:

- objective growth rate of $\lambda_o = -5 \text{ s}^{-1}$, except for the CUED annular combustor for which it is set to $\lambda_o = -1 \text{ s}^{-1}$,
- backtracking parameters $\alpha = 0.1$ and $\beta = 0.8$,
- maximum allowed change in a parameter given as 5% of its current magnitude, except for the LPP annular combustor for which it is set to 1%,
- stopping condition: $\mathcal{J}(\delta p) < 0.01$.

The analysed frequency range for the longitudinal combustor and the LPP annular combustor is from 0 to 1000 Hz and for the CUED annular combustor is from 0 to 2000 Hz.

6.3.1 Stabilizing the longitudinal combustor

To stabilize the longitudinal combustor we consider the following cases:

1. Areas and mean radii are allowed to change.
2. Areas, mean radii and lengths are allowed to change.

Variations in areas and mean radii

For case 1 the areas and mean radii of the configuration are varied. Fig. 6.5 shows the initial and final configurations for the longitudinal combustor and table 6.1 summarizes the changes in each of the sections.

We observe that large changes in some parameters are required in order to stabilize the system. This is because there are several strongly-unstable modes in the configuration. From the sensitivity analysis in Fig. 5.15a it is known that the flame holder area is the most influential parameter, and that its increase causes the growth rate to increase. The results of the optimization via both algorithms show a decrease in the flame holder area. This shows that sensitivity analysis in itself is a powerful tool to identify the regions which are more influential when changed. The other common pattern between the two routines is the reduction in the neck area, which is the second most influential parameter in the sensitivity analysis.

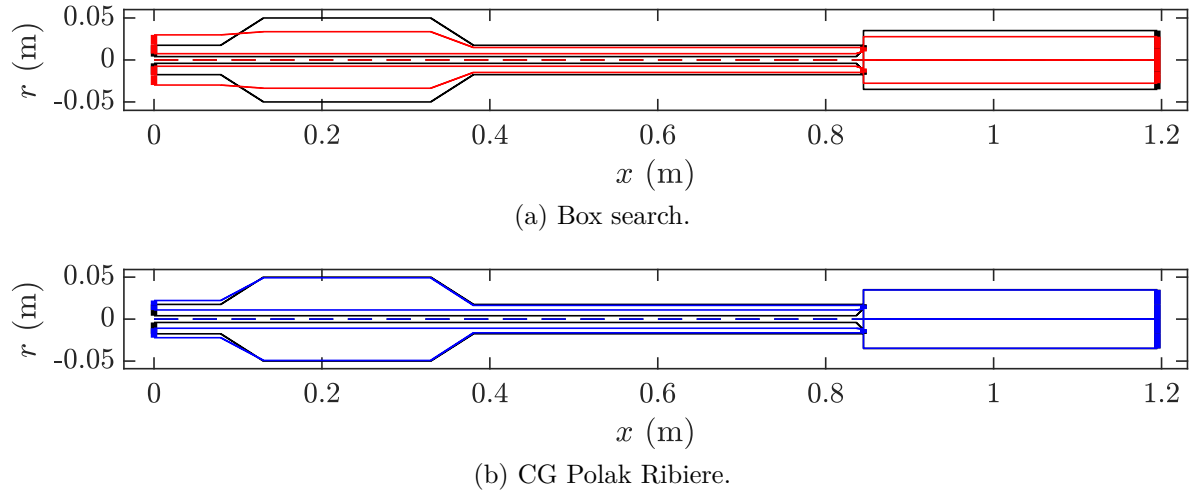


Fig. 6.5 Initial and final configuration of the longitudinal combustor after stabilizing all of the unstable modes by changing the areas and mean radii. The initial configuration is shown in black. The final configuration is shown in red for the box search algorithm and in blue for the CG algorithm.

Algorithm	Inlet	Plenum	Neck	Flame holder	Enclosure
Areas: $(A/A_0 - 1)$					
Box Search	1.8808	-0.5665	-0.4356	-0.2428	-0.3727
CG PR	0.2814	-0.0729	-0.4910	-0.1780	-0.0157
Mean radii: $(R/R_0 - 1)$					
Box Search	0.7379	-0.2379	0.0384	-0.1618	-0.2080
CG PR	0.5370	0.1130	0.2660	-0.0571	-0.0079

Table 6.1 Relative change of the final area/mean radius with respect to the initial area/mean radius of a section for case 1 in the stabilization of the longitudinal combustor.

Variations in areas, mean radii and lengths

For case 2, areas, mean radii and lengths are allowed to vary simultaneously. To avoid having a base flow about to choke at the bluff body the maximum allowed change for the box search algorithm is changed to 4.5%. Fig. 6.6 shows the initial and final configurations and table 6.2 summarizes the changes in each section.

The results show that the box search algorithm allows the changes in length to be as prominent as the changes in areas. The CG algorithm shows that, as expected from the sensitivity analysis, the variations in length are very small compared to those in area. In

fact, most of the configuration follows a similar pattern in the change in areas as in case 1. Most of the variations in length follow the trends predicted by the sensitivity analysis.

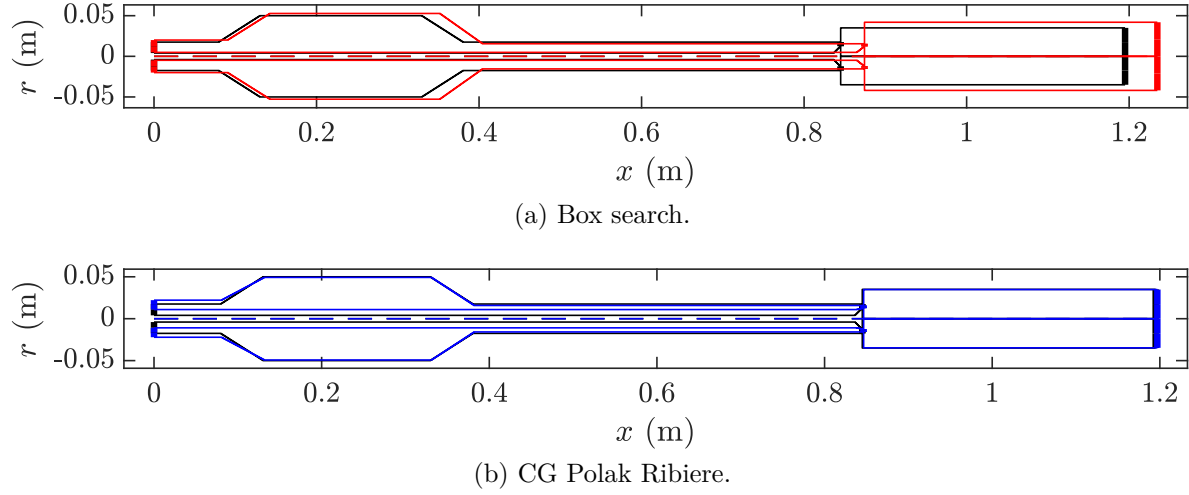


Fig. 6.6 Initial and final configuration of the longitudinal combustor after stabilizing all of the unstable modes by changing the areas, mean radii and lengths. The initial configuration is shown in black. The final configuration is shown in red for the box search algorithm and in blue for the CG algorithm.

Algorithm	Inlet	Area increase	Plenum	Area decrease	Neck	Area decrease	Flame holder	Enclosure
Areas: $(A/A_0 - 1)$								
Box Search	0.2994	–	0.1107	–	-0.2575	–	-0.3847	0.4350
CG PR	0.2772	–	-0.0707	–	-0.5518	–	-0.3925	-0.0132
Mean radii: $(R/R_0 - 1)$								
Box Search	0.1580	–	0.0672	–	-0.0538	–	-0.0803	0.1979
CG PR	0.5360	–	0.1142	–	0.2407	–	-0.0555	-0.0066
Lengths: $(L/L_0 - 1)$								
Box Search	0.1391	0.0219	0.0500	0.0347	0.0101	0.0898	–	0.0297
CG PR	0.0116	0.0081	0.0008	0.0021	0.0001	-0.0030	–	0.0011

Table 6.2 Relative change of the final area/mean radius/length with respect to the initial area/mean radius/length of a section for case 2 in the stabilization of the longitudinal combustor.

As mentioned previously, there are many configurations that will match the requirements of being stable and we can obtain a different stable configuration by changing any of the optimization parameters. In order to show an example, the previous case is re-run, however, this time the unstable mode at 58 Hz is stabilized first. The lowest frequency mode is the least sensitive of all the unstable eigenvalues, so any change that could potentially stabilize higher frequency modes changes this mode only slightly. By optimizing this mode first, the system requires fewer changes to become fully stable. The results of this variation are shown in Fig. 6.7 and table 6.3.

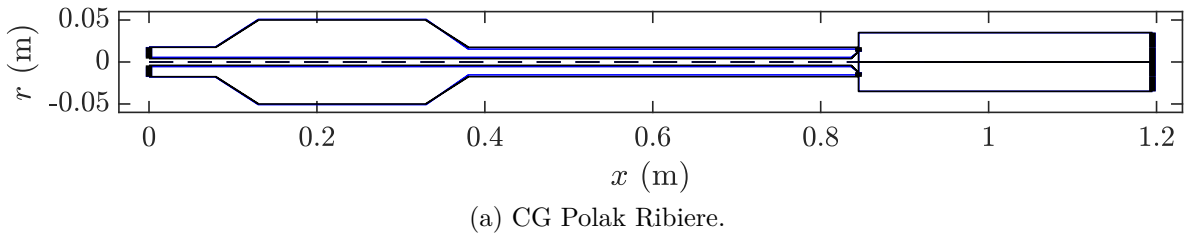


Fig. 6.7 Initial and final configuration of the longitudinal combustor after stabilizing all of the unstable modes by changing the areas, mean radii and lengths. The initial configuration is shown in black. The final configuration is shown in blue for the CG algorithm with the lowest frequency mode stabilized first.

Algorithm	Inlet	Area increase	Plenum	Area decrease	Neck	Area decrease	Flame holder	Enclosure
Areas: $(A/A_0 - 1)$								
CG PR	0.2772	–	-0.0707	–	-0.5518	–	-0.3925	-0.0132
Mean radii: $(R/R_0 - 1)$								
CG PR	0.5360	–	0.1142	–	0.2407	–	-0.0555	-0.0066
Lengths: $(L/L_0 - 1)$								
CG PR	0.0116	0.0081	0.0008	0.0021	0.0001	-0.0030	–	0.0011

Table 6.3 Relative change of the final area/mean radius/length with respect to the initial area/mean radius/length of a section for case 2 (lowest frequency mode first) in the stabilization of the longitudinal combustor.

Fig. 6.7 shows that only the inlet, neck and flame holder areas require large changes in order to stabilize the full system.

The most effective ways to stabilize this combustor are to reduce the flame holder area and to reduce the neck area.

In terms of the performance of the optimization algorithms, we observe that in the case where only the areas and mean radii are varied, both algorithms produce configurations with similar magnitudes of relative change. However, when the lengths are introduced, the box search algorithm produces larger changes in parameters with small sensitivities (lengths). In contrast, the CG algorithm, due to its steepest descent nature, follows a similar path as the first case and produces little changes to the parameters with small sensitivities. Therefore, if one is seeking a configuration which can be stabilized by introducing smaller changes, the CG algorithm is better.

6.3.2 Stabilizing the LPP annular combustor

The inclusion of an azimuthal direction in the eigenvalue problem requires the consideration of azimuthal wave numbers higher than 0. Given that all of the changes in the system are symmetric, no azimuthal modal coupling is introduced. Therefore the sensitivities of the eigenvalues of azimuthal mode n are the same as those of azimuthal number $-n$.

From the boundary error plot in Fig. 3.12 we observe that there are three resonant modes (one each for $n = 0$, $n = +1$, and $n = -1$). They have relatively small growth rates so we expect that only small changes will be required to stabilize the system. To ensure that higher order n modes are not unstable we consider azimuthal wave numbers $|n| \leq 3$. We further note that the eigenvalues are symmetric in n , which means that when all the unstable modes are included in the cost function, the system will prioritize the stability of the circumferential modes ($|n| \geq 1$) because they will be present twice.

For this configuration 5 cases are examined:

1. Variations in areas.
2. Variations in areas and mean radii.
3. Variations in areas and lengths.
4. Variations in areas, lengths and mean radii.
5. Variations in areas, lengths, mean radii and time delay.

Variations in areas

For the first case, only the areas are allowed to change. The final configurations are shown in Fig. 6.8 and summarized in table 6.4. We observe that the box search algorithm favours changes in the plenum while the CG algorithm favours changes in the premix

ducts. Most of the predictions from the sensitivity analysis (Fig. 5.18a) follow through to these results.

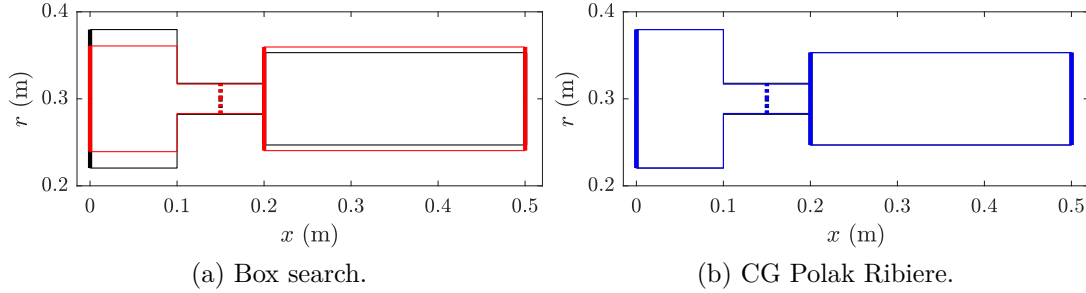


Fig. 6.8 Initial and final configuration of the LPP annular combustor after stabilizing all of the unstable modes by changing the areas. The initial configuration is shown in black. The final configuration is shown in red for the box search algorithm and in blue for the CG algorithm.

Algorithm	Plenum	Premix ducts (inlet)	Premix ducts (outlet)	Combustion chamber
Areas: $(A/A_0 - 1)$				
Box Search	-0.2366	-0.1017	-0.1017	0.1225
CG PR	-0.0002	-0.1102	-0.1102	0.0018

Table 6.4 Relative change of the final area with respect to the initial area of a section for case 1 in the stabilization of the LPP annular combustor.

Variations in areas and mean radii

For the second case, the variation in areas and mean radii is allowed. The initial and final configurations are shown in Fig. 6.9 with their corresponding changes summarized in table 6.5. We observe that the box search algorithm reduces considerably the area of the plenum and premix ducts, while expanding the combustion chamber. The CG algorithm produces a very similar configuration as in case 1. Note that, while the box search algorithm produces small changes in the mean radius, the CG algorithm produces virtually none. This is explained due to the small sensitivities to changes in the mean radii when compared to the sensitivities to changes in areas.

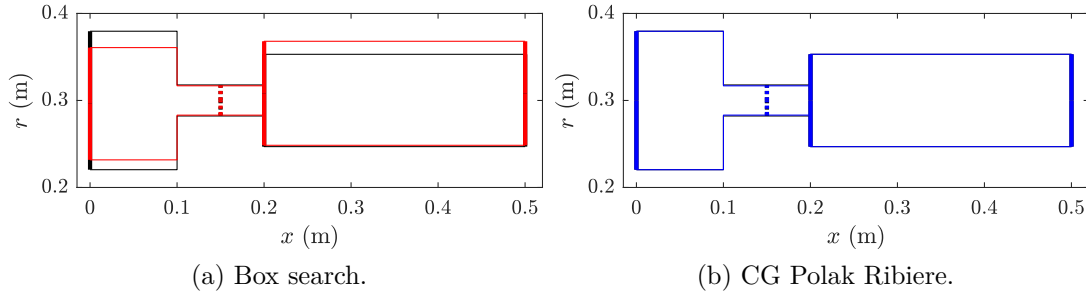


Fig. 6.9 Initial and final configuration of the LPP annular combustor after stabilizing all of the unstable modes by changing the areas and mean radii. The initial configuration is shown in black. The final configuration is shown in red for the box search algorithm and in blue for the CG algorithm.

Algorithm	Plenum	Premix ducts (inlet)	Premix ducts (outlet)	Combustion chamber
Areas: $(A/A_0 - 1)$				
Box Search	-0.1995	-0.1066	-0.1066	0.1577
CG PR	-0.0001	-0.1113	-0.1113	0.0009
Mean radii: $(R/R_0 - 1)$				
Box Search	-0.0125	0.0000	0.0000	0.0275
CG PR	-0.0000	0.0000	0.0000	0.0000

Table 6.5 Relative change of the final area/mean radius with respect to the initial area/mean radius of a section for case 2 in the stabilization of the LPP annular combustor.

Variations in areas and lengths

For the third case, variations in areas and lengths are allowed. The initial and final configurations can be seen in Fig. 6.10 and summarized in table 6.6. We observe a similar behaviour as that in case 2: the box search algorithm produces larger changes than the CG algorithm and the CG algorithm takes the same path as in the previous two cases. As in case 2 (variations in areas and mean radii) the changes in length are very small when compared to the changes in areas, especially in the CG routine.

Variations in areas, lengths and mean radii

For the fourth case, the areas, lengths and mean radii are allowed to change. The initial and final configurations are shown in Fig. 6.11 and the changes are summarized in table

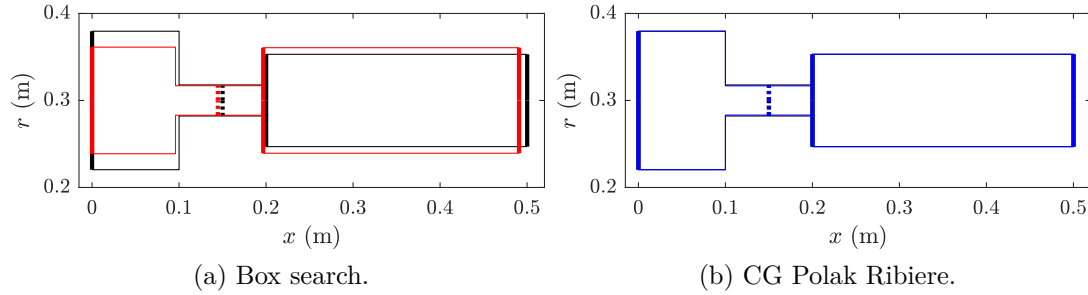


Fig. 6.10 Initial and final configuration of the LPP annular combustor after stabilizing all of the unstable modes by changing the areas and lengths. The initial configuration is shown in black. The final configuration is shown in red for the box search algorithm and in blue for the CG algorithm.

Algorithm	Plenum	Premix ducts (inlet)	Premix ducts (outlet)	Combustion chamber
Areas: $(A/A_0 - 1)$				
Box Search	-0.2300	-0.0956	-0.0956	0.1429
CG PR	-0.0002	-0.1124	-0.1124	0.0018
Lengths: $(L/L_0 - 1)$				
Box Search	-0.0410	-0.0264	0.0408	-0.0199
CG PR	-0.0001	0.0001	0.0000	0.0001

Table 6.6 Relative change of the final area/length with respect to the initial area/length of a section for case 3 in the stabilization of the LPP annular combustor.

6.7. The box search algorithm follows a path similar to a combination of cases 2 and 3 and the CG algorithm produces a similar configuration as in the previous three cases. This demonstrates, once again, the small magnitude in the sensitivities of the mean radius and lengths.

Variations in areas, lengths, mean radii and time delay.

The last case is similar to case 4 but the time delay is also allowed to change. This parameter is often associated with the fuel convection time in the injection process and is altered by changing the fuel injector. The initial and final configurations can be seen in Fig. 6.12 and the changes are summarized in table 6.8. Using a box search algorithm the overall changes are similar to those in case 4. The time delay only changes by 4.5 %

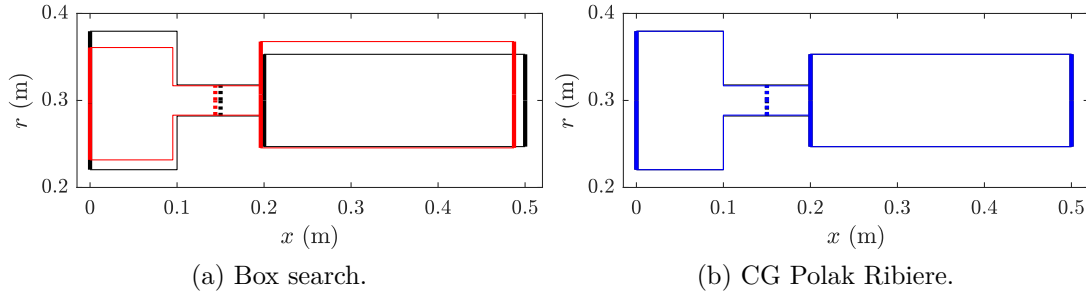


Fig. 6.11 Initial and final configuration of the LPP annular combustor after stabilizing all of the unstable modes by changing the areas, lengths and mean radii. The initial configuration is shown in black. The final configuration is shown in red for the box search algorithm and in blue for the CG algorithm.

Algorithm	Plenum	Premix ducts (inlet)	Premix ducts (outlet)	Combustion chamber
Areas: $(A/A_0 - 1)$				
Box Search	-0.1987	-0.1019	-0.1019	0.1769
CG PR	-0.0001	-0.1092	-0.1092	0.0009
Mean radii: $(R/R_0 - 1)$				
Box Search	-0.0124	0.0000	0.0000	0.0220
CG PR	-0.0000	0.0000	0.0000	0.0000
Lengths: $(L/L_0 - 1)$				
Box Search	-0.0491	-0.0229	0.0438	-0.0298
CG PR	-0.0001	0.0001	0.0000	0.0001

Table 6.7 Relative change of the final area/length/mean radius with respect to the initial area/length/mean radius of a section for case 4 in the stabilization of the LPP annular combustor.

(from 1.500×10^{-3} s to 1.567×10^{-3} s). This small change is explained by the fact that the algorithm takes into account how a change in the time delay also affects the stable eigenvalues, many of which are rendered less stable by changes that stabilize unstable modes (see Fig. 5.17). With a CG algorithm we observe a similar behaviour to that in case 4, but with slightly smaller changes in the geometric parameters (especially the area of the premix ducts) and a large change in the time delay. This change is explained due to the large magnitude in the sensitivity to changes in the time delay and the fact

that the CG algorithm does not take into account how the stable modes are affected by changing this parameter.

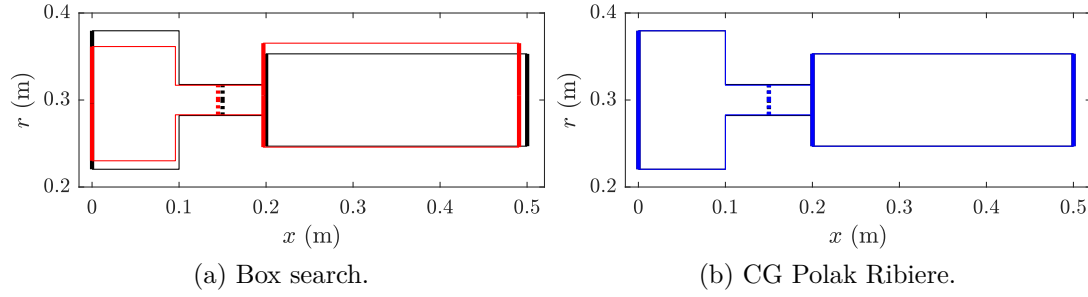


Fig. 6.12 Initial and final configuration of the LPP annular combustor after stabilizing all of the unstable modes by changing the areas, lengths, mean radii and time delay. The initial configuration is shown in black. The final configuration is shown in red for the box search algorithm and in blue for the CG algorithm.

Algorithm	Plenum	Premix ducts (inlet)	Premix ducts (outlet)	Combustion chamber
Areas: $(A/A_0 - 1)$				
Box Search	-0.1867	-0.0956	-0.0956	0.1469
CG PR	-0.0001	-0.0913	-0.0913	0.0009
Mean radii: $(R/R_0 - 1)$				
Box Search	-0.0140	0.0000	0.0000	0.0186
CG PR	-0.0000	0.0000	0.0000	0.0000
Lengths: $(L/L_0 - 1)$				
Box Search	-0.0420	-0.0203	0.0409	-0.0205
CG PR	-0.0001	0.0001	0.0001	0.0001
Time delay: $(\tau/\tau_0 - 1)$ at the heat source				
Box Search	0.0445			
CG PR	0.2619			

Table 6.8 Relative change of the final area/length/mean radius/time delay with respect to the initial area/length/mean radius/time delay of a section for case 5 in the stabilization of the LPP annular combustor.

We can draw some practical conclusions from the optimization routines in which many parameters can change. The first concerns the magnitude of the changes when more parameters are allowed to change. It may be intuitive to think that increasing the number of changeable parameters will decrease the magnitude of the required changes, given that there are more degrees of freedom available to the optimization routine. This is true sometimes but not always. The inclusion of another variable in the optimization routine changes the path that the algorithm takes to find a stable configuration. This new path can point in a direction that requires more changes in all of the parameters (as in most of the previous cases).

In terms of performance of the algorithms, the box search algorithm produces larger changes into the system, while the CG algorithm follows a similar path every time, unless a variable with a large sensitivity (the time delay) is introduced in the optimization routine.

For the LPP annular combustor, using a CG algorithm, the most prominent changes are to reduce the premix ducts area and to change the time delay. These are the same changes suggested for the stabilization of the longitudinal combustor.

6.3.3 Stabilizing the CUED annular combustor

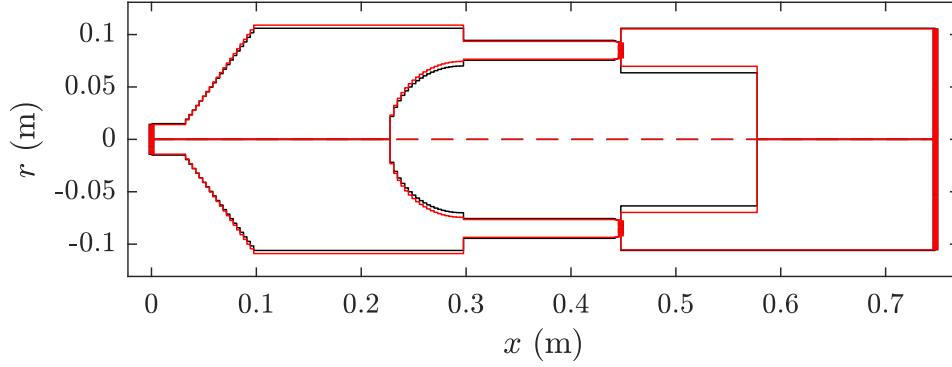
The last configuration to be stabilized is the CUED annular combustor. Given that it is unstable for high azimuthal wave numbers ($|n| = 8$) the optimization routine is run considering only the positive values of n to speed up the computations. That is, we consider $n = 0, 1, 2, \dots, 8$. Then given that we are not introducing modal coupling, the symmetric nature of the eigenvalues ensures that all azimuthal wave numbers $|n| \leq 8$ are stabilized. By looking only at positive values of n , the path taken by the optimization routine changes, but the desired outcome (stability) does not. We examine the following cases:

- Variations in areas and mean radii.
- Variations in areas, mean radii and lengths.

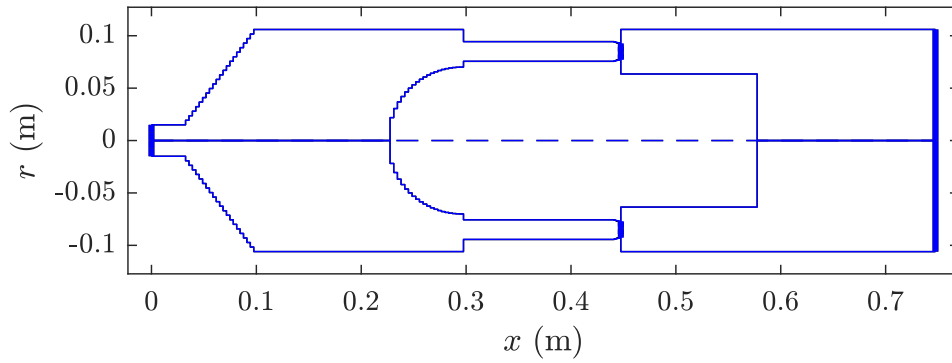
Variations in areas and mean radii

The initial and final configurations are shown in Fig. 6.13 and the changes in each of the sections are summarized in table 6.9. For the box search algorithm the largest changes are in the flame holder area, which increased 26% followed by a decrease in the premix ducts area of 18.9%. The rest of the configuration undergoes comparable changes in both

areas and mean radii in almost all of the sections. Using a CG algorithm the largest change is found in the flame holder area which increases by 30.6%, followed by a small decrease of 2.8% in the premix ducts area, while the rest of the configuration changes only slightly.



(a) Box search.



(b) CG Polak Ribiere.

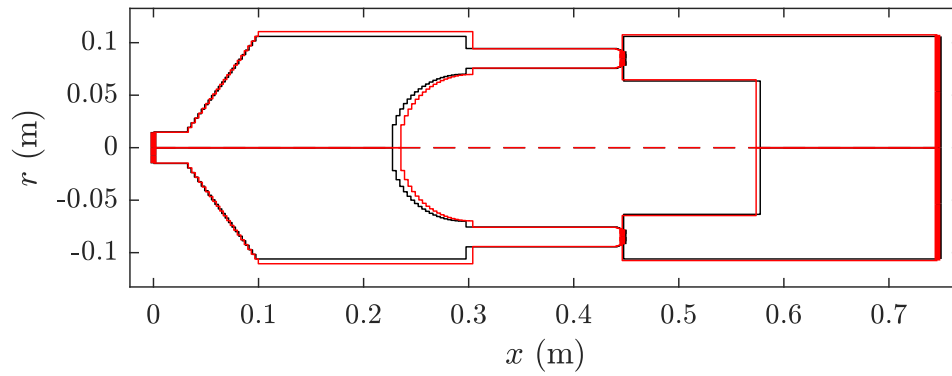
Fig. 6.13 Initial and final configuration of CUED annular combustor after stabilizing all of the unstable modes by changing the areas and mean radii. The initial configuration is shown in black. The final configuration is shown in red for the box search algorithm and in blue for the CG algorithm.

Variations in areas, mean radii and lengths

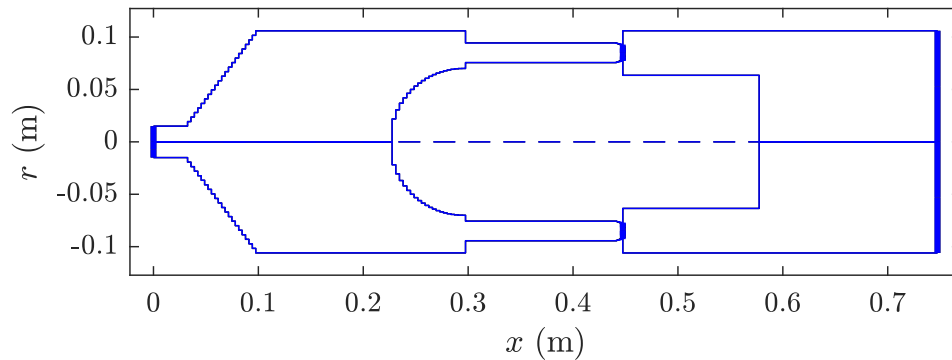
For the last case the areas, lengths and mean radii are allowed to change. The initial and final configurations are shown in Fig. 6.14 and the changes are summarized in table 6.10. With the introduction of the length as an optimization variable the box search algorithm reduces the changes required in the flame holder area to an increase of 10% and now the dominant change is at the sphere end, which increases by 16.2%. The CG algorithm behaves almost the same as in the previous case.

Algorithm	Inlet duct	Plenum	Sphere end	Premix ducts	Flame holder	Combustion chamber	Outlet duct
Areas: $(A/A_0 - 1)$							
Box Search	-0.1133	0.0574	0.0026	-0.1889	0.2598	-0.1328	-0.0114
CG PR	0.0014	-0.0018	-0.0044	-0.0275	0.3058	0.0000	0.0000
Mean radii: $(R/R_0 - 1)$							
Box Search	-0.0583	0.0283	0.0418	0.0000	0.0000	0.0331	-0.0057
CG PR	0.0007	-0.0009	-0.0002	0.0000	0.0000	0.0000	0.0000

Table 6.9 Relative change of the final area/mean radius with respect to the initial area/mean radius of a section for case 1 in the stabilization of the CUED annular combustor.



(a) Box search.



(b) CG Polak Ribiere.

Fig. 6.14 Initial and final configuration of CUED annular combustor after stabilizing all of the unstable modes by changing the areas, mean radii and lengths. The initial configuration is shown in black. The final configuration is shown in red for the box search algorithm and in blue for the CG algorithm.

Algorithm	Inlet duct	Area increase	Plenum	Sphere end	Premix ducts	Area decrease	Flame holder	Combustion chamber	Outlet duct
Areas: $(A/A_0 - 1)$									
Box Search	-0.0407	–	0.0877	0.1616	-0.0550	–	0.0996	0.0241	0.0287
CG PR	0.0014	–	-0.0017	-0.0043	-0.0279	–	0.3057	0.0000	0.0000
Mean radii: $(R/R_0 - 1)$									
Box Search	-0.0206	–	0.0429	0.0243	0.0000	–	0.0000	0.0157	0.0142
CG PR	0.0007	–	-0.0009	-0.0002	0.0000	–	0.0000	0.0000	0.0000
Lengths: $(L/L_0 - 1)$									
Box Search	0.0207	0.0251	0.0439	-0.0231	-0.0529	-0.0220	–	-0.0197	0.0151
CG PR	0.0001	0.0001	0.0001	-0.0007	-0.0002	-0.0060	–	-0.0000	0.0000

Table 6.10 Relative change of the final area/length/mean radius with respect to the initial area/length/mean radius of a section for case 2 in the stabilization of the CUED annular combustor.

6.3.4 Summary of optimization results

In summary, three thermoacoustic systems are stabilized by making small changes to their geometric parameters. Two different algorithms are used: a box search algorithm and a CG algorithm. The box search algorithm allows any parameter to change within some percentage of their current magnitude. With this algorithm, the configurations require large changes to achieve stability. The CG algorithm follows a direction close to the steepest descent direction. This produces configurations that require significantly less changes in order to become stable.

Using a CG algorithm the most influential changes required to achieve stability in all the configurations are:

1. The reduction of the neck or premix ducts area.
2. Modification of the FTF parameters.
 - (a) In the case of the longitudinal combustor and the CUED annular combustor a change in the flame holder area.
 - (b) In the case of the LPP annular combustor an increase in the time delay.

Point 2a is explained because the flame holder area is proportional to the time delay of the FTF as can be seen in the nondimensional frequencies of Eqs. (A.12) and (A.13). In general the geometric changes done during the optimization process de-phase the

unsteady heat release from the pressure fluctuations enough such that the work done at the boundaries is larger than the work done by the heat source. This basically ensures that the Rayleigh criterion for instabilities Eq. (1.2) is not met.

Chapter 7

Conclusions and future work

In this thesis the low order network modelling approach to analyse thermoacoustic systems is reviewed. Then adjoint methods are developed in order to extract gradients of the eigenvalue with respect to system parameters. Using gradients, systems are stabilized with various optimization algorithms. The outcome of this thesis is the generation of PILOT, a low order thermoacoustic tool with adjoint-based sensitivity analysis and optimization.

In chapter 2 the wave-based low order network model of [Stow and Dowling \(2001, 2003, 2004\)](#) is presented as a tool to analyse linear thermoacoustic oscillations. The main components are straight ducts, which propagate acoustic, entropy and vorticity waves. These are connected with different sets of jump conditions to represent a full combustion system. The network model produces a nonlinear eigenvalue problem from which the frequencies, stabilities and modeshapes can be studied. Due to its modularity and the possibility of including a mean flow, these models are very versatile, much more so than Galerkin methods. The major disadvantage of this approach is that it only works with frequencies low enough such that the radial or transverse modes are cut off in the ducts and with area changes and heat sources which span over a distance short enough such that they can be considered acoustically compact.

Low order network models are computationally fast, and are used in industry and academia.

Chapter 3 presents five different configurations: the Rijke tube, a choked combustor, a longitudinal combustor, a generic LPP annular combustor and the laboratory scale annular combustor built in CUED. Each is modelled using the low order network tool from chapter 2 and their stability is examined. Due to the small number of elements in the configuration of the Rijke tube and the choked combustor, their nonlinear eigenvalue

problems are explicitly derived. Then the modeshapes of the dominant eigenvalue are investigated. For the longitudinal combustor a FTF that mimics the real flame is derived. Stability analysis shows an unstable mode with a frequency close to the one in which the burner is observed to saturate into a limit cycle. The generic LPP annular combustor introduces an azimuthal direction in the configuration. This is examined using wave numbers larger than 0. Stability analysis shows two unstable modes: one corresponding to a longitudinal mode and the other to a helical mode. The CUED combustor is modelled using another FTF and stability analysis shows a handful of unstable modes. The dominant eigenvalue corresponds to a helical mode with a frequency close to the one observed in experiments. Despite the simplicity of the modelling approach, these models are able to predict the stability of the real configurations and assist the investigation on how to mitigate them. Further development of these configurations requires more elaborate FTFs and boundary conditions to be included in the longitudinal combustor (Graham, 2012) and the CUED annular combustor. This will provide the model with a more accurate description of the flame dynamics and therefore aid in the prediction of the unstable modes.

Chapter 4 is devoted to the development of adjoint methods in wave based approaches. For the nonlinear eigenvalue problem obtained using the tools from chapter 2 there exists a corresponding adjoint eigenvalue problem. This is derived using a continuous or a discrete method.

In the continuous approach, the adjoint equations are derived by a Lagrangian formalism. Using the Rijke tube as a worked example, we mathematically show that the adjoint variables are governed by a wave equation. The adjoint equations are then solved in the same way as the direct equations, by obtaining the eigenvalues and right eigenvectors of the adjoint matrix. In the discrete approach, the adjoint eigenvector is simply the left eigenvector of the direct matrix. For the wave-based model in this thesis, the continuous approach provides greater physical understanding in terms of receptivity because the adjoint spatial functions are known.

This analysis shows that the equations governing duct acoustics, without considering boundary conditions, are self-adjoint. We also show that the system with no unsteady heat release and reflection coefficients with magnitude different from 1 is self-adjoint under the transformation $t \rightarrow -t$, which is equivalent to saying that forward-propagating waves become backward-propagating waves and vice versa. The thermoacoustic system becomes non-self-adjoint when there is velocity-coupled unsteady heat release, in agreement with findings available in the literature.

Finally, we derive the continuous adjoint equations for both unsteady and steady flows for all the modules presented in chapter 2.

In chapter 5 sensitivity analysis of the thermoacoustic configurations is performed. By combining the eigenfunctions from the direct and adjoint systems, we obtain the base state sensitivities and feedback sensitivities of the different configurations. When a change in the base state variable does not modify the base flow its sensitivity is easier to implement with the discrete approach. Otherwise the continuous approach is preferred. The feedback sensitivity is easier to implement with the continuous approach. Both adjoint methods provide the same results, which are validated against finite-difference calculations.

The base state sensitivity provides the gradient of the eigenvalue with respect to any parameter of the model in a single calculation. Hence, it reveals how to make eigenvalues more or less stable. The feedback sensitivity provides the gradient of the eigenvalue with respect to linear feedback mechanisms. In this paper, it is obtained for co-located sensors and actuators.

The base state sensitivity analysis of the Rijke tube and the choked combustor shows that, as expected, the most influential stability parameter is the time delay between velocity and heat release.

Feedback sensitivity analysis is carried out in the Rijke tube and the choked combustor showing the influence of the devices that react to pressure, velocity and density fluctuations and force the mass, momentum or energy equations. The optimal position to locate a feedback device is given by the product of the direct and adjoint eigenfunctions. In a self-adjoint system, the adjoint eigenfunction is identical to the direct eigenfunction, so the optimal position can be determined from the direct eigenfunctions alone. In a non-self-adjoint system, however, the adjoint eigenfunction differs from the direct eigenfunction and the optimal placement is altered accordingly. This needs to be taken into account in thermoacoustic systems, which are non-self-adjoint. For example, this information can aid the design of retrofitted devices such as Helmholtz resonators.

The low Mach number Rijke tube model is improved by estimating parameters from experimental data. Then feedback sensitivity analysis is performed to study the effects of (i) a drag device and (ii) a secondary heat source. These results are compared with the experimental results in [Jamieson and Juniper \(2017b\)](#). For the drag device, unsteady feedback analysis is able to predict qualitatively the growth rate shift observed in experiments. The frequency shift, however, is 3 orders of magnitude different from that found in the experiment. Nonetheless the results still show the correct trend with varying mesh position. For the secondary heat source the inclusion of the base flow feedback

sensitivity predicts qualitatively and quantitatively the growth rate and frequency shifts observed in experiments. All discrepancies arise from the modelling approach and not from the adjoint method. The model imposes a fixed velocity at the inlet, while the experiment is driven by bouyancy.

Base state sensitivity analysis of geometric parameters is performed on three configurations: the longitudinal combustor, the LPP annular combustor and the CUED annular combustor. The most sensitive geometric parameter is the cross-sectional area of each duct, mainly due to its influence on the base flow. Where a FTF is used, the flame holder area has the largest sensitivity. In all the configurations the second most influential parameter is the neck area in the longitudinal combustor or the premix ducts area in the annular combustors.

Chapter 6 presents two optimization algorithms to stabilize thermoacoustic configurations: the box search algorithm and the conjugate gradient algorithm. The box search algorithm stabilizes a configuration by changing every parameter that makes the system more stable by a given percentage. Depending on the number of unstable modes, this algorithm tends to cause large changes to parameters. The conjugate gradient algorithm stabilizes a configuration following a direction close to the steepest descent direction. This algorithm produces large changes in a reduced number of parameters, leaving the least sensitive parameters almost untouched. Most of the predictions from the sensitivity analysis in the initial configurations are observed in the final and stable configurations. The reduction of the neck or premix ducts area and the flame holder area are the most common changes that promote the stability of the analysed thermoacoustic systems, because the fluctuating heat release reduces when the mean flow velocity before the heat source increases. When the system is not very unstable as with the LPP annular combustor, only small changes are required and, by employing a global optimization routine, it is likely that a stable configuration could be found with even smaller changes than the ones showed in this thesis. These proposed changes are preferable to the addition of passive devices such as Helmholtz resonators, which add weight, cost, and complexity.

Adjoint-based sensitivity analysis and optimization could become an indispensable tool for the design of thermoacoustically-stable combustors. It is easy to add other constraints, either by adapting the cost function or by preventing the algorithm from entering regions of the design space.

Thermoacoustic systems can be stabilized with small geometry modifications because thermoacoustic oscillations are very sensitive to small changes. This also means that any model of a system is severely prone to systematic error in the measurement of its parameters. It is useful that adjoint-based sensitivity analysis reveals the most influential

parameters. This also highlights, however, that experiments are required to ensure that the model, on which the sensitivity analysis is based, is an accurate description of reality.

7.1 Future work

In order to get a better representation of the physics behind the low order modelling approach, further development of the network modules is required. Some recommendations are the development of better approximations of the current modules and boundary conditions or the inclusion of new elements such as the compositional waves developed in [Magri et al. \(2016c\)](#) for the study of indirect noise. To obtain better predictions, data driven analysis is required to find the optimal model parameters that fit these models. By applying statistical methods to low order thermoacoustic models: state estimation, parameter estimation and model assessment is being performed. These improvements allow for a more accurate prediction of the stability of the system and thus of the sensitivity analysis of real configurations.

In terms of global optimization, the question arises of which of the many stable configurations is best. To correctly assess this question, a robustness analysis is required. There are configurations which require little changes to become stable but that become unstable with small variations. On the other hand, there are configurations that require large changes to become stable but that are less sensitive to small variations. From a manufacturing and operational perspective the latter configuration would be more advisable. Therefore, the condition to find a stable configuration might not be enough. Instead the aim should be to obtain a stable configuration with small gradients such that the variations that might appear, for example, due to manufacturing processes, will not cause the system to be unstable. Essentially this requires the combination of adjoint methods with uncertainty quantification ([Magri et al., 2016b](#)).

These methods can be extended to Helmholtz solvers, which can analyse complex geometries. On numerical modelling, a Helmholtz solver which aims to solve the inhomogeneous wave equation and by means of adjoint methods assess the sensitivity of thermoacoustic systems is under development. This model includes the sensitivity of the surfaces of the domain, which is required to perform shape optimization. This modelling approach should be able to provide direct comparison to the results presented in this thesis at low Mach number, and extend to more complex geometries.

Finally, on the experimental side, we suggest development of a modular burner with simple laminar flames for which the FTFs are well known. Once the optimization has

been carried out, different duct sizes could be tested on the burner to experientially demonstrate its stabilization.

References

- Aguilar, J. G. (2015). Sensitivity analysis in low order thermoacoustic networks. Technical Report December, University of Cambridge. (Cited on pages [51](#) and [76](#).)
- Aguilar, J. G. and Juniper, M. P. (2018a). Adjoint methods for elimination of thermoacoustic oscillations in a model annular combustor via small geometry modifications. *Proceedings of ASME Turbo Expo 2018: Turbomachinery Technical Conference and Exposition*. (Cited on pages [31](#) and [48](#).)
- Aguilar, J. G. and Juniper, M. P. (2018b). Shape optimization in low-order thermoacoustic networks. In *Proceedings of GPPS Forum 18*. (Cited on pages [31](#) and [48](#).)
- Aguilar, J. G., Magri, L., and Juniper, M. P. (2017). Adjoint-based sensitivity analysis of low-order thermoacoustic networks using a wave-based approach. *Journal of Computational Physics*, 341:163–181. (Cited on pages [31](#), [48](#), and [75](#).)
- Balachandran, R. (2005). *Experimental Investigation of the Response of Turbulent Premixed Flames to Acoustic Oscillations*. PhD thesis, University of Cambridge. (Cited on pages [12](#), [31](#), [37](#), [38](#), [39](#), and [154](#).)
- Balachandran, R., Ayoola, B., Kaminski, C., Dowling, A., and Mastorakos, E. (2005). Experimental investigation of the nonlinear response of turbulent premixed flames to imposed inlet velocity oscillations. *Combustion and Flame*, 143(1-2):37–55. (Cited on page [31](#).)
- Balachandran, R., Dowling, A. P., and Mastorakos, E. (2008). Non-linear response of turbulent premixed flames to imposed inlet velocity oscillations of two frequencies. *Flow, Turbulence and Combustion*, 80(4):455–487. (Cited on page [31](#).)
- Bauerheim, M. (2014). *Étude théorique et numérique des effets de brisures de symétrie sur les modes thermo-acoustiques azimuthaux dans les chambres annulaires*. (Theoretical and numerical study of symmetry breaking effects on azimuthal thermoacoustic modes in annular combustors. PhD thesis, Institut National Polytechnique de Toulouse. (Cited on page [153](#).)
- Bauerheim, M., Nicoud, F., and Poinso, T. (2015a). Theoretical analysis of the mass balance equation through a flame at zero and non-zero mach numbers. *Combustion and Flame*, 162(1):60–67. (Cited on page [26](#).)
- Bauerheim, M., Staffellbach, G., Worth, N. A., Dawson, J. R., Gicquel, L. Y., and Poinso, T. (2015b). Sensitivity of LES-based harmonic flame response model for turbulent

- swirled flames and impact on the stability of azimuthal modes. *Proceedings of the Combustion Institute*, 35(3):3355–3363. (Cited on pages 42, 44, and 45.)
- Bellucci, V., Schuermans, B., Nowak, D., Flohr, P., and Paschereit, C. O. (2005). Thermoacoustic Modeling of a Gas Turbine Combustor Equipped With Acoustic Dampers. *Journal of Turbomachinery*, 127(2):372. (Cited on pages 5 and 16.)
- Bloxside, G. J., Dowling, A. P., and Langhorne, P. J. (1988). Reheat buzz: an acoustically coupled combustion instability. Part 2. Theory. *Journal of Fluid Mechanics*, 193:445–473. (Cited on page 22.)
- Bothien, M. R. (2008). *Impedance Tuning : A Method for Active Control of the Acoustic Boundary Conditions of Combustion Test Rigs*. PhD thesis, Technische Universität Berlin. (Cited on page 16.)
- Bothien, M. R., Noiray, N., and Schuermans, B. (2013). A Novel Damping Device for Broadband Attenuation of Low-Frequency Combustion Pulsations in Gas Turbines. *Journal of Engineering for Gas Turbines and Power*, 136(4):041504. (Cited on pages 9 and 16.)
- Boyd, S. and Vandenberghe, L. (2010). *Convex Optimization*. Cambridge University Press, Cambridge, 1st edition. (Cited on pages 109 and 111.)
- Caeiro, F., Sovardi, C., Förner, K., and Polifke, W. (2017). Shape optimization of a Helmholtz resonator using an adjoint method. *International Journal of Spray and Combustion Dynamics*, 9(4):394–408. (Cited on page 11.)
- Cargill, A. M. (1982). Low frequency acoustic radiation from a jet pipe - a second order theory. *Journal of Sound and Vibration*, 83(3):339–354. (Cited on page 25.)
- Cho, J. H. and Lieuwen, T. C. (2003). Modeling the Response of Premixed Flames to Mixture Ratio Perturbations. In *Volume 2: Turbo Expo 2003*, number January 2003, pages 67–76. ASME. (Cited on page 152.)
- Chu, B. T. (1956). Stability of systems containing a heat source: the Rayleigh criterion. (Cited on pages 3 and 22.)
- Chu, B.-T. (1965). On the energy transfer to small disturbances in fluid flow (Part I). *Acta Mechanica*, 1(3):215–234. (Cited on page 3.)
- Chu, B.-T. and Kovásznyai, L. S. G. (1958). Non-linear interactions in a viscous heat-conducting compressible gas. (Cited on page 4.)
- Connor, J. O., Worth, N. A., and Dawson, J. R. (2013). Circumferential Instability in a Model Annular Gas Turbine. *ASME Turbo Expo*, pages 1–15. (Cited on page 42.)
- Crocco, L. (1969). Research on combustion instability in liquid propellant rockets. *Symposium (International) on Combustion*, 12(1):85–99. (Cited on page 23.)
- Crocco, L. and Cheng, S.-I. (1956). *Theory of Combustion Instability in Liquid Propellant Rocket Motors*. Published for and on behalf of the Advisory Group for Aeronautical Research and Development, North Atlantic Treaty Organization by Butterworths Scientific Publications. (Cited on page 6.)

- Culick, F. E. C. (1988). Combustion instabilities in liquid-fueled propulsion systems - an overview. *AGARD Conference on Combustion Instabilities in Liquid-Fueled Propulsion Systems*, 450(450):1. (Cited on page 5.)
- Culick, F. E. C. (2006). *Unsteady motions in combustion chambers for propulsion systems*, volume 323. RTO AGARDograph/AG-AVT-039. North Atlantic Treaty Organization (NATO). (Cited on page 2.)
- Dawson, J. R. and Worth, N. a. (2013). Flame dynamics and unsteady heat release rate of self-excited azimuthal modes in an annular combustion chamber. *submitted to Combustion and Flame*, 161(10):2565–2578. (Cited on page 42.)
- Dowling, A. P. (1995). The calculation of thermoacoustic oscillations. *Journal of Sound and Vibration*, 180(4):557–581. (Cited on pages 5, 6, 26, and 92.)
- Dowling, A. P. (1997). Nonlinear self-excited oscillations of a ducted flame. *Journal of Fluid Mechanics*, 346:271–290. (Cited on page 6.)
- Dowling, a. P. (1999). A kinematic model of a ducted flame. *Journal of Fluid Mechanics*, 394:51–72. (Cited on pages xvii, 6, 149, and 150.)
- Dowling, A. P. and Hubbard, S. (2000). Instability in lean premixed combustors. *Proceedings of the Institution of Mechanical Engineers, Part A: Journal of Power and Energy*, 214(4):317–332. (Cited on pages 149 and 153.)
- Dowling, A. P. and Mahmoudi, Y. (2015). Combustion noise. *Proceedings of the Combustion Institute*, 35(1):65–100. (Cited on pages 4 and 16.)
- Dowling, A. P. and Morgans, A. S. (2005). Feedback control of combustion oscillations. *Annual Review of Fluid Mechanics*, 37(1):151–182. (Cited on pages 7 and 8.)
- Dowling, A. P. and Stow, S. R. (2003). Acoustic analysis of gas turbine combustors. *Journal of Propulsion and Power*, 19(5):751–764. (Cited on pages 16, 17, and 26.)
- Ducruix, S., Durox, D., and Candel, S. (2000). Theoretical and experimental determinations of the transfer function of a laminar premixed flame. *Proceedings of the Combustion Institute*, 28(1):765–773. (Cited on page 149.)
- Evesque, S. and Polifke, W. (2002). Low-Order Acoustic Modelling for Annular Combustors: Validation and Inclusion of Modal Coupling. In *Volume 1: Turbo Expo 2002*, number February, pages 321–331. ASME. (Cited on page 21.)
- Fleifil, M., Annaswamy, A. M., Ghoneim, Z. A., and Ghoniem, A. F. (1996). Response of a laminar premixed flame to flow oscillations: A kinematic model and thermoacoustic instability results. *Combustion and Flame*, 106(4):487–510. (Cited on page 149.)
- Fosas de Pando, M., Schmid, P. J., and Sipp, D. (2017). On the receptivity of aerofoil tonal noise: an adjoint analysis. *Journal of Fluid Mechanics*, 812:771–791. (Cited on page 10.)
- Freund, J. B. (2011). Adjoint-based optimization for understanding and suppressing jet noise. *Journal of Sound and Vibration*, 330(17):4114–4122. (Cited on page 10.)

- Ghirardo, G. and Juniper, M. P. (2013). Azimuthal instabilities in annular combustors: standing and spinning modes. *Proceedings of the Royal Society A: Mathematical, Physical and Engineering Sciences*, 469(2157):20130232–20130232. (Cited on page 6.)
- Giannetti, F. and Luchini, P. (2007). Structural sensitivity of the first instability of the cylinder wake. *Journal of Fluid Mechanics*, 581:167. (Cited on pages 9 and 75.)
- Giauque, A., Huet, M., Clero, F., Ducruix, S., and Richecoeur, F. (2013). Thermoacoustic Shape Optimization of a Subsonic Nozzle. *Journal of Engineering for Gas Turbines and Power*, 135(10):102601. (Cited on page 11.)
- Goh, C. S. and Morgans, A. S. (2013). The influence of entropy waves on the thermoacoustic stability of a model combustor. *Combustion Science and Technology*, 185(2):249–268. (Cited on page 34.)
- Graham, O. S. (2012). *Modelling the thermoacoustic response of premixed flames*. PhD thesis, University of Cambridge. (Cited on pages 132, 149, and 151.)
- Gunzburger, M. (1997). Inverse design and optimisation methods. Introduction into mathematical aspects of flow control and optimization. In *von Karman Institute for Fluid Dynamics, Lecture Series 1997-05*. (Cited on page 49.)
- Han, X., Li, J., and Morgans, A. S. (2015). Prediction of combustion instability limit cycle oscillations by combining flame describing function simulations with a thermoacoustic network model. *Combustion and Flame*, 162(10):3632–3647. (Cited on pages 16 and 38.)
- Higgins, B. (1802). On the sound produced by a current of hydrogen gas passing through a tube. *Journal of Natural Philosophy, Chemistry and the Arts*, 1:129–131. (Cited on page 2.)
- Hill, D. C. (1992). A theoretical approach for analyzing the restabilization of wakes. In *Presented at AIAA Aersopce Science Meeting Exhib. 30th, Reno, NV, AIAA Pap.*, volume 0067. (Cited on page 9.)
- Huang, Y. and Yang, V. (2009). Dynamics and stability of lean-premixed swirl-stabilized combustion. *Progress in Energy and Combustion Science*, 35(4):293–364. (Cited on page 7.)
- Hubbard, S. and Dowling, A. (1998). Acoustic instabilities in premix burners. In *4th AIAA/CEAS Aeroacoustics Conference*, Reston, Virigina. American Institute of Aeronautics and Astronautics. (Cited on pages xvii, 149, and 154.)
- Ihme, M. (2017). Combustion and Engine-Core Noise. *Annual Review of Fluid Mechanics*, 49(1):277–310. (Cited on page 4.)
- Jameson, A. (1995). Optimum aerodynamic design using CFD and control theory. (Cited on pages 10 and 47.)
- Jamieson, N. P. and Juniper, M. P. (2017a). Experimental Sensitivity Analysis and the Equivalence of Pulsed Forcing and Feedback Control in Thermoacoustic Systems. In *Volume 4A: Combustion, Fuels and Emissions*, page V04AT04A035. ASME. (Cited on page 11.)

- Jamieson, N. P. and Juniper, M. P. (2017b). Experimental sensitivity analysis of a linearly stable thermoacoustic system via a pulsed forcing technique. *Experiments in Fluids*, 58(9):1–12. (Cited on pages 11, 90, 92, 93, 96, and 133.)
- Jamieson, N. P., Rigas, G., and Juniper, M. P. (2017). Experimental sensitivity analysis via a secondary heat source in an oscillating thermoacoustic system. *International Journal of Spray and Combustion Dynamics*, 0(0):1–11. (Cited on pages xix, 11, and 94.)
- Jankovic, M. S. (1988). Analytical solutions for the n th derivatives of eigenvalues and eigenvectors for a nonlinear eigenvalue problem. *AIAA Journal*, 26(2):204–205. (Cited on page 79.)
- Johnson, C. E., Neumeier, Y., Neumaier, M., Zinn, B. T., Darling, D. D., and Sattinger, S. S. (2001). Demonstration of Active Control of Combustion Instabilities on a Full-Scale Gas Turbine Combustor. In *Volume 2: Coal, Biomass and Alternative Fuels; Combustion and Fuels; Oil and Gas Applications; Cycle Innovations*, page V002T02A062. ASME. (Cited on page 8.)
- Jomaas, G., Zheng, X., Zhu, D., and Law, C. (2005). Experimental determination of counterflow ignition temperatures and laminar flame speeds of C2–C3 hydrocarbons at atmospheric and elevated pressures. *Proceedings of the Combustion Institute*, 30(1):193–200. (Cited on page 152.)
- Juniper, M. P. (2011). Triggering in the horizontal Rijke tube: non-normality, transient growth and bypass transition. *Journal of Fluid Mechanics*, 667:272–308. (Cited on page 10.)
- Juniper, M. P., Hanifi, A., and Theofilis, V. (2014). Modal Stability Theory. *Applied Mechanics Reviews*, 66(2):021004. (Cited on page 7.)
- Juniper, M. P. and Sujith, R. I. (2018). Sensitivity and Nonlinearity of Thermoacoustic Oscillations. *Annual Review of Fluid Mechanics*, 50(1):661–689. (Cited on pages 11, 107, and 111.)
- Keller, J. J. (1995). Thermoacoustic oscillations in combustion chambers of gas turbines. *AIAA Journal*, 33(12):2280–2287. (Cited on page 6.)
- Krüger, U., Hüren, J., Hoffmann, S., Krebs, W., and Bohn, D. (1999). Prediction of Thermoacoustic Instabilities with Focus on the Dynamic Flame Behavior for the 3A-Series Gas Turbine of Siemens KWU. *ASME Paper 99-GT-111*, pages 1–11. (Cited on page 15.)
- Langhorne, P. J. (1988). Reheat buzz: an acoustically coupled combustion instability. Part 1. Experiment. *Journal of Fluid Mechanics*, 193(-1):417. (Cited on page 149.)
- Levine, H. and Schwinger, J. (1948). On the radiation of sound from an unflanged circular pipe. *Physical Review*, 73(4):383–406. (Cited on page 25.)
- Li, J. and Morgans, A. S. (2016). Simplified models for the thermodynamic properties along a combustor and their effect on thermoacoustic instability prediction. *Fuel*, 184:735–748. (Cited on page 19.)

- Li, J., Xia, Y., Morgans, A. S., and Han, X. (2017). Numerical prediction of combustion instability limit cycle oscillations for a combustor with a long flame. *Combustion and Flame*, 185:28–43. (Cited on page 16.)
- Lieuwen, T. (2003). Modeling premixed combustion-acoustic wave interactions: A review. *Journal of Propulsion and Power*, 19(5):765–781. (Cited on page 6.)
- Lieuwen, T. (2005). Nonlinear kinematic response of premixed flames to harmonic velocity disturbances. *Proceedings of the Combustion Institute*, 30(2):1725–1732. (Cited on pages xv and 29.)
- Lieuwen, T., Torres, H., Johnson, C., and Zinn, B. T. (2001). A Mechanism of Combustion Instability in Lean Premixed Gas Turbine Combustors. *Journal of Engineering for Gas Turbines and Power*, 123(1):182. (Cited on page 2.)
- Lieuwen, T. and Zinn, B. T. (2000). Application of Multipole Expansions To Sound Generation From Ducted Unsteady Combustion Processes. *Journal of Sound and Vibration*, 235(3):405–414. (Cited on page 5.)
- Lieuwen, T. C. and Yang, V., editors (2005). *Combustion instabilities in gas turbine engines: operational experience, fundamental mechanisms, and modeling*. AIAA. (Cited on pages 2, 8, and 36.)
- Lieuwen, T. C. and Yang, V. (2013). *Gas Turbine Emissions*. Cambridge University Press. (Cited on page 107.)
- Lipatnikov, A. N. and Chomiak, J. (2002). Turbulent flame speed and thickness: Phenomenology, evaluation, and application in multi-dimensional simulations. *Progress in Energy and Combustion Science*, 28(1):1–74. (Cited on page 152.)
- Luchini, P. and Bottaro, A. (2014). Adjoint Equations in Stability Analysis. *Annual Review of Fluid Mechanics*, 46(1):493–517. (Cited on pages 9, 10, 47, and 87.)
- Luchini, P., Giannetti, F., and Pralits, J. (2009). Structural Sensitivity of the Finite-Amplitude Vortex Shedding Behind a Circular Cylinder. In Braza, M. and Hourigan, K., editors, *IUTAM Symposium on Unsteady Separated Flows and their Control*, pages 151–160, New York. Springer. (Cited on page 10.)
- Magri, L. (2015). *Adjoint methods in thermo-acoustic and combustion instability*. PhD thesis. (Cited on page 79.)
- Magri, L., Bauerheim, M., and Juniper, M. P. (2016a). Stability analysis of thermo-acoustic nonlinear eigenproblems in annular combustors. Part I. Sensitivity. *Journal of Computational Physics*, 325:395–410. (Cited on pages 11 and 79.)
- Magri, L., Bauerheim, M., Nicoud, F., and Juniper, M. P. (2016b). Stability analysis of thermo-acoustic nonlinear eigenproblems in annular combustors. Part II. Uncertainty quantification. *Journal of Computational Physics*, 325:411–421. (Cited on pages 11 and 135.)

- Magri, L. and Juniper, M. P. (2013a). A Theoretical Approach for Passive Control of Thermoacoustic Oscillations: Application to Ducted Flames. *Journal of Engineering for Gas Turbines and Power*, 135(9):091604. (Cited on page 11.)
- Magri, L. and Juniper, M. P. (2013b). Sensitivity analysis of a time-delayed thermoacoustic system via an adjoint-based approach. *Journal of Fluid Mechanics*, 719:183–202. (Cited on pages 10, 53, 75, and 89.)
- Magri, L. and Juniper, M. P. (2014a). Adjoint-based linear analysis in reduced-order thermo-acoustic models. *International Journal of Spray and Combustion Dynamics*, 6(3):225–246. (Cited on pages 11, 51, 87, and 89.)
- Magri, L. and Juniper, M. P. (2014b). Global modes, receptivity, and sensitivity analysis of diffusion flames coupled with duct acoustics. *Journal of Fluid Mechanics*, 752(1):237–265. (Cited on page 11.)
- Magri, L., O’Brien, J., and Ihme, M. (2016c). Compositional inhomogeneities as a source of indirect combustion noise. *Journal of Fluid Mechanics*, 799:R4. (Cited on pages 4 and 135.)
- Mangesius, H. and Polifke, W. (2011). A discrete-time, state-space approach for the investigation of non-normal effects in thermoacoustic systems. *International Journal of Spray and Combustion Dynamics*, 3(4):331–350. (Cited on page 53.)
- Marble, F. and Candel, S. (1977). Acoustic disturbance from gas non-uniformities convected through a nozzle. *Journal of Sound and Vibration*, 55(2):225–243. (Cited on pages 4, 24, and 34.)
- Marino, L. and Luchini, P. (2009). Adjoint analysis of the flow over a forward-facing step. *Theoretical and Computational Fluid Dynamics*, 23(1):37–54. (Cited on page 10.)
- Markstein, G. H. (1964). *Unsteady flame propagation*. Pergamon Press, Oxford, England. (Cited on page 149.)
- Marquet, O., Sipp, D., and Jacquin, L. (2008). Sensitivity analysis and passive control of cylinder flow. *Journal of Fluid Mechanics*, 615:221–252. (Cited on pages 10, 64, 65, and 71.)
- Matveev, K. (2003). *Thermoacoustic instabilities in the Rijke tube: experiments and modeling*. PhD thesis, California Institute of Technology. (Cited on page 31.)
- McBride, B. J., Zehe, M. J., and Gordon, S. (2002). NASA Glenn Coefficients for Calculating Thermodynamic Properties of Individual Species. *Technical report NASA*, 211556(September):291. (Cited on page 38.)
- Mensah, G. A., Magri, L., and Moeck, J. P. (2017). Methods for the calculation of thermoacoustic stability margins and Monte-Carlo free uncertainty quantification. *ASME Turbo Expo GT2017-64829*, pages 1–13. (Cited on page 11.)
- Mensah, G. A., Magri, L., Orchini, A., and Moeck, J. P. (2018). Effects of Asymmetry on Thermoacoustic Modes in Annular Combustors: A higher-Order Perturbation Study. *Proceedings of ASME Turbo Expo 2018: Turbomachinery Technical Conference and Exposition*, pages 1–11. (Cited on page 11.)

- Mensah, G. A. and Moeck, J. P. (2016). Assessment of thermoacoustic instabilities based on high-order adjoint perturbation theory. *Proceedings of the International Symposium: Thermoacoustic instabilities in gas turbines and rocket engines: industry meets academia*, (GTRE - 032):1–9. (Cited on page [11](#).)
- Mensah, G. A. and Moeck, J. P. (2017). Acoustic Damper Placement and Tuning for Annular Combustors: An Adjoint-Based Optimization Study. *Journal of Engineering for Gas Turbines and Power*, 139(6):061501. (Cited on page [11](#).)
- Mongia, H. C., Held, T. J., Hsiao, G. C., and Pandalai, R. P. (2003). Challenges and progress in controlling dynamics in gas turbine combustors. *Journal of Propulsion and Power*, 19(5):822–829. (Cited on page [7](#).)
- Morgans, A. S. and Duran, I. (2016). Entropy noise: A review of theory, progress and challenges. *International Journal of spray and combustion dynamics*, 8(4):285–298. (Cited on page [34](#).)
- Morgans, A. S. and Stow, S. R. (2007). Model-based control of combustion instabilities in annular combustors. *Combustion and Flame*, 150(4):380–399. (Cited on pages [13](#), [31](#), [40](#), and [41](#).)
- Muller, D. A. (2014). Pyro Board: 2D Rubens’ Tube! (Cited on page [1](#).)
- Myers, M. K. (1991). Transport of energy by disturbances in arbitrary steady flows. *Journal of Fluid Mechanics*, 226(-1):383. (Cited on page [3](#).)
- Nicoud, F., Benoit, L., Sensiau, C., and Poinso, T. (2007). Acoustic modes in combustors with complex impedances and multidimensional active flames. *AIAA Journal*, 45(2):426–441. (Cited on page [5](#).)
- Nicoud, F. and Poinso, T. (2005). Thermoacoustic instabilities: Should the Rayleigh criterion be extended to include entropy changes? *Combustion and Flame*, 142(1-2):153–159. (Cited on page [3](#).)
- Nicoud, F. and Wiecek, K. (2009). About the zero Mach number assumption in the calculation of thermoacoustic instabilities. *International Journal of Spray and Combustion Dynamics*, 1(1):67–111. (Cited on pages [5](#), [6](#), and [94](#).)
- Nielsen, E. J., Diskin, B., and Yamaleev, N. K. (2010). Discrete Adjoint-Based Design Optimization of Unsteady Turbulent Flows on Dynamic Unstructured Grids. *AIAA Journal*, 48(6):1195–1206. (Cited on page [10](#).)
- Noiray, N., Durox, D., Schuller, T., and Candel, S. (2008). A unified framework for nonlinear combustion instability analysis based on the flame describing function. *Journal of Fluid Mechanics*, 615:139. (Cited on page [6](#).)
- Noiray, N. and Schuermans, B. (2013). On the dynamic nature of azimuthal thermoacoustic modes in annular gas turbine combustion chambers. *Proceedings of the Royal Society A: Mathematical, Physical and Engineering Sciences*, 469(2151):20120535–20120535. (Cited on page [6](#).)

- Oefelein, J. C. and Yang, V. (1993). Comprehensive Review of Liquid-Propellant Combustion Instabilities in F-1 Engines. *Journal of Propulsion and Power*, 9(5):657–677. (Cited on pages 7 and 8.)
- Orchini, A. and Juniper, M. P. (2016a). Flame Double Input Describing Function analysis. *Combustion and Flame*, 171:87–102. (Cited on page 6.)
- Orchini, A. and Juniper, M. P. (2016b). Linear stability and adjoint sensitivity analysis of thermoacoustic networks with premixed flames. *Combustion and Flame*, 165:97–108. (Cited on page 11.)
- Orf, A. and Cant, R. S. (1996). Reaction rate modelling for premixed turbulent methane-air flames. *Joint Meeting of the Portuguese, British, Spanish and Swedish Sections of the Combustion Institute*. (Cited on page 152.)
- Paschereit, C. O., Schuermans, B., Polifke, W., and Mattson, O. (2002). Measurement of Transfer Matrices and Source Terms of Premixed Flames. *Journal of Engineering for Gas Turbines and Power*, 124(2):239. (Cited on page 149.)
- Peters, M. C. a. M., Hirschberg, a., Reijnen, a. J., and Wijnands, a. P. J. (1993). Damping and reflection coefficient measurements for an open pipe at low Mach and low Helmholtz numbers. *Journal of Fluid Mechanics*, 256(-1):499. (Cited on page 25.)
- Poinsot, T. and Veynante, D. (2005). *Theoretical and Numerical Combustion*. Edwards, 2nd edition. (Cited on page 6.)
- Pralits, J. O., Brandt, L., and Gianneti, F. (2010). Instability and sensitivity of the flow around a rotating circular cylinder. *Journal of Fluid Mechanics*, 650:513. (Cited on page 10.)
- Preetham (2007). *Modeling the Response of Premixed Flames to Flow Disturbances*. PhD thesis, Georgia Institute of Technology. (Cited on page 149.)
- Press, W., Teukolsky, S., Vetterling, W., Flannery, B., Ziegel, E., Press, W., Flannery, B., Teukolsky, S., and Vetterling, W. (1992). *Numerical Recipes: The Art of Scientific Computing*. Cambridge University Press, Cambridge, 2nd edition. (Cited on page 110.)
- Putnam, A. a. and Dennis, W. R. (1954). Burner Oscillations of the Gauze-Tone Type. *The Journal of the Acoustical Society of America*, 26(5):716–725. (Cited on page 3.)
- Qadri, U. A., Mistry, D., and Juniper, M. P. (2013). Structural sensitivity of spiral vortex breakdown. *Journal of Fluid Mechanics*, 720(1957):558–581. (Cited on page 10.)
- Rayleigh, L. (1878). The Explanation of Certain Acoustical Phenomena. *Nature*, 18:319–321. (Cited on pages 2 and 3.)
- Richards, G. a., Straub, D. L., and Robey, E. H. (2003). Passive Control of Combustion Dynamics in Stationary Gas Turbines. *Journal of Propulsion and Power*, 19(5):795–810. (Cited on page 7.)
- Richards, G. A., Thornton, J. D., Robey, E. H., and Arellano, L. (2007). Open-Loop Active Control of Combustion Dynamics on a Gas Turbine Engine. *Journal of Engineering for Gas Turbines and Power*, 129(1):38. (Cited on page 8.)

- Rigas, G., Jamieson, N. P., Li, L. K. B., and Juniper, M. P. (2016). Experimental sensitivity analysis and control of thermoacoustic systems. *Journal of Fluid Mechanics*, 787:R1 1–11. (Cited on page 11.)
- Rijke, P. L. (1859). Notiz über eine neue Art, die in einer an beiden Enden offenen Röhre enthaltene Luft in Schwingungen zu versetzen. *Annalen der Physik und Chemie*, 183(6):339–343. (Cited on page 31.)
- Rolland, E. O., De Domenico, F., and Hochgreb, S. (2017). Theory and application of reverberated direct and indirect noise. *Journal of Fluid Mechanics*, 819:435–464. (Cited on page 16.)
- Rubens, H. and Krigar-Menzel, O. (1905). Flammenröhre für akustische Beobachtungen. *Annalen der Physik*, 322(6):149–164. (Cited on page 1.)
- Schmid, P. J. and Brandt, L. (2014). Analysis of fluid systems: stability, receptivity, sensitivity. *Applied Mechanics Reviews*, 66(March 2014). (Cited on pages 7 and 47.)
- Schmitt, P., Poinso, T., Schuermans, B., and Geigle, K. P. (2007). Large-eddy simulation and experimental study of heat transfer, nitric oxide emissions and combustion instability in a swirled turbulent high-pressure burner. *Journal of Fluid Mechanics*, 570:17. (Cited on page 15.)
- Schuermans, B., Bellucci, V., and Paschereit, C. O. (2003). Thermoacoustic Modeling and Control of Multi Burner Combustion Systems. In *Volume 2: Turbo Expo 2003*, number GT2003-38688, pages 509–519. ASME. (Cited on page 16.)
- Schuller, T., Durox, D., and Candel, S. (2003). A unified model for the prediction of laminar flame transfer functions: Comparisons between conical and V-flame dynamics. *Combustion and Flame*, 134(1-2):21–34. (Cited on page 149.)
- Selle, L., Lartigue, G., Poinso, T., Koch, R., Schildmacher, K. U., Krebs, W., Prade, B., Kaufmann, P., and Veynante, D. (2004). Compressible large eddy simulation of turbulent combustion in complex geometry on unstructured meshes. *Combustion and Flame*, 137(4):489–505. (Cited on page 5.)
- Silva, C. F., Magri, L., Runte, T., and Polifke, W. (2016). Uncertainty Quantification of Growth Rates of Thermoacoustic Instability by an Adjoint Helmholtz Solver. *Journal of Engineering for Gas Turbines and Power*, 139(1):011901. (Cited on page 11.)
- Sipp, D., Marquet, O., Meliga, P., and Barbagallo, A. (2010). Dynamics and Control of Global Instabilities in Open-Flows: A Linearized Approach. *Applied Mechanics Reviews*, 63(3):030801. (Cited on page 10.)
- Spagnoli, B. and Airiau, C. (2008). Adjoint analysis for noise control in a two-dimensional compressible mixing layer. *Computers & Fluids*, 37(4):475–486. (Cited on page 10.)
- Staffelbach, G., Gicquel, L., Boudier, G., and Poinso, T. (2009). Large Eddy Simulation of self excited azimuthal modes in annular combustors. *Proceedings of the Combustion Institute*, 32(2):2909–2916. (Cited on page 15.)

- Stow, S. R. and Dowling, A. P. (2001). Thermoacoustic oscillations in an annular combustor. *ASME Turbo Expo*, pages 2001–GT–0037. (Cited on pages 12, 16, 17, 19, and 131.)
- Stow, S. R. and Dowling, A. P. (2003). Modelling of Circumferential Modal Coupling due to Helmholtz resonators. *ASME Turbo Expo*. (Cited on pages 12, 16, 40, and 131.)
- Stow, S. R. and Dowling, A. P. (2004). Low-order modelling of thermoacoustic limit cycles. *ASME Turbo Expo*. (Cited on pages 12, 16, 20, 21, 41, and 131.)
- Stow, S. R. and Dowling, A. P. (2009). A Time-Domain Network Model for Nonlinear Thermoacoustic Oscillations. *Journal of Engineering for Gas Turbines and Power*, 131(3):031502. (Cited on page 16.)
- Stow, S. R., Dowling, A. P., and Hynes, T. P. (2002). Reflection of circumferential modes in a choked nozzle. *Journal of Fluid Mechanics*, 467:1–25. (Cited on pages 23, 61, and 62.)
- Strobio-Chen, L., Bomberg, S., and Polifke, W. (2016). Propagation and generation of acoustic and entropy waves across a moving flame front. *Combustion and Flame*, 166:170–180. (Cited on pages 22 and 36.)
- Strykowski, P. J. and Sreenivasan, K. R. (1990). On the formation and suppression of vortex ‘shedding’ at low Reynolds numbers. *Journal of Fluid Mechanics*, 218(-1):71. (Cited on pages 9 and 10.)
- Trefethen, L. N. and Embree, M. (2005). *Spectra and Pseudospectra*. Princeton University Press, New Jersey, 1st edition. (Cited on page 30.)
- Umeh, C. O., Kammer, L. C., and Barbu, C. (2007). Active Combustion Control by Fuel Forcing at Non-Coherent Frequencies. In *Volume 2: Turbo Expo 2007*, pages 471–479. ASME. (Cited on page 8.)
- Worth, N. A. and Dawson, J. R. (2013a). Modal dynamics of self-excited azimuthal instabilities in an annular combustion chamber. *Combustion and Flame*, 160(11):2476–2489. (Cited on pages 42 and 153.)
- Worth, N. A. and Dawson, J. R. (2013b). Self-excited circumferential instabilities in a model annular gas turbine combustor: Global flame dynamics. *Proceedings of the Combustion Institute*, 34(2):3127–3134. (Cited on pages 13, 31, 42, 43, 44, 45, and 153.)
- Yu, H. (2017). Inverse Uncertainty Quantification in Thermoacoustics. Technical Report August, University of Cambridge. (Cited on page 91.)
- Zahn, M., Schulze, M., Hirsch, C., and Sattelmayer, T. (2016). Impact of Quarter Wave Tube Arrangement on Damping of Azimuthal Modes. In *Volume 4A: Combustion, Fuels and Emissions*, number GT2016-56450, page V04AT04A025. ASME. (Cited on page 7.)
- Zhao, D. and Li, X. (2015). A review of acoustic dampers applied to combustion chambers in aerospace industry. *Progress in Aerospace Sciences*, 74:114–130. (Cited on page 7.)

- Zhao, D., Lu, Z., Zhao, H., Li, X. Y., Wang, B., and Liu, P. (2018). A review of active control approaches in stabilizing combustion systems in aerospace industry. *Progress in Aerospace Sciences*, 97(April 2017):35–60. (Cited on page [7](#).)
- Zhao, D. and Morgans, A. S. (2009). Tuned passive control of combustion instabilities using multiple Helmholtz resonators. *Journal of Sound and Vibration*, 320(4-5):744–757. (Cited on page [8](#).)
- Zhao, D., Morgans, A. S., and Dowling, A. P. (2011). Tuned Passive Control of Acoustic Damping of Perforated Liners. *AIAA Journal*, 49(4):725–734. (Cited on page [9](#).)

Appendix A

Flame transfer functions

Flame transfer functions (FTF) are a key element in the analysis of linear thermoacoustic oscillations. They are used to track the response of the flame, and hence the heat release fluctuations, to incident perturbations of the velocity or the equivalence ratio. Therefore, FTFs are the fundamental component that close the loop between acoustics and combustion.

FTFs can be obtained by experimental or numerical investigation, such as in [Ducruix et al. \(2000\)](#); [Langhorne \(1988\)](#); [Paschereit et al. \(2002\)](#) or by analytical methods such as in [Schuller et al. \(2003\)](#). In the latter branch we have the pioneering work of [Fleifil et al. \(1996\)](#), which used a level set method to track the evolution flame front (originally introduced by [Markstein \(1964\)](#)) and then relate it to the unsteady heat release kinematics from which the flame transfer function is derived. The method was applied to a conical flame, and the FTF obtained was a function of the perturbations of the flame area only, which were directly related to the velocity perturbations at the base of the flame. Many other studies in thermoacoustics followed a similar procedure to obtain FTFs for different flame models. For example, [Dowling \(1999\)](#) used a similar procedure to analyse a V-shaped flame, and goes a step further by developing a flame describing function to analyse the nonlinear regime in which the burner operates. Later on [Hubbard and Dowling \(1998\)](#) and [Dowling and Hubbard \(2000\)](#), extended the types of perturbation studied by considering that the laminar flame speed and the enthalpy of reaction are also a function of the equivalence ratio perturbations. More extensions include the use of flame stretch and strain effects ([Preetham, 2007](#)), as well as different methods to account for the total time that a fluctuation takes to reach the flame front ([Graham, 2012](#)).

For this thesis, we use an extended version of the FTF of the V-shaped flame presented in [Dowling \(1999\)](#) which is derived in the following section. We also present the FTF of the annular cone used in [Hubbard and Dowling \(1998\)](#) for completeness.

A.1 V-shaped FTF

Flame front kinematics

Consider the burner given in Fig. A.1. In order to obtain an analytical flame model, we assume that the flow is one dimensional and that the geometry is axisymmetric.

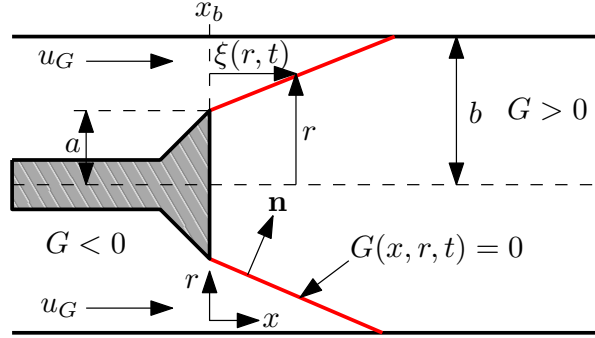


Fig. A.1 Geometry of the flame holder and flame initiation surface from Dowling (1999).

The flame front kinematics are modelled with a kinematic transport equation also known as the G-equation:

$$\frac{\partial G}{\partial t} + \mathbf{u} \cdot \nabla G = S_c |\nabla G|, \quad (\text{A.1})$$

where $G(x, r, t) = 0$ is the flame initiation surface, $\mathbf{u} = \langle u_G, 0 \rangle$ is the velocity vector and S_c is the flame propagation speed. We designate $G_0 = x - \xi(r, t)$ as the position of the flame front. Then, after substitution into Eq. (A.1) and some manipulation, we obtain an equation that allows us to track the evolution of the flame front:

$$\frac{\partial \xi}{\partial t} = u_G - S_c \sqrt{1 + \left(\frac{\partial \xi}{\partial r} \right)^2}. \quad (\text{A.2})$$

The relationship between the flame front (ξ) and the flame area (A_f) is:

$$dA_f = 2\pi r \sqrt{1 + \left(\frac{\partial \xi}{\partial r} \right)^2} dr, \quad (\text{A.3})$$

which when integrated from $r = a$ to $r = b$, provides the mean area of the flame.

Heat release

The time variation of the spatially integrated heat release $Q(t)$ is given by:

$$Q(t) = \int_{A_f} \eta \rho h_r(\phi) S_c(\phi) \, dA_f \quad (\text{A.4})$$

where η is the combustion efficiency, ρ is the density of the unburned mixture, $h_r(\phi)$ is the enthalpy of reaction, $S_c(\phi)$ is the flame propagation speed and A_f is the flame surface area. h_r and S_c are assumed to depend on the equivalence ratio ϕ only.

Density

Through all this analysis we will consider that the variations in density due to the change in temperature at the flame front are negligible. Hence, we will approximate it as $\rho = \bar{\rho}$.

Equivalence ratio

For our model we assume that the perturbations need to convect from the base of the flame until they reach the flame front, which gives a mean convection time delay of $\bar{\xi}/\bar{u}$. Here we have used \bar{u} to denote the mean value of u_G . In the linear regime, where we assume the existence of small harmonic perturbations, we can approximate the equivalence ratio fluctuations by:

$$\hat{\phi} = -\bar{\phi} \frac{\hat{u}}{\bar{u}} e^{-i\omega \bar{\xi}/\bar{u}}. \quad (\text{A.5})$$

Enthalpy of reaction

For the applications that are going to be analysed, the fuel used is ethylene (C_2H_4) -air mixture. To model the enthalpy of reaction of such fuel we follow [Graham \(2012\)](#) and assume the following form:

$$h_r = \frac{3.2 \times 10^6 \min(\phi, 1)}{1 + 0.067\phi} \, \text{J kg}^{-1}. \quad (\text{A.6})$$

To ensure that the function is continuous everywhere, we substitute the $\min(\phi, 1)$ function by a smooth approximation of the Heaviside step function $H_s(\phi)$:

$$\min(\phi, 1) = \phi - H_s(\phi - 1)(\phi - 1), \quad \text{where} \quad H_s(\phi - 1) = \frac{1}{2} \left(1 + \tanh \left(\frac{\phi - 1}{\delta} \right) \right). \quad (\text{A.7})$$

where $\delta = 1 \times 10^{-5}$ is a small value that controls the sharpness of the step.

Flame speed

Depending on the operating conditions, the flame speed S_c can be in the laminar regime (denoted by S_L) or in the turbulent regime (denoted by S_T). The laminar flame speeds of several hydrocarbons was approximated by [Orf and Cant \(1996\)](#) using the following formula which is a function of the equivalence ratio only:

$$S_L = k_1 \phi^{k_2} e^{-k_3(\phi - k_4)^2}, \quad (\text{A.8})$$

where the constants $k_1 = 16.83104 \text{ ms}^{-1}$, $k_2 = 4.51397$, $k_3 = 1.10530$, $k_4 = -0.72341$ where obtained by regression of the data presented in [Jomaas et al. \(2005\)](#), for the case of the laminar flame speed of ethylene in air at atmospheric conditions. Since the experimental cases that we are modelling are in the turbulent regime we use the extension given in [Lipatnikov and Chomiak \(2002\)](#) to approximate the turbulent flame speed from the laminar flame speed:

$$S_T = S_L \left(1 + C \left(\frac{u_T}{S_L} \right)^n \right)^{1/n}, \quad (\text{A.9})$$

where $C = 2.1$ and $n = 2$ are constants of the model and $u_T = 1.1476 \text{ ms}^{-1}$ is the r.m.s. turbulent velocity, which is treated as a constant to adjust the flame length in order to match the experimental results.

Flame transfer function

Given the previous considerations, for linear perturbations in the frequency domain expanding Eq. (A.4) and dividing by the mean quantities gives:

$$\frac{\hat{Q}}{\bar{Q}} = \frac{\int_{A_f} \hat{h}_r d\bar{A}_f}{\bar{h}_r \bar{A}_f} + \frac{\int_{A_f} \hat{S}_T d\bar{A}_f}{\bar{S}_T \bar{A}_f} + \frac{\int_{A_f} d\hat{A}_f}{\bar{A}_f}. \quad (\text{A.10})$$

After integration, each of the terms can be further subdivided into the different contributions ([Cho and Lieuwen, 2003](#)):

$$\frac{\hat{Q}}{\bar{Q}} = \frac{\hat{u}}{\bar{u}} (\mathcal{F}_u + \mathcal{F}_\phi) \quad \text{with} \quad \mathcal{F}_\phi = \mathcal{F}_h + \mathcal{F}_{S_D} + \mathcal{F}_{S_A}. \quad (\text{A.11})$$

Here, \mathcal{F}_u is the transfer function due to velocity perturbations at the flame base and \mathcal{F}_ϕ is the transfer function due to equivalence ratio perturbations convected from the

base of the flame to the flame front. The latter is further subdivided into \mathcal{F}_h , \mathcal{F}_{S_D} and \mathcal{F}_{S_A} which are the transfer functions due to equivalence ratio perturbations through the enthalpy of reaction, the direct contribution of the flame speed to the unsteady heat release and the contribution of the flame speed through the fluctuations induced in the flame area respectively. Their transfer functions are given by:

$$\mathcal{F}_u = \frac{2}{i\Omega/V(a+b)} \left(a - be^{-i\Omega/V} + \frac{b-a}{i\Omega/V} (1 - e^{-i\Omega/V}) \right), \quad (\text{A.12a})$$

$$\mathcal{F}_h = - \left(\frac{\bar{\phi}}{\bar{h}_r} \frac{dh_r}{d\phi} \bigg|_{\bar{\phi}} \right) \frac{2}{i\Omega V(a+b)} \left(a - be^{-i\Omega V} + \frac{b-a}{i\Omega V} (1 - e^{-i\Omega V}) \right), \quad (\text{A.12b})$$

$$\mathcal{F}_{S_D} = - \left(\frac{\bar{\phi}}{\bar{S}_T} \frac{dS_T}{d\phi} \bigg|_{\bar{\phi}} \right) \frac{2}{i\Omega V(a+b)} \left(a - be^{-i\Omega V} + \frac{b-a}{i\Omega V} (1 - e^{-i\Omega V}) \right), \quad (\text{A.12c})$$

$$\begin{aligned} \mathcal{F}_{S_A} = & - \left(\frac{\bar{\phi}}{\bar{S}_T} \frac{dS_T}{d\phi} \bigg|_{\bar{\phi}} \right) \frac{2}{i\Omega/V(a+b)} \frac{\bar{u}^2}{\bar{S}_T^2} \left(\left(a - be^{-i\Omega/V} + \frac{b-a}{i\Omega/V} (1 - e^{-i\Omega/V}) \right) \dots \right. \\ & \left. - \left(a - be^{-i\Omega V} + \frac{b-a}{i\Omega V} (1 - e^{-i\Omega V}) \right) \right). \end{aligned} \quad (\text{A.12d})$$

Here we have used the non dimensional frequency $\Omega = \omega(b-a)/\bar{S}_T$ and the elongation factor $V = \sqrt{1 - \bar{S}_T^2/\bar{u}^2}$. As noted in [Dowling and Hubbard \(2000\)](#) for a similar flame, the component given by \mathcal{F}_{S_A} presents saturation. That is, unlike the rest of the components, it does not decay with increasing frequency.

Application to the CUED annular combustor

The V-shaped flame is characteristic of the CUED combustor as reported in [Worth and Dawson \(2013a\)](#). The major differences presented between this model and the experiment include the fact that flame merging, and swirling is not accounted for in the FTF; which according to [Worth and Dawson \(2013a,b\)](#) are key features in the self excitation of the combustion chamber.

To model the FTF of such system we have used as geometric parameters $a = \sqrt{A_1/\pi}$ and $b = \sqrt{2A_1/\pi}$, where A_1 represents the area in between a single premix duct and the bluff body. These values produce a similar flame front structure to that modelled using LES in [Bauerheim \(2014\)](#) and allow us to track the dependency of the flame front with respect to the burner area. Given that the experiment used premixed conditions,

we consider that $\mathcal{F}_\phi = 0$. Using the parameters for this configuration (§ 3.7), Fig. A.2, shows the total FTF for a single burner.

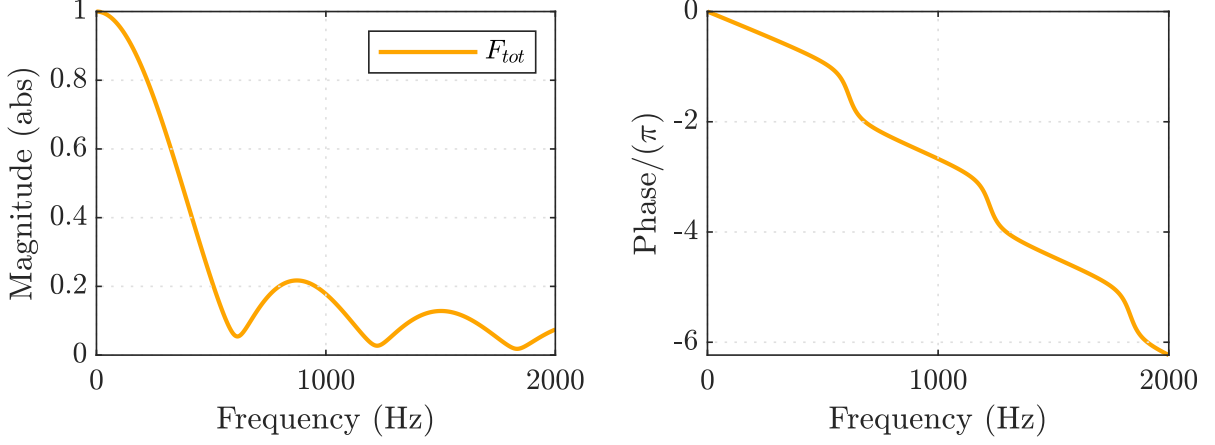


Fig. A.2 Flame transfer function for a single burner used in the CUED annular combustor.

A.2 Annular cone FTF

The second flame transfer function follows directly from the previous one. It is derived in [Hubbard and Dowling \(1998\)](#) and presented here for completeness. The major consideration is that now there are two flame fronts (denoted by $\xi(r, t)$ and $\zeta(r, t)$) that merge exactly at the middle as shown in Fig. A.3. We also considered that it is an elongated flame and therefore $V \approx 1$. To match the flame length ([Balachandran, 2005](#)) we set $u_T = 0.38254 \text{ ms}^{-1}$. The result is an axisymmetric flame with the following FTF:

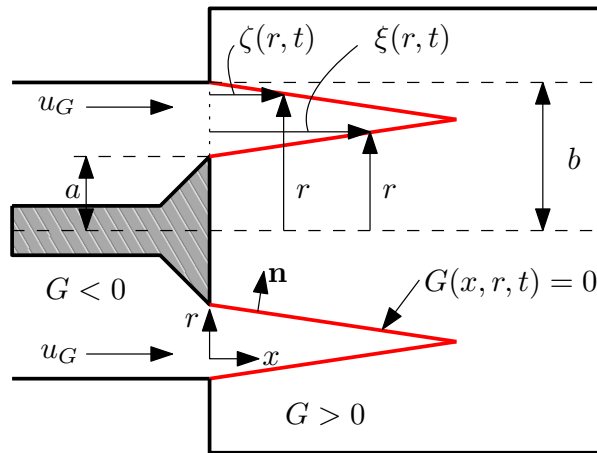


Fig. A.3 Geometry of the flame holder and flame initiation surface, adapted from [Hubbard and Dowling \(1998\)](#).

$$\mathcal{F}_u = \frac{1}{i\Omega} (1 - e^{-i\Omega}), \quad (\text{A.13a})$$

$$\mathcal{F}_h = - \left(\frac{\bar{\phi}}{\bar{h}_r} \frac{dh_r}{d\phi} \bigg|_{\bar{\phi}} \right) \frac{1}{i\Omega} (1 - e^{-i\Omega}), \quad (\text{A.13b})$$

$$\mathcal{F}_{S_D} = - \left(\frac{\bar{\phi}}{\bar{S}_T} \frac{dS_T}{d\phi} \bigg|_{\bar{\phi}} \right) \frac{1}{i\Omega} (1 - e^{-i\Omega}), \quad (\text{A.13c})$$

$$\mathcal{F}_{S_A} = \left(\frac{\bar{\phi}}{\bar{S}_T} \frac{dS_T}{d\phi} \bigg|_{\bar{\phi}} \right) e^{-i\Omega}, \quad (\text{A.13d})$$

where $\Omega = \omega(b - a)/(2\bar{S}_T)$ is a non dimensional frequency that depends on the external duct radius b , the internal duct radius a and the mean flame speed. The components of the FTF as applied to the longitudinal combustor (§ 3.5) are given in Fig. A.4.

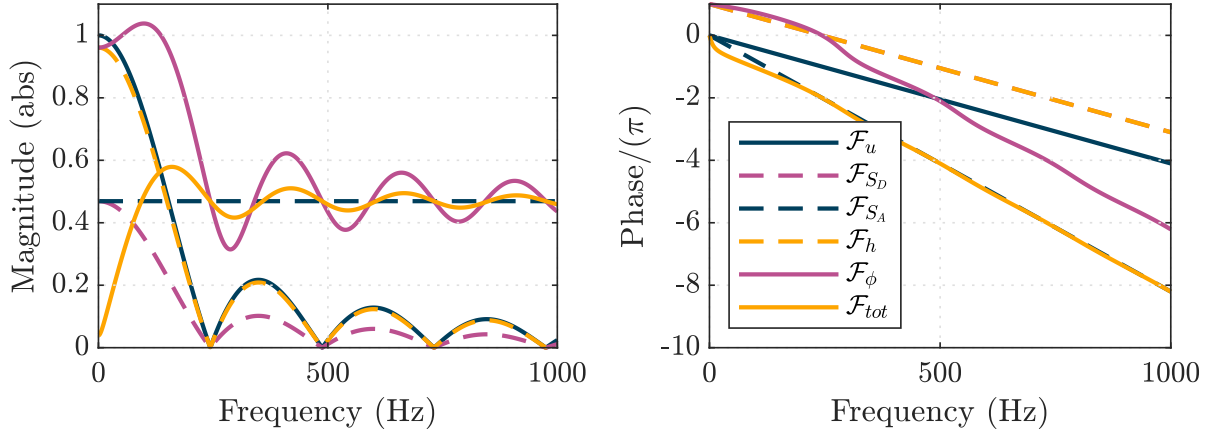


Fig. A.4 Components of the flame transfer function for the longitudinal combustor.

Appendix B

Mean Flow matrix $L(\omega)$

The components of the mean flow matrix $L(\omega)$ are:

$$\begin{aligned}
L_{11} &= \frac{\bar{\rho}_2}{\bar{\rho}_1} \left((1 - \bar{M}_1) - R_u e^{-i\omega\tau_u} (1 + \bar{M}_1) \right) - \left(\frac{\bar{\rho}_2}{\bar{\rho}_1} - 1 \right) k e^{-i\omega\tau} (1 - R_u e^{-i\omega\tau}), \\
L_{12} &= \frac{\bar{c}_1}{\bar{c}_2} \left((\bar{M}_2 + 1) + R_d e^{-i\omega\tau_d} (\bar{M}_2 - 1) \right), \\
L_{13} &= \frac{\bar{c}_1}{\bar{c}_2} \left(-\bar{M}_2 + R_e e^{-i\omega\tau_e} (\bar{M}_2 - 1) \right), \\
L_{21} &= -(\bar{M}_1 - 1)^2 - R_u e^{-i\omega\tau_u} (\bar{M}_1 + 1)^2, \\
L_{22} &= (\bar{M}_2 + 1)^2 + R_d e^{-i\omega\tau_d} (\bar{M}_2 - 1)^2, \\
L_{23} &= -\bar{M}_2^2 + R_e e^{-i\omega\tau_e} (\bar{M}_2 - 1)^2, \\
L_{31} &= \frac{1 - \gamma \bar{M}_1}{\gamma - 1} + \frac{\bar{M}_1^2}{2} (3 - \bar{M}_1) - N \left(1 - \bar{M}_1 - k e^{-i\omega\tau} \right) \dots \\
&\quad - R_u e^{-i\omega\tau_u} \left(\frac{1 + \gamma \bar{M}_1}{\gamma - 1} + \frac{\bar{M}_1^2}{2} (3 + \bar{M}_1) - N \left(1 + \bar{M}_1 - k e^{-i\omega\tau} \right) \right) \dots \\
&\quad + k \frac{\bar{Q}/A}{\bar{u}_1} \frac{e^{-i\omega\tau}}{\bar{\rho}_1 \bar{c}_1^2} (1 - R_u e^{-i\omega\tau}), \\
L_{32} &= \frac{\bar{c}_2}{\bar{c}_1} \left(\frac{1 + \gamma \bar{M}_2}{\gamma - 1} + \frac{\bar{M}_2^2}{2} (3 + \bar{M}_2) - R_d e^{-i\omega\tau_d} \left(\frac{1 - \gamma \bar{M}_2}{\gamma - 1} + \frac{\bar{M}_2^2}{2} (3 - \bar{M}_2) \right) \right), \\
L_{33} &= \frac{\bar{c}_2}{\bar{c}_1} \left(-\frac{1}{2} \bar{M}_2^3 + R_e e^{-i\omega\tau_e} \left((\bar{M}_2 - 1) \left(\frac{1}{\gamma - 1} - \bar{M}_2 + \frac{\bar{M}_2^2}{2} \right) \right) \right),
\end{aligned}$$

where

$$N = \frac{1}{2} \left(\bar{M}_1^2 - \bar{M}_2^2 \frac{\bar{p}_2}{\bar{p}_1} \right) + \frac{1 - \bar{p}_2/\bar{p}_1}{\gamma(\gamma - 1)}.$$

Appendix C

Sensitivities to base flow modifications at the jump conditions

For the jump conditions governed by mass, axial momentum and energy fluxes, consider the sensitivities to base flow modifications at the jump conditions in vector form: $\mathbf{J}_i = [J_{M_i}, J_{X_i}, J_{E_i}]^T$. Assuming that the adjoint variables of the unsteady jump conditions are given by a_m^+ , a_x^+ , a_θ^+ and a_e^+ , and that the vector direct unsteady variables is given by: $\hat{\mathbf{q}}_i = [\hat{p}_i^*, \hat{\rho}_i^*, \hat{u}_i^*, \hat{w}_i^*]^T$, the sensitivities to base flow modifications become:

$$\mathbf{J}_i = \left(a_m^+ \mathbf{B}_{m_i} + a_x^+ \mathbf{B}_{x_i} + a_\theta^+ \mathbf{B}_{\theta_i} + a_e^+ \mathbf{B}_{e_i} \right) \hat{\mathbf{q}}_i, \quad (\text{C.1})$$

where, by considering

$$\mathbf{f}_c = \left[\bar{h}_i(\gamma_i - 1) - \bar{c}_i^2 - \frac{1}{2} \bar{u}_i^2(\gamma_i + 1), \gamma_i \bar{u}_i, 0, -(\gamma_i - 1) \right]^T,$$

and $\Gamma_i = \gamma_i \bar{p}_i - \bar{\rho}_i \bar{u}_i^2$, the matrices that depend only on base flow variables become:

$$\mathbf{B}_{m_i} = \frac{1}{\Gamma_i} \left[\begin{array}{c|c|c} \mathbf{0} & \mathbf{f}_c & -\frac{\bar{\rho}_i}{\bar{u}_i} \left(\mathbf{f}_c + \begin{bmatrix} \bar{c}_i^2 - \bar{u}_i^2 \\ 0 \\ 0 \end{bmatrix} \right) \\ \hline \mathbf{0} & 2\bar{u}_i \mathbf{f}_c & -2\bar{\rho}_i \begin{bmatrix} \bar{c}_i^2 - \bar{u}_i^2 \\ 0 \\ 0 \end{bmatrix} \\ \hline \mathbf{0} & \mathbf{0} & \mathbf{0} \end{array} \right], \quad (\text{C.2})$$

$$\mathbf{B}_{x_i} = \frac{1}{\Gamma_i} \left[\begin{array}{c|c|c} \mathbf{0} & 2\bar{u}_i \mathbf{f}_c & -2\bar{\rho}_i \begin{bmatrix} \bar{c}_i^2 - \bar{u}_i^2 \\ 0 \\ 0 \end{bmatrix} \\ \hline \mathbf{0} & \mathbf{0} & \mathbf{0} \\ \hline \mathbf{0} & \mathbf{0} & \mathbf{0} \end{array} \right], \quad (\text{C.3})$$

$$\mathbf{B}_{\theta_i} = \left[\begin{array}{c|c|c} \mathbf{0} & \mathbf{0} & \mathbf{0} \\ \hline \mathbf{0} & \mathbf{0} & -R_i \\ \hline \mathbf{0} & \mathbf{0} & 0 \end{array} \right], \quad (\text{C.4})$$

$$\begin{aligned}
\mathbf{B}_{e_i} = & \frac{1}{\Gamma_i} \left[\begin{array}{c|c|c} \frac{\gamma_i}{\gamma_i - 1} \mathbf{f}_c & \left(\bar{h}_i - \frac{\bar{c}_i^2}{\gamma_i - 1} + \frac{3}{2} \bar{u}_i^2 \right) \mathbf{f}_c & -\frac{\bar{\rho}_i}{\bar{u}_i} \left(\left(\bar{h}_i - \frac{\bar{u}_i^2}{2} \right) \mathbf{f}_c + (\bar{c}_i^2 - \bar{u}_i^2) \begin{bmatrix} \bar{u}_i^2 \\ 0 \\ 1 \end{bmatrix} \right) \end{array} \right] \cdots \\
& + \frac{\Lambda}{\Gamma_i} \left[\begin{array}{c|c|c|c|c} -\bar{M}_i^2 \mathbf{f}_c + (1 - \bar{M}_i^2) \begin{bmatrix} \bar{h}_i + \frac{\bar{u}_i^2}{2} \\ 0 \\ -1 \end{bmatrix} & \frac{\bar{u}_i^2}{\gamma_i} \mathbf{f}_c - \frac{\bar{c}_i^2 - \bar{u}_i^2}{\gamma_i} \begin{bmatrix} \bar{h}_i + \frac{\bar{u}_i^2}{2} \\ 0 \\ -1 \end{bmatrix} & \begin{bmatrix} \bar{h}_i + \frac{\bar{u}_i^2}{2} \\ 0 \\ -1 \end{bmatrix} & \mathbf{0} & \mathbf{0} \end{array} \right], \tag{C.5}
\end{aligned}$$

with

$$\Lambda = \frac{dc_p(\bar{T}_i)}{d\bar{T}_i} \frac{(\gamma_i - 1)\bar{T}_i}{R_g}.$$

Similarly, for jump conditions that depend on the mass and energy fluxes, together with entropy conservation, the sensitivities to base flow modifications $\mathbf{G}_i = [G_{M_i}, G_{S_i}, G_{E_i}]^T$ are given by:

$$\mathbf{G}_i = \left(a_m^+ C_{m_i} + a_x^+ C_{s_i} + a_\theta^+ C_{\theta_i} + a_e^+ C_{e_i} \right) \hat{\mathbf{q}}_i, \tag{C.6}$$

where, by considering:

$$\mathbf{g}_c = \frac{1}{\bar{\rho}_i} \left[- \left(\bar{h}_i + \frac{1}{2} \bar{u}_i^2 + \bar{c}_i^2 \right), -\frac{\bar{m}_i \bar{c}_i^2}{R_g}, 1 \right]^T, \tag{C.7}$$

and $\beta_i = \bar{c}_i^2 - \bar{u}_i^2$, the matrices become:

$$C_{m_i} = \frac{1}{\beta_i} \left[\begin{array}{c|c|c} \mathbf{0} & \mathbf{g}_c & -\frac{\bar{\rho}_i}{\bar{u}_i} (\mathbf{g}_c) - \frac{1}{\bar{u}_i} \begin{bmatrix} \bar{c}_i^2 - \bar{u}_i^2 \\ 0 \\ 0 \end{bmatrix} \end{array} \right] \mathbf{0}, \tag{C.8}$$

$$\begin{aligned}
C_{s_i} = & \frac{c_p(\bar{T}_i)}{\bar{m}_i \beta_i} \left[\begin{array}{c|c|c} \frac{\gamma_i}{\bar{c}_i^2} \mathbf{g}_c + \frac{1 - \bar{M}_i^2}{\bar{\rho}_i} \begin{bmatrix} \gamma_i \\ \bar{m}_i (\gamma_i - 1) \\ 0 \end{bmatrix} & -\mathbf{g}_c - \frac{1}{\bar{\rho}_i} \begin{bmatrix} \bar{c}_i^2 - \bar{u}_i^2 \\ 0 \\ 0 \end{bmatrix} & \mathbf{0} \end{array} \right] \cdots \\
& + \frac{dc_p(\bar{T}_i)}{d\bar{T}_i} \left[\begin{array}{c|c|c} -\gamma_i \left(\mathbf{g}_c + \frac{\bar{c}_i^2 - \bar{u}_i^2}{\bar{\rho}_i} \begin{bmatrix} 1 \\ \bar{m}_i \\ 0 \end{bmatrix} \right) & \bar{c}_i^2 \left(\mathbf{g}_c + \frac{\bar{c}_i^2 - \bar{u}_i^2}{\bar{\rho}_i} \begin{bmatrix} 1 \\ \bar{m}_i \\ 0 \end{bmatrix} \right) & \mathbf{0} \end{array} \right] \mathbf{0}, \tag{C.9}
\end{aligned}$$

$$C_{\theta_i} = \left[\begin{array}{c|c|c|c} \mathbf{0} & \mathbf{0} & \mathbf{0} & -R_i \\ \hline & & & 0 \\ \hline & & & 0 \end{array} \right], \tag{C.10}$$

$$\begin{aligned}
\mathbf{C}_{e_i} = & \frac{1}{\beta_i} \left[\begin{array}{c|c} \frac{\gamma_i}{\gamma_i - 1} \mathbf{g}_c & \left(\bar{h}_i - \frac{\bar{c}_i^2}{\gamma_i - 1} + \frac{3}{2} \bar{u}_i^2 \right) \mathbf{g}_c \\ \hline \end{array} - \frac{\bar{\rho}_i}{\bar{u}_i} \left(\bar{h}_i - \frac{\bar{u}_i^2}{2} \right) \mathbf{g}_c - \frac{1}{\bar{u}_i} (\bar{c}_i^2 - \bar{u}_i^2) \begin{bmatrix} \bar{u}_i^2 \\ 0 \\ 1 \end{bmatrix} \middle| \begin{array}{c} \mathbf{0} \\ \hline \end{array} \right] \cdots \\
& + \frac{\Lambda}{\beta_i} \left[\begin{array}{c|c} -\mathbf{g}_c - \frac{\bar{c}_i^2 - \bar{u}_i^2}{\bar{\rho}_i} \begin{bmatrix} 1 \\ \frac{\bar{m}_i}{R_g} \\ 0 \end{bmatrix} & \begin{array}{c|c} \frac{\bar{c}_i^2}{\gamma_i} \left(\mathbf{g}_c + \frac{\bar{c}_i^2 - \bar{u}_i^2}{\bar{\rho}_i} \begin{bmatrix} 1 \\ \frac{\bar{m}_i}{R_g} \\ 0 \end{bmatrix} \right) & \begin{array}{c} \mathbf{0} \\ \hline \mathbf{0} \end{array} \end{array} \right].
\end{aligned} \tag{C.11}$$

Appendix D

The triviality of choice of side on which a perturbation is applied

In this appendix we prove that, to first order, the side on which a perturbation is applied has no influence in the computation of the unsteady feedback sensitivity. Let subscript 1 denote the position just before the perturbation (x_0^-) and subscript 2 the position just after (x_0^+). Given the assumption that the base flow variables do not change after the perturbation then, $\bar{u}_2 = \bar{u}_1 = \bar{u}$, and similar expressions for the other variables. We begin by rewriting the momentum and energy equations from Eq. 5.9 using $\epsilon = \mathcal{F}_u$:

$$\bar{\rho}\bar{u}(\hat{u}_2 - \hat{u}_1) + (\hat{p}_2 - \hat{p}_1) = \epsilon\hat{u}_1, \quad (\text{D.1})$$

$$\bar{u}(\hat{p}_2 - \hat{p}_1) + \gamma\bar{p}(\hat{u}_2 - \hat{u}_1) = 0. \quad (\text{D.2})$$

Equating the momentum equation (D.1) to zero gives:

$$\bar{\rho}\bar{u}\left(\hat{u}_2 - \hat{u}_1\left(1 + \frac{\epsilon}{\bar{\rho}\bar{u}}\right)\right) + (\hat{p}_2 - \hat{p}_1) = 0. \quad (\text{D.3})$$

Divide the equation by $(1 + \frac{\epsilon}{\bar{\rho}\bar{u}})$:

$$\bar{\rho}\bar{u}\left(\frac{1}{(1 + \frac{\epsilon}{\bar{\rho}\bar{u}})}\hat{u}_2 - \hat{u}_1\right) + \frac{1}{(1 + \frac{\epsilon}{\bar{\rho}\bar{u}})}(\hat{p}_2 - \hat{p}_1) = 0. \quad (\text{D.4})$$

For small values of $\frac{\epsilon}{\bar{\rho}\bar{u}}$ the fraction in the equation can be expanded. To first order it gives:

$$\bar{\rho}\bar{u}\left(\left(1 - \frac{\epsilon}{\bar{\rho}\bar{u}}\right)\hat{u}_2 - \hat{u}_1\right) + \left(1 - \frac{\epsilon}{\bar{\rho}\bar{u}}\right)(\hat{p}_2 - \hat{p}_1) = 0. \quad (\text{D.5})$$

Rearranging:

$$\bar{\rho}\bar{u}(\hat{u}_2 - \hat{u}_1) + (\hat{p}_2 - \hat{p}_1) = \epsilon\hat{u}_2 + \frac{\epsilon}{\bar{\rho}\bar{u}}(\hat{p}_2 - \hat{p}_1). \quad (\text{D.6})$$

To prove that $(\hat{p}_2 - \hat{p}_1)$ is of order ϵ , recast Eq. (D.1):

$$(\hat{p}_2 - \hat{p}_1) = \epsilon\hat{u}_1 - \bar{\rho}\bar{u}(\hat{u}_2 - \hat{u}_1), \quad (\text{D.7})$$

From the energy equation (D.2) we have that:

$$(\hat{u}_2 - \hat{u}_1) = -\frac{\bar{u}}{\bar{\rho}\bar{c}^2}(\hat{p}_2 - \hat{p}_1). \quad (\text{D.8})$$

Substituting back into Eq. (D.7) gives:

$$(\hat{p}_2 - \hat{p}_1) = \epsilon\hat{u}_1 + \bar{M}^2(\hat{p}_2 - \hat{p}_1), \quad (\text{D.9})$$

Rearranging:

$$(\hat{p}_2 - \hat{p}_1) = \frac{\epsilon}{1 - \bar{M}^2}\hat{u}_1. \quad (\text{D.10})$$

Hence, the unsteady pressure difference is of order ϵ , substituting this result back into equation (D.6) and removing second order terms gives:

$$\bar{\rho}\bar{u}(\hat{u}_2 - \hat{u}_1) + (\hat{p}_2 - \hat{p}_1) = \epsilon\hat{u}_2 \quad (\text{D.11})$$

Hence, it has been shown that, to first order, the side on which the perturbation is applied has no influence in the computation of the unsteady feedback mechanisms.

Appendix E

Computing matrix δL for the Rijke tube

Once the boundary conditions have been applied, by taking the Laplace transform of the perturbed wave solutions (i.e., Eq. (5.18)) we obtain:

$$A_+^{ii} = A_{-1} \left(R_u e^{-i\omega\tau_u} + E_{A_{+1}} \right), \quad (\text{E.1a})$$

$$A_-^{ii} = A_{-1} (1 + E_{A_{-1}}), \quad (\text{E.1b})$$

$$A_+^{iii} = A_{+2} (1 + E_{A_{+2}}), \quad (\text{E.1c})$$

$$A_-^{iii} = A_{+2} (R_d e^{-i\omega\tau_d} + E_{A_{-2}}), \quad (\text{E.1d})$$

where

$$\begin{aligned} E_{A_{+1}} = & \frac{1}{2} \left(\mathcal{F}_{p_1} \left(R_u e^{-i\omega\tau_u} + e^{-i\omega\tau_a} \right) + \frac{\mathcal{F}_{u_1}}{\bar{\rho}_1 \bar{c}_1} \left(R_u e^{-i\omega\tau_u} - e^{-i\omega\tau_a} \right) \dots \right. \\ & \left. + \frac{\mathcal{Q}_{p_1}}{\bar{c}_1} \left(R_u e^{-i\omega\tau_u} + e^{-i\omega\tau_a} \right) + \frac{\mathcal{Q}_{u_1}}{\bar{\rho}_1 \bar{c}_1^2} \left(R_u e^{-i\omega\tau_u} - e^{-i\omega\tau_a} \right) \right), \end{aligned} \quad (\text{E.2a})$$

$$\begin{aligned} E_{A_{-1}} = & \frac{1}{2} \left(\mathcal{F}_{p_1} \left(R_u e^{-i\omega(\tau_u - \tau_a)} + 1 \right) + \frac{\mathcal{F}_{u_1}}{\bar{\rho}_1 \bar{c}_1} \left(R_u e^{-i\omega(\tau_u - \tau_a)} - 1 \right) \dots \right. \\ & \left. - \frac{\mathcal{Q}_{p_1}}{\bar{c}_1} \left(R_u e^{-i\omega(\tau_u - \tau_a)} + 1 \right) - \frac{\mathcal{Q}_{u_1}}{\bar{\rho}_1 \bar{c}_1^2} \left(R_u e^{-i\omega(\tau_u - \tau_a)} - 1 \right) \right), \end{aligned} \quad (\text{E.2b})$$

$$\begin{aligned} E_{A_{+2}} = & \frac{1}{2} \left(-\mathcal{F}_{p_2} \left(1 + R_d e^{-i\omega(\tau_d - \tau_c)} \right) - \frac{\mathcal{F}_{u_2}}{\bar{\rho}_2 \bar{c}_2} \left(1 - R_d e^{-i\omega(\tau_d - \tau_c)} \right) \dots \right. \\ & \left. - \frac{\mathcal{Q}_{p_2}}{\bar{c}_2} \left(1 + R_d e^{-i\omega(\tau_d - \tau_c)} \right) - \frac{\mathcal{Q}_{u_2}}{\bar{\rho}_2 \bar{c}_2^2} \left(1 - R_d e^{-i\omega(\tau_d - \tau_c)} \right) \right), \end{aligned} \quad (\text{E.2c})$$

$$E_{A_{-2}} = \frac{1}{2} \left(-\mathcal{F}_{p_2} \left(e^{-i\omega\tau_c} + R_d e^{-i\omega\tau_d} \right) - \frac{\mathcal{F}_{u_2}}{\bar{\rho}_2 \bar{c}_2} \left(e^{-i\omega\tau_c} - R_d e^{-i\omega\tau_d} \right) \dots \right. \\ \left. + \frac{\mathcal{Q}_{p_2}}{\bar{c}_2} \left(e^{-i\omega\tau_c} + R_d e^{-i\omega\tau_d} \right) + \frac{\mathcal{Q}_{u_2}}{\bar{\rho}_2 \bar{c}_2^2} \left(e^{-i\omega\tau_c} - R_d e^{-i\omega\tau_d} \right) \right), \quad (\text{E.2d})$$

where $\tau_a = 2(b-a)/\bar{c}_1$ and $\tau_c = 2(c-b)/\bar{c}_2$. After substitution of these expressions into the jump conditions Eq. (2.25) we get the perturbed problem:

$$(L + \delta L) (\hat{\mathbf{q}} + \delta \hat{\mathbf{q}}) = \mathbf{0}, \quad (\text{E.3})$$

where L and $\hat{\mathbf{q}}$ are given by Eq. (3.6), and δL is:

$$\delta L = \begin{bmatrix} -E_{A_{+1}} - E_{A_{-1}} & E_{A_{+2}} + E_{A_{-2}} \\ (E_{A_{-1}} - E_{A_{+1}}) \left(1 + \frac{\gamma-1}{\gamma \bar{p}_1} \beta e^{-i\omega\tau} \right) & \frac{\bar{c}_2}{\bar{c}_1} (E_{A_{+2}} - E_{A_{-2}}) \end{bmatrix}. \quad (\text{E.4})$$